

University of Southampton Research Repository ePrints Soton

Copyright © and Moral Rights for this thesis are retained by the author and/or other copyright owners. A copy can be downloaded for personal non-commercial research or study, without prior permission or charge. This thesis cannot be reproduced or quoted extensively from without first obtaining permission in writing from the copyright holder/s. The content must not be changed in any way or sold commercially in any format or medium without the formal permission of the copyright holders.

When referring to this work, full bibliographic details including the author, title, awarding institution and date of the thesis must be given e.g.

AUTHOR (year of submission) "Full thesis title", University of Southampton, name of the University School or Department, PhD Thesis, pagination

UNIVERSITY OF SOUTHAMPTON

FACULTY OF NATURAL AND ENVIRONMENTAL SCIENCES

Ocean and Earth Sciences



Investigating the drivers of perturbations to the Cenozoic carbon-climate system

by

David Ian Armstrong McKay

Thesis for the degree of Doctor of Philosophy

UNIVERSITY OF SOUTHAMPTON

ABSTRACT

FACULTY OF NATURAL AND ENVIRONMENTAL SCIENCES

Ocean and Earth Sciences

Thesis for the degree of Doctor of Philosophy

INVESTIGATING THE DRIVERS OF PERTURBATIONS TO THE CENOZOIC CARBON-CLIMATE SYSTEM

David Ian Armstrong McKay

Over the course of the Cenozoic the Earth system has shifted from a CO₂-rich 'Greenhouse' climate state to a CO₂-poor 'Icehouse' climate state. This trend is punctuated by numerous perturbations to the carbon-climate system, but the extent of the coupling between the carbon cycle and climate system, the drivers of these perturbations, and their relationship to the longer-term Cenozoic trend is still debated. In this thesis, I use biogeochemical modelling and numerical analysis to explore the key research question: 'What were the drivers of carbon-climate system perturbations during the Cenozoic?', with a focus on perturbations during the Eocene-Oligocene Transition and the mid-Miocene, the role of tipping points during these periods, and the long-term evolution of the ocean carbonate system.

The potential impact of the Columbia River Basalt large igneous province on the mid-Miocene Earth system is investigated using two biogeochemical box models. This modelling indicates that 'cryptic degassing' from intrusive and/or crust-contaminated magma of a magnitude within the estimated possible range can drive the observed carbon cycle perturbation and warming around 16.0 Ma, but cannot by itself explain other features of the mid-Miocene palaeorecords.

The hypothesised drivers of the Eocene-Oligocene Transition (EOT) carbon cycle perturbation are explored using a biogeochemical box model. The results suggest that the glacioeustatic fractionation of carbonate burial from shelf to basin can explain most of the deepening of the carbonate compensation depth (CCD) at the EOT, but that the benthic carbon isotope excursion most likely requires additional drivers.

The shelf-basin carbonate burial fractionation hypothesis is examined further in order to quantify the relationship between shelf carbonate burial extent, the CCD, and changing sea-level during the Cenozoic. This analysis confirms that carbonate burial fractionation can drive most of the CCD deepening at the EOT but is less important either before or since then, and also indicates that the sensitivity of the CCD to sea level change has significantly declined during the Cenozoic.

Palaeorecords of a number of perturbations to the carbon-climate system during the Cenozoic are analysed in search for 'early warning signals' (EWS) indicative of systemic instability and impending critical transitions, and the reliability of this method when applied to palaeorecords is critically explored. EWS are found prior to some (e.g. the EOT and Palaeocene-Eocene Thermal Maximum) but not all of the events, and the results and technique are judged to be moderately reliable.

Table of Contents

Table	of Con	tents	i
List o	f Tables	S	v
List o	f Figure	es	vii
Decla	ration o	of Authorship	xiii
Ackno	owledge	ements	xv
Some	though	its on modelling, complexity and climate change	xvii
List o	f Abbre	eviations and Symbols	xix
Chapt	ter 1:	Introduction and Background	1
1.1	The Go	oldilocks question	1
1.2	Cenozo	oic climate change	3
	1.2.1	Long-term Cenozoic cooling	3
	1.2.2	Abrupt climate shifts	5
	1.2.3	Cenozoic climate chronology	6
	1.2.4	Palaeoclimatology and the Anthropocene	8
1.3	The ge	ological carbon cycle: conceptual and numerical models	9
	1.3.1	A conceptual model of the carbon cycle	9
	1.3.2	Numerical models of the carbon cycle	16
1.4	Thesis	aims and structure	23
	1.4.1	Key research questions	23
	1.4.2	Thesis structure	24
Chap	ter 2:	Estimating the impact of the cryptic degassing of	Large
	Igneo	ous Provinces: A mid-Miocene case-study	25
2.1	Abstra	ct	25
2.2	Introdu	uction	26
2.3	The mi	id-Miocene and the Columbia River Basalt eruptions	28
2.4	Materi	als and Methods	30
	2.4.1	Modelling	30
	2.4.2	MTW08 sensitivity analyses	32

	2.4.3	Eruption chronology	32
	2.4.4	Cryptic degassing estimates	33
2.5	Result	s and Discussion	37
	2.5.1	Modelled emission scenario	38
	2.5.2	The CCD and the mid-Miocene Climate Transition	40
	2.5.3	Mid-Miocene climate change	41
2.6	Conclu	sions	43
2.7	Acknow	wledgements	43
2.8	Suppor	rting Information	44
	2.8.1	Model parameters	44
	2.8.2	Sensitivity analyses	46
Chap	ter 3:	Global carbon cycle perturbation across the Eocene	e-
	Oligo	ocene climate transition	49
3.1	Abstra	ct	49
3.2	Backgr	round	50
	3.2.1	The Eocene-Oligocene Transition	50
	3.2.2	Potential drivers of the EOT carbon cycle perturbation	51
	3.2.3	Study aims	55
3.3	Metho	d	55
	3.3.1	Modelling	55
	3.3.2	Hypotheses	56
3.4	Result	s and Discussion	58
	3.4.1	Scenarios	58
	3.4.2	Implications	68
3.5	Conclu	sions	71
3.6	Acknow	wledgements	72
3.7	Suppor	rting Information	73
	3.7.1	The SWC scenario and the climate-weathering feedback	73
	3.7.2	Extra calcium input feedbacks	74
	3.7.3	Model parameters	75

Chap	ter 4:	Declining sensitivity of the carbonate compensat	ion
	dept	h to sea level during the Cenozoic	77
4.1	Abstra	ct	77
4.2	Backgr	ound	78
	4.2.1	Evolution of the Cenozoic carbonate system	78
	4.2.2	Potential drivers of Cenozoic CCD change	79
	4.2.3	Study aims	82
4.3	Metho	dology	82
	4.3.1	Carbonate burial rates and extent	82
	4.3.2	Linking hypsometry and carbonate burial	84
	4.3.3	Shelf carbonate burial extent, sea level, and the CCD	87
	4.3.4	Climate change, tectonics, and the CCD	92
4.4	Result	s and Discussion	93
	4.4.1	Cenozoic case studies	93
	4.4.2	Cenozoic implications	96
	4.4.3	Why is the EOT unique?	97
	4.4.4	Other potential drivers of Cenozoic CCD change	98
4.5	Conclu	sions	100
4.6	Acknow	wledgements	101
Chap	ter 5:	Can early warning signals be reliably detected in	ı the
	Ceno	zoic palaeoclimate record?	103
5.1	Abstra	ct	103
5.2	Introd	uction	104
5.3	Backgr	round	105
	5.3.1	Critical transitions and early warning signals	105
	5.3.2	Potential tipping points in the palaeoclimate record	106
5.4	Metho	dology	110
	5.4.1	Early warning signal analysis	110
	5.4.2	Palaeorecords	
5.5	Rogult	s and Discussion	119

	5.5.1	Eocene-Oligocene Transition	114
	5.5.2	Palaeocene-Eocene Thermal Maximum	117
	5.5.3	Mid-Miocene Climate Transition	120
	5.5.4	Oligocene-Miocene Transition	123
	5.5.5	Early Miocene 'null' case	126
	5.5.6	K/Pg boundary and the Deccan Traps	129
	5.5.7	Sensitivity to parameter selection	132
	5.5.8	Is early warning signal analysis reliable for the palaeorece	ord?
			133
5.6	Conclu	isions	134
5.7	Acknow	wledgements	134
5.8	Suppor	rting Information	135
	5.8.1	Sliding window sensitivity analyses	135
	5.8.2	Data-point spacing	147
Chap	ter 6:	Summary and Further Work	151
6.1	Summ	ary of findings	151
6.2	Recom	mendations for further work	153
6.3	What v	were the drivers of carbon-climate system perturbations du	ring
	the Ce	nozoic?	156
List	of Refer	ences	159

List of Tables

Table 2-1:	Estimated increase in chemical weathering and silicon and phosphorus input to the ocean due to the GRB eruptions
Table 2-2:	Carbon emission estimates for the Columbia River Basalt for different degassing scenarios and sources
Table 2-3:	MTW08 biogeochemical parameters used in Chapter 2 44
Table 2-4:	LOSCAR biogeochemical parameters used in Chapter 2 45
Table 2-5:	Isotopic parameters and initial values for both MTW08 and LOSCAR used in Chapter 2
Table 3-1:	MTW08-Eocene biogeochemical parameters used in Chapter 3 75
Table 3-2:	Isotopic parameters and initial values for MTW08 used in Chapter 3
Table 5-1:	Summary of the results of conducting early warning signal analysis in Chapter 5

List of Figures

Figure 1-1:	Long-term correlation of atmospheric CO ₂ (reconstructed from
	proxies and the GEOCARB III model) and Icehouse/Greenhouse
	cycles during the Phanerozoic2
Figure 1-2:	Palaeorecords of Cenozoic benthic $\delta^{18}O$, benthic $\delta^{13}C$, carbonate
	compensation depth (CCD) and atmospheric CO ₂ (atmCO ₂)
	reconstructions
Figure 1-3:	Simplified schematic of the global carbon cycle at the present day
Figure 1-4:	Bjerrum plot of the speciation of Dissolved Inorganic Carbon in
	the ocean
Figure 1-5:	Diagram of the relative positions of the Calcite Saturation
	Horizon (CSH), the lysocline, and the CCD, and their
	relationship to ocean bathymetry, $CaCO_3$ accumulation rate, and sediment $CaCO_3$ wt%
Figure 1-6:	Systems diagram illustrating the climate-weathering negative
	feedback loop
Figure 1-7:	A schematic of the modern carbonate-silicate geochemical cycle
	as represented in the 'BLAG' model
Figure 1-8:	Schematic representation of the MTW08 model, illustrating its
	physical scheme and biogeochemical cycling
Figure 1-9:	Schematic of the LOSCAR model in its Palaeocene/Eocene
	configuration
Figure 2-1:	Comparison of palaeorecords between 10 and 22 Ma of benthic
	for a minifera δ^{13} C and δ^{18} O, equatorial Pacific CCD palaeodepth,
	and atmCO2 reconstructions
Figure 2-2:	a) Map illustrating the location and the extent of the Columbia
-	River Basalts, the Grande Ronde Basalt formation and
	associated dyke swarms. b) Illustration of the main Columbia

	River Basalt formations with each formation's extrusive volume	
	and the eruption chronology used in this study	.29
Figure 2-3:	Palaeorecords of the mid-Miocene climate and carbon cycle	.30
Figure 2-4:	The main results of our MTW08 and LOSCAR simulations	
	compared against mid-Miocene palaeorecords	.37
Figure 2-5:	Simulation results of carbonate weathering flux, deep ocean	
	carbonate ion concentration, and change in CCD for our best-fit	
	MTW08 emissions scenario	.39
Figure 2-6:	Simulation results of Particulate Organic Carbon (POC) burial	
	rates, POC $\delta^{13}C$ and change in benthic $\delta^{13}C$ for our best-fit	
	MTW08 emissions scenario	.39
Figure 2-7:	Sensitivity analysis of adjusting volcanic $\delta^{13}C$ from -4 ‰ to -12 ‰	
	in our best-fit MTW08 scenario	.46
Figure 2-8:	Sensitivity analysis of changing the silicate and carbonate	
	weathering exponents in our best-fit MTW08 scenario	.47
Figure 2-9:	Sensitivity analysis of changing the key MTW08 parameters in	
	our best-fit MTW08 scenario	.48
Figure 3-1:	Palaeorecords of benthic $\delta^{18}O$, benthic $\delta^{13}C$, CCD, carbonate	
	accumulation, and $_{\mbox{\scriptsize atm}} CO_2$ reconstructions across the Eocene	
	Oligocene Transition (EOT)	.51
Figure 3-2:	Simulation results for the carbonate burial fractionation (CBF)	
	scenario compared against EOT palaeorecords	.59
Figure 3-3:	Simulation results for the increased ocean ventilation (IOV)	
	scenario compared against EOT palaeorecords	.61
Figure 3-4:	Simulation results for the carbon capacitor exchange (CCE)	
	scenario compared against EOT palaeorecords	.63
Figure 3-5:	Simulation results for the decreased CaCO ₃ export or increased	
	Corg burial (EBR) scenario compared against EOT palaeorecords	.64
Figure 3-6:	Simulation results for the silicate weathering and calcium (SWC)	
	scenario compared against EOT palaeorecords	.66

Figure 3-7:	Simulation results for different combinations of the best-fit scenarios shown in previous figures compared against EOT palaeorecords
Figure 3-8:	Sensitivity test results for the silicate weathering and calcium (SWC) scenario illustrating the impact of the climate-weathering feedback on the deepening of the CCD across the EOT
Figure 3-9:	Systems diagram illustrating the feedbacks associated with increasing calcium input to the ocean in the SWC scenario
Figure 4-1:	Cenozoic palaeorecords of benthic $\delta^{13}C$, CCD, and $_{atm}CO_2$ reconstructions
Figure 4-2:	Schematic illustrating shelf-basin carbonate burial fractionation due to eustatic sea level fall
Figure 4-3:	Global hypsometric curve of the Earth's surface plotted from the NOAA Hypsographic Curve based on ETOPO1
Figure 4-4:	Histograms of the area of the seafloor between 3000 and 5500 mbmsl for each 1 m depth interval (bottom x-axis, blue line) and in 500 m depth bins (top x-axis, red bars)
Figure 4-5:	Reconstruction of Cenozoic sea level relative to modern sea level 87
Figure 4-6:	The hypsometry of the Earth's surface within 500 m of modern sea level
Figure 4-7:	Bar chart illustrating the estimated deepening of the CCD in response to different processes driving shelf carbonate extent decline during the Cenozoic and the EOT in particular90
Figure 4-8:	Cenozoic plots of reconstructed sea level relative to modern, estimated shelf carbonate burial extent, CCD deepening relative to 50 My, and the sensitivity of the CCD to falling sea level 91
Figure 4-9:	Cross-plot illustrating the changing sensitivity of the CCD to hypothetical falls in sea level during the last 70 My
Figure 4-10:	CCD deepening required to extend basin carbonate extent by 100000 km ²

Figure 5-1:	Cenozoic palaeorecords of benthic δ^{18} O, benthic δ^{13} C, CCD, and atm CO ₂ reconstructions with the events focused on in Chapter 5
	labelled
Figure 5-2:	EWS analyses of benthic $\delta^{18}O$ in the run-up to the EOT115
Figure 5-3:	EWS analyses of benthic $\delta^{13}C$ in the run-up to the EOT116
Figure 5-4:	EWS analyses of benthic $\delta^{18}O$ in the run-up to the Palaeocene-Eocene Thermal Maximum (PETM).
Figure 5-5:	EWS analyses of benthic $\delta^{13}C$ in the run-up to the PETM
Figure 5-6:	EWS analyses of benthic $\delta^{18}O$ in the run-up to the mid-Miocene Climate Transition (MMCT).
Figure 5-7:	EWS analyses of benthic $\delta^{13}C$ in the run-up to the MMCT122
Figure 5-8:	EWS analyses of benthic $\delta^{18}O$ in the run-up to the Oligocene-Miocene Transition (OMT)
Figure 5-9:	EWS analyses of benthic $\delta^{13}C$ in the run-up to the OMT125
Figure 5-10:	EWS analyses of benthic $\delta^{18}O$ from the late Oligocene to the early Miocene
Figure 5-11:	EWS analyses of benthic $\delta^{13}C$ from the late Oligocene to the early Miocene
Figure 5-12:	EWS analyses of benthic $\delta^{18}O$ in the run-up to the K/Pg boundary
Figure 5-13:	EWS analyses of benthic $\delta^{13}C$ in the run-up to the K/Pg boundary
Figure 5-14:	EWS analyses of benthic $\delta^{18}O$ in the run-up to the EOT with variable sliding window length
Figure 5-15:	EWS analyses of benthic $\delta^{13}C$ in the run-up to the EOT with variable sliding window length.
Figure 5-16:	EWS analyses of benthic $\delta^{18}O$ in the run-up to the PETM with variable sliding window length

Figure 5-17:	EWS analyses of benthic δ^{13} C in the run-up to the PETM with variable sliding window length
Figure 5-18:	EWS analyses of benthic $\delta^{18}O$ in the run-up to the MMCT with variable sliding window length
Figure 5-19:	EWS analyses of benthic $\delta^{13}C$ in the run-up to the MMCT with variable sliding window length
Figure 5-20:	EWS analyses of benthic $\delta^{18}O$ in the run-up to the OMT with variable sliding window length
Figure 5-21:	EWS analyses of benthic $\delta^{13} C$ in the run-up to the OMT with variable sliding window length
Figure 5-22:	EWS analyses of benthic $\delta^{18}O$ from the late Oligocene to the early Miocene with variable sliding window length
Figure 5-23:	EWS analyses of benthic $\delta^{13}C$ from the late Oligocene to the early Miocene with variable sliding window length
Figure 5-24:	EWS analyses of benthic $\delta^{18}O$ in the run-up to the K/Pg boundary with variable sliding window length
Figure 5-25:	EWS analyses of benthic $\delta^{13}C$ in the run-up to the K/Pg boundary with variable sliding window length
Figure 5-26:	Time since the previous data-point plotted for each data-point, illustrating the variable spacing of the data-points for the isotope records prior to the EOT
Figure 5-27:	Time since the previous data-point plotted for each data-point, illustrating the variable spacing of the data-points for the isotope records prior to the PETM
Figure 5-28:	Time since the previous data-point plotted for each data-point, illustrating the variable spacing of the data-points for the isotope records prior to the MMCT.
Figure 5-29:	Time since the previous data-point plotted for each data-point, illustrating the variable spacing of the data-points for the isotope records prior to the OMT

Figure 5-30:	Time since the previous data-point plotted for each data-point,		
	illustrating the variable spacing of the data-points for the isotope		
	records during the late Oligocene and early Miocene149		
Figure 5-31:	Time since the previous data-point plotted for each data-point,		
	illustrating the variable spacing of the data-points for the isotope		
	records prior to the K/Pg boundary149		

Declaration of Authorship

I, David I. Armstrong McKay, declare that the thesis entitled Investigating the drivers of perturbations to the Cenozoic carbon-climate system and the work presented in the thesis are my own and have been generated by me as the result of my own original research.

I confirm that:

- This work was done wholly or mainly while in candidature for a research degree at this University;
- 2. Where any part of this thesis has previously been submitted for a degree or any other qualification at this University or any other institution, this has been clearly stated;
- 3. Where I have consulted the published work of others, this is always clearly attributed;
- 4. Where I have quoted from the work of others, the source is always given. With the exception of such quotations, this thesis is entirely my own work;
- 5. I have acknowledged all main sources of help;
- 6. Where the thesis is based on work done by myself jointly with others, I have made clear exactly what was done by others and what I have contributed myself;
- 7. Parts of this work have been published as:

Armstrong McKay, D. I., T. Tyrrell, P. A. Wilson, and G. L. Foster (2014), Estimating the impact of the cryptic degassing of Large Igneous Provinces: A mid-Miocene case-study, *Earth and Planetary Science Letters*, 403, 254–262.

Armstrong McKay, D. I., T. Tyrrell and P. A. Wilson (in revision), Global carbon cycle perturbation across the Eocene-Oligocene climate transition, *Paleoceanography*.

Signed:	 	
- 6		
Date:	 	

Acknowledgements

Firstly I would like to thank my supervisors Toby Tyrrell and Paul Wilson for their guidance of my growing academic skills, for persevering with comments on the numerous manuscript iterations presented to them, and for providing invaluable academic advice on many occasions. I would also like to thank my panel chairs Heiko Pälike and Kevin Oliver for their advice on my PhD direction and manuscript drafts, Gavin Foster for his collaboration on the work presented in Chapter 2, and Andy Ridgwell and James Dyke for additional discussion and advice during this PhD.

My family and close friends have been a constant source of support and compassion throughout my PhD, with special thanks going to my parents and my partner Rachael for consistently encouraging and caring for me throughout it all (and to Mum and Rachael for proofreading this thesis). My friends, housemates, and various student and community groups have also been a great source of fun and relaxation over the last four years – many convivial pints and conservation bonfires were had in the making of this PhD.

The lively NOCS PhD community has also played a big part in my PhD life. Being part of the PG committee and the teams behind the Post Seminar Social Hour of Educational Discussion (PSSHED, i.e. definitely not Happy Hour) and the PG Chronicle has provided many an opportunity for productive and enjoyable procrastination, while the Palaeo group has provided yet more loosely science-related drinking opportunities. The CTHULHU (Complex earTH system nUmerical modeLling and pHysical Understanding) discussion group was also a brief but enjoyable collaboration – thanks goes to those of my colleagues who improbably agreed that a discussion group with a convoluted acronym named after a terrifying and vengeful elder god was a Good Idea. Beyond Southampton my PhD provided the opportunity to meet many new colleagues and friends elsewhere, with the legendary Urbino Summer School in Paleoclimatology deserving a special mention (Prego!).

My PhD has given me plenty of opportunities for travel to various conferences and summer schools for which I am also thankful, with particularly memorable trips to Goldschmidt and ICP (on a sleeper and high-speed train loop to Florence and Barcelona via Paris), IUGG in Prague, CBEP in Ferrara, and EGU in Vienna. Mark Hopwood also gave me the opportunity to turn the computer off and do some 'real' fieldwork for once in Hardangerfjord, Norway, which was also much appreciated.

Thanks also goes to my whisky collection, which in recent months especially has smoothed the end to many a long working day. In particular, Bushmills, Jameson,

Tullamore Dew, Talisker, Whisky Breton and Laphroaig have been of great assistance to this thesis.

Finally, I am thankful to the Natural Environment Research Council (NERC) for providing studentship funding (grant number NE/J500112/1) to enable this project.

Some thoughts on modelling, complexity and climate change

"Finding simplicity in complexity is the driving force behind scientific modelling processes. What is regarded as an achievement within research is the ability to test a hypothesis on any given problem by creating simple models that can explain a complex reality. Simplification is a process that is initiated by the desire to capture the essence of a complex problem. This simplification can be formed either objectively or subjectively. But total objectivity in research is a mere illusion and modellers often find themselves slipping into the practice of over-complexity, or being locked into certain routines or subjective opinions."

Hördur V. Haraldsson & Harald U. Sverdrup, Finding Simplicity in Complexity in Biogeochemical Modelling, in Environmental Modelling: Finding Simplicity in Complexity, Edited by J. Wainwright & M. Mulligan, 2004

"The original moment for the creation of a system...comes when an observer makes a cut. Before the cut... only an undifferentiated complexity exists, impossible to comprehend in its noisy multifariousness... The cut helps to tame the noise of the world by introducing a distinction between inside and outside. What is inside is further divided and organized... What is outside is left behind, an undifferentiated unity."

N. Katherine Hayles, Making the Cut, in Observing Complexity: Systems Theory and Postmodernity, 2000

"Essentially, all models are wrong, but some are useful."

George E. P. Box (& Norman R. Draper), Empirical Model-Building and Response Surfaces, 1987

"To retain respect for either models or sausages, one must not watch too carefully what goes into them."

Adapted by Andy J. Ridgwell from a remark attributed to Otto Von Bismarck, 2001

"The climate system is an angry beast, and we are poking at it with sticks."

Wallace S. Broecker, c. 1991

List of Abbreviations and Symbols

[]: Concentration in seawater

%: Permil (parts per thousand)

¹²C: Carbon-12 stable isotope

¹³C: Carbon-13 stable isotope

atmCO₂: Atmospheric CO₂

Ca²⁺: Calcium ion

CaCO₃: Calcium carbonate

CCD: Carbonate (or Calcite if specified) Compensation Depth

CO₂: Carbon dioxide

CO₃²·: Carbonate ion

Corg: Organic Carbon

DIC: Dissolved Inorganic Carbon

DOC: Dissolved Organic Carbon

EECO: Early Eocene Climatic Optimum

EOT: Eocene-Oligocene Transition

EWS: Early warning signals

K/Pg: Cretaceous/Palaeogene Boundary

ka: Thousand years ago

ky: Thousand years

Ma: Million years ago

MCO: Miocene Climatic Optimum

MECO: Mid-Eocene Climatic Optimum

MMCT: Mid-Miocene Climate Transition

My: Million years

NH: Northern Hemisphere

OMT: Oligocene-Miocene Transition

PCO: Pliocene Climatic Optimum

pCO₂: Partial pressure of CO₂

PETM: Palaeocene-Eocene Thermal Maximum

PFSC: Permafrost Soil Carbon

Pg: Petagrams (10¹⁵ g), equivalent to Gigatonnes (Gt)

PIC: Particulate Inorganic Carbon

POC: Particulate Organic Carbon

ppm(v): Parts per million (volume)

wt%: Weight percent

 $\delta^{13}C$: Carbon stable isotopic signature (ratio of ^{13}C to ^{12}C measured in ‰)

 $\delta^{18}O$: Oxygen stable isotopic signature (ratio of ^{18}O to ^{16}O measured in ‰)

 Ω : Saturation state of the ocean with respect to calcite (or aragonite if

specified)

Chapter 1:

Introduction and Background

In this chapter the scientific context and rationale of this thesis is outlined, beginning with the broad question of the continuous habitability of the Earth followed by a discussion of both long and short-term climate change during the Cenozoic and the role of palaeoclimatology in the study of the Anthropocene. Conceptual and numerical models of the carbon cycle are then explored before a more detailed description is given of the biogeochemical models used in this thesis. Finally, the aims and structure of this thesis are outlined.

1.1 The Goldilocks question

Earth has remained consistently hospitable since life first emerged as early as ~3.8 billion years (By) ago [Ohtomo et al., 2014], but this continued habitability is difficult to explain. Solar luminosity was ~30 % lower when the Earth formed but our planet did not permanently freeze in its early history. Similarly, the gradual increase in energy reaching the Earth since then has not triggered a runaway greenhouse effect. This apparent paradox is known as the 'faint young sun problem' [Sagan and Mullen, 1972; Rampino and Caldeira, 1994. This behaviour would require either elevated planetary albedo or elevated concentrations of greenhouse gases, with the latter suspected to be the primary factor in preventing a runaway icehouse on the early Earth and during subsequent 'Snowball Earth' episodes [Walker, 1985; Kirschvink, 1992; Berner, 1994; Hoffman, 1998; Pavlov et al., 2000]. Declining concentrations of greenhouse gases are then hypothesised to have countered the gradual increase in solar luminosity. However, despite the stabilising influence of declining greenhouse gas concentrations the Earth's climate has still fluctuated considerably during the last ~3.8 By, primarily between 'Icehouse' states characterised by globally cool temperatures and polar ice sheets and 'Greenhouse' states characterised by warm and ice-free conditions [Fischer, 1982; Veizer et al., 1999, 2000]. Variable atmospheric CO₂ concentrations, rather than fluctuating solar or cosmic radiation, are hypothesised to be the primary driver of climate fluctuations during at least the Phanerozoic [Berner, 1991; Shaviv and Veizer, 2003; Royer et al., 2004a, 2004b; Came et al., 2007] (Figure 1-1), suggesting that atmospheric CO₂ has

acted as the primary control on long-term climate dynamics. These fluctuations in CO₂ and the climate state have never become extreme enough to exterminate life during the past ~3.8 By, with Greenhouse conditions never intensifying so much as to lead to runaway global warming as on Venus [Ingersoll, 1969; Rasool and De Bergh, 1970; Goldblatt et al., 2013]. This continuous Goldilockean 'just right' climate has been interpreted as implying that there are feedbacks in the Earth system, such as the climate-weathering feedback or modulation by life itself, that are strong enough to act as an ultimate climate 'thermostat' that limits the range climate can change within and so prevents both permanent Snowball or Venusian climates [Lovelock, 1972, 1979; Lovelock and Margulis, 1974; Walker et al., 1981; Berner et al., 1983; Watson and Lovelock, 1983; Berner, 1992; Dyke and Weaver, 2013]. Alternatively our observation of this history might be subject to the weak anthropic principle, with the relative stability of Earth's climate at least partially down to chance [Watson, 2004; Tyrrell, 2013]. Despite considerable research on this topic over the last few decades, the debate over the dominant drivers of long-term CO2 and climate change has not yet been settled. In particular, the decline of atmospheric CO2 and global temperatures during the last 66 million years (My) is of particular dispute.

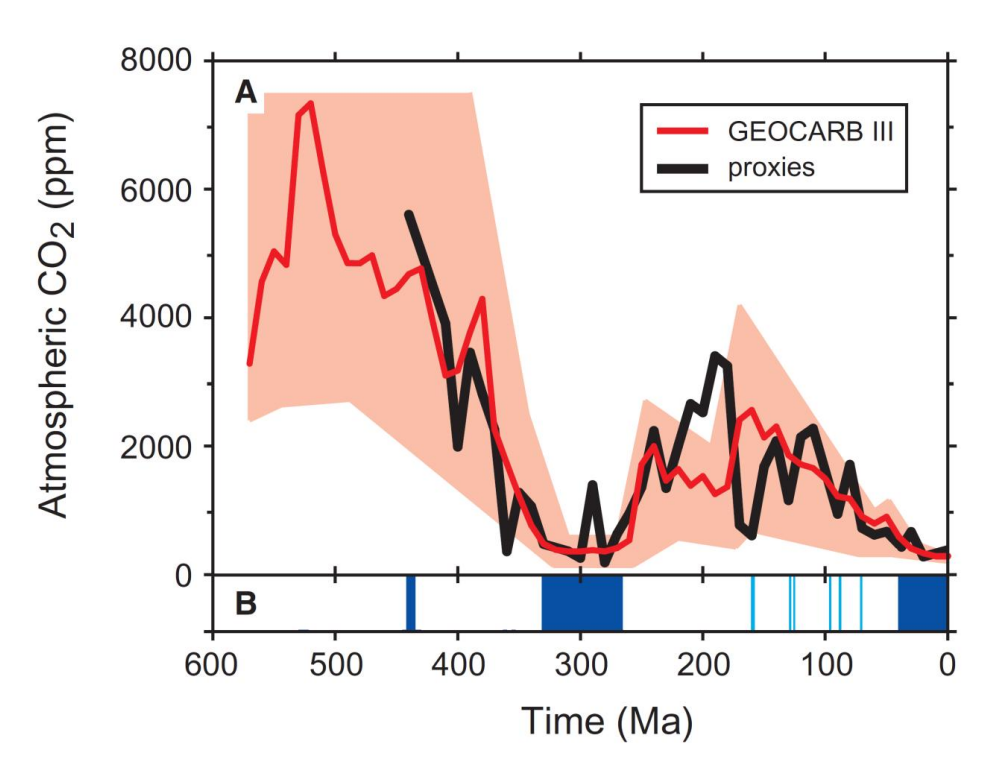


Figure 1-1: Long-term correlation of a) atmospheric CO₂ (reconstructed from proxies (black line) and the GEOCARB III model (red line, red band for uncertainty based on sensitivity analysis)), and b) Icehouse/Greenhouse cycles (with glaciations marked by the blue bars) during the Phanerozoic (reproduced and modified from *Royer et al.* [2004a] with fair-use permission from copyright-holder *Geological Society of America*)

1.2 Cenozoic climate change

1.2.1 Long-term Cenozoic cooling

During the course of the Cenozoic era, which spans the last 66 My, Earth's climate has shifted from the Greenhouse state that began in the Triassic to the Icehouse state we remain in today, as revealed by the positive trend in the global stack of benthic oxygen isotope data recorded in benthic foraminifera [Zachos et al., 2001b, 2008] (Figure 1-2). During this time atmospheric CO₂ (atmCO₂) has gradually declined, with atmCO₂ falling from ~1000 ppm in the Eocene to below ~300 ppm during the late Miocene [Pearson and Palmer, 2000; Royer et al., 2001; Beerling and Royer, 2011]. This decline has been hypothesised to be the result of either declining volcanic outgassing as mid ocean ridge spreading rates decreased and the subduction of carbonate-rich sediment in the Tethys Ocean ceased; increased silicate weathering rates due to the uplift of the Himalayas and the Tibetan Plateau drawing down atm CO2 through the Urey reaction (see Section 1.3.1.4); or increased organic carbon and carbonate burial in seafloor sediment due to increasing productivity and preservation rates [Berner, 1991; Larson, 1991; Raymo and Ruddiman, 1992; Raymo, 1994; Derry and France-Lanord, 1996; France-Lanord and Derry, 1997; Kump and Arthur, 1997; Royer et al., 2004a; Kent and Muttoni, 2008, 2013; Lefebvre et al., 2013]. The decline in atmCO₂ is in turn hypothesised to have driven global cooling via the greenhouse effect, resulting in the shift from a high-atmCO₂ Greenhouse world to a low-atmCO₂ Icehouse world [Arrhenius, 1897; Hansen et al., 2008].

Several other potential drivers of Cenozoic cooling not involving the carbon cycle have also been proposed. It has been suggested that the opening of the Drake Passage and Tasman Gateway in the Southern Ocean allowed the formation and strengthening of the Antarctic Circumpolar Current, which in turn thermally isolated Antarctica enough to initiate regional cooling and ice sheet growth [Frakes and Kemp, 1972; Kennett and Shackleton, 1976; Kennett, 1977; Flower, 1999; Exon et al., 2000; Smith and Pickering, 2003; Sijp et al., 2014]. The changing albedo of the Earth's surface would have also had a significant impact on global climate. Changing global palaeogeography due to continental drift favoured warmer global temperatures during periods such as the mid-Miocene, by reducing albedo and topography and increasing ocean heat transport [Henrot et al., 2010; Herold et al., 2011; Knorr et al., 2011], and the Cretaceous-Palaeogene [Barron et al., 1980, 1984; Barron, 1981, 1985; Barron and Washington, 1984; Bice et al., 2000], while the drift of Antarctica

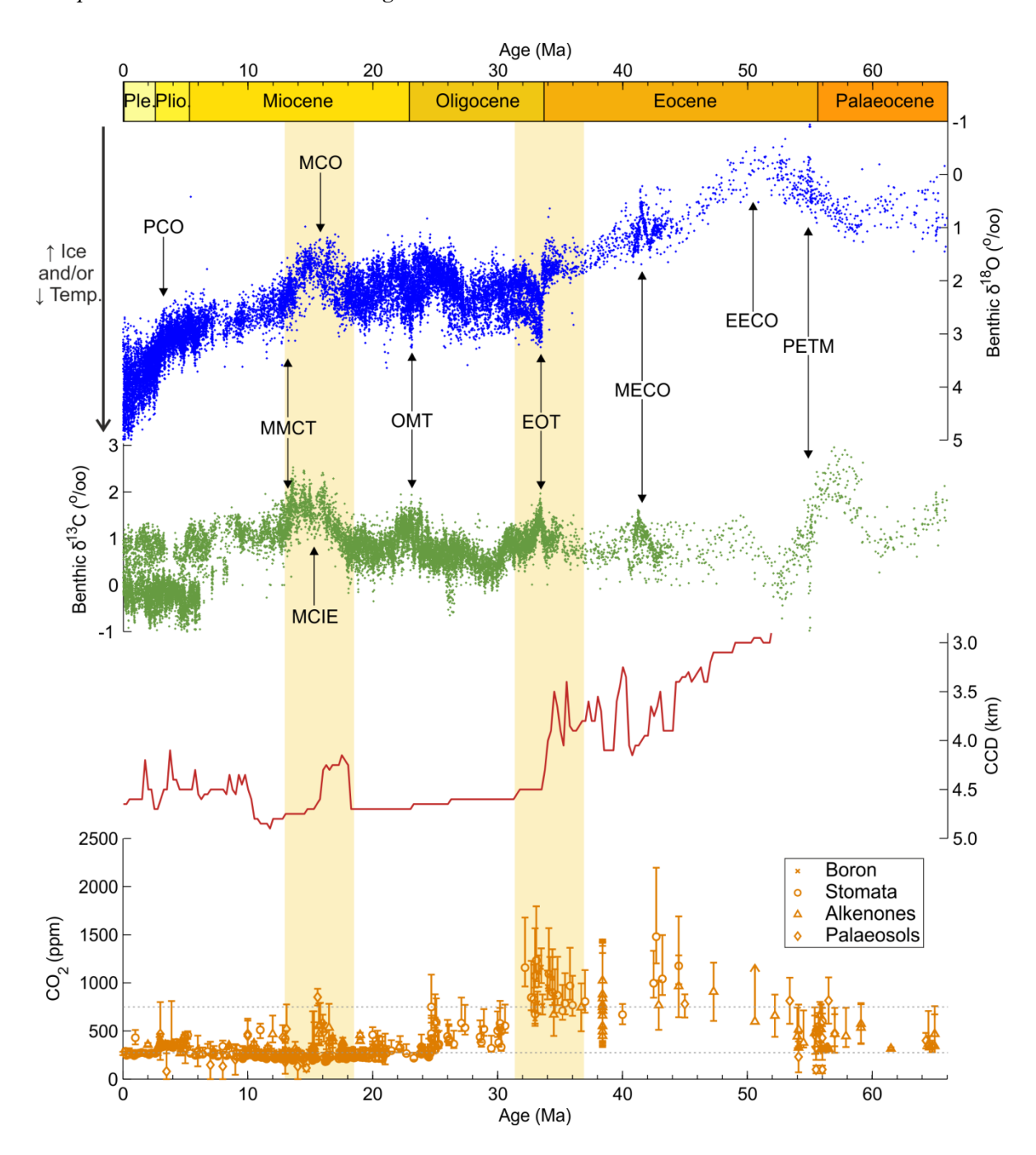


Figure 1-2: Palaeorecords of Cenozoic a) benthic δ^{18} O, b) benthic δ^{13} C, c) carbonate compensation depth (CCD) reconstructed from the equatorial Pacific, and d) atmospheric CO₂ reconstructions [Zachos et al., 2001b, 2008; Beerling and Royer, 2011; Pälike et al., 2012]. Significant climate and carbon cycle events are labelled, the grey dotted lines in the bottom panel mark the hypothesised ~750 ppm and ~280 ppm Antarctic and Greenland glaciation thresholds respectively, Epochs are labelled on the top axis (Ple. is the Pleistocene, Plio. is the Pliocene), and the yellow bars mark the periods focused on in this thesis. Notable events in the palaeorecords are labelled and include the Pliocene Climatic Optimum (PCO), mid-Miocene Climate Transition (MMCT), Monterey Carbon Isotope Excursion (MCIE), Miocene Climatic Optimum (MCO), Oligocene-Miocene Transition (OMT), Eocene-Oligocene Transition (EOT), Mid-Eocene Climatic Optimum (MECO), Early Eocene Climatic Optimum (EECO), and the Palaeocene-Eocene Thermal Maximum (PETM).

to the South Pole during the Phanerozoic may have been a necessary precursor to allow large-scale glaciation [Crowell and Frakes, 1970]. The establishment of polar ice sheets also increased both regional and global albedo, creating a positive feedback on glaciation by encouraging further cooling [Robin, 1988; DeConto and Pollard, 2003; DeConto et al., 2008, while changing vegetation biome patterns also had an impact on global climate [Loptson et al., 2014]. As a result it may be speculated that cooling due to tectonically driven changes in ocean circulation and palaeogeography could have preceded and then encouraged atmCO₂ drawdown through responses such as increased ocean productivity and ventilation, with falling atmCO₂ in turn acting as a positive feedback on global cooling rather than acting as its primary driver. However, modelling of the initiation of ice sheets indicates that glaciation is most sensitive to _{atm}CO₂ declining past critical thresholds (750-950 ppm for Antarctica, ~280 ppm for Northern Hemisphere) and that the Antarctic Circumpolar Current intensified as a result of the establishment of the Antarctic ice sheet, suggesting that Antarctic thermal isolation was primarily a feedback to rather than a driver of ice growth [DeConto and Pollard, 2003; DeConto et al., 2008; Sijp et al., 2011; Goldner et al., 2014; Ladant et al., 2014a, 2014b].

Two major hypotheses for the primary driver of the Cenozoic cooling trend can therefore be established: 1) declining atmospheric CO₂ due to changes in the geological carbon cycle (such as declining outgassing or increased silicate weathering) drove global cooling and was in turn reinforced by gradual palaeogeographic changes and positive feedbacks at critical ice-growth thresholds, and 2) changes in palaeogeography and ocean/atmosphere circulation triggered the initial cooling trend and Antarctic ice growth, a trend which was subsequently amplified and globalised by the albedo effect and increased organic carbon burial drawing down atmCO₂.

1.2.2 Abrupt climate shifts

The long-term Cenozoic cooling trend is interrupted by several abrupt climate shifts and transient excursions, including episodes of extreme warming, rapid glacial advances, and significant carbon cycle perturbations [Zachos et al., 2001b] (Figure 1-2). Cenozoic ice sheet growth and global cooling occurred mainly during rapid climate shifts at the Eocene-Oligocene Transition, the mid-Miocene Climate Transition, and during the early Pleistocene [Lear, 2000]. Cenozoic cooling was also interrupted by transient episodes of relative global warmth such as the Palaeocene-Eocene Thermal Maximum and other early Eocene hyperthermals, the early Eocene

Climatic Optimum, the mid-Eocene Climatic Optimum, the Miocene Climatic Optimum, and the Pliocene Climatic Optimum. Many of these warm episodes are associated with significant perturbations to the carbon cycle, hypothesised to be due to phenomena such as methane hydrate dissociation or Large Igneous Province eruptions, and as such are potential examples of past greenhouse gas-triggered global warming. The impact of these events and their relation to the longer term climate trend are summarised in the next section.

1.2.3 Cenozoic climate chronology

1.2.3.1 Eocene warmth and hyperthermals

Following the K/Pg mass extinction event at ~66 Ma the climate of the early and mid-Palaeocene was subject to relatively mild greenhouse conditions, but from 59 to 52 Ma global temperatures rose by >5 °C with the Earth reaching its warmest state during the Cenozoic in the Early Eocene Climatic Optimum (EECO) between 52 and 50 Ma [Zachos et al., 2001b; Billups and Schrag, 2003; Bijl et al., 2009; Westerhold et al., 2011]. This warming trend is punctuated by repeated hyperthermal events, the best-known of which is the Palaeocene-Eocene Thermal Maximum (PETM) which featured rapid global warming, a carbon isotope excursion, and ocean acidification [Zachos et al., 2005, 2008; McInerney and Wing, 2011; Foster et al., 2013; Littler et al., 2014]. The PETM is hypothesised to have been triggered by the rapid release of 2000-13000 Pg of isotopically light carbon to the ocean-atmosphere system from a source such as the dissociation of oceanic methane hydrate deposits, oxidisation of organic carbon reservoirs such as peat or permafrost, or metamorphic degassing associated with the North Atlantic Volcanic Province [Svensen et al., 2004; Panchuk et al., 2008; Zeebe et al., 2009; Cui et al., 2011; Dickens, 2011; DeConto et al., 2012]. As such, the PETM and other Eocene hyperthermals are potential examples of tipping points in the carbon-climate system, where gradual forcing of the climate system eventually results in a rapid change reinforced by positive feedback loops until a new equilibrium is reached [McNeall et al., 2011].

1.2.3.2 Descent into the Icehouse

Following the warmth of the EECO, global temperature declined during the remainder of the Eocene [Zachos et al., 2001b]. This cooling trend was only interrupted by the Mid-Eocene Climatic Optimum (MECO), a transient warming and carbon cycle perturbation of disputed origins [Bohaty et al., 2009; Bijl et al., 2010;

Edgar et al., 2010; Sluijs et al., 2013]. This cooling eventually culminated in the Eocene-Oligocene Transition (EOT) around 34 Ma, during which large ice sheets first became established on Antarctica, sea levels dropped by 50 to 75 m, the carbonate compensation depth (CCD) permanently deepened by ~500 m while shallow-water carbonate platforms rapidly declined in extent, benthic δ^{13} C temporarily increased, and global temperatures dropped by ~5 °C [Miller et al., 1991; Coxall et al., 2005; Lear et al., 2008; Merico et al., 2008; Coxall and Wilson, 2011; Houben et al., 2012]. The EOT is hypothesised to be another example of a critical transition, with rapid glaciation commencing once atmCO₂ fell below a tipping point of 750-950 ppm [Dakos et al., 2008; DeConto et al., 2008; Ladant et al., 2014b]. Icehouse conditions became more fully established during the Oligocene, and atmCO₂ dropped from ~1000 ppm in the Eocene to ~500 ppm and below in the Oligocene. However, Antarctic ice sheet extent and global sea levels remained relatively variable during the Oligocene, while the Oligocene-Miocene Transition featured significant glacial advance and retreat coupled with a carbon cycle perturbation [Miller et al., 1991; Zachos et al., 2001a; Wade and Pälike, 2004; Palike et al., 2006; Liebrand et al., 2011; Mawbey and Lear, 2013].

1.2.3.3 Miocene Doubthouse

Icehouse conditions temporarily abated during the Miocene Climatic Optimum (MCO) from ~17.0 to ~14.6 Ma [Vincent and Berger, 1985; Wright et al., 1992; Kennett and Flower, 1993; Holbourn et al., 2005, 2007]. Global temperatures were 2 to 4 °C warmer than today and the Antarctic ice sheet retreated significantly, while the Monterey Carbon Isotope Excursion (MCIE), CCD shoaling, and extensive organic carbon burial indicate a contemporaneous carbon cycle perturbation potentially linked to the Columbia River Basalt eruptions [Flower, 1999; You et al., 2009; You, 2010; Passchier et al., 2011; Foster et al., 2012]. This partial reversion to greenhouse conditions was short-lived though, and icehouse conditions were restored during the mid-Miocene Climate Transition (MMCT) from ~14.6 to ~12.5 Ma with an abrupt benthic δ^{18} O and δ^{13} C shift at ~13.9 Ma [Miller et al., 1991; Flower and Kennett, 1993, 1994; Holbourn et al., 2005, 2007].

1.2.3.4 Pliocene warmth and Pleistocene glacials

Following the MMCT, Antarctic ice sheets and cool global temperatures persisted throughout the late Miocene and into the Pliocene [*Zachos et al.*, 2001b]. Transient warming occurred around 3.3 to 3.0 Ma during the Pliocene Climatic Optimum (PCO), during which the Earth was ~3 °C warmer than pre-industrial and

sea level was 12 to 32 m higher than today [Haywood and Valdes, 2004; Lunt et al., 2010; Miller et al., 2012]. The warmth of the Pliocene ended at ~2.72 Ma with a significant cooling step and the onset of Northern Hemisphere glaciation, which was subsequently followed by large-scale Northern Hemisphere glaciation and the Pliocene-Pleistocene glacial-interglacial cycles [Maslin et al., 1998; Lisiecki and Raymo, 2005; Bailey et al., 2013].

1.2.4 Palaeoclimatology and the Anthropocene

The burning of fossil fuels by humans during the industrial age has resulted in the rapid increase in atmCO₂ concentrations and the onset of anthropogenic global warming over the last ~150 years [IPCC, 2001, 2013]. Today atmospheric CO₂ concentrations exceed 400 ppm, a level not seen in the palaeorecord since 3.3 to 3.0 Ma during the PCO [Haywood and Valdes, 2004], and global surface temperature is now ~0.8 °C higher than pre-industrial conditions. Projections of future emissions indicate that $_{atm}CO_2$ concentrations of ~500 to ~1000 ppm might be expected by the end of this century, levels likely not attained on Earth since the mid-Miocene or even the Eocene, which will result in a further 0.3 to 4.8 °C of global warming relative to 1986-2005 depending on the value of climate sensitivity [IPCC, 2001, 2013; Beerling and Royer, 2011]. However, uncertainty exists around the long-term sensitivity of the Earth system to rapid perturbations to the carbon cycle, the presence of tipping points in the Earth system, and the degree to which Earth system models correctly capture these elements [Shellito et al., 2003; Hansen et al., 2008; Lunt et al., 2010; McNeall et al., 2011; Rohling et al., 2012; Foster and Rohling, 2013; Martínez-Botí et al., 2015]. Studying palaeoclimate records allows this sensitivity to be investigated and Earth system models to be tested against real-world scenarios, and therefore can help reduce the uncertainties on future projections of the unfolding Anthropocene hyperthermal.

1.3 The geological carbon cycle: conceptual and numerical models

1.3.1 A conceptual model of the carbon cycle

1.3.1.1 Carbon cycle structure

In order to investigate the dynamics of past carbon cycle perturbations it is necessary to understand the basic principles of the carbon cycle and how these are in turn represented in numerical models. The carbon cycle describes the biogeochemical cycling of carbon throughout the Earth system between the geosphere (the solid Earth), pedosphere (the thin soil layer on the terrestrial surface of the solid Earth), biosphere (living organisms), hydrosphere (the Earth's water, including the ocean and terrestrial water) and the atmosphere, as illustrated in Figure 1-3 [Kump et al., 1999]. The carbon cycle can be further subdivided into sub-cycles focused on organic and inorganic carbon and on short and long timescales. The short-timescale 'exogenic' carbon cycle consists of the fairly rapid (10° to 10³ y) exchange of carbon between the atmosphere, ocean, biosphere and soil (or sediment in the ocean), whereas the longtimescale 'geological' carbon cycle also incorporates the slow (>10⁴ y) entry of carbon into sedimentary reservoirs and the return of this carbon via weathering, metamorphism, and volcanism. As can be seen in Figure 1-3, the biggest reservoir of carbon in the carbon cycle is sedimentary rock, but it is within the 'slowest' part of the carbon cycle with a flux of ~0.2 Pg C y-1 and so despite its size it only plays a major role in the carbon cycle on geological timescales. The ocean today holds ~39000 Pg C, with most of this carbon held in the intermediate and deep ocean in the form of bicarbonate, and is thus the largest reservoir within the exogenic carbon cycle. In contrast, the biosphere today contains only ~600 Pg C in the form of biomass (but was probably larger in the warm Palaeogene), and prior to anthropogenic emissions the atmosphere contained ~590 Pg C in the form of atmospheric CO₂ (but today has reached ~830 Pg C and was significantly larger in the Palaeogene). However, both of these reservoirs have a rapid turnover and, along with carbon cycle 'capacitors' [Dickens, 2011] such as permafrost and methane hydrates (~1700 Pg C and 500 to 3000 Pg C respectively [Buffett and Archer, 2004a; Tarnocai et al., 2009; Koven et al., 2011; Wallmann et al., 2012]), are capable of causing short-term disruptions to the carbon cycle on sub-millennial timescales.

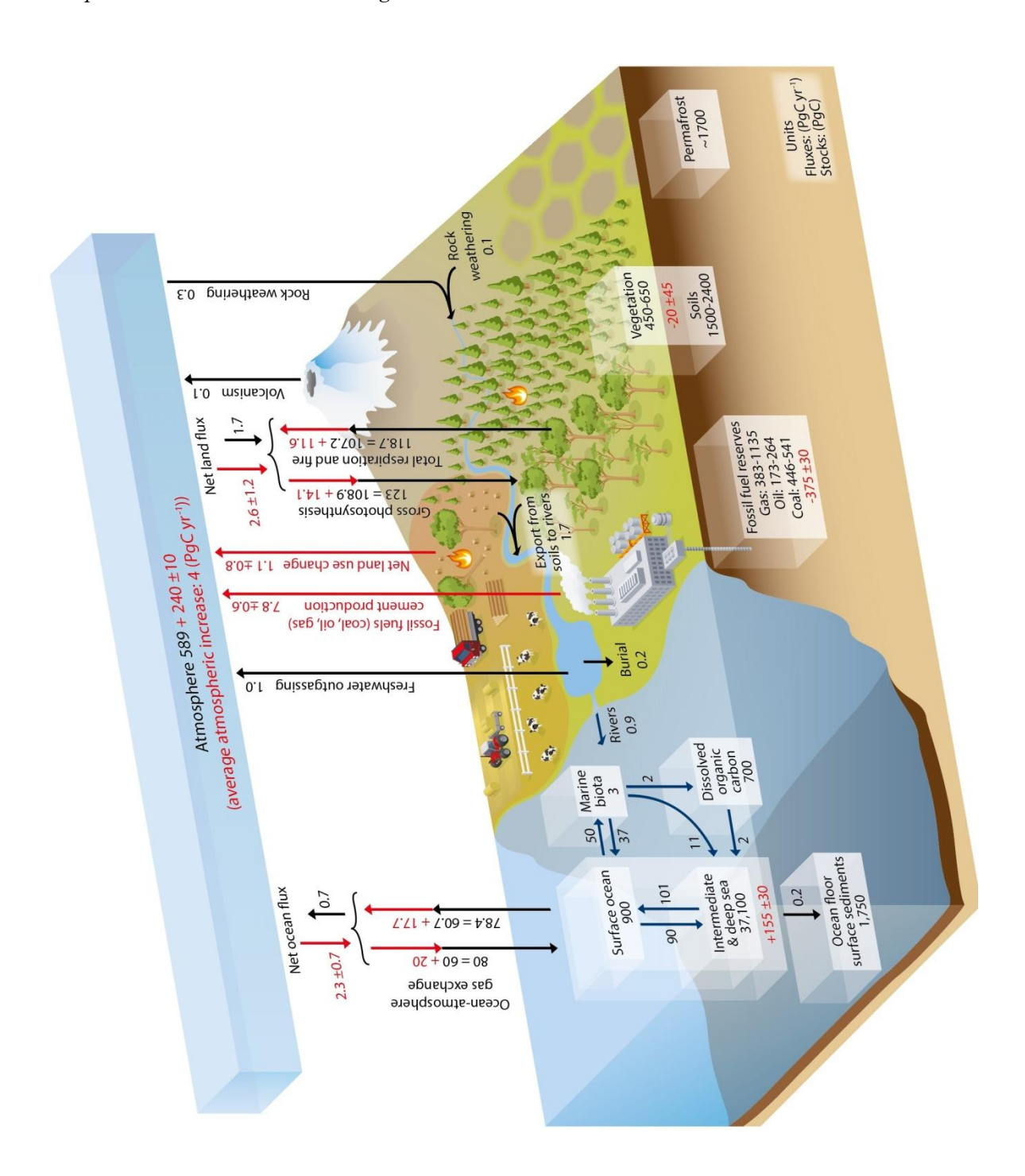


Figure 1-3: Simplified schematic of the global carbon cycle at the present day. Black labels and arrows represent pre-industrial (<1750 Common Era (CE)) fluxes and stocks, red labels and arrows represent the current (2000-2009 CE) anthropogenic perturbation to the carbon cycle. Reservoir stocks are in petagrams (10^{15} g) of carbon (Pg C) and fluxes are in Pg C y⁻¹. The less substantial methane components of the carbon cycle are not illustrated here. Reproduced from IPCC AR5 [Figure 6-1; *IPCC*, 2013], copyright IPCC. The geosphere carbon reservoir is not illustrated in this figure but consists of ~40000 Pg C in carbonate and ~10000 Pg C in organic carbon stored in sedimentary rocks, with a flux of ~0.2 Pg C y⁻¹ from seafloor sediments and <0.05 Pg C y⁻¹ from soils into this reservoir (with the volcanism and rock weathering fluxes out of this reservoir already shown) [*Kump et al.*, 1999].

1.3.1.2 The organic carbon cycle and the biological bump

The organic carbon ($C_{\rm org}$) cycle mostly consists of the exchange of carbon between the atmosphere and the biosphere, with a small amount of slow 'leakage' to the geosphere and back. The primary process driving this part of the carbon cycle is photosynthesis, performed by primary producers either in the ocean or on land, which removes CO_2 from the atmosphere and (reliant on nutrient supply) converts it into $C_{\rm org}$ (represented as CH_2O in Equation 1-1) and oxygen:

$$CO_2 + H_2O \leftrightarrow CH_2O + O_2$$
 Equation 1-1

Upon the death of the primary producer this $C_{\rm org}$ is then either consumed and respired by consumers or buried in soil or ocean sediment, where most of the $C_{\rm org}$ subsequently decomposes and is oxidised before returning to the ocean or atmosphere (reversing Equation 1-1). The production and export of particulate organic matter in the ocean results in the transfer of carbon and nutrients from the surface to deep ocean, where the majority is remineralised and eventually cycled back to the surface along with nutrients in what is known as the 'biological pump'. Of the small proportion of $C_{\rm org}$ buried in the soil or ocean sediment a small fraction is sequestered within sedimentary rocks where it is often 'cooked' to form kerogen. $C_{\rm org}$ can remain incorporated in the sedimentary reservoir for millions of years before eventually being uplifted, weathered, oxidised, and returned to the atmosphere as CO_2 .

1.3.1.3 The inorganic carbon cycle and carbonate chemistry

The inorganic carbon cycle is centred on air-sea gas exchange, the formation and weathering of carbonate rocks, and the speciation of Dissolved Inorganic Carbon (DIC) in the ocean. The inorganic carbon cycle begins with atmCO₂ dissolving into the ocean through air-sea gas exchange until the atmosphere and the surface ocean are in equilibrium:

$$CO_2 + H_2O \leftrightarrow H_2CO_3$$
 Equation 1-2

Dissolved CO_2 combines with a water molecule to form carbonic acid (H_2CO_3) (Equation 1-2), but carbonic acid readily dissociates to form bicarbonate ions (HCO_3^-) and perhaps carbonate ions (CO_3^{2-}) if possible, releasing hydrogen ions (H^+) in the process and therefore increasing the acidity of the ocean:

$$H_2CO_3 \leftrightarrow H^+ + HCO_3^-$$
 Equation 1-3
$$HCO_3^- \leftrightarrow H^+ + CO_3^{2-}$$
 Equation 1-4

The proportion of these species of DIC depends on the pH of the ocean, with high pH favouring an increased concentration of CO₃²⁻ and a lower pH favouring increased concentrations of HCO₃⁻ and/or dissolved CO₂ (either CO_{2(aq)} or H₂CO₃) (Figure 1-4). Together, Equations 1-2 to 1-4 describe the process of ocean acidification.

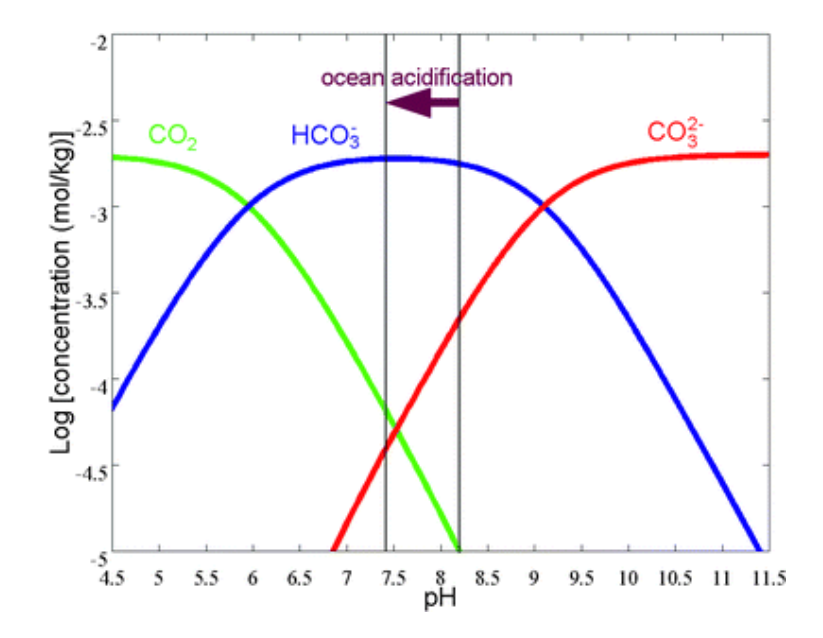


Figure 1-4: Bjerrum plot of the speciation of Dissolved Inorganic Carbon (DIC) in the ocean for DIC = 2100 μ mol L⁻¹, S = 35, and T = 25 °C (reproduced from *Hofmann and Schellnhuber* [2010] with permission from the *Royal Society of Chemistry*). The purple arrow illustrates the expected ocean acidification in the 21st century under the IPCC's business-asusual emission scenario, illustrating how rapid carbon addition to the atmosphere results in a decrease in [CO₃²⁻¹] and an increase in dissolved CO₂.

Many marine organisms, such as foraminifera, coccolithophores and corals, use HCO_3^- to build their shells, but do so more readily where the ocean is saturated with respect to calcite (or aragonite, depending on the organism's choice of carbonate polymorph). The saturation state (Ω) is defined as:

$$\Omega = \frac{[Ca^{2+}]*[CO_3^{2-}]}{K_{sp}}$$
Equation 1-5

where K_{sp} is the solubility product for calcite (or aragonite), and Ω =1 when the water is saturated with respect to calcite (or aragonite). When Ω >>1 carbonate-precipitating organisms can more easily synthesise calcium carbonate (CaCO₃) from seawater and when they die export CaCO₃ to the shallow and, since the evolution of pelagic calcifiers in the mid-Mesozoic [*Ridgwell*, 2005], deep ocean. However, Ω decreases with depth due to increasing pressure, and at about the depth where Ω =1, CaCO₃ deposited on the seafloor will begin to dissolve. This horizon is known as the carbonate (or calcite) saturation horizon (CSH), and the depth at which carbonate dissolution exceeds carbonate rain is known as the carbonate compensation depth

(CCD) (Figure 1-5). The lysocline is defined as the depth where carbonate dissolution is first noticeable on the ocean floor or in sediment cores.

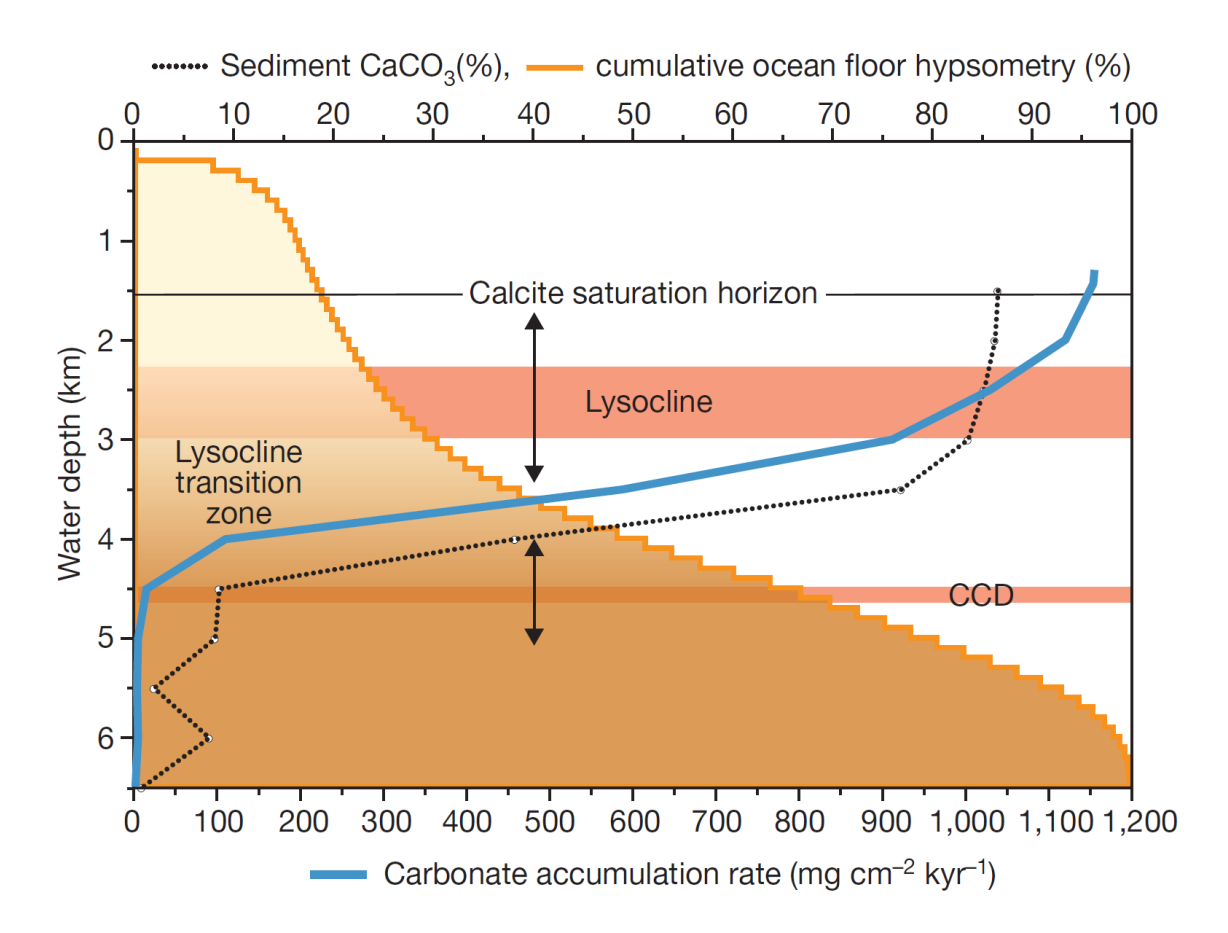


Figure 1-5: Diagram illustrating the relative positions of the carbonate (here calcite) saturation horizon (CSH), the lysocline and the carbonate compensation depth (CCD), and their relationship to ocean bathymetry, CaCO₃ accumulation rate and sediment CaCO₃ wt% (reproduced from *Pälike et al.* [2012] with permission from *Nature*).

1.3.1.4 The carbonate-silicate geochemical cycle and the climate-weathering feedback

Atmospheric CO₂ is not the only source of DIC in the ocean, with the terrestrial weathering of both silicate and carbonate rocks delivering bicarbonate ions to the ocean according to the following equations:

Carbonate:
$$CaCO_3 + H_2O + CO_2 \rightarrow Ca^{2+} + 2HCO_3^-$$
 Equation 1-6

Silicate:
$$CaSiO_3 + 2H_2O + 2CO_2 \rightarrow Ca^{2+} + 2HCO_3^- + SiO_2 + H_2O$$
 Equation 1-7

where CaSiO₃ (i.e. Wollastonite) represents an approximation of silicate mineralogy. The precipitation of carbonate in the ocean is described by the following:

$$Ca^{2+} + 2HCO_3^- \rightarrow CaCO_3 + H_2O + CO_2$$
 Equation 1-8

which is the reverse of the carbonate weathering equation (Equation 1-6), indicating

that the carbonate weathering to carbonate precipitation pathway has no long-term net impact. However, as silicate weathering requires twice as much CO_2 as carbonate weathering (Equation 1-7), the silicate weathering to carbonate precipitation pathway has the following net result:

$$CaSiO_3 + CO_2 \rightarrow CaCO_3 + SiO_2$$
 Equation 1-9

Coupled with its inverse (representing metamorphism) this reaction is known as the 'Urey Reaction' [*Urey*, 1952], and it indicates that the weathering of silicate lithologies results in the net drawdown of atmCO₂ when the resultant precipitated carbonate is sequestered in ocean sediment (as first suggested by *Chamberlin* [1898]). This relationship would result in the total drawdown of atmCO₂ within ~1 million years if unopposed [*Kump et al.*, 1999], but volcanism and carbonate metamorphism release CO₂ into the atmosphere at a similar rate and so there is an approximate balance of inputs and outputs of CO₂ to the atmosphere. However, the rate of silicate weathering is dependent on climatic factors such as temperature and rainfall, and so tends to increase if the climate becomes warmer and wetter. This would gradually result in declining concentrations of atmCO₂, but this in turn counteracts the original climate change to form the negative feedback loop illustrated in Figure 1-6 [*Walker et al.*, 1981].

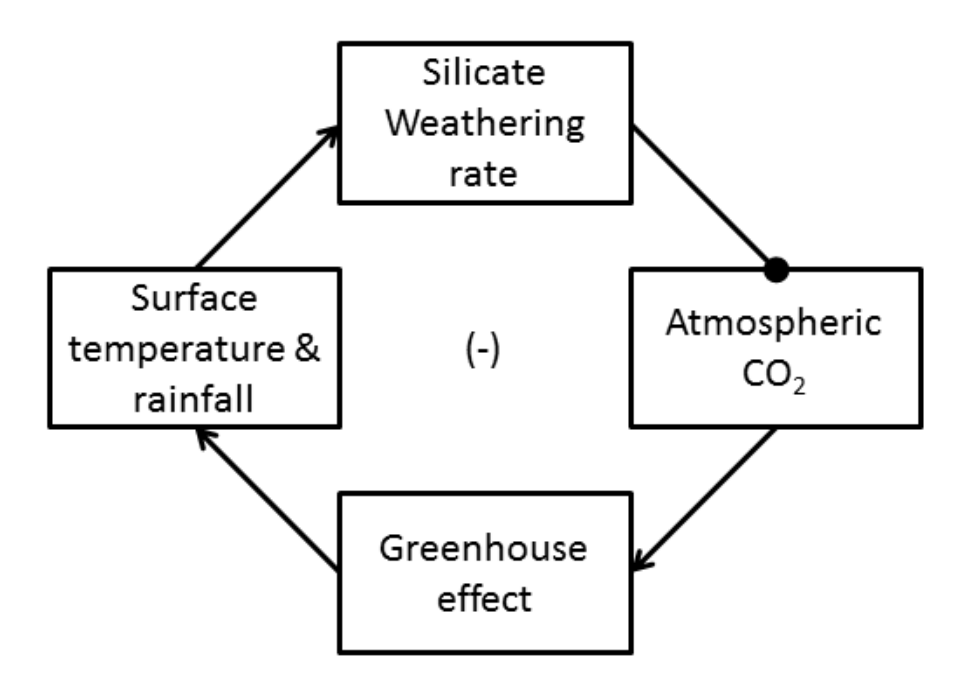


Figure 1-6: Systems diagram illustrating the climate-weathering negative feedback loop (based on [*Kump et al.*, 1999]). Pointed arrows indicate positive impact, circled arrows indicate negative impact, and (-) indicates this is a negative feedback loop.

14

1.3.1.5 Modelling the long-term regulation of atmospheric CO₂

The climate-weathering feedback described in Section 1.3.1.4 is hypothesised to maintain atm CO₂ in long-term equilibrium by counteracting deviations in CO₂ concentration over timescales of >10 ky. This hypothesis was the basis of the original 'BLAG' model (Figure 1-7) [Berner et al., 1983], in which atmCO₂ is assumed to primarily be a function of volcanic outgassing and silicate weathering rate, while the ocean, atmosphere, and biosphere carbon reservoirs remain at steady state. The difference between the weathering and precipitation of magnesium and calcium carbonates is also explicitly modelled. The BLAG model was further developed into the GEOCARB model, of which several iterations added features such as the organic carbon cycle, included improved climate feedbacks, changing palaeogeography, the emergence of gymnosperms and angiosperms, and the sulphur and oxygen cycles [Kasting, 1984; Berner, 1991, 1994, 2006; Berner and Kothavala, 2001]. The BLAG/GEOCARB models to a first order succeeded in recreating the long-term trends observed in the atmCO₂ proxies throughout the Phanerozoic (Figure 1-1), which suggests that the primary control on atmCO2 concentration during the Phanerozoic was elevated outgassing from increased seafloor spreading rates during the Mesozoic and early Palaeozoic (combined with the lack of vascular plants prior to the Devonian) [Berner and Kothavala, 2001].

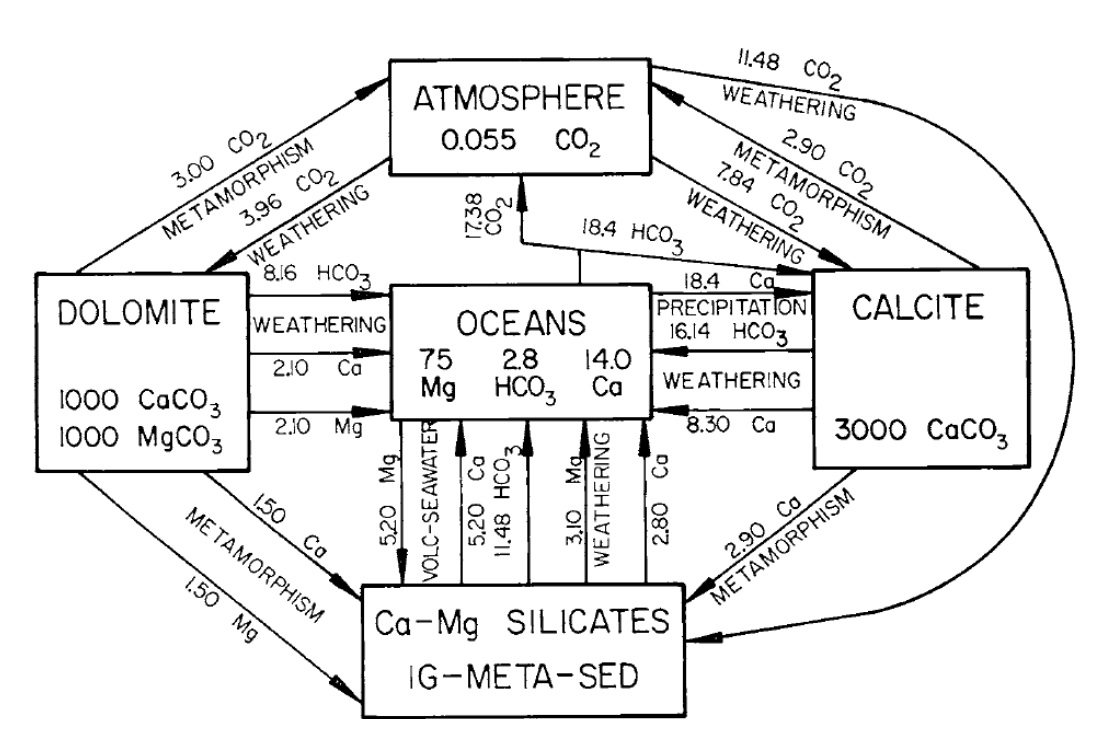


Figure 1-7: A schematic of the modern carbonate-silicate geochemical cycle as represented in the 'BLAG' model (reproduced from *Berner et al.* [1983] with permission from the *American Journal of Science*). Fluxes are corrected for pyrite weathering and formation and are in 10^{18} moles per My (reservoir sizes are in 10^{18} moles).

A different approach to modelling long-term atmCO2 trends is to upgrade the 0dimensional approach to weathering rates in the BLAG/GEOCARB models to fully capture the heterogenic response of weathering to climatic and tectonic changes. Rather than assume that global silicate weathering rate reacts homogenously to atmCO2 concentration, models such as GEOCLIM include a 2-dimensional representation of weathering rates that allows silicate weathering to be heterogeneous [Donnadieu et al., 2004a, 2004b, 2006; Goddéris et al., 2007]. Whereas in GEOCARB-type models volcanic emissions (or 'source-side' CO₂ processes) are the dominant control on long-term atmCO₂ concentrations and silicate weathering merely reacts to volcanically-driven atmCO2 changes, in GEOCLIM-type models 'sink-side' CO2 processes also become an important control if silicate weathering rates or silicate weatherability increase in a particular region even if the change is not global. As an example, it has been hypothesised that either the emplacement of or continental driftdriven movement of highly weatherable and extensive Large Igneous Province basalts into tropical regions could drive the rapid drawdown of atmCO2 without a globalised increase in weathering rates [Kent and Muttoni, 2008, 2013; Schaller et al., 2012, 2014; Lefebvre et al., 2013].

1.3.2 Numerical models of the carbon cycle

1.3.2.1 History of carbon cycle modelling

There have been many attempts at incorporating the conceptual models of the carbon cycle outlined in Section 1.3.1 into numerical models that are capable of successfully capturing both past and future carbon cycle behaviour. The first carbon cycle models were developed as simple box models in order to understand conceptually the destination of CO₂ released by fossil fuel combustion in the ocean-atmosphere system [e.g. Bolin and Eriksson, 1959; Craig, 1957; Revelle and Suess, 1957]. These models focused on the dissolution of CO₂ into the ocean and its speciation once dissolved (Section 1.3.1.3) and the role of the marine biosphere (Section 1.3.1.2), and thus resolved most of the shorter-term exogenic carbon cycle. Subsequently these models were improved and developed to include other elements such as the terrestrial biosphere, soils, higher spatial resolution, a dynamic CCD, and climate feedbacks [Keeling, 1973; Revelle and Munk, 1977; Siegenthaler and Oeschger, 1978; Bjöorkström, 1979; Bolin et al., 1981; Sundquist, 1986; Walker and Kasting, 1992; Ridgwell et al., 2007], while more recent models such as LOSCAR and GENIE also incorporate sediment processes [Ridgwell and Hargreaves, 2007; Zeebe et al., 2009;

Zeebe, 2012]. The incorporation of the climate-weathering feedback [Berner et al., 1983; Berner, 1991, 1994, 2006; Walker and Kasting, 1992; Berner and Kothavala, 2001; Donnadieu et al., 2004a, 2004b, 2006; Goddéris et al., 2007] completes the carbonate-silicate geochemical cycle and has thus allowed long-term simulations of the geological carbon cycle (Sections 1.3.1.4 and 1.3.1.5). Various versions of these simple carbon cycle models have been further developed and incorporated into more complex Earth system models, which include Earth system models of intermediate complexity (EMICs) with moderate resolution and complexity such as GENIE, and the comprehensive and high-resolution global climate models (GCMs) that incorporate a detailed representation of the carbon cycle. This thesis uses two recently developed box models of the carbon cycle that are described in detail below.

1.3.2.2 JModels

The JModels (www.noc.soton.ac.uk/jmodels/) were developed as a suite of conceptual-type biogeochemical box models to resolve each of the carbon, phosphorus, silicon, and nitrogen cycles, with the intention of being as simple as possible to reduce model run-time and be easy to use but still capable of resolving all of the major fluxes and processes of the respective cycles. The original carbon JModel is based on a simple 3-box global ocean (based on Walker and Kasting [1992]) and encompasses the carbon and phosphorous cycles. It has been used to investigate the impact of anthropogenic emissions on the ocean [Chuck et al., 2005; Tyrrell et al., 2007; Bernie et al., 2010] and the origin of δ^{13} C anomalies in the Pleistocene [Hoogakker et al., 2006]. The carbon JModel includes the carbonate system, air-sea gas exchange, the biological pump, calcium carbonate formation and cycling, and carbon isotopes in an open system. Although the carbon JModel is useful to check hypotheses on carbon cycle perturbations quickly, the lack of a silicate weathering feedback limits its use for long-term carbon cycle modelling. In response to this, *Merico et al.* [2008] redeveloped the carbon JModel, hereafter in this thesis referred to as 'MTW08', to also include the silicon cycle and the climate-weathering feedback in order to study the Eocene-Oligocene Transition. MTW08 is described in further detail below.

1.3.2.3 MTW08

The ocean in MTW08 is split vertically into surface (the euphotic zone, 0 to 100 m), middle (the mixed layer above the thermocline, 100 to 500 m), and deep (below the thermocline, 500 to 3730 m) boxes (Figure 1-8). As the ocean is global it does not resolve latitudinal or regional processes and has a spatially and temporally averaged

input of nutrients, DIC and alkalinity. As illustrated in Figure 1-8, the processes controlling the distribution of DIC include ocean-atmosphere CO₂ exchange, riverine DIC input, CO₂ uptake by organisms and its eventual remineralisation and burial, precipitation and dissolution of CaCO₃, and ocean mixing. Alkalinity is controlled by the riverine input of bicarbonate and nitrate, the biological uptake and remineralisation of nitrate, the precipitation, dissolution and burial of CaCO₃, and ocean mixing (Figure 1-8). Carbonate chemistry is controlled by the routines of *Zeebe and Wolf-Gladrow* [2001] (www.soest.hawaii.edu/oceanography/faculty/zeebe files/CO2 System in Seawater/csys.html), with pH, [CO₃²⁻], and dissolved CO₂ calculated at each time-step from DIC and alkalinity. CaCO₃ production is linked to C_{org} production via the 'rain ratio', which is defined as the molar ratio of particulate inorganic carbon (PIC) to particulate organic carbon (POC) export.

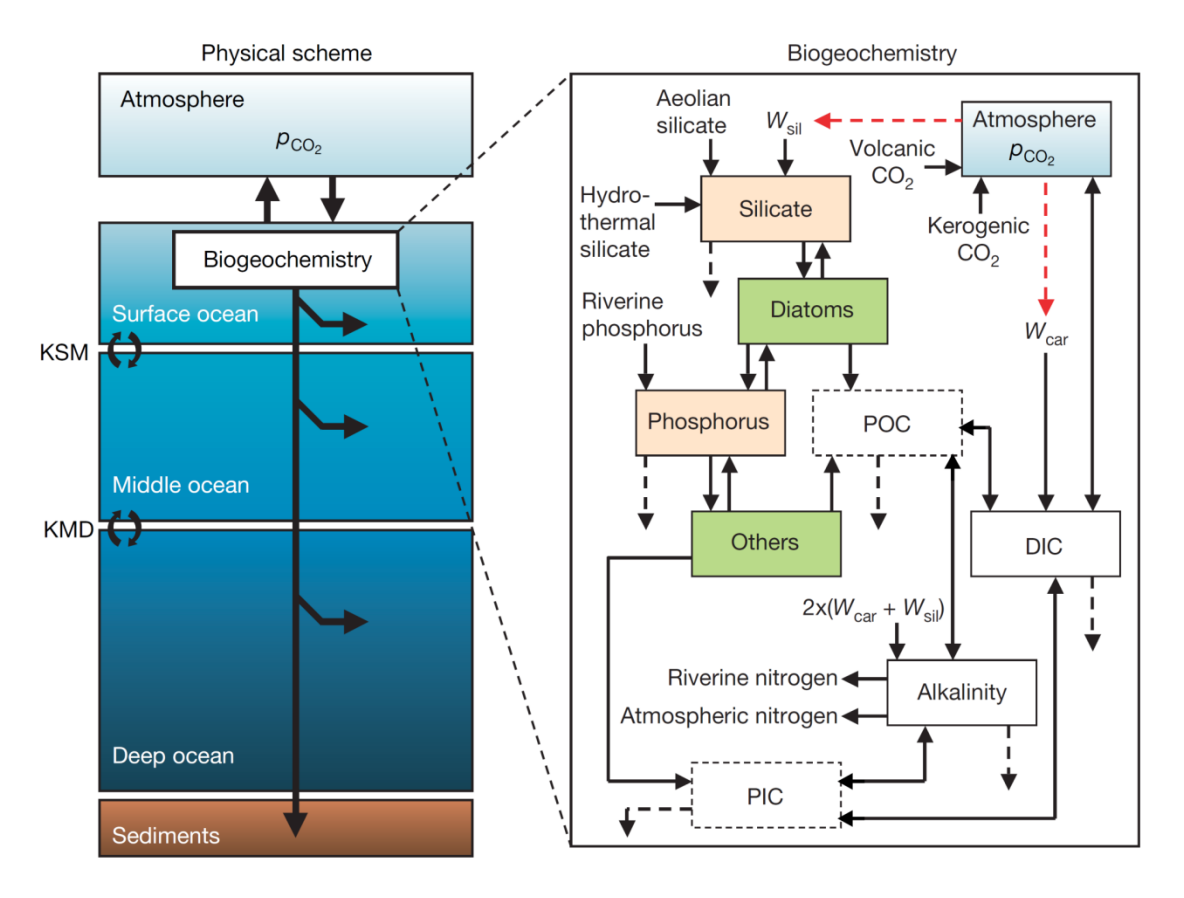


Figure 1-8: Schematic representation of the MTW08 model, illustrating its physical scheme (left) and biogeochemical cycling (right) (reproduced and modified from *Merico et al.* [2008] with permission from *Nature*). The black arrows in the physical scheme represent remineralisation and sedimentation fluxes, while in the biogeochemistry scheme the dashed black arrows represent export out of the surface ocean and the silicate and carbonate feedbacks (dependent on atmCO₂ concentration) are indicated by the dashed red arrows. Abbreviations: PIC, particulate inorganic carbon; POC, particulate organic carbon; W_{car}, carbonate weathering (delivering DIC and Alkalinity to the ocean via rivers); W_{sil}, silicate weathering (delivering Alkalinity and silica to the ocean via rivers); KSM and KMD, mixing between surface and middle boxes and between middle and deep boxes, respectively.

The silicate and carbonate weathering processes are parameterised by the following equations [Walker and Kasting, 1992]:

Carbonate Weathering:
$$W_{car} = f_{car} * \left(\frac{pco_2}{pco_{2(ini)}}\right)^{1.0}$$
 Equation 1- 10

Silicate Weathering:
$$W_{sil} = f_{sil} * \left(\frac{pco_2}{pcO_{2(ini)}}\right)^{0.3}$$
 Equation 1- 11

where f is the initial weathering flux of each parameter, pCO_2 is the current partial pressure of $_{\rm atm}CO_2$, $pCO_{2(ini)}$ is the model's initial partial pressure of $_{\rm atm}CO_2$, and the weathering exponent (default set at 1.0 for carbonate weathering and 0.3 for silicate weathering) dictates the strength of the feedback. The weathering of $C_{\rm org}$ -rich rocks and the oxidation and release of CO_2 from this process is also represented as a constant input of CO_2 to the atmosphere, as is the emission of CO_2 by volcanism.

MTW08 features fully dynamic calcite and aragonite compensation depths (CCD & ACD). The critical carbonate ion concentration ([CO₃²·]_{crit}), below which sea water is undersaturated with respect to carbonate, is calculated as a function of depth [Jansen et al., 2002]:

Calcite:
$$[CO_3^{2-}]_{crit}(z) = 88.7 * exp[0.189 * (z - 3.82)]$$
 Equation 1-12

Aragonite:
$$[CO_3^{2-}]_{crit}(z) = 117.5 * exp[0.176(z - 3.06)]$$
 Equation 1-13

MTW08 calculates the value of deep ocean [CO₃²⁻] and then uses Equations 1-12 and 1-13 to calculate the depth at which $[CO_3^{2-}]_{crit} = [CO_3^{2-}]$. Ocean bathymetry is based on the ETOPO5 dataset (ngdc.noaa.gov/mgg/global/etopo5.html), from which the proportion of ocean area at different depths was calculated, and each grid cell weighted by the cosine of its latitude to prevent bias towards high latitudes. These data are then used to calculate the fraction of ocean area above or below the CCD (and the ACD), which determines the proportion of the CaCO₃ export flux that is either buried or dissolved. CaCO3 dissolution in MTW08 is only dependent on the CaCO3 export flux and the fraction of sea floor receptive to CaCO₃ burial, and therefore does not take into account any within-sediment processes. As a result, it does not include chemical erosion, sediment chemistry, or respiration-driven dissolution (as in Zeebe and Westbroek [2003]). This assumption holds well when the ocean is not acidifying (as is the case during much of the Cenozoic), but it does not hold as well in an acidifying ocean when the chemical erosion of previously deposited CaCO3 in the bioturbated portion of sediment becomes more important. Respiratory dissolution can also potentially decouple the lysocline from the saturation horizon [Sigman et al., 1998] but is not included in MTW08.

For Chapter 3 the impact of changes in the ocean [Mg²⁺]/[Ca²⁺] ratio on ocean Ω has also been added as the EOT is hypothesised to feature significant changes in [Ca²⁺]. To do this the estimated impact of the [Mg²⁺]/[Ca²⁺] ratio on the stoichiometric solubility product of calcite and aragonite and the dissociation constants of carbonic acid are incorporated into the model [Ben-Yaakov and Goldhaber, 1973; Mucci and Morse, 1984; Tyrrell and Zeebe, 2004]. More advanced formulations of the impact of [Mg²⁺]/[Ca²⁺] on carbonate chemistry have recently been developed [Hain et al., 2015], but this formulation has not yet been included into MTW08.

Phytoplankton in MTW08 are split between silicifying (diatoms) and non-silicifying (others) plankton (Figure 1-8). Phosphorus is used as the primary nutrient of both plankton groups in MTW08 (as it is assumed to be the ultimate limiting nutrient [Tyrrell, 1999]), while the diatom group is also dependent on silica. MTW08 takes account of the impact of plankton 'vital effects' on the difference between their δ^{13} C and DIC using the following equation [$Spero\ et\ al.$, 1997]:

$$\delta^{13}C_{shell} = \delta^{13}C_{DIC} - 0.008([CO_3^{2-}] - 300)$$
 Equation 1-14

The CO₂ effect on the δ^{13} C of POC, known as the photosynthetic isotope effect, is also accounted for [Hofmann et al., 1999]:

$$\delta^{13}C_{org} = \delta^{13}C_{DIC} - \frac{9866}{T_K} + 24.12 - 17 \log_{10}([CO_{2(aq)}]) + 3.4$$
 Equation 1-15

Compared to other, more complex models of the carbon cycle MTW08 has several drawbacks. As MTW08 has a 1-dimensional physical structure it is incapable of resolving latitudinal or regional processes such as ocean circulation re-organisation, the solubility pump, or variable CCDs between different ocean basins. MTW08 also lacks any dynamic ocean-atmosphere circulation, a terrestrial biosphere, or an ocean sediment component that can capture post-deposition chemical processes and carbonate burn-down during ocean acidification. Other issues include the simplistic representation of carbonate preservation (either 100 % or 0 % above and below the CCD respectively) and of PIC export (fixed to POC export via the rain ratio). Nonetheless MTW08 does have several advantages which make it suitable for use in this thesis. Despite its simplicity and physical naivety, MTW08 is relatively biogeochemically advanced and successfully captures the dynamics of both the shortterm and long-term carbon cycle, and yet also has a relatively fast run-time. This makes it particularly well-suited to simulations of carbon cycle perturbations in the palaeoclimate record, many of which lasted ~1 million years or more and therefore require models with rapid run-times but that still capture the main carbon cycle

feedbacks. The inclusion of the phosphorus and silicon cycles and the separation of silicifying and calcifying plankton also allows some degree of plankton dynamics. Analyses of the sensitivity of MTW08 to parameter selection have demonstrated that MTW08 simulation results have been relatively robust to parameter choices [Merico et al., 2008; Chapter 2 – Armstrong McKay et al., 2014].

1.3.2.4 LOSCAR

The LOSCAR (Long-term Ocean-atmosphere-Sediment CArbon-cycle Reservoir; [Zeebe et al., 2009; Zeebe, 2012]) model is also used in this thesis in Chapter 2 in conjunction with MTW08 so that the results of MTW08 can be compared and contrasted with a carbon cycle model with a differing configuration and set of assumptions. As with MTW08, LOSCAR is a carbon cycle box model (also based on Walker and Kasting [1992]), but LOSCAR is also coupled to a computationally-efficient sediment module to simulate the fate of buried carbonate better (from Zeebe and Zachos [2007]). The sediment module calculates %CaCO3 in the bioturbated section of sediment (typically the upper 8 cm) as a function of CaCO3 rain, dissolution, burial, and chemical erosion. LOSCAR also splits the ocean into several basins, including the Atlantic, Pacific, Indian, high-latitude, and (if set up in the Palaeocene/Eocene configuration) Tethys oceans, each of which (except high-latitude) are in turn split into surface, intermediate and deep boxes (Figure 1-9).

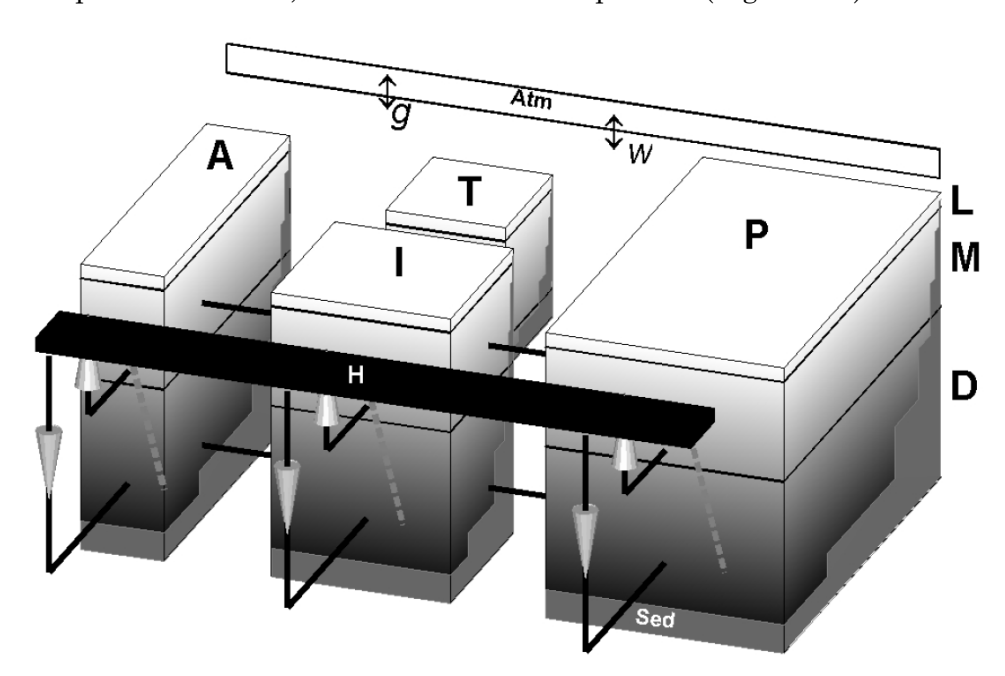


Figure 1-9: Schematic of the LOSCAR model in its Palaeocene/Eocene configuration (reproduced from *Zeebe* [2012] under Creative Commons Attribution 3.0 licence). The global ocean is split into the Atlantic (A), Indian (I), Pacific (P), Tethys (T) and High-latitude (H) oceans, of which all except the latter are split into surface (L), intermediate (M) and deep (D) boxes. Weathering fluxes (w), gas exchange (g) with the atmosphere (Atm), and burial/erosion in sediment (Sed.) are indicated.

LOSCAR includes complete biogeochemical cycles of carbon (including both ¹²C and ¹³C), alkalinity, phosphate, and oxygen, but not of silicon and therefore does not resolve silicifying plankton separately from other plankton as in MTW08. Carbonate chemistry parameters are calculated from the DIC and Alkalinity parameters using the algorithms of *Zeebe and Wolf-Gladrow* [2001]. Long-term _{atm}CO₂ regulation is achieved via parameterising weathering rates as a function of _{atm}CO₂ concentration, as in MTW08 (but with differing weathering exponent parameters). LOSCAR has been used to model the carbon cycle perturbations during the Palaeocene-Eocene Thermal Maximum, the Mid-Eocene Climatic Optimum and the K/Pg boundary [*Zeebe et al.*, 2008, 2009; *Sluijs et al.*, 2013; *Tyrrell et al.*, 2015].

1.4 Thesis aims and structure

1.4.1 Key research questions

It is clear that the Earth's transition from greenhouse to icehouse climate conditions during the Cenozoic was closely related to changes in the carbon cycle. Significant perturbations to the carbon cycle accompany most of the major Cenozoic climate events, indicating a tightly coupled carbon-climate system. However, the relationship between many of these carbon cycle perturbations and both the climate event with which they coincide and the longer-term Cenozoic cooling trend is still uncertain. In particular, the drivers of the carbon cycle perturbations during the Eocene-Oligocene Transition and the mid-Miocene, their impact on the climate system, the role of tipping points during these periods, and the impact of declining shelf carbonate burial on the carbon cycle all remain debated. By investigating the Earth system response to Cenozoic carbon cycle and climate perturbations using numerical modelling and analysis, this thesis aims to explore the following key research question:

What were the drivers of carbon-climate system perturbations during the Cenozoic?

This overarching question can be further split into several pending research questions that will be focused on and addressed in this thesis:

- 1. Were Large Igneous Provinces capable of significantly impacting the carbonclimate system during the Cenozoic?
- 2. Was the Miocene Climatic Optimum driven by emissions from the Columbia River Basalt large igneous province eruptions?
- 3. To what extent did shelf-basin carbonate burial fractionation drive the deepening of the carbonate compensation depth at the Eocene-Oligocene Transition and during the rest of the Cenozoic?
- 4. Did processes other than carbonate burial fractionation contribute to the Eocene-Oligocene Transition carbon cycle perturbation?
- 5. Why has the carbonate compensation depth remained relatively deep and stable since the Eocene Oligocene Transition?
- 6. Were the main Cenozoic carbon-climate perturbations the result of tipping points being reached in the carbon-climate system, and are they preceded by 'early warning signals' in the palaeorecord?
- 7. How reliable is early warning signal analysis when used on palaeorecords?

1.4.2 Thesis structure

This thesis tackles the questions outlined in Section 1.4.1 over the course of the next four chapters. Chapter 2 investigates the potential biogeochemical and climate impact of the Columbia River Basalt eruptions during the Miocene Climatic Optimum using both MTW08 and LOSCAR. In Chapter 3 the relationship between the glaciation at the Eocene-Oligocene Transition and the associated carbon cycle perturbation is explored using MTW08. Chapter 4 examines the relationship between shelf carbonate burial extent, the carbonate compensation depth, and changing sealevel in order to investigate and quantify the shelf-basin carbonate burial fractionation hypothesis. In Chapter 5 palaeorecords across various Cenozoic carbon-climate perturbations are analysed in order to find evidence of early warning signals that might yield information on the nature of these events, and the utility of this method when applied to palaeorecords evaluated. Finally, in Chapter 6 the findings of this thesis and the further questions it gives rise to are discussed and summarised.

Chapter 2:

Estimating the impact of the cryptic degassing of Large Igneous Provinces: A mid-Miocene case-study

In this chapter the potential impact of the 'cryptic degassing' of the Columbia River Basalt eruptions during the mid-Miocene is investigated using two biogeochemical models. This chapter is a reproduction of an article published in Earth and Planetary Science Letters: "Armstrong McKay, D. I., T. Tyrrell, P. A. Wilson, and G. L. Foster (2014), Estimating the impact of the cryptic degassing of Large Igneous Provinces: A mid-Miocene case-study, Earth and Planetary Science Letters, 403, 254–262, doi:10.1016/j.epsl.2014.06.040". Supporting online-only information is included at the end of this chapter (Section 2.8).

2.1 Abstract

Large Igneous Provinces (LIPs) have been emplaced throughout Earth's history, erupting great quantities (>10⁴ km³) of lava in long-lived (>10⁵ y) events that have been linked to major environmental disruptions. The largest LIP eruptions (e.g. Siberian Traps) are widely considered to have had an impact on global climate through basalt CO₂ degassing but the impact of the more numerous smaller LIPs is debated. Here we test the hypothesis that LIPs had a greater impact on Earth's climate history than previously estimated because of the 'cryptic degassing' of intruded and crust-contaminated magma, injecting extra CO₂ over and above that coming from sub-aerial basalts. We use biogeochemical box models to investigate the potential impact of the Columbia River Basalts (CRB) during the mid-Miocene where

¹ Some minor edits have been made to this chapter from the published article, including a corrected error in a label on Figure 2-1, clarifications to small parts of Sections 2.5.1 and 2.5.2 in order to provide additional detail in the explanation of model results, and the harmonisation of terminology with the rest of this thesis.

multiple palaeorecords for this geologically relatively recent event enable more rigorous data-model comparison. We find that the effect on the long-term carbon cycle of basalt degassing from the CRB alone is negligible, but that a total CRB emission of 4090-5670 Pg of carbon with 3000-4000 Pg of this carbon emitted during the Grande Ronde Basalt eruptions, a flux within the acceptable estimated range when cryptic degassing is included, does well in reproducing the record of benthic δ^{13} C and atmospheric CO₂ change during the core of the Miocene Climatic Optimum. Nevertheless, mechanisms other than degassing are required to drive observed warmth before 16.3 Ma and to match observed carbonate compensation depth behaviour after ~15.4 Ma. Hence, our findings rule out the possibility that CRB emplacement alone can fully explain the mid-Miocene record but they demonstrate the enhanced climate impact that occurs when substantial cryptic degassing accompanies LIP emplacement.

2.2 Introduction

Large Igneous Provinces (LIPs) erupt great quantities of lava during long-lived events that can release significant volumes of carbon into the ocean-atmosphere system [Coffin and Eldholm, 1994; Courtillot and Renne, 2003; Ernst et al., 2005; Bryan and Ernst, 2008]. While the LIPs with the largest volumes (e.g. the Siberian Traps or the Central Atlantic Magmatic Province) are widely accepted to have triggered episodes of carbon cycle perturbation, global warmth and ecological crisis [Wignall, 2001, 2005; Grard et al., 2005; Sobolev et al., 2011], the case for LIPs with smaller (≤2x10⁶ km³) volumes (e.g. the Deccan Traps or the Columbia River Basalt), emitting sufficient CO₂ to cause a significant global impact is a subject of debate [Caldeira and Rampino, 1990; Taylor and Lasaga, 1999; Self et al., 2006; Diester-Haass et al., 2009; Kender et al., 2009]. However, estimates of LIP CO₂ emissions often do not take into account all of the potential sources of excess or 'cryptic' degassing, which include the often extensive volume of intrusive magma emplaced beneath LIPs [Grard et al., 2005; Menand and Phillips, 2007; Shinohara, 2008; Karlstrom and Richards, 2011, the metamorphic degassing of carbon-rich country rocks [Svensen et al., 2004, 2009; Erwin, 2006; Retallack and Jahren, 2008; Ganino and Arndt, 2009, 2010; Aarnes et al., 2011b; Iacono-Marziano et al., 2012], and the potential impact of the recycling of mafic crust into the LIP magma source [Sobolev et al., 2011]. These considerations imply that, under favourable circumstances, many LIPs may have a greater climatic impact than is widely accepted. Here we present the results of a feasibility study to quantify the potential additional impact on the long-term carbon cycle and climate of cryptic degassing using the mid-Miocene Columbia River Basalt (CRB) event for which multiple high-resolution palaeorecords are available.

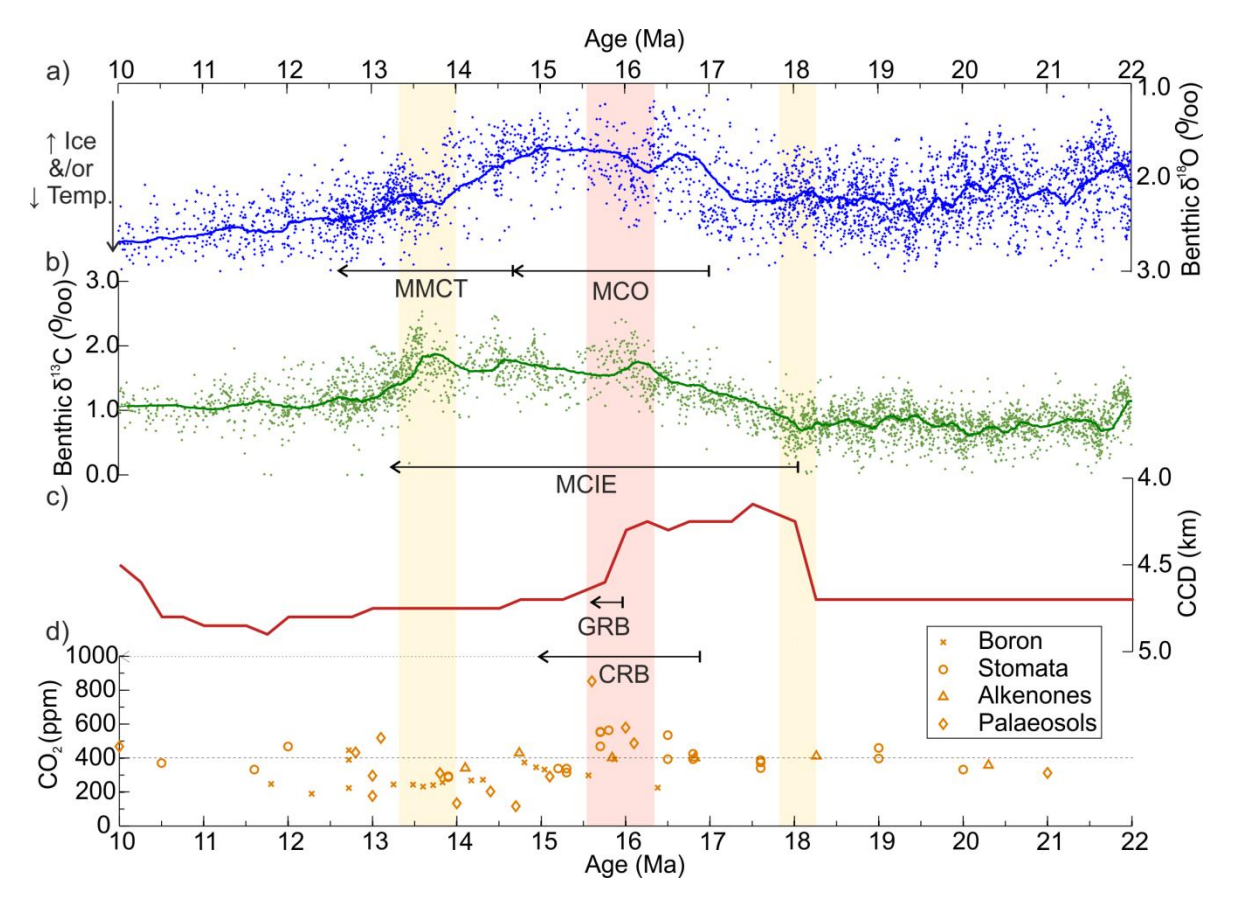


Figure 2-1: Comparison of palaeorecords between 10 and 22 Ma of: benthic foraminifera a) δ^{13} C (green dots) and b) δ^{18} O (blue dots) compilations and their secular trends (solid blue/green lines illustrate the 100-point moving average) [Zachos et al., 2008], c) equatorial Pacific CCD palaeodepth (solid red line [Pälike et al., 2012]), and d) atmospheric CO₂ reconstructed using boron (orange crosses [Foster et al., 2012]), alkenone (orange triangles [Zhang et al., 2013]), stomata and palaeosol (orange circles and diamonds, respectively [Beerling and Royer, 2011]) based techniques with the 400 ppm level marked by the dashed black line. The durations of the Miocene Climatic Optimum (MCO), mid-Miocene Climate Transition (MMCT), Monterey Carbon Isotope Excursion (MCIE), and Columbia River Basalt (CRB) main eruption phase (with the minor Saddle Mountain eruptions shown by dotted arrow) and the Grande Ronde Basalt (GRB) eruptions are illustrated. Perturbations to the palaeorecords at ~18.0, ~16.0 and ~14.0 Ma are highlighted by the orange and red bars, with the red bar marking the perturbation which is the focus of this study and shown in greater detail in Figure 2-3.

2.3 The mid-Miocene and the Columbia River Basalt eruptions

Published composite records of benthic stable isotope and CaCO₃ accumulation presented in Figure 2-1 indicate broadly contemporaneous anomalies (carbonate compensation depth (CCD) shoaling, benthic δ^{13} C maximum, benthic δ^{18} O minimum, ice sheet extent minimum) in the long-term carbon cycle and climate system during the early to middle Miocene, including the Monterey Carbon Isotope Excursion (MCIE) and Miocene Climatic Optimum (MCO) [Vincent and Berger, 1985; Billups and Schrag, 2003; Zachos et al., 2008; Passchier et al., 2011; Pälike et al., 2012]. These marked perturbations occurred at about the same time as the onset of the emplacement of the bulk of the CRB in the Cascadia region of North America over multiple eruption phases between ~16.8 and 15.0 Ma [Hooper, 1988, 1997; Barry et al., 2010, 2013; Baksi, 2013; Reidel et al., 2013b; Wolff and Ramos, 2013] (Figure 2-2), with the initiation of the CRB eruptions coinciding with the core of both the MCO and the MCIE (Figure 2-1). In detail, the peak of the carbon cycle perturbation occurs ca. 16.0 Ma (Figure 2-3), coinciding with the eruption, between 16.3 and 15.9 Ma, of the ~152,000 km³ Grande Ronde Basalt (GRB) formation over ~400 ky (responsible for ~70% of the CRB; Figure 2-2 [Barry et al., 2013; Reidel and Tolan, 2013; Reidel et al., 2013b; Wolff and Ramos, 2013]). Using a Gaussian filter to remove signals below 420 ky in the benthic foraminifera δ^{13} C palaeorecord from ODP Site 1146 reveals a + 0.3 ‰ excursion in the secular trend of benthic δ^{13} C between 16.3 and 15.8 Ma (Figure 2-3, panel a) [Holbourn et al., 2007]. Atmospheric CO₂ reconstructions feature elevated CO₂ during the MCO, perhaps peaking between 16.3 Ma and 15.8 Ma at 400-500 ppmv despite evidence of increased organic carbon burial during the Monterey Excursion, and then declining by ~13.9 Ma (Figure 2-3, panel c) [Vincent and Berger, 1985; Kürschner et al., 2008; Foster et al., 2012; Zhang et al., 2013]. The CCD also deepens by ~300 m in the equatorial Pacific at ~16.0 Ma, which has been suggested to represent a recovery from an equatorial "carbonate famine" hypothesised to have caused the CCD to initially shoal at ~18.0 Ma (Figure 2-1; Figure 2-3, panel b) [Lyle, 2003; Lyle et al., 2010; Pälike et al., 2012]. These correlations have led some authors to invoke CRB activity as the main driver of mid-Miocene climate change [e.g. Hodell and Woodruff, 1994; Kender et al., 2009; Foster et al., 2012]. Others have concluded that CRB emissions had a negligible impact on atmospheric CO₂ [Taylor and Lasaga, 1999; Diester-Haass et al., 2009].

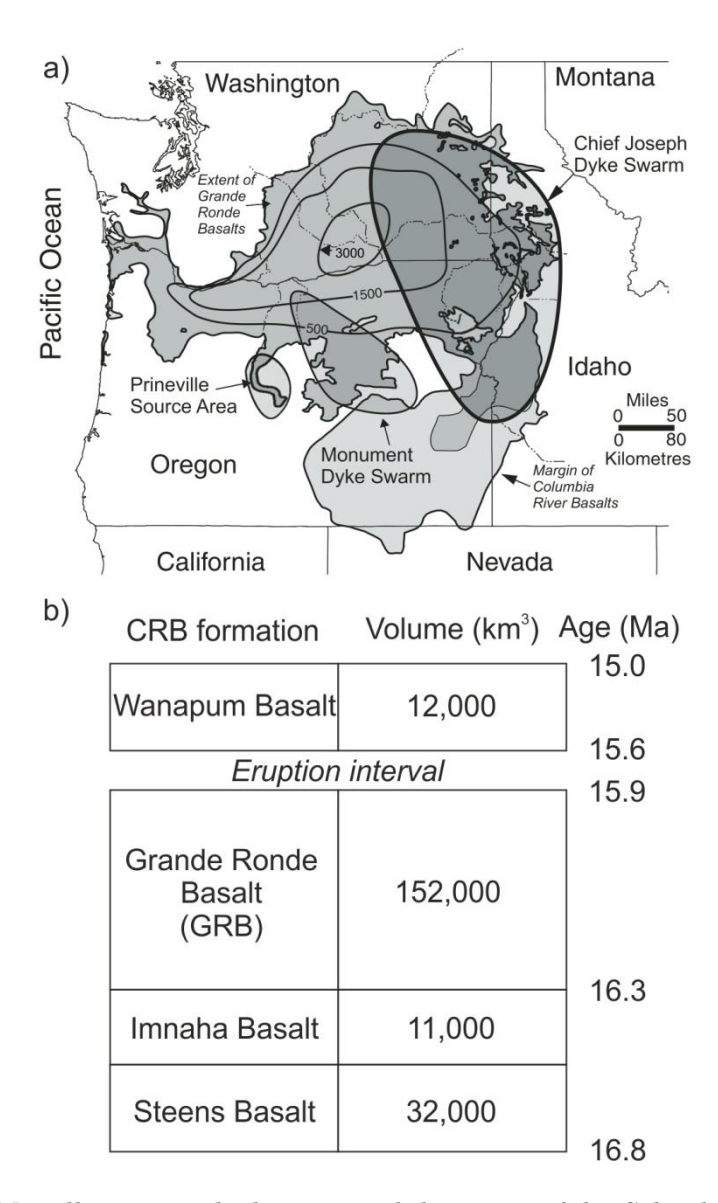


Figure 2-2: a) Map illustrating the location and the extent of the Columbia River Basalts (CRB), the Grande Ronde Basalt (GRB) formation within the CRB (with the GRB's thickness in metres illustrated by the isopachs), and the GRB's associated dyke swarms. Figure adapted from *Reidel et al.* [2013b] with permission from the *Geological Society of America*. b) Illustration of the main Columbia River Basalt formations with each formation's extrusive volume (to the nearest 1000 km³ [*Reidel et al.*, 2013b]) and the CRB eruption chronology used in this study.

To investigate the potential importance for Miocene climate of CRB cryptic degassing we use model simulations to determine the magnitude and duration of carbon emissions necessary to reproduce the observed patterns in benthic δ^{13} C, the CCD, and atmospheric CO₂ and evaluate the feasibility of these emission scenarios against the range of potential emissions calculated for the CRB.

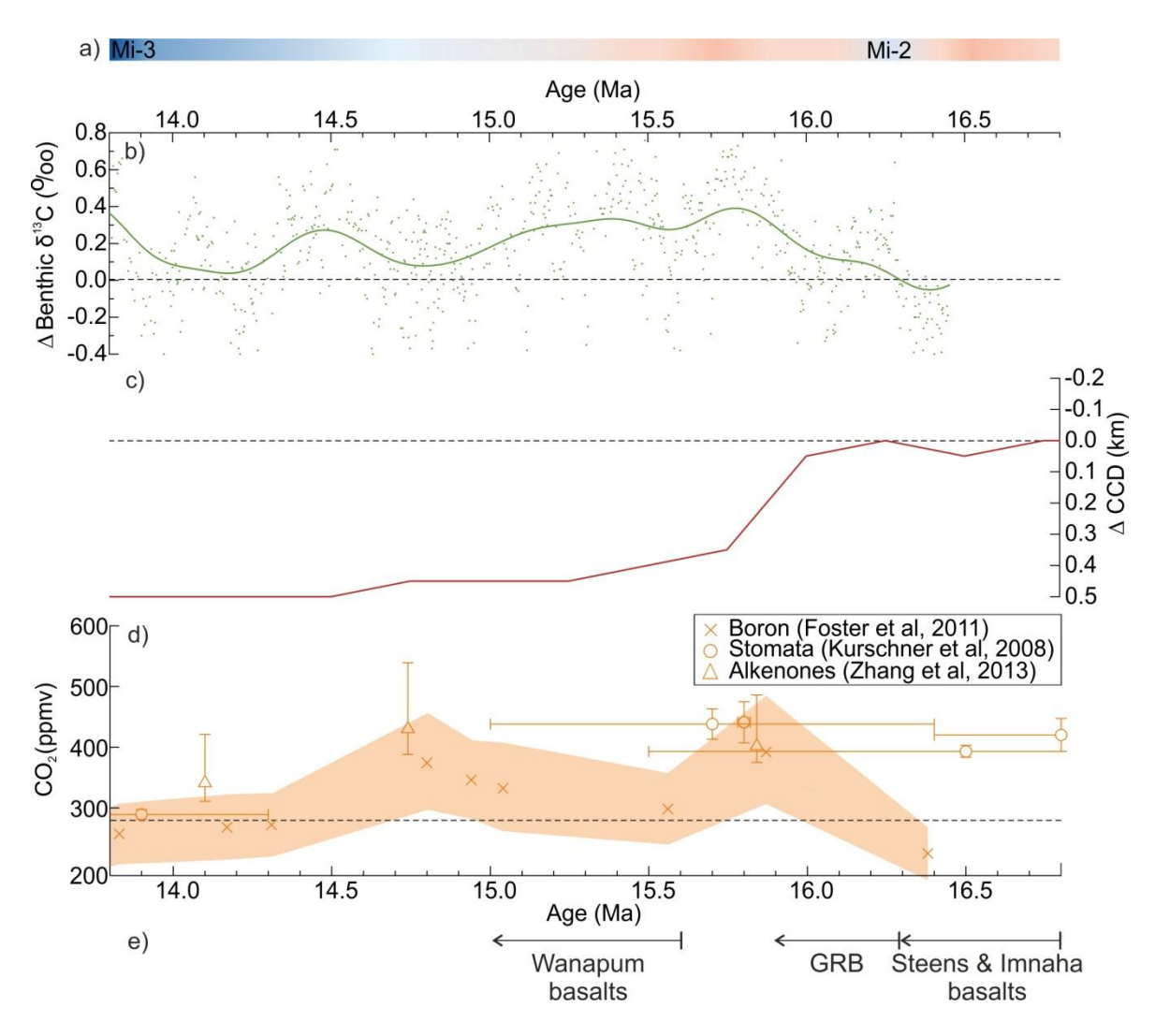


Figure 2-3: Palaeorecords of the mid-Miocene climate and carbon cycle. a) Occurrence of Antarctic glacial minima and maxima marked by the red and blue bars respectively with 'Mi-2' and 'Mi-3' glaciations labelled [Miller et al., 1991; Passchier et al., 2011; Feakins et al., 2012]. Palaeorecords of: b) benthic foraminifera δ^{13} C from IODP site 1146 (green dots) and its secular trend (calculated by using a Gaussian filter to remove signals below 420 ky; green line; Δ=0 pinned at 16.3 Ma) [Holbourn et al., 2007], c) reconstruction of CCD palaeodepth in the equatorial Pacific (red line; Δ =0 pinned at 16.3 Ma; [Pälike et al., 2012]), and d) reconstructions of atmospheric CO₂ based on boron isotopes (orange crosses with orange band for error; [Foster et al., 2012]), leaf stomata (orange circles with error bars; [Kürschner et al., 2008]), and alkenone δ^{13} C (orange triangles with error bars; [Zhang et al., 2013]).

2.4 Materials and Methods

2.4.1 Modelling

We use two biogeochemical box models to simulate the carbon emissions necessary to drive the changes seen in the palaeorecord: i) the model of *Merico et al*. [2008] (hereafter referred to as MTW08), and ii) the LOSCAR model [*Zeebe et al.*, 2009]. MTW08 is an open system model containing all the major fluxes and processes in the carbon, phosphorus, and silicon cycles, including the carbonate system, air-sea

gas exchange, the organic matter pump, CO2 drawdown by silicate weathering, calcium carbonate formation and cycling, and carbon isotopes [Merico et al., 2008]. In contrast, LOSCAR (the Long-term Ocean-atmosphere-Sediment CArbon cycle Reservoir model) includes a simplified phosphorous cycle and no silicon cycle but includes a sediment component coupled to the ocean-atmosphere routines, allowing the carbonate system to be better represented by including dissolution processes within the sediment column [Zeebe et al., 2009; Zeebe, 2012]. LOSCAR also includes regional boxes for each ocean basin in contrast to the global ocean of MTW08, providing a better comparison to the Pacific-focused palaeorecords used in this study. Both models are limited by low spatial resolution, uncertainties in mid-Miocene estimates for model parameters, and the lack of dynamic ocean, atmosphere and terrestrial biosphere components. Both models are tuned with estimates for mid-Miocene parameters (Supporting Tables 2-3 to 2-5) and then perturbed by CRB emission scenarios with varying increases in volcanic baseline emissions above the model baseline. MTW08 is also used to simulate the impacts of fresh basalt weathering through additional inputs of phosphorus and silicon, which we estimate are increased by 1.5 and 2.2 % respectively above baseline inputs during the GRB eruptions before declining to 0.1% above baseline over the next 500 ky as the most reactive basalt is weathered away [Taylor and Lasaga, 1999] (Table 2-1).

Table 2-1 Estimated liberation rates of silicon and phosphorus due to the chemical weathering of the freshly emplaced basalts of the CRB and the estimated resultant increase in baseline silicon and phosphorus input to the ocean over 400 ky during the GRB eruptions

Estimate	Chemical weathering rate (t km ⁻² y ⁻¹) ^a	Si liberation rate (mol km ⁻² y ⁻¹) ^b	P liberation rate (mol km ⁻² y ⁻¹) ^d	GRB Si release (% MTW08 baseline) ^c	GRB P release (% MTW08 baseline) ^c
Modern CRB	24.2	3.0x10 ¹⁰	2.4x10 ³	0.9	1.3
Mid-Miocene CRB ('fresh' basalt effect)	64.0	8.0x10 ¹⁰	8.9x10 ³	2.3	3.5
Resultant surplus ^e	39.8	5.0x10 ¹⁰	5.6x10 ³	1.5	2.2

^a Chemical weathering rates are based on *Dessert et al.* [2003] and *Taylor and Lasaga* [1999]

Silicon liberation rates based on Dessert et al. [2003]

^c MTW08 baseline riverine Si and P input listed in Supporting Information

d Phosphorus liberation rates based on scaling Japanese basalt weathering rates [Hartmann and Moosdorf, 2011] to the chemical weathering rate

^e Surplus P and Si release simulated during the basalt eruptions before decreasing at a constant rate to ~0.1% by 15.1 Ma to represent declining 'freshness' [*Taylor and Lasaga*, 1999]

2.4.2 MTW08 sensitivity analyses

After finding an emission scenario that produces the closest match to the palaeorecords we performed various sensitivity analyses in order to judge the sensitivity of our results to our chosen model parameter settings. To establish the impact of the strength of climate-weathering feedbacks on our results the strength of the climate-weathering feedback in MTW08 is varied. CO₂-dependent weathering in MTW08 is formulated as in *Walker and Kasting* [1992]:

$$W_{car} = f_{car} \times (pCO_2/pCO_{2(ini)})^{\alpha_c}$$
 Equation 2-1

$$W_{sil} = f_{sil} \times (pCO_2/pCO_{2(ini)})^{\alpha_s}$$
 Equation 2-2

where W_{car} and W_{sil} are the current carbonate and silicate weathering rates, f_{car} and f_{sil} are the initial carbonate and silicate weathering flux, $CO_{2(ini)}$ is the initial atmospheric CO_2 , α_c is the carbonate weathering exponent and is 1.0 in MTW08 and 0.4 in LOSCAR, and α_s is the silicate weathering exponent and is 0.3 in MTW08 and 0.2 in LOSCAR. By repeating our best-fit simulations with different carbonate and silicate weathering exponent values we can analyse the sensitivity of our results to the strength of the climate-weathering feedback used in MTW08. The sensitivity of our results to other key parameters in MTW08, including carbonate and silicate weathering, deep ocean mixing, the rain ratio, and sediment carbon burial, is also analysed by calculating a sensitivity index using the formula:

$$S = \left| \frac{p(Y'-Y)}{Y(p'-p)} \right|$$
 Equation 2-3

where S is the sensitivity index, p the parameter value, Y the model results for p, and 'denotes the parameter value and model results after the \pm 10 % change in p [Haefner, 1996]. A sensitivity index value of S \leq \pm 0.5 indicates that the variable Y is robust with respect to changes in the parameter p, whereas Y is sensitive to changes in p if S >> \pm 1. We also vary the isotopic value of volcanic emissions from the typical value of -4 % (Supporting Table 2-5) in order to analyse the sensitivity of our results to the volcanic carbon δ^{13} C parameter.

2.4.3 Eruption chronology

There are several different eruption chronologies proposed for the CRB eruptions based on different dating methods. Data from ⁴⁰Ar/³⁹Ar and K/Ar dating

suggests that the GRB erupted between $15.99\pm0.20~\mathrm{Ma}$ and $15.57\pm0.15~\mathrm{Ma}$ [Barry et al., 2010, 2013], but these dates are subject to relatively large errors and the methodology behind these dates has been criticised for potentially underestimating ages [Baksi, 2013; Wolff and Ramos, 2013]. Recent re-dating of the geomagnetic polarity time scale and in particular the "Steens reversal" instead indicates the GRB eruption must have started at 16.29 ± 0.07 Ma and lasted 400-500 ky [Jarboe et al., 2010; Baksi, 2013; Wolff and Ramos, 2013]. The pre-GRB Steens and Imnaha eruptions are estimated to have begun between 16.9 and 16.4 Ma, while the Wanapum eruptions are estimated to have either erupted slowly over 600-800 ky up to as late as 14.5 Ma or to have been rapidly erupted by as early as 15.78 ± 0.06 Ma [Jarboe et al., 2010; Baksi, 2013; Barry et al., 2013; Wolff and Ramos, 2013]. In this study we base our simulated eruptions primarily on the eruption chronology summarised by Wolff and Ramos [2013], with the Steens and Imnaha basalts erupting between 16.8 and 16.3 Ma and the GRB between 16.3 and 15.9 Ma, although we simulate the Wanapum basalts erupting between 15.6 and 15.0 Ma instead of 15.3 to 14.5 Ma [Barry et al., 2013] (Figure 2-2, panel b). We also note that cryptic degassing could have begun while magma migrated through the intrusive sill-dike complex prior to surface eruptions, a scenario which has been hypothesised to have occurred up to several hundred thousand years prior to the Siberian Traps eruption [Wolff et al., 2008; Sobolev et al., 2011; Wolff and Ramos, 2013]. This could result in the timing of cryptic degassing differing from that of the basalt eruptions, which means that it is therefore possible that the GRB eruptions could have started as late as 16.0 Ma but its cryptic degassing may still have begun at \sim 16.3 Ma. In this study we can constrain the timing of significant cryptic degassing from the observed palaeorecord perturbations, but constraining the extrusive eruption chronology is challenging as the impact of these emissions on the palaeorecords is likely to be negligible relative to the impact of cryptic degassing.

2.4.4 Cryptic degassing estimates

We define cryptic degassing as the emissions from a LIP beyond the degassing of just its sub-aerial basalts and which are therefore more difficult to constrain and often only partially considered when estimating LIP emissions. Our primary method for estimating cryptic degassing is by estimating the release of CO₂ from intrusive, non-erupted magma as well as from sub-aerial basalts. This degassing is calculated by assuming an average basaltic CO₂ content of 0.2-0.5 wt% and 70-80 % degassing

efficiency, yielding a minimum of 1.1 Tg C km⁻³ in our low degassing scenario and a maximum of 3.1 Tg C km⁻³ in our high degassing scenario (Table 2-2) [Self et al., 2006; Shinohara, 2008]. We assume that all of this CO₂ can reach the atmosphere via either surface fissure eruptions, fracture-fault systems present in the Columbia Basin before the eruption of the CRB, or fracturing around intrusive bodies triggered by devolatilisation-induced overpressure [Aarnes et al., 2012; Reidel et al., 2013a]. Subaerial emissions are calculated as the degassing from erupted basalts only, intrusive emissions are calculated as the degassing from the intrusive volume associated with the CRB, and total emissions include both sources. In the case of the GRB the extrusive volume is well constrained at ~152,000 km³ out of a total CRB volume of ~207,000 km³ [Bryan and Ernst, 2008; Reidel et al., 2013b], while estimates of the intrusive volume associated with the CRB range from an equivalent intrusive to extrusive volume implied by petrologic modelling [Wolff and Ramos, 2013] up to ~1,125,000 km³ estimated from seismic refraction profiles [Coffin and Eldholm, 1994], giving a total CRB magma volume of between 420,000 and 1,335,000 km³. Intrusive magma degassing is more difficult to estimate than extrusive degassing though, and as a result this introduces additional uncertainty to our estimates of total magma degassing [Yoshimura and Nakamura, 2012]. We define the ratio of the total emissions to just the extrusive emissions as the Emissions Amplification Factor (EAF), which based on our estimates is 2.0 to 6.4 for both our low and high degassing emission scenarios (Table 2-2). The emissions used in our simulations for each CRB formation are calculated by scaling the emission estimates for the whole CRB by the relative extrusive volume of these formations.

CRB magma may have also been further enriched in CO₂, H₂O, and other volatiles beyond the levels we assume in our calculations above due to crustal contamination of the magma feeding the eruptions, a process which *Sobolev et al.* [2011] suggests caused significant additional degassing from the Siberian Traps. Both petrological studies and simulations of the origins of the CRB indicate that the magma feeding the CRB is likely to have experienced similar crustal contamination and potential volatile enrichment prior to the GRB eruptions [*Camp and Hanan*, 2008; *Wolff et al.*, 2008; *Liu and Stegman*, 2012; *Ramos et al.*, 2013; *Rodriguez and Sen*, 2013; *Wolff and Ramos*, 2013], indicating that a similar amplification of emissions as hypothesised for the Siberian Traps may have occurred during the CRB eruptions. We crudely approximate the impact of these potential additional emissions simply by scaling the crust-contaminated emissions of the Siberian Traps hypothesised by *Sobolev et al.* [2011] (~46,360 Pg C) by the volume of each CRB

degassing source relative to the volume of the Siberian Traps (the total CRB being ~12 % the volume of the Siberian Traps) (Table 2-2). An EAF of 2.0 to 6.4 also applies to this crustal-contamination emission scenario.

An additional source of cryptic degassing beyond magma degassing is the metamorphism of the country rock, which is hypothesised to have caused large-scale emissions during other LIPs [e.g. Svensen et al., 2004]. The scale of country rock metamorphosis associated with the CRB is partly obscured by the complex geology of the Columbia Basin, but the presence of carbonates, natural gas, and coal in parts of the basin all point to a potentially significant source of additional carbon [Lasmanis, 1991; LaMaskin et al., 2011]. Significant country rock degassing has been simulated to result from the intrusion of sills through various different lithologies, with a \sim 15 m thick sill intruding through organic-rich shale predicted to release ~ 1700 kg CH₄ per m² of sill extent [Aarnes et al., 2011a, 2011b]. These simulations also suggest that metamorphic degassing of limestone and shale primarily releases CH₄ rather than CO₂ and so could further amplify the CRB's short-term warming potential, while the presence of evaporites could also lead to the release of ozone layer-damaging methyl chloride. If we assume that the Chief Joseph and Monument fissure-dykes that the GRB erupted from were fed by an underlying sill as part of a shallow dyke-sill complex (covering an area of ~100,000 km² for the Chief Joseph swarm; Figure 2-2 panel a [Wolff et al., 2008; Reidel et al., 2013a; Rodriguez and Sen, 2013; Wolff and Ramos, 2013), then this sill would yield metamorphic degassing emissions of up to ~1100 Pg C if the sill was intruded through coal, ~280 Pg C through limestones and ~2400 Pg C through organic-rich shale, while further metamorphic degassing would be expected from country rock dissected by the fissure dykes linked to this sill [Aarnes et al., 2011b]. However, the extent of sills underlying the CRB and the total number, length and depth of the dykes of the Chief Joseph, Monument, and other smaller dyke swarms remain poorly constrained, making it difficult to accurately estimate metamorphic degassing for the CRB. As a result we cautiously estimate that metamorphic degassing could yield on the order of an additional ~102 to 103 Pg of carbon, which would further amplify the maximum CRB cryptic degassing beyond our estimates in Table 2-2.

Table 2-2Carbon emission estimates for the entire Columbia River Basalt for different degassing scenarios and sources, and the resultant range of the Emission Amplification Factor (EAF) for the CRB

	Emissions for each degassing source (Pg C)						
Emission scenario	Sub-aerial basalts (SAB)	Minimum intrusive magma	Maximum intrusive magma	Minimum total magma	Maximum total magma	Minimum EAF	Maximum EAF ^c
Low degassing ^a	230	230	1240	460	1470		
High degassing ^a	650	650	3500	1300	4150	2.0	6.4
Crust- contaminated ^b	970	970	5220	1940	6190		

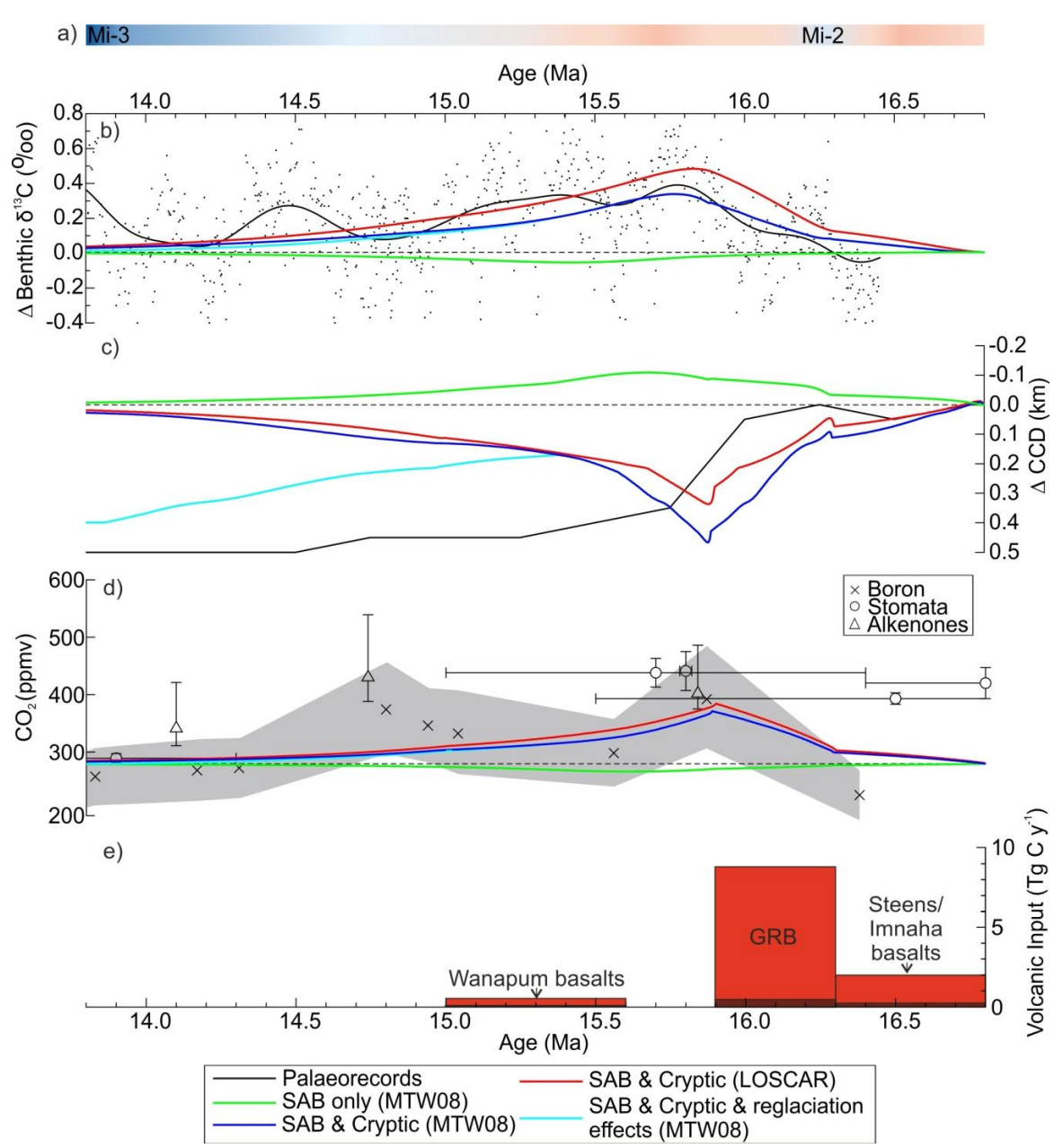
^a Low (0.2 % wt. CO₂, 70 % efficient) and high (0.5 % wt. CO₂, 80 % efficient) degassing estimates based on *Self et al.* [2006] and *Shinohara* [2008].

^b Crust-contamination emissions scaled from hypothesised Siberian Traps emissions of *Sobolev et al.* [2011] by relative volume.

^c Metamorphic degassing (e.g. *Svensen et al.* [2004]) is also likely to have been significant

^c Metamorphic degassing (e.g. *Svensen et al.* [2004]) is also likely to have been significant enough to add to further amplify emissions beyond this value but this impact is currently poorly constrained.

2.5 Results and Discussion



The main results of our MTW08 and LOSCAR simulations compared against mid-Miocene palaeorecords. a) Occurrence of Antarctic glacial minima and maxima marked by the red and blue bars respectively with the Mi-2 and Mi-3 glaciations labelled [Miller et al., 1991; Passchier et al., 2011; Feakins et al., 2012]. Model results relative to steady-state values of: b) benthic δ¹³C (benthic foraminifera in MTW08, deep ocean DIC in LOSCAR), c) CCD palaeodepth (global in MTW08, Pacific in LOSCAR), and d) atmospheric CO₂ for our sub-aerial basalt degassing only simulation in MTW08 (green line), our best-fit MTW08 simulation (dark blue line, with additional run with post-CRB glaciation effects shown by the light blue line), and our best-fit LOSCAR simulation (red line); plotted against palaeorecords (with Δ =0 pinned to either models' steady-state value at 16.3 Ma for the relevant model output; presented here in black for clarity instead of the colours shown in Figure 2-3) of: b) benthic foraminifera δ^{13} C from IODP site 1146 (black dots) and its secular trend (black line [Holbourn et al., 2007]), c) reconstruction of CCD palaeodepth in the equatorial Pacific (black line [Pälike et al., 2012]), and d) reconstructions of atmospheric CO2 based on boron isotopes (black crosses, grey band for error [Foster et al., 2012]), leaf stomata (black circles with error bars [Kürschner et al., 2008]), and alkenone δ^{13} C (black triangles with error bars [Zhang et al., 2013]). e) Volcanic emissions scenario for the best-fit MTW08 scenario divided according to CRB formation and emission source (cryptic degassing, red; sub-aerial basalt degassing, dark red).

2.5.1 Modelled emission scenario

In Figure 2-4 we compare palaeorecords with model simulations for δ^{13} C, CCD and atmospheric CO2. We find that sub-aerial basalt degassing alone has a negligible effect in our simulations, but that adding cryptic degassing results in excursions similar to those seen in the palaeorecords. In some respects these results are counterintuitive because they simulate: 1) a deepening of the CCD despite increasing atmospheric CO₂, and 2) a positive benthic δ^{13} C excursion despite the release of isotopically light (-4 %) volcanic carbon. The CCD result is attributable to the emission of carbon over a long (>10 ky) time-scale acting to stimulate increased terrestrial carbonate weathering such that the increased flux of alkalinity to the ocean overcompensates for the initial reduction in [CO₃²-] driven by ocean acidification (Figure 2-5). The increase in benthic δ^{13} C is driven by a combination of the climatedriven long-term increase in carbonate weathering increasing the overall δ^{13} C of weathered carbon entering the ocean [Payne and Kump, 2007], and partially by the increased burial of organic carbon (Corg) (due to increased productivity with increased riverine phosphorus delivery) with a decreased δ^{13} C value in response to increasing CO₂ as a result of the photosynthetic isotope effect [Kump and Arthur, 1999] (Figure 2-5 and Figure 2-6). The burial of this light C_{org} helps to counteract the further impact of the isotopically light volcanic carbon, and combined with increased carbonate weathering input leaves dissolved inorganic carbon and thus benthic foraminifera enriched in ¹³C. Crust-contaminated magma, however, is predicted to emit CO₂ with an isotopic value of -12 \% [Sobolev et al., 2011] while country rock emissions can vary from 0 to 1.5 % (from carbonates) to -20 to -50 % (from shales, Supporting Table 2-5 [Svensen et al., 2004; Ganino and Arndt, 2009]). Our sensitivity analysis of volcanic δ^{13} C illustrates that giving volcanic carbon an isotopic value of -12 \% results in a δ^{13} C excursion similar to but slightly larger than in our best-fit simulation in MTW08 (Supporting Figure 2-7), indicating that our main conclusions are not particularly sensitive to uncertainty in this parameter.

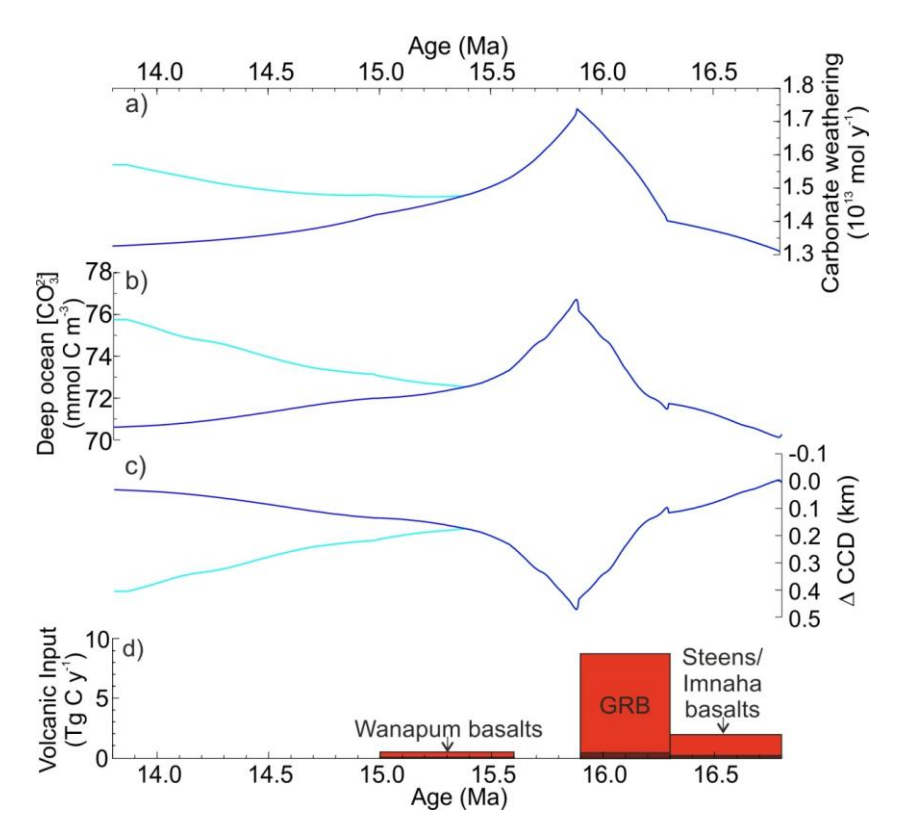


Figure 2-5: Simulation results in MTW08 of: a) carbonate weathering flux, b) deep ocean carbonate ion concentration, and c) change in CCD (relative to 16.3 Ma) for our best-fit MTW08 emissions scenario illustrated in panel d) (dark blue line, with additional run with post-CRB glaciation effects shown by the light blue line).

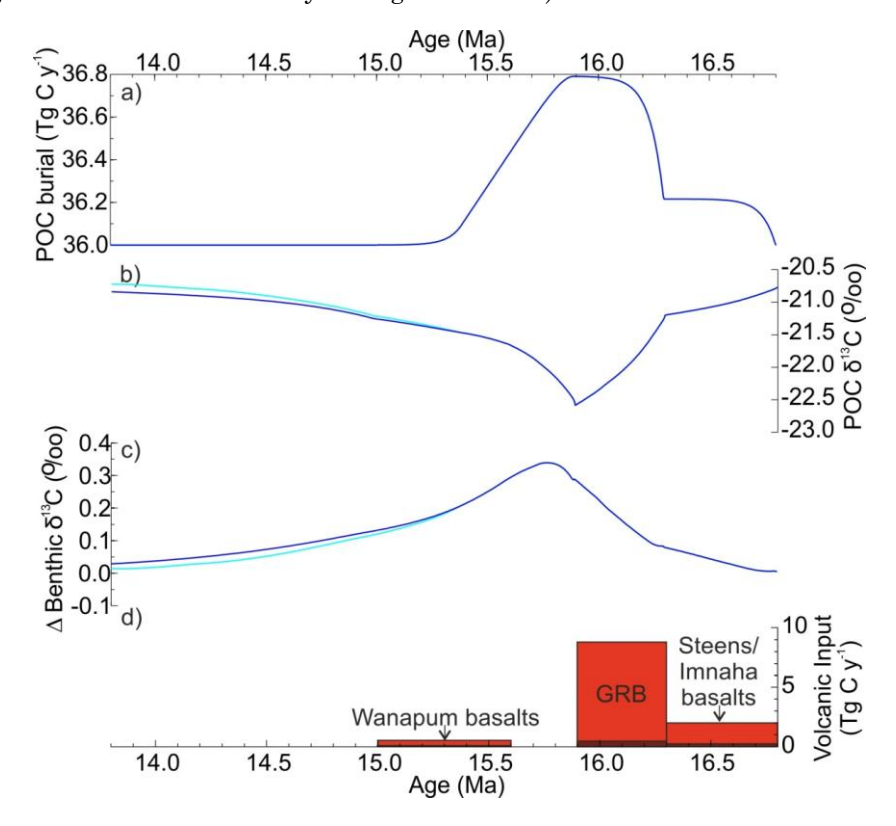


Figure 2-6: Simulation results in MTW08 of: a) Particulate Organic Carbon (POC) burial rates, b) POC δ^{13} C, and c) change in benthic δ^{13} C (relative to 16.3 Ma) for our best-fit MTW08 emissions scenario illustrated in panel d) (dark blue line, with additional run with post-CRB glaciation effects shown by the light blue line). Note the difference between the rate of decrease in POC δ^{13} C and the rate of increase in POC burial.

We find that in MTW08 an emission scenario of 1000 Pg C from the Steens and Imnaha eruptions, 3500 Pg C from the GRB eruptions, and 280 Pg C from the Wanapum eruptions fit the palaeorecords prior to 15.4 Ma best, while in LOSCAR the best fit is found with slightly reduced emissions of 850 Pg C from the Steens and Imnaha eruptions, 3000 Pg C from the GRB eruptions, and 240 Pg C from the Wanapum eruptions. The difference between the LOSCAR and MTW08 emission scenarios is primarily the result of the additional basalt weathering applied in MTW08, which implies that ~790 Pg C is drawn down by the weathering of fresh basalt during the CRB eruptions. Taking weathering uncertainties into account we estimate that a total CRB emission of 4090-5670 Pg C (an EAF of 6.3 to 8.7 based on the high degassing scenario or 4.2 to 5.8 based on the crust-contaminated scenario), with 3000 to 4000 Pg C of this emitted during just the GRB eruptions, best fits the palaeorecords. This emission range falls within the upper end of the range 460 to 6190 Pg C that we calculate to be feasible for the CRB (Table 2-2), demonstrating that a major perturbation to the long-term carbon cycle and climate can only be achieved by invoking high degassing rates and a major contribution from cryptic degassing. Sensitivity analysis of the impact of the strength of the climate-weathering feedback indicates that although our results are moderately sensitive to the strength of this feedback (Supporting Figure 2-8) it has to be significantly different from the values used in MTW08, LOSCAR and other models to significantly affect our results [Walker et al., 1981; Walker and Kasting, 1992; Merico et al., 2008; Zeebe, 2012]. Sensitivity analysis of the impact of our choice of model parameters also indicates that our results are also moderately sensitive to the silicate weathering rate and sediment burial fraction of carbon export parameters in MTW08 (Supporting Figure 2-9), but this sensitivity has a negligible impact on the overall result of requiring CRB carbon emissions greater than that possible from just sub-aerial basalt degassing in order to match the palaeorecords.

2.5.2 The CCD and the mid-Miocene Climate Transition

Both models fail to create the sustained CCD deepening seen in the palaeorecords, suggesting that some other mechanism drove part or all of the CCD deepening after ~15.4 Ma. A sustained CCD deepening can successfully be simulated through a combination of a shift in carbonate burial to the deep ocean and increased carbonate weathering as a result of either ice sheet growth causing sea level to fall and shelf carbonate deposits to be exposed after 15.4 Ma or elevated continental

weathering (simulated as a 30 % shelf burial reduction and a 20 % increase in carbonate weathering) [Merico et al., 2008; Shevenell et al., 2008; Passchier et al., 2011; Sandroni and Talarico, 2011; Barry et al., 2013; Kender et al., 2014] (Figure 2-4). This result implies that the early Miocene CCD shoaling observed in the equatorial Pacific could be the result of reduced carbonate weathering rates and elevated sea levels associated with the mid-Miocene glacial minima which began at ~17.6 Ma [Passchier et al., 2011]. Alternatively, the 16.0 Ma deepening could be the result of an increase in carbonate productivity after a "carbonate famine" starting at 18.0 Ma [Lyle, 2003; Pälike et al., 2012], but no process able to drive this 2 My reduction of carbonate export has yet been proposed. A decrease in the CaCO₃:Corg rain ratio would also result in a CCD deepening via a decrease in CaCO3 burial and therefore an increase in deep ocean [CO₃²-], but this would also lead to an increase in benthic δ^{13} C in contradiction to the observed recovery in benthic δ^{13} C [Kender et al., 2014]. As a result it is clear that, in our simulations, the permanent CCD deepening can be driven by the cooling trend resulting in shelf-basin carbonate burial fractionation and elevated carbonate weathering after ~15.4 Ma, but as the initial CCD deepening at ~16.0 Ma occurs during a time of relative warmth this suggests that the CRB had a role in deepening the CCD earlier than otherwise would have occurred [Passchier et al., 2011; Feakins et al., 2012]. On the other hand it is important to note that the high-quality CCD records available from the eastern equatorial Pacific may not be globally representative, and that as the CCD shoalings at ~18.0 Ma and ~10.0 Ma (see Figure 2-1) are unconnected to the CRB it is also possible that the ~16.0 Ma deepening may primarily be driven by a different process not discussed above. For other LIPs it is therefore likely that they could have also triggered a deepening of the CCD, but these deepenings may have been relatively transient and so may be difficult to observe in the low-resolution CCD palaeorecords currently available.

2.5.3 Mid-Miocene climate change

Proxy records and climate model simulations suggest that the warmth of the MCO (2 to 4 °C warmer than today) can be largely explained by atmospheric CO₂ concentrations increasing to >400 ppmv [Flower, 1999; Kürschner et al., 2008; You et al., 2009; Henrot et al., 2010; You, 2010; Herold et al., 2011; Knorr et al., 2011; Foster et al., 2012]. Our simulations show a ~90 ppmv increase from 280 ppmv by 15.9 Ma, suggesting that at least some of this increase could have been derived from the CRB.

This CO₂ increase would have increased radiative forcing by 1.5 Wm⁻² by 15.9 Ma (based on a CO₂ baseline of 280 ppmv), causing a global warming of 0.9 to 1.9 °C (assuming a climate sensitivity of 2.2 to 4.8 °C per CO₂ doubling [Rohling et al., 2012]) compared to the observed mid-Miocene warmth of 2 to 4 °C relative to the Holocene. More warming could be achieved either with a higher climate sensitivity including slow feedbacks, with a long-term icehouse climate sensitivity of 6 °C per CO₂ doubling yielding 2.4 °C of warming [Hansen et al., 2008; Park and Royer, 2011], or from changes in other boundary conditions such as palaeogeography [You et al., 2009; Henrot et al., 2010; Herold et al., 2011]. Although our estimate of CRB-driven temperature increase only reaches the lower limit of total mid-Miocene warming it does coincide with the second MCO warmth maximum and ice sheet extent minimum around 15.7 Ma, implying that the CRB could have helped intensify the MCO and delayed the subsequent reglaciation of the Antarctic during the mid-Miocene Climate Transition [Billups and Schrag, 2003; Holbourn et al., 2007, 2013; Shevenell et al., 2008; Passchier et al., 2011; Feakins et al., 2012; Foster et al., 2012]. However, the first MCO warmth maximum at ~16.5 Ma pre-dates the simulated onset of the GRB cryptic degassing by ~200 ky and is preceded by the relatively small emissions of the Steens and Imnaha basalt eruptions, implying that the CRB was not the sole cause of the MCO. The timing of the equatorial Pacific CCD deepening also suggests there was no major pulse in emissions before ~16.3 Ma as no major changes in the CCD are observed between 18.0 and 16.0 Ma. These observations imply that some other process may have driven warming independently of the CRB in the early stages of the MCO, and that this process may also be linked to the ~18.0 Ma CCD shoaling and the MCIE. Other LIPs may have also occurred during similar times of background climate variability, thus complicating the interpretation of LIP-driven climate change and emphasising the importance of establishing an accurate chronology of eruption phases and climate events when establishing the magnitude of LIP-driven climate change.

The timing of our best-fit emissions scenario also implies that the GRB cryptic degassing began around the same time as the 'Mi-2' glacial maximum at ~16.2 Ma [Miller et al., 1991]. It is possible that enough sulphate aerosols and other volatiles may have been released to have triggered an initial, short-term episode of cooling prior to the longer-term warming effect of CO_2 becoming dominant [Thordarson and Self, 1996; Sobolev et al., 2011]. The Deccan Traps and other LIPs are estimated to have released ~7 Tg SO_2 km⁻³, which implies an emission of ~1.1x10³ Pg SO_2 (an emission rate of ~2.6 Tg SO_2 y⁻¹ over 400 ky) from the GRB sub-aerial basalts, and up to ~9.3x10³ Pg SO_2 (~23.4 Tg SO_2 y⁻¹) for the maximum total GRB volume [Self et al.,

2006]. This is significantly more than the background atmosphere SO₂ content of <1 Tg, implying that GRB cryptic degassing could have initially triggered global cooling before the gradual increase in atmospheric CO₂ led to warming dominating as cryptic degassing reached its end. It is well established that larger LIPs are associated with significant releases of SO₂ [Wignall, 2001; Self et al., 2006; Sobolev et al., 2011], but our results imply that other small LIPs may also coincide with an initial episode of cooling prior to longer-term warming peaking after eruptions decline.

2.6 Conclusions

We find that we can successfully simulate perturbations to the benthic δ^{13} C, CCD, and atmospheric CO₂ palaeorecords at ~16.0 Ma with the emission of 4090-5670 Pg C from the CRB, of which 3000-4000 Pg C is emitted during the GRB eruptions between 16.3 and 15.9 Ma, and that the CRB is capable of these emissions if a major role is invoked for cryptic degassing from intrusive volcanic activity. Even this emission scenario cannot account for the warmth of the entire MCO though, implying that some other driver of global warmth existed prior to 16.3 Ma, and we also find that some other process after 15.4 Ma such as reglaciation must have occurred to keep the CCD deepened after this time. If the same cryptic degassing sources were involved in other LIPs then our results imply that those LIPs would have also had a more significant impact on global climate and ocean biogeochemistry than previously estimated and their impacts therefore require reappraisal.

2.7 Acknowledgements

This work was supported by a Natural Environment Research Council studentship to D.I.A.M (grant number NE/J500112/1). We thank Agostino Merico and Richard Zeebe for sharing their respective models and advice on using them, Heiko Pälike and Ann Holbourn for sharing their data, Jon Blundy for comments on the likely extent of intrusive and underplated magma, and Kevin Oliver, Lee Kump, Ellen Thomas and several anonymous reviewers for constructive feedback on earlier drafts of this manuscript.

2.8 Supporting Information

2.8.1 Model parameters

Table 2-3: MTW08 biogeochemical parameters (where different from *Merico et al.* [2008]).

Parameter	Description	Units	MTW08 value
KSM ^a	Mixing coefficients of surface-middle layers	my ⁻¹	16.4
KMD ^a	Mixing coefficients of middle-deep layers	my ⁻¹	2.7
RP^b	Riverine phosphorus	$\mathrm{mmol}\;\mathrm{m}^{-2}\;\mathrm{y}^{-1}$	0.1
RS^b	Riverine silicate	$\mathrm{mmol}\;\mathrm{m}^{-2}\;\mathrm{y}^{-1}$	11.3
RN^b	Riverine nitrogen	$\mathrm{mmol}\;\mathrm{m}^{-2}\;\mathrm{y}^{-1}$	3.4
HS	Hydrothermal input of silicate	$\mathrm{mmol}\;\mathrm{m}^{-2}\;\mathrm{y}^{-1}$	0.8
T _{surf} ^c	Temperature of surface ocean	°C	23.0
$T_{deep}^{}c}$	Temperature of deep ocean	°C	10.0
$pCO_{2(ini)}$	Partial pressure of CO ₂ in atmosphere (initial)	p.p.m.v.	280.3
FCAR ^b	Baseline carbonate weathering rate	mmol y ⁻¹	1.31x10 ¹⁶
FSIL ^b	Baseline silicate weathering rate	mmol y ⁻¹	3.52x10 ¹⁵
VOLC ^b	Volcanic CO ₂ emissions into the atmosphere	mmol y ⁻¹	2.58x10 ¹⁵
KERO⁵	Kerogenic CO ₂ emissions into the atmosphere	mmol y ⁻¹	2.11x10 ¹⁵
[Ca] ^d	Calcium ion concentration	mmol m ⁻³	14800.0
Mg/Ca ^d	Magnesium/calcium ion ratio	N/A	3.7
S	Salinity	ppt	38
SHARA/CAL ^e	Fraction of calcite/aragonite buried in shallow settings	N/A	0.07

^a Lower KSM and KMD based on likelihood of slower ocean overturning due to smaller ice sheets and a lower meridional temperature gradient [*Flower and Kennett*, 1994]

b RP, RS, RN, FCAR, FSIL, VOLC and KERO based on Merico et al. [2008] and Li et al. [2009]

^c Ocean temperature estimated to be higher than modern during the Miocene [Flower, 1999]

d [Ca] and Mg/Ca based on Tyrrell and Zeebe [2004]

^e Shallow ocean carbonate burial estimated to be higher than modern during the Miocene [*Opdyke and Wilkinson*, 1988]

Table 2-4: LOSCAR biogeochemical parameters (where different from the pre-industrial setup of *Zeebe* [2012]).

Parameter	Description	Units	LOSCAR value	
PCO2SI	Steady-state pCO ₂	p.p.m.v.	280.0	
THC	Conveyor transport	Sv	20	
RRAIN	Rain ratio of Corg to CaCO ₃	N/A	6.7	
FSHLF	Ratio of shallow/deep CaCO ₃ rain	N/A	2.0	
FINC	Initial CaCO ₃ riverine flux	mol C y ⁻¹	13.1x10 ¹²	
CALC ^a	Seawater [Ca ²⁺]	mol kg ⁻¹	14.8e-3	
MAGN ^a	Seawater [Mg ²⁺]	mol kg ⁻¹	46.0e-3	
a [Colord Ma/Co boood on Tiggell and Zoobo [2004]				

^a [Ca] and Mg/Ca based on *Tyrrell and Zeebe* [2004]

Table 2-5: Isotopic parameters and initial values for both MTW08 and LOSCAR. Default LOSCAR values are the pre-industrial setup values from *Zeebe* [2012].

Parameter	Description	MTW08 initial value (‰)	LOSCAR initial value (‰)
$\delta^{13}C_{surf}$	Surface ocean box (initial state)	1.25	Default
$\delta^{13}C_{\text{mid}}$	Middle ocean box (initial state)	-0.16	Default
$\delta^{13}C_{\text{deep}}$	Deep ocean box (initial state)	-1.15	Default
$\delta^{13}C_{\text{atm}}$	Atmosphere (initial state)	-7.74	Default
$\delta^{13}C_{\text{riv}}$	Baseline riverine input (linked to FCAR)	0.28	Default
$\delta^{13}C_{\text{phy}}$	Phytoplankton fractionation	-21.0	Default
$\delta^{13}C_{\text{vol}}$	Volcanic input	-4.0	Default
$\delta^{13}C_{ker}$	Kerogenic input	-20.0	Default

2.8.2 Sensitivity analyses

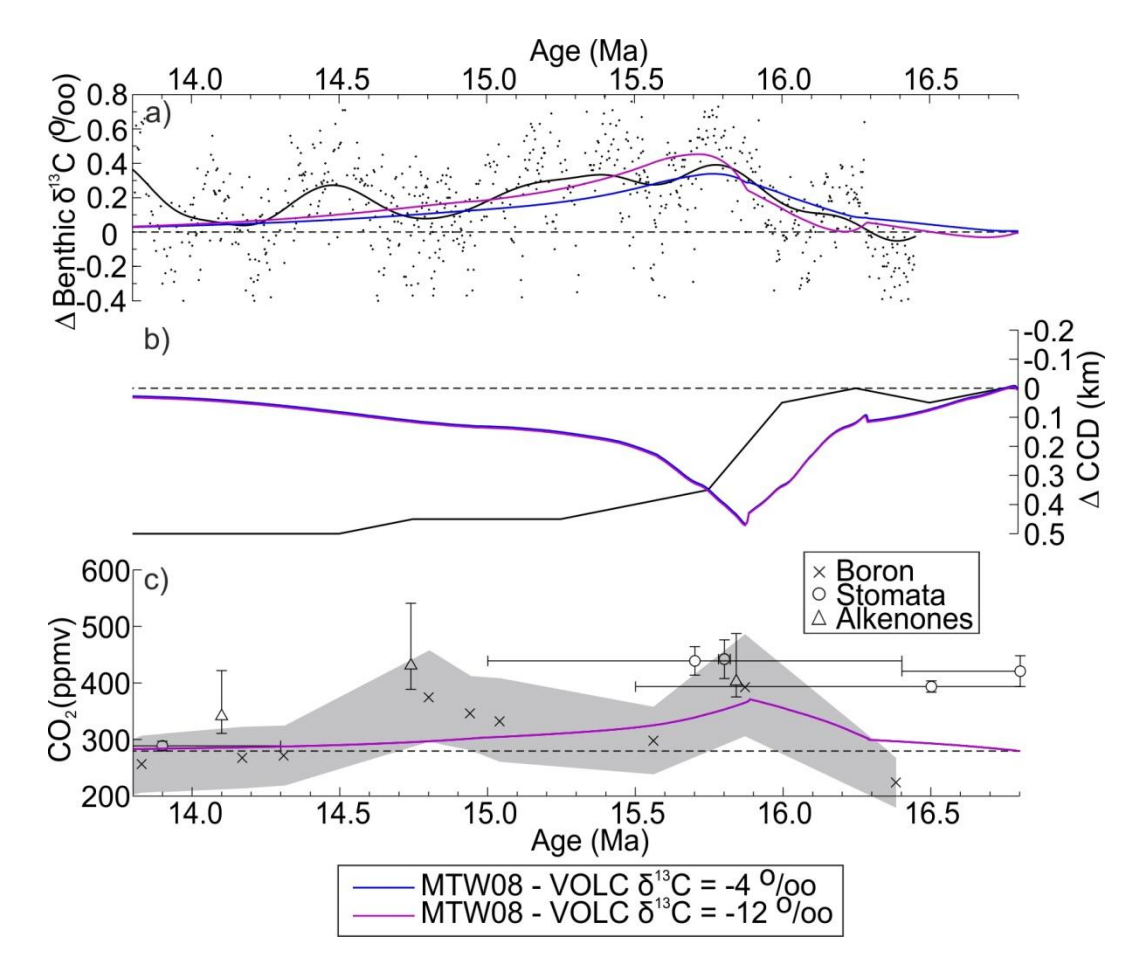


Figure 2-7: Sensitivity analysis of adjusting volcanic $\delta^{13}C$ from-4 ‰ (blue, the same scenario represented by the light blue line in Figure 2-4) to -12 ‰ (purple) in our best-fit MTW08 scenario, plotted against the palaeorecords shown in Figure 2-3 and Figure 2-4. Although the form of the benthic $\delta^{13}C$ perturbation in the -12 ‰ scenario is not identical the perturbation is of a similar magnitude and duration as in the -4 ‰ scenario, implying that a lighter $\delta^{13}C$ value for the additional volcanic emissions does not have a significant impact on the conclusions of this study.

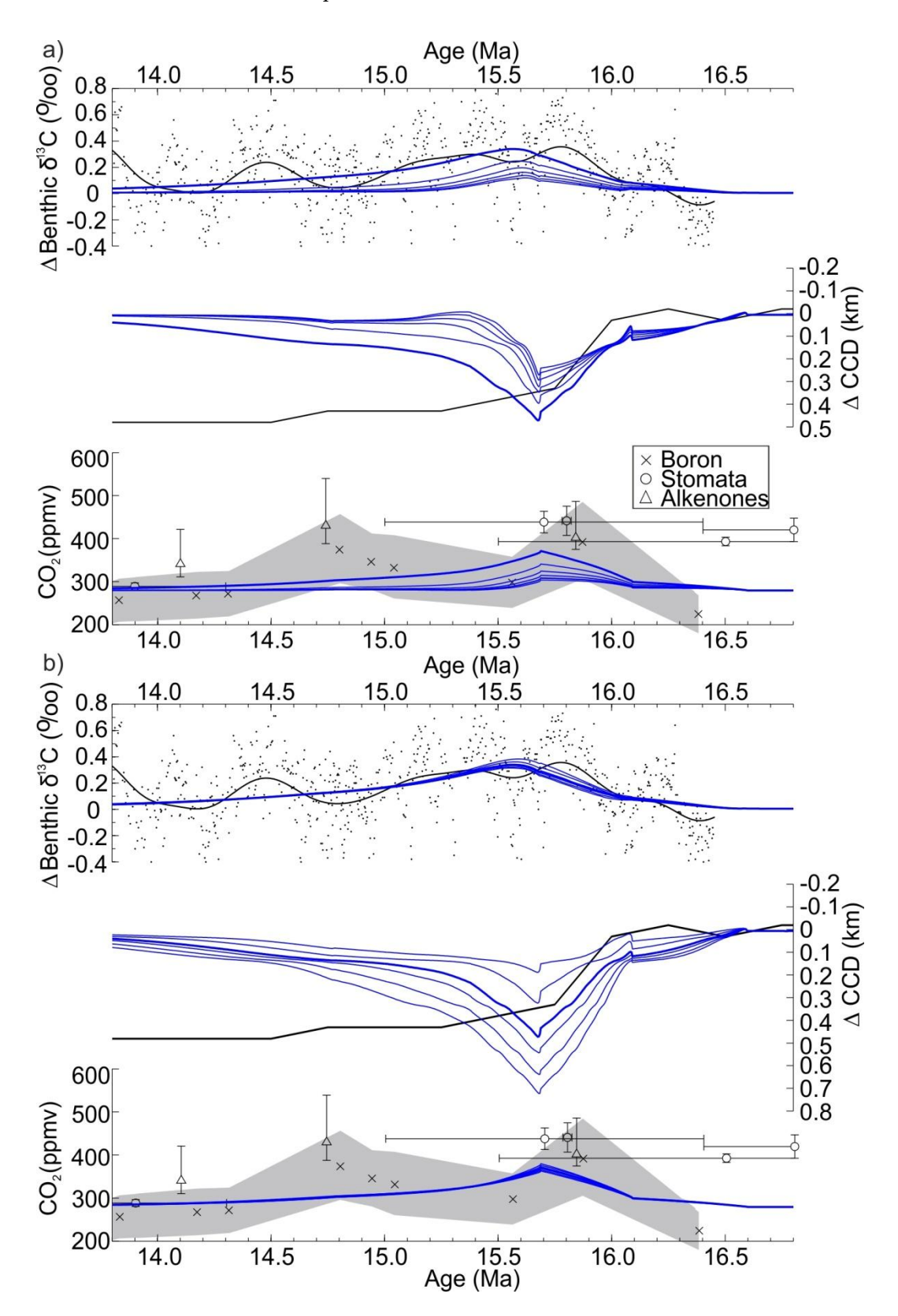


Figure 2-8: a) Sensitivity analysis of changing the silicate weathering exponent in our best-fit MTW08 scenario, plotted against the palaeorecords shown in Figure 2-3 and Figure 2-4. The results (thin blue lines, fixed $\alpha_c = 1.0$ and a variable $\alpha_s = 0.3$ (as used in study, thick line), 0.6, 0.9, 1.2, 1.5, and 1.8) illustrate the moderate sensitivity of $\delta^{13}C$ and atmospheric CO_2 and the lower sensitivity of CCD to the value chosen for the silicate weathering exponent. However, the higher silicate weathering exponent values fall substantially outside of best estimates while the pattern of the excursions remain similar to the palaeorecord, suggesting that this sensitivity does not have a significant impact on the conclusions of this study. b) Sensitivity analysis of changing the carbonate weathering exponent in our best-fit MTW08

scenario, plotted against the palaeorecords shown in Figure 2-3 and Figure 2-4. The results (thin blue lines, fixed α_s = 0.3 and a variable α_c = 0.3, 0.6, 1.0 (as used in study, thick line), 1.2, 1.5, and 1.8) illustrate the relatively low sensitivity of $\delta^{13}C$ and atmospheric CO_2 and the moderate sensitivity of the CCD to the carbonate weathering exponent. However, for most of the scenarios the CCD remains within palaeodepth error (± 250 m), suggesting that this sensitivity does not have a significant impact on the conclusions of this study.

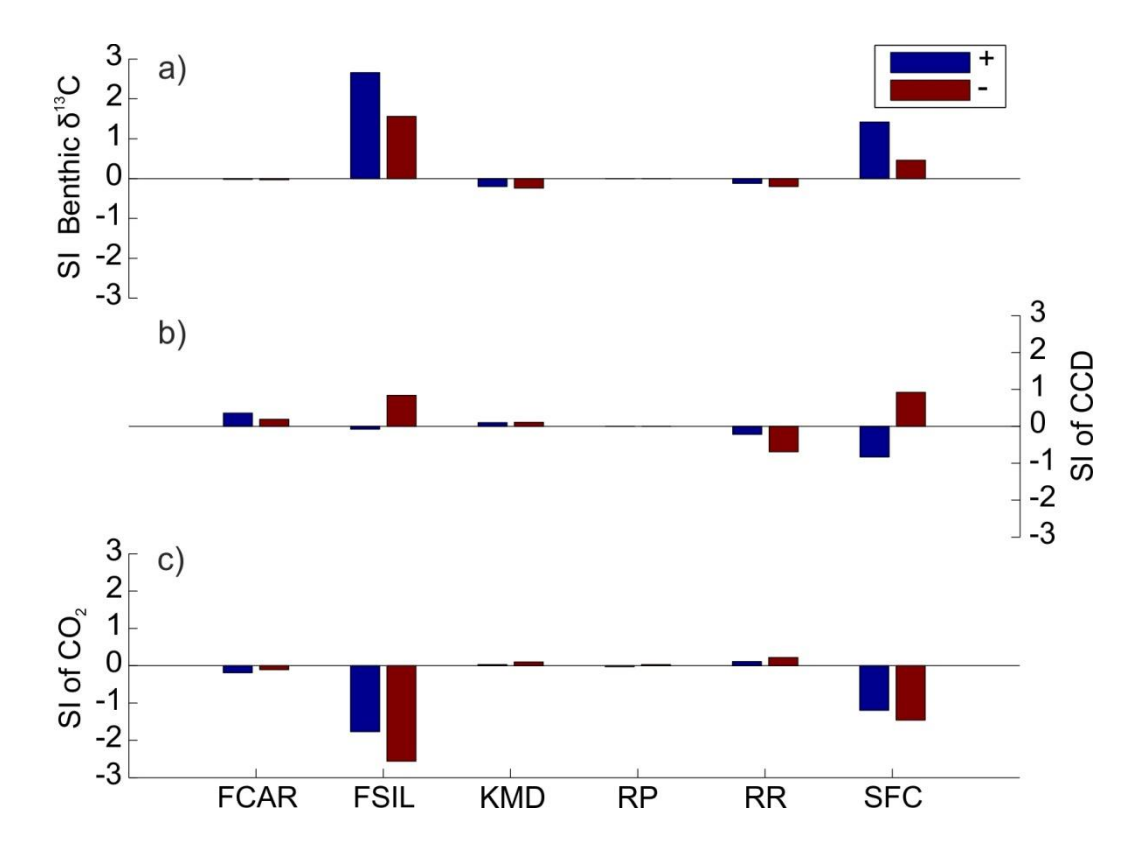


Figure 2-9: Sensitivity analysis of the key MTW08 parameters on our best-fit MTW08 scenario. The sensitivity index (SI) is calculated for each of the major parameters (FCAR (carbonate weathering rate), FSIL (silicate weathering rate), KMD (mid to deep ocean mixing), RR (rain ratio of inorganic to organic carbon export), and SFC (sediment burial fraction of carbon export)) and each major model output ((a) benthic δ^{13} C, b) CCD, and c) atmospheric CO₂) for both positive (blue bars) and negative (red bars) perturbations. This analysis illustrates that our results are relatively robust to the values of FCAR, KMD and RR (S \leq ±1) and the moderate sensitivity of our results to the values of FSIL and SFC (±1<S<±3). However, although the results are moderately sensitive to FSIL and SFC the general temporal dynamics of the perturbations do not diverge much from the best-fit results obtained with nominal parameters and the sensitivity index value for these parameters are not significantly greater than 1, and so this sensitivity does not have a significant impact on the overall conclusions of this study.

Chapter 3:

Global carbon cycle perturbation across the Eocene-Oligocene climate transition

In this chapter the hypothesised drivers of the carbon cycle perturbation across the Eocene-Oligocene Transition are investigated using a biogeochemical model. This chapter forms the basis of a manuscript in revision for publication in Paleoceanography with the following authors: Armstrong McKay, D. I., Tyrrell, T., and Wilson, P. A. Supporting online-only information is included at the end of this chapter (Section 3.7).

3.1 Abstract

The Eocene-Oligocene Transition (EOT), ~34 million years ago, marks a tipping point in the long-term Cenozoic greenhouse to icehouse climate transition. Palaeorecords reveal stepwise rapid cooling and ice growth across the EOT tightly coupled to a transient benthic δ^{13} C excursion and permanent deepening of the carbonate compensation depth (CCD). Based on biogeochemical box model experiments, Merico et al. [2008] suggest that glacioeustatic sea-level fall and resulting shelf to basin fractionation of carbonate burial can account for the carbon cycle perturbation, but this finding is controversial. Alternative proposed mechanisms include increased ocean ventilation, decreased carbonate to organic carbon rain ratio, increased silicate weathering, and increased ocean calcium concentration. Here we report experiments to test these competing hypotheses using an improved version of the biogeochemical box model of Merico et al. [2008]. We find that no single hypothesis acting alone can account for the observed carbon cycle perturbation. Changes in oceanic calcium concentration, silicate weathering rate, and rain ratio each yield a response that is fundamentally at odds with the form and/or sign of geological records. Shelf-basin carbonate burial fractionation (CCD change) and a combination of shelf carbonate weathering, sequestration of isotopically light carbon into expanding permafrost or peatlands (δ¹³C excursion), and a possible additional contribution from increased ocean ventilation offer the most convincing explanations for the palaeoceanographic observations. The extensive reservoir of Antarctic permafrost

carbon that must have developed during the descent into the Cenozoic icehouse was eroded prior to the EOT and/or sequestered below advancing ice sheets.

3.2 Background

3.2.1 The Eocene-Oligocene Transition

The first permanent, large-scale ice sheets on Antarctica were established during the Eocene-Oligocene Transition (EOT) ~34 million years ago, the point at which Earth's climate transitioned from a late Cretaceous-early Palaeogene greenhouse state to a late Palaeogene-Neogene icehouse state [Zachos et al., 2001b]. Palaeorecords of high latitude climate change (benthic δ^{18} O) reveal stepwise cooling and ice sheet growth at ~34.0 Ma (EOT-1) and ~33.7 Ma (Oi-1) (Figure 3-1a) [Coxall et al., 2005; Coxall and Wilson, 2011], with a cooling of between 2 and 6 °C mostly during the first step and ice sheet growth equivalent to 60 to 130% of modern Antarctic ice volume mostly during the second step [Coxall et al., 2005; Lear et al., 2008; Miller et al., 2008; Liu et al., 2009; Scher et al., 2011; Tigchelaar et al., 2011; Wade et al., 2011; Bohaty et al., 2012]. These steps are accompanied by a $\leq 1.0 \% \delta^{13}$ C excursion in benthic foraminifera between 34.0 and 33.7 Ma (Figure 3-1b), along with a deepening of the carbonate compensation depth (CCD), initially by around 1200 m but by around 500 m in the long-term (Figure 3-1c), suggesting a strong coupling between this climatic shift and the carbon cycle [Coxall et al., 2005; Rea and Lyle, 2005; Coxall and Wilson, 2011; Pälike et al., 2012]. The δ^{18} O records take a form similar to that indicated by the results of coupled global climate-ice sheet model experiments [DeConto and Pollard, 2003; DeConto et al., 2008; Ladant et al., 2014b] in which a slow decline of atmospheric CO₂ (atmCO₂) (Figure 3-1d [Pearson et al., 2009; Pagani et al., 2011) and superimposed orbital forcing bring about the crossing of a critical threshold for the initiation of rapid Antarctic glaciation.

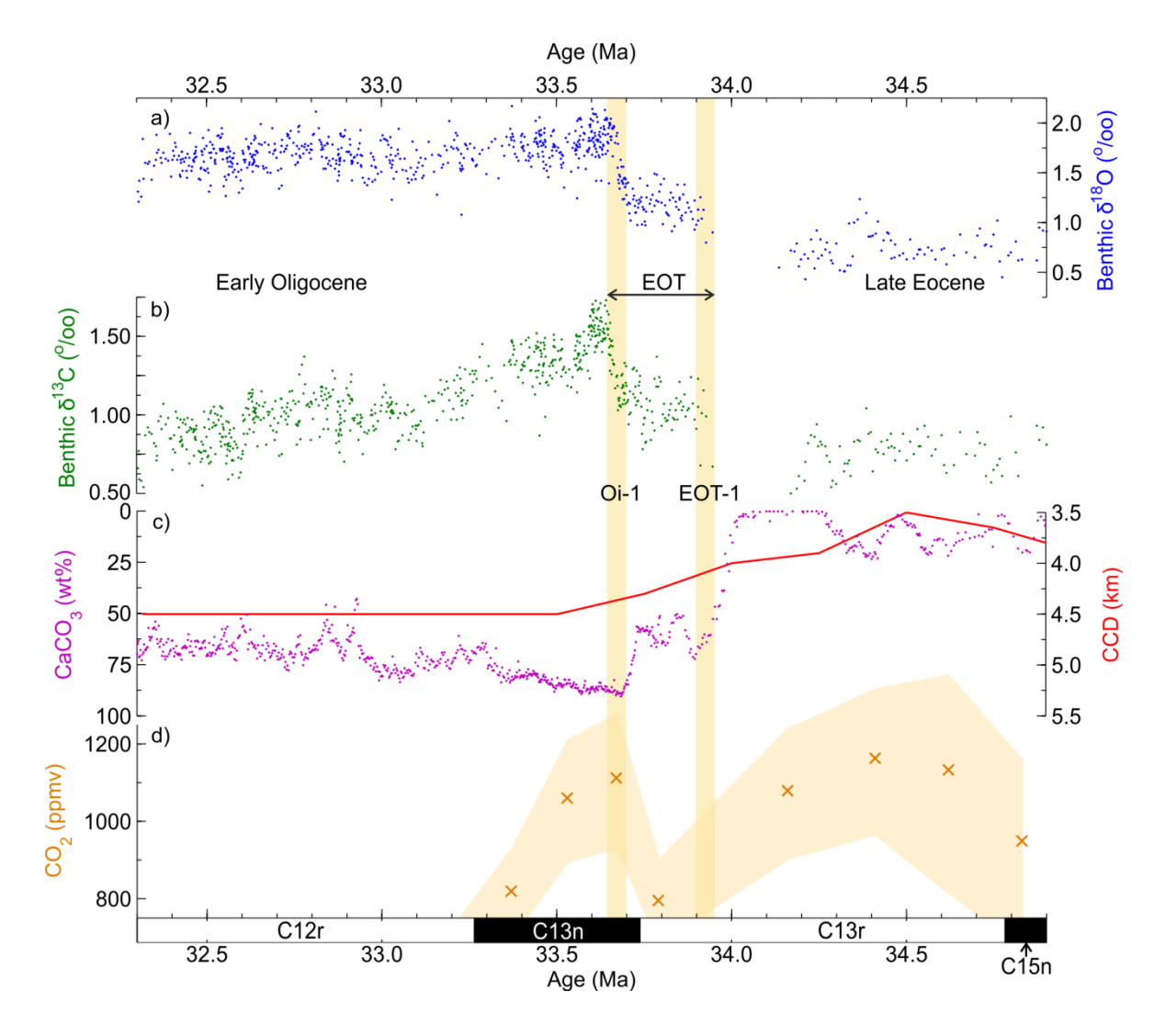


Figure 3-1: Palaeorecords across the Eocene Oligocene Transition (EOT). a) Benthic δ^{18} O from ODP Site 1218 (8°53′N, 135°22′W in the equatorial Pacific) (blue) [Coxall and Wilson, 2011], b) benthic δ^{13} C from ODP Site 1218 (green) [Coxall and Wilson, 2011], c) the long-term behaviour of the CCD in the equatorial Pacific (red line) [Pälike et al., 2012] and CaCO₃ wt% from IODP Site 1218 as a qualitative proxy for CCD deepening at Site 1218 (purple) [Coxall et al., 2005; Coxall and Wilson, 2011; using the age model of Westerhold et al., 2014], and d) atmospheric CO₂ reconstructed from the boron isotope pH proxy (orange crosses, shaded band for error) [Pearson et al., 2009] between the late Eocene and the early Oligocene. The EOT-1 and Oi-1 cooling and glaciation steps are indicated by the yellow bars, and the Geomagnetic Polarity Timescale [Ogg and Smith, 2004] is shown along the bottom axis.

3.2.2 Potential drivers of the EOT carbon cycle perturbation

3.2.2.1 Carbonate burial and weathering

Merico et al. [2008] used a biogeochemical box model to test several mechanisms proposed in the contemporary literature for the EOT carbon cycle perturbation, including increases in organic carbon (C_{org}) burial rates, global silicate weathering rates, and siliceous plankton productivity. However, these hypotheses were ultimately rejected on the basis of failing to simultaneously match both the

permanent CCD deepening and the temporary positive benthic δ^{13} C excursion observed in the palaeorecord. The only hypothesis found to replicate successfully these two simulation targets was a shift in CaCO3 burial from shallow shelf seas to the deep ocean, coupled with a temporary increase in carbonate weathering from freshly exposed carbonate shelves. These changes were hypothesised to be driven by the 50 to 75 m fall in sea level associated with the growth of the Antarctic ice sheet [Pekar et al., 2002; Lear et al., 2004; Miller et al., 2008; de Boer et al., 2010; Houben et al., 2012]. In this explanation of events the fall in sea level reduces the area of shallow shelf sea available for carbonate burial, which results in an increase in the calcite (and aragonite) saturation state (Ω) of the ocean and consequently a deepening of the CCD until the increase in deep ocean carbonate burial compensates for the reduction in shelf burial [Berger and Winterer, 1975; Opdyke and Wilkinson, 1988; Kump and Arthur, 1997; Coxall et al., 2005; Lear and Rosenthal, 2006; Merico et al., 2008]. Proxies suggest that the establishment of the Antarctic ice sheet temporarily induced high mechanical and chemical weatherability on Antarctica which, along with the exposure of large areas of previously un-weathered shelf carbonates, led to heightened global carbonate weathering rates [Zachos et al., 1999; Griffith et al., 2011; Scher et al., 2011; Basak and Martin, 2013; Moore, 2013]. However, this hypothesis requires a big shift in carbonate burial from shallow to deep water (~99 % in Merico et al. [2008]) and a substantial temporary increase in carbonate weathering rates (300 % in Merico et al. [2008]) to match fully the amplitude of change seen in the palaeorecords. It has been suggested that the sea level fall across the EOT is insufficiently large and unique enough to have caused such a large and permanent change in both shelf carbonate burial rates and weathering [Rea and Lyle, 2005; Miller et al., 2009].

3.2.2.2 Ventilation and productivity

As an alternative to shelf-basin carbonate burial fractionation it has been suggested that cooling and ice sheet growth resulted in increased ocean mixing rates, which is postulated to in turn ventilate the deep ocean and reduce deep-ocean acidity enough to deepen the CCD [Miller et al., 2009; Goldner et al., 2014]. Increased ocean mixing has also been invoked as means of stimulating plankton productivity, and in particular diatom productivity in the Southern Ocean, by upwelling nutrients from deep water, which results in a positive benthic δ¹³C perturbation due to elevated Corg export and burial relative to carbonate [Salamy and Zachos, 1999; Zachos and Kump, 2005; Scher and Martin, 2006; Berger, 2007; Dunkley Jones et al., 2008; Scher et al., 2011]. An increase in Corg burial can also be achieved through an increase in Corg

preservation, for example through a shift in production to upwelling zones with high sedimentation rates or due to cooler deep water from greater polar deep-water formation [Zachos et al., 1996; Olivarez Lyle and Lyle, 2006; John et al., 2014]. All of these hypotheses were tested by Merico et al. [2008] but their efficacy was called into question. The results of those experiments indicated that ocean mixing and productivity can be ruled out as sole drivers of the observed carbon cycle perturbation because both mechanisms produce a permanent rather than a temporary δ^{13} C excursion and a temporary rather than a permanent CCD deepening. Furthermore, the observations of Griffith et al. [2010] cast doubt on the likelihood of there having been a significant increase in plankton productivity across the EOT. Such an increase would, all else remaining equal, be expected to lead to a decrease in the global $CaCO_3$: C_{org} surface export ratio (known as the rain ratio), but barite accumulation rate data instead suggest an increase in the rain ratio.

3.2.2.3 Silicate weathering and calcium

Another hypothesised driver of the EOT CCD deepening is an increase in the input of calcium ion (Ca2+) to the ocean through increased silicate weathering resulting in an increase in ocean Ω [Rea and Lyle, 2005]. Increased silicate weathering, potentially due to increased glacial erosion in Antarctica facilitating greater chemical weatherability, has also been invoked as a source of additional alkalinity input to the ocean to help deepen the CCD as well as providing a positive feedback on glaciation through the drawdown of atmCO₂ [Zachos and Kump, 2005; Griffith et al., 2011; Scher et al., 2011; van de Flierdt, 2011; Basak and Martin, 2013]. Ca²⁺ input to the ocean is primarily derived from continental weathering and oceanic hydrothermal systems. The dual effects of continental weathering on ocean Ω (directly through Ca²⁺ and indirectly through alkalinity delivery) both act to raise its value and so would result in the deepening of the CCD and increased Ca²⁺ removal through burial [Farkaš et al., 2007b; Komar and Zeebe, 2011]. To exert any significant impact on Ca^{2+} concentration in the ocean ($[Ca^{2+}]$) it is therefore necessary to decouple the input of Ca²⁺ from alkalinity input. This is possible through increased dolomitisation, hydrothermal Ca²⁺ input, or sulphuric-acid driven weathering [Heuser et al., 2005; Farkaš et al., 2007a], but a large change in Ca²⁺ delivery is required to overcome the long (~1 My) residence time of Ca²⁺ in the ocean. Palaeorecords of δ^{44/40}Ca across the EOT show a negative excursion in bulk carbonate of ~0.6 \% which has been attributed to increased Ca2+ flux to the ocean as a result of a long-term increase in silicate weathering rates [De La Rocha, 2000; Fantle, 2010]. However, δ^{44/40}Ca records

generated across the EOT on marine barites, which are posited to provide a better record of calcium isotope changes, yield a smaller shift in reconstructed seawater $\delta^{44/40}$ Ca, suggesting little change in silicate weathering rates and Ca²⁺ delivery to the ocean across the EOT [*Griffith et al.*, 2011].

3.2.2.4 Carbon capacitors and cooling

Other potential drivers of carbon cycle disruptions across the EOT involve various reservoirs of sedimentary C_{org} capable of rapid exchange with the oceanatmosphere system. These include carbon stored in permafrost, marine methane hydrates, peat, wetlands, and soil. Permafrost Soil Carbon (PFSC) deposits in the Northern Hemisphere (NH) currently contain up to ~1700 Pg of carbon [Tarnocai et al., 2009; Koven et al., 2011], but modelling of the early Eocene suggests that the late Eocene inventory was more than double this present day figure (~3700 Pg C: ~1700 Pg C in Antarctica; ~2000 Pg C in NH [DeConto et al., 2012]) and bigger even than the inventory of the last glacial when approximately 2700 Pg C is estimated to have been sequestered by PFSC [Zimov et al., 2009; Zech et al., 2011]. Modern peatlands are estimated to contain between 180 and 455 Pg C of a total global soil inventory of \sim 2400 Pg C, and this reservoir is hypothesised to have sequestered a further \sim 500 Pg C during the Last Glacial Maximum [Klinger, 1991; Batjes, 1996; Klinger et al., 1996; MacDonald et al., 2006]. Methane hydrates in marine sediments are estimated to contain between 450 and 3000 Pg C today and are hypothesised to have had a similar inventory in the Eocene [Buffett and Archer, 2004b; Dickens, 2011; Wallmann et al., 2012], although the total inventory is uncertain even in the modern. Together, these three reservoirs contain a substantial inventory of carbon, and changes to their storage capacity are capable of rapidly perturbing the exogenic carbon cycle.

We might expect the storage capacity of these 'carbon capacitors' [Dickens, 2011] to have grown during the EOT because of global and particularly high latitude cooling. In fact, the growth and subsequent decline of methane hydrate reservoirs has been invoked as a potential driver of the EOT δ^{13} C excursion [Berger, 2007]. Arctic PFSC is modelled to expand by ~ 1300 Pg as $_{\rm atm}$ CO₂ falls from 900 to 550 ppmv [DeConto et al., 2012] while a simulation of modern PFSC indicates that permafrost processes enhance carbon sequestration [Koven et al., 2011], and so PFSC expansion can potentially act as a positive feedback on cooling. We might also expect CO₂ drawdown through these mechanisms to have been opposed by CO₂ release through the erosive action of advancing ice sheets on Antarctic permafrost. Yet recent discoveries of pre-glacial soils preserved beneath the Greenland ice sheet and

methanogenesis continuing in sub-Antarctic sediments indicate that a significant proportion of PFSC can survive the growth of ice sheets without being eroded [Wadham et al., 2012; Bierman et al., 2014], and PFSC sequestration below ice sheets has been invoked as part of the glacial burial hypothesis to explain Pleistocene $_{\rm atm}CO_2$ variability [Zeng, 2003]. If a significant proportion of Antarctic PFSC was sequestered below advancing ice sheets or in sediments then expansion of PFSC or other $C_{\rm org}$ reservoirs elsewhere in response to global cooling could have resulted in a net positive $\delta_{\rm ^{13}C}$ excursion and a drawdown of $_{\rm atm}CO_2$ across the EOT.

3.2.3 Study aims

To test each of the competing hypothesised mechanisms responsible for the EOT carbon cycle perturbation we undertake biogeochemical box model simulations to determine the changes necessary for each hypothesis to match the geochemical excursions observed in the palaeorecord. We then evaluate whether these changes are feasible within the constraints of the late Eocene Earth system.

3.3 Method

3.3.1 Modelling

We use an improved version of the biogeochemical box model of *Merico et al*. [2008] (hereafter referred to as MTW08) to explore new hypotheses not considered in *Merico et al*. [2008] and re-examine longer standing hypotheses in more detail. MTW08 is an open system containing all the major fluxes and processes in the carbon, phosphorus, and silicon cycles, including the carbonate system, air-sea gas exchange, the organic matter pump, CO₂ drawdown by silicate weathering, calcium carbonate formation and cycling, and carbon isotopes. For this study we have also added the impact of dynamic changes in the ocean [Mg²⁺]/[Ca²⁺] ratio on ocean Ω to the model in order to capture better the impact of hypothesised changes in [Ca²⁺] during the EOT. To do this we incorporate the estimated impact of the [Mg²⁺]/[Ca²⁺] ratio on the stoichiometric solubility product of calcite and aragonite and the dissociation constants of carbonic acid [*Ben-Yaakov and Goldhaber*, 1973; *Mucci and Morse*, 1984; *Tyrrell and Zeebe*, 2004]. MTW08 is limited by low spatial resolution, uncertainties in late Eocene estimates for model parameters, and the lack of dynamic ocean-atmosphere circulation, terrestrial biosphere, or ocean sediment components. MTW08

parameters were tuned with estimates for late Eocene conditions (Supporting Tables 3-1 and 3-2) and perturbed by various different scenarios for each of the hypotheses outlined in Section 3.3.2. Our simulation targets are: 1) a permanent, 500 m deepening of the CCD with an initial over-deepening of up to \sim 1200 m, and 2) a >+0.7 ‰ benthic δ^{13} C excursion over \sim 1 My with rapid increases at EOT-1 and Oi-1 with a peak of \sim +1.0 ‰ at Oi-1. Previous analyses of the sensitivity of MTW08 to parameter selection have demonstrated that the results of MTW08 simulations are relatively robust to parameter choices [*Merico et al.*, 2008; Chapter 2 – *Armstrong McKay et al.*, 2014].

3.3.2 Hypotheses

Based on our assessment of the literature (discussion in Section 3.2), we define five hypotheses to test. Next we describe how each of these hypotheses is simulated in this study.

3.3.2.1 Carbonate Burial Fractionation (CBF)

In this hypothesis a glacioeustatic fall in sea level results in a decrease in shelf carbonate burial and, through carbonate compensation, an increase in ocean Ω and a deepening of the CCD until ocean Ω returns to equilibrium. It also includes the weathering of formerly submerged carbonate shelves, which we simulate as more enriched in ¹³C than pelagic carbonate (δ¹³C of 1.5 ‰ vs. 0.28 ‰ in the Eocene MTW08 tuning based on palaeorecords and modern data from Great Bahama Bank [Swart and Eberli, 2005; Merico et al., 2008; Swart, 2008; Swart et al., 2009; Oehlert et al., 2012]) and so can contribute to a positive benthic δ^{13} C excursion. To simulate this hypothesis, we reduce the proportion of carbonate burial in shallow settings (from the model baseline of ~45 %; a very conservative estimate for the shelf-rich Eocene but the same as Merico et al. [2008] to allow direct comparison) and temporarily add additional carbonate weathering to represent increased weatherability by varying proportions. In some runs a simultaneous increase in Corg-rich (e.g. shale) and silicate lithology weathering and an increase in riverine nutrient input to the ocean are also simulated to represent the weathering of non-carbonate components of exposed shelves [Scher et al., 2011]. Some estimates of weathering rate differences between the Holocene and the Last Glacial Maximum indicate that carbonate weathering rates are enhanced relative to silicate weathering in response to glaciation in the modern Earth system, and so based on this and the extensive shelf carbonate platforms of the

Eocene we assume that carbonate weathering would increase by a greater magnitude even if the weathering of C_{org}-rich and silicate lithologies are enhanced at the EOT [Gibbs and Kump, 1994].

3.3.2.2 Increased Ocean Ventilation (IOV)

In this hypothesis an increase in ocean ventilation results in a reduction in deep ocean acidity and thus deepens the CCD. It also stimulates (at least for a time) an increase in productivity through the upwelling of deep-water nutrients thereby hypothetically driving an increase in ocean δ^{13} C. To simulate this hypothesis we take the same approach as *Merico et al.* [2008] and increase the surface-to-middle and the middle-to-deep ocean mixing rates (from the Eocene MTW08 baseline of 18.25 and 3.0 my⁻¹ respectively) in two steps at EOT-1 and Oi-1 by varying proportions. This increase is simulated both as temporary and permanent, although it is unlikely that the cooling at the EOT produced a permanent increase in mixing rates once ocean temperature gradients stabilised.

3.3.2.3 Carbon Capacitor Exchange (CCE)

In this hypothesis, not considered by *Merico et al.* [2008], cooling across the EOT results in the net expansion of carbon capacitors such as PFSC in the Northern Hemisphere that, in turn, produces a positive benthic δ^{13} C excursion through oceanic depletion in 12 C. Although methane hydrates have been proposed as a potential 12 C-rich sink during the EOT [*Berger*, 2007] the impact of changing sea level and continental shelf loss complicate the likely response of this reservoir at the EOT. We therefore focus on the potential reaction of two related carbon capacitors, the 12 C-rich PFSC and peatland reservoirs. To simulate this hypothesis we directly remove carbon from the atmosphere (at a δ^{13} C of -23 % to represent a sink such as PFSC or peat; a sink with a more negative δ^{13} C would require commensurately less carbon and vice versa) during both Oi-1 and EOT-1 by varying magnitudes. To simulate the counterhypothesis of net PFSC erosion rather than uptake we instead add carbon with the same isotopic composition to the atmosphere.

3.3.2.4 Export and Burial Ratio changes (EBR)

In this hypothesis either a decrease in $CaCO_3$ export and burial, driven by a decrease in the rain ratio, or an increase in C_{org} burial, driven by increasing C_{org} preservation in seafloor sediments, results in the positive benthic $\delta^{13}C$ excursion through decreased ^{13}C or increased ^{12}C removal from the ocean. A reduction in $CaCO_3$

burial should also deepen the CCD to compensate for the reduction in $[CO_3^{2-}]$ removal, while increasing C_{org} preservation would reduce the concentration of deep-ocean Dissolved Inorganic Carbon (DIC). To simulate these hypotheses we perform two different experiments. In one we reduce the rain ratio (from the Eocene MTW08 baseline ratio of 0.298) resulting in reduced $CaCO_3$ export. In the second experiment we increase the proportion of C_{org} buried in sediment (from the Eocene MTW08 baseline of ~ 0.1 %) which in turn also decreases the proportion of C_{org} remineralised in the deep ocean. The changes in both experiments occur during two steps at EOT-1 and Oi-1 and various magnitudes of change are tested.

3.3.2.5 Increased Silicate Weatherability and Calcium flux to the ocean (SWC)

In this hypothesis increasing concentrations of Ca^{2+} and/or alkalinity in the ocean, attributable to either an increase in silicate weathering or a direct increase in Ca^{2+} input decoupled from weathering, results in an increase in ocean Ω and therefore a deepening of the CCD while also drawing down $_{atm}CO_2$ and in turn acting as a positive feedback on glaciation. To simulate this hypothesis we try two different experiments. In one we simulate an increase in silicate weathering rates above the Eocene model baseline level to deliver an increased supply of both Ca^{2+} and alkalinity to the ocean. In another we increase the input of Ca^{2+} to the ocean without also increasing weathering rates in order to isolate the influence of Ca^{2+} addition.

3.4 Results and Discussion

3.4.1 Scenarios

3.4.1.1 Carbonate Burial Fractionation (CBF)

Figure 3-2 illustrates the results of varying the magnitudes of shelf carbonate burial and/or weathering by differing amounts. We first replicate the favoured scenario of *Merico et al.* [2008] with a temporary 300 % stepped increase in carbonate weatherability by the time of Oi-1 to match the benthic δ^{13} C excursion and a permanent 99 % reduction in the proportion of carbonate buried on shelves to permanently deepen the CCD by ~600 m. However, the magnitude of increase in carbonate weathering that is required to match the benthic δ^{13} C excursion also produces an initial CCD over-deepening of ~2000 m compared to the target of ~1200 m, indicating that such a large increase in carbonate weathering may be excessive if

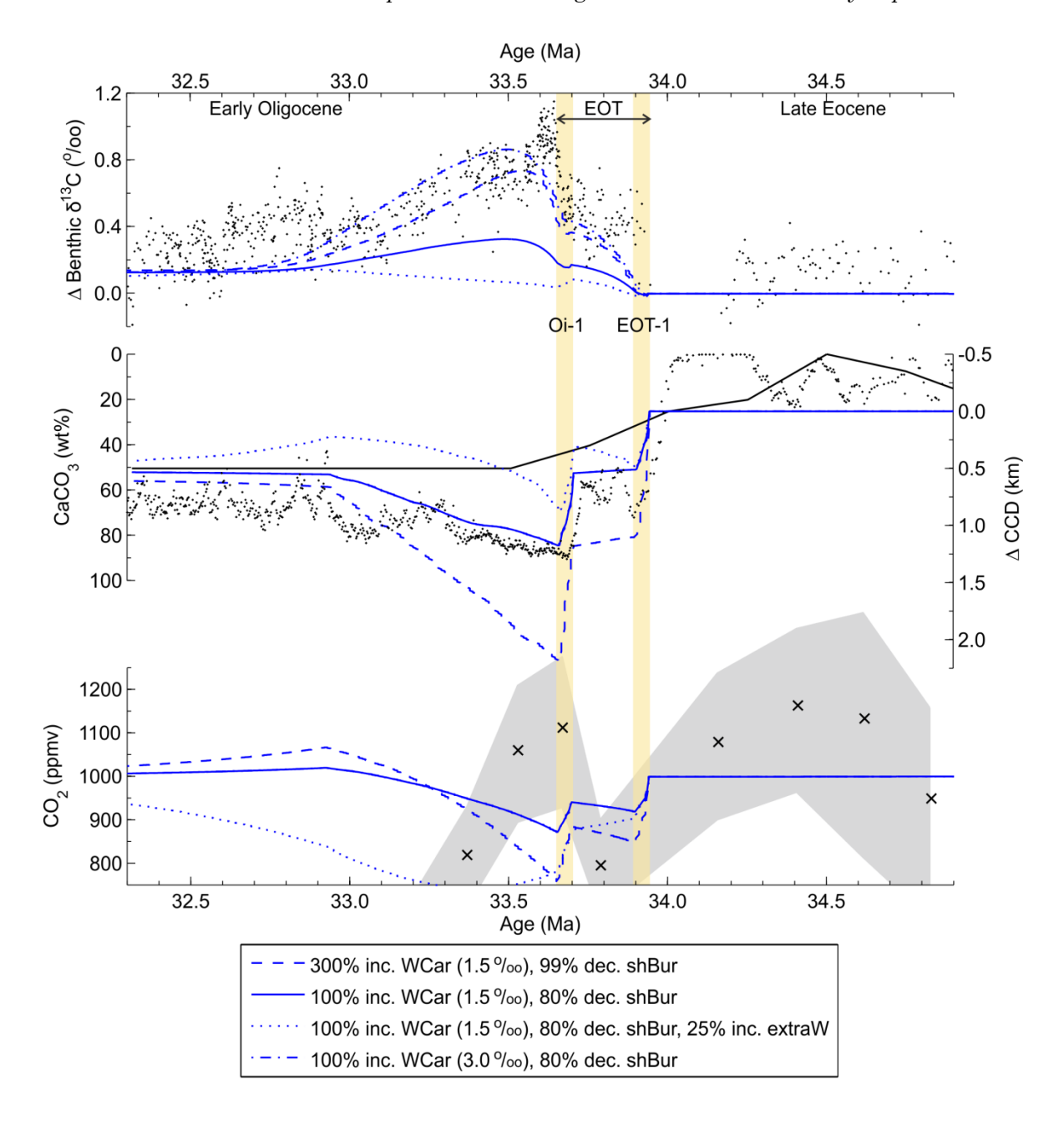


Figure 3-2: Simulation results for the carbonate burial fractionation (CBF) scenario. a) Benthic δ^{13} C, b) global CCD, and c) atmospheric CO₂ outputs compared against EOT palaeorecords (see caption of Figure 3-1 for details; benthic δ^{13} C and CCD have been pinned to Δ =0 at 34.0 Ma; palaeorecords in black) [Coxall et al., 2005; Pearson et al., 2009; Coxall and Wilson, 2011; Pälike et al., 2012; Westerhold et al., 2014]. The simulation scenarios are a two-step 300 % increase in weathering (WCar) of shallow carbonates with δ^{13} C value of 1.5 ‰ coupled with a 99 % reduction in shallow water carbonate burial (shBur) (blue dashed line), a two-step 100 % increase in carbonate weathering (1.5 ‰) coupled with an 80 % reduction in shallow water carbonate burial (blue solid line), a run identical to the latter scenario but with an additional 25 % increase in silicate and kerogen weathering and a 25 % increase in riverine phosphate and nitrate input (extraW) (dotted blue line), and the same prior scenario again but with shelf carbonate δ^{13} C of 3.0 ‰ (dot-dashed blue line). The EOT-1 and Oi-1 cooling and glaciation steps within the EOT are highlighted by the yellow bars.

the records from the equatorial Pacific are globally representative. The 300% increase in global weathering rates is also much greater than that estimated for the Last Glacial Maximum and also results in a decrease in atmCO₂ of ~200 ppm [Gibbs and

Kump, 1994; Munhoven, 2002]. More seriously, this scenario demands the permanent loss of nearly all (99 %) shallow-water carbonate burial, a prediction fundamentally at odds with the geological record [Opdyke and Wilkinson, 1988]. A more modest permanent 80% reduction in shelf carbonate burial (as indicated by Opdyke and Wilkinson [1988]) and a temporary 100% stepped increase in carbonate weatherability are both more in line with the geological record and are still capable of permanently deepening the CCD by ~500 m, with an initial over-deepening of a further ~500 m, and causing a ~100 ppm decrease in atmCO₂. On the other hand, this scenario is not capable of matching the whole δ^{13} C excursion unless the 13 C enrichment of shelf carbonates (see section 3.3.2.1) is increased from 1.5 ‰ to 3.0 ‰ – a degree of enrichment that is modest in comparison to that observed in the modern [Swart and Eberli, 2005, but few data sets are available from shelf carbonates of early Palaeogene age to test this hypothesis. We therefore conclude that shelf carbonate weathering can explain the full benthic δ^{13} C excursion if shelf carbonates were significantly enriched in ¹³C relative to pelagic carbonate, but the enrichment of Palaeogene shelf carbonates is uncertain and lower enrichment yields only a partial match to the benthic $\delta^{13}C$ palaeorecord.

In these first two CBF experiments we assume that only carbonate weatherability increased during the EOT. However, an associated but lower amplitude increase in non-carbonate weathering is possible [Opdyke and Wilkinson, 1988; Gibbs and Kump, 1994; Munhoven, 2002]. To account for the possible impact of increases in non-carbonate weathering we also illustrate the results of a re-run of the permanent 80% reduction in shelf carbonate burial and temporary 100% stepped increase in carbonate weatherability scenario but with additional increases in silicate and kerogen weatherability as well as riverine nutrient input to the ocean. Adding a temporary 25 % increase in silicate and kerogen weatherability and a temporary 25 % increase in the delivery of phosphorus and nitrogen by rivers reduces the initial overdeepening of the CCD, almost completely attenuates the benthic δ^{13} C excursion, and reduces atmCO₂ by ~250 ppm (Figure 3-2). The CCD changes are the result of the climate-weathering feedback resulting in additional atmCO2 drawdown, which in turn leads to a decrease in global weathering rates and alkalinity input to the ocean. The atmCO₂ changes are also the result of increased nutrient input resulting in a spike in primary production, which preferentially exports ¹²C from surface to deep waters and thus counteracts the positive δ^{13} C excursion. Adding additional silicate and kerogen weatherability therefore reduces the match between this scenario and the simulation targets.

3.4.1.2 Increased Ocean Ventilation (IOV)

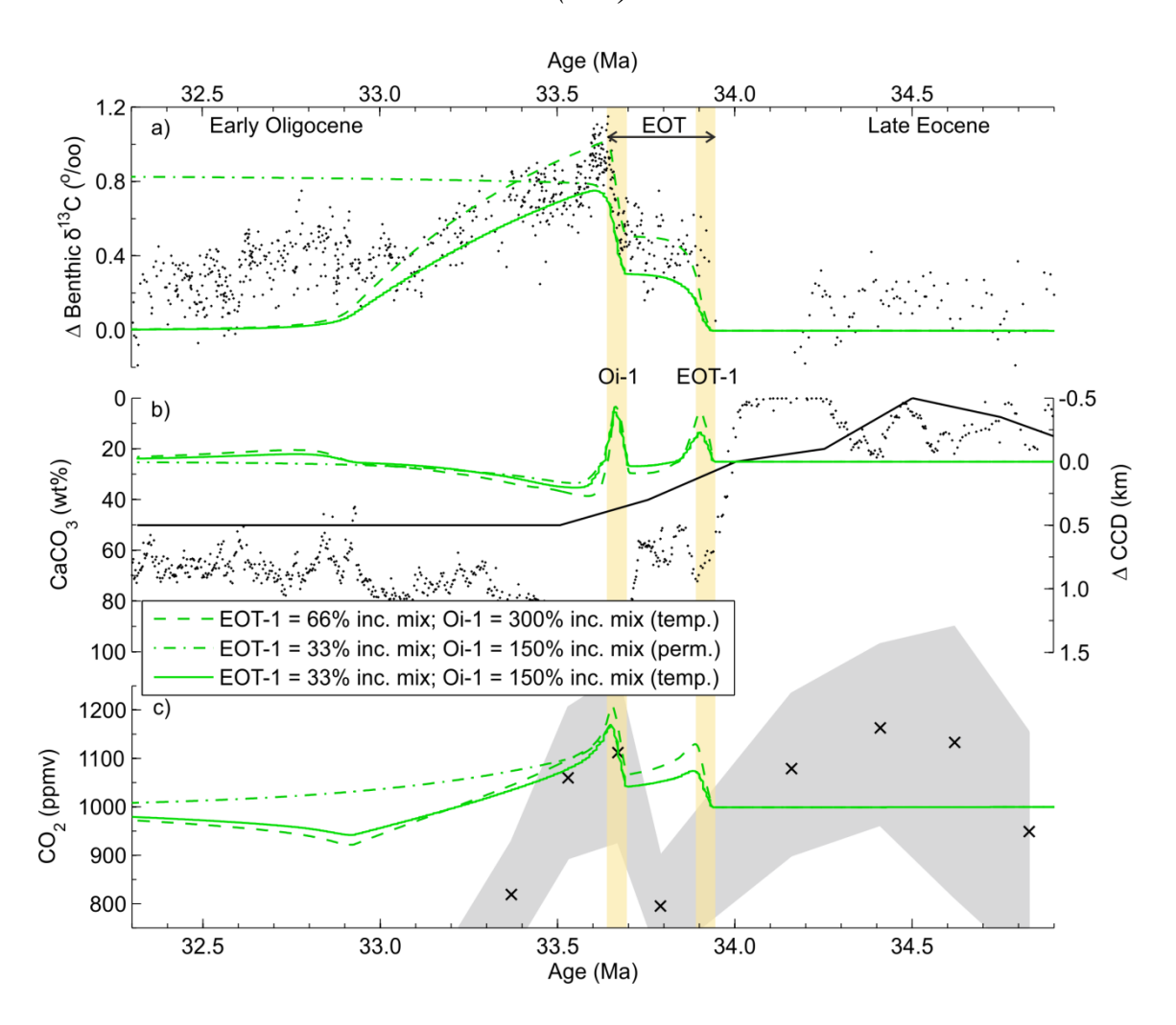


Figure 3-3: Simulation results for the increased ocean ventilation (IOV) scenario. a) Benthic δ^{13} C, b) global CCD, and c) atmospheric CO₂ outputs compared against EOT palaeorecords (see caption of Figure 3-2 for details) [Coxall et al., 2005; Pearson et al., 2009; Coxall and Wilson, 2011; Pälike et al., 2012; Westerhold et al., 2014]. The simulation scenarios are a temporary two-step increase in ocean mixing rates (mix) of 66 % at EOT-1 and 300 % at Oi-1 (dashed green line), a permanent two-step increase in ocean mixing rates of 33 % at EOT-1 and 150 % at Oi-1 (dot-dashed green line), and a temporary two-step increase in ocean mixing rates of 33 % at EOT-1 and 150 % at Oi-1 (solid green line). The EOT-1 and Oi-1 cooling and glaciation steps within the EOT are highlighted by the yellow bars.

Figure 3-3 illustrates the results of increasing ocean mixing rates, hypothesised to be due to increased deep water formation and an increased meridional temperature gradient. Increasing ocean mixing rates leads to an increase in benthic δ^{13} C as a result of the impact of permanently decreased shallow-water [CO₃²⁻] (as its concentration converges with the CO₃-poor deep ocean) on carbon isotope fractionation [Spero et al., 1997], which leads to elevated δ^{13} C in carbonate formed in the surface box and therefore an increase in 13 C export from the surface to the middle and deep-water boxes. This fractionation has a greater impact than the simultaneous negative δ^{13} C shift in POC driven by the effect of the increase in

dissolved CO₂ in the surface box via the photosynthetic isotope effect [Kump and Arthur, 1999]. Although the coupled increase in deep water [CO₃²⁻] conversely results in a negative δ^{13} C shift for benthic foraminifera calcification as a result of the same fractionation effect, this effect is not sufficient to overcome the large positive shift in deep-water DIC δ^{13} C. To match the benthic δ^{13} C palaeorecord we find that we need to temporarily increase ocean mixing rates by 66 % above baseline during and after EOT-1 and to 300 % above baseline during Oi-1. A more modest 150 % stepped increase produces a smaller temporary increase in benthic δ^{13} C. Neither of these simulations produces a permanently deepened CCD, as the carbonate compensation mechanism buffers deep water against permanent increases in both [CO₃²⁻] and ocean Ω through increased CaCO₃ burial, and the CCD temporarily shoals during the steps themselves. Permanently increasing mixing rates results in a permanently rather than temporarily elevated benthic δ^{13} C. It is clear, therefore, that while suggestions of increased ocean ventilation as a mechanism for permanently de-acidifying the deep ocean [e.g. Miller et al., 2009] are untenable, increased ocean mixing is a potentially viable mechanism for driving the benthic δ^{13} C excursion. All of these simulations produce a rapid ~100 ppm increase in atmCO₂ during both glaciation steps as a result of surface-water acidification followed by a gradual recovery with a small overshoot, which partially resembles the atm CO_2 rebound during and after the EOT in the $\delta^{11}B$ derived atmCO₂ reconstruction but does not resemble the drop observed in the alkenone-derived atmCO2 reconstruction.

3.4.1.3 Carbon Capacitor Exchange (CCE)

Figure 3-4 illustrates the results of simulated changes in carbon capacitors across the EOT. We find that to recreate the sharp step increases in the benthic δ^{13} C palaeorecord we need to draw down 700 Pg C (at a δ^{13} C of -23 ‰) during EOT-1 and 1000 Pg C during Oi-1, but the effect of these perturbations are short-lived and cannot explain the ~1 My duration of the benthic δ^{13} C excursion. A more modest uptake of 500 Pg C during both EOT-1 and Oi-1 results in rapid benthic δ^{13} C increases of ~0.5 ‰ during both of these events. In contrast, a net release of 500 Pg C during both EOT-1 and Oi-1, which would occur if, for example, more carbon is released by PFSC erosion on Antarctica than is taken up into carbon capacitor expansion elsewhere, results in decreases in benthic δ^{13} C in contrast to the sharp positive excursions seen in the palaeorecord. It can be speculated that that the short-lived decrease observed in the bulk δ^{13} C palaeorecord prior to EOT-1 [Coxall and Wilson, 2011] could potentially be attributable to PFSC erosion as ice sheets began to spread from the

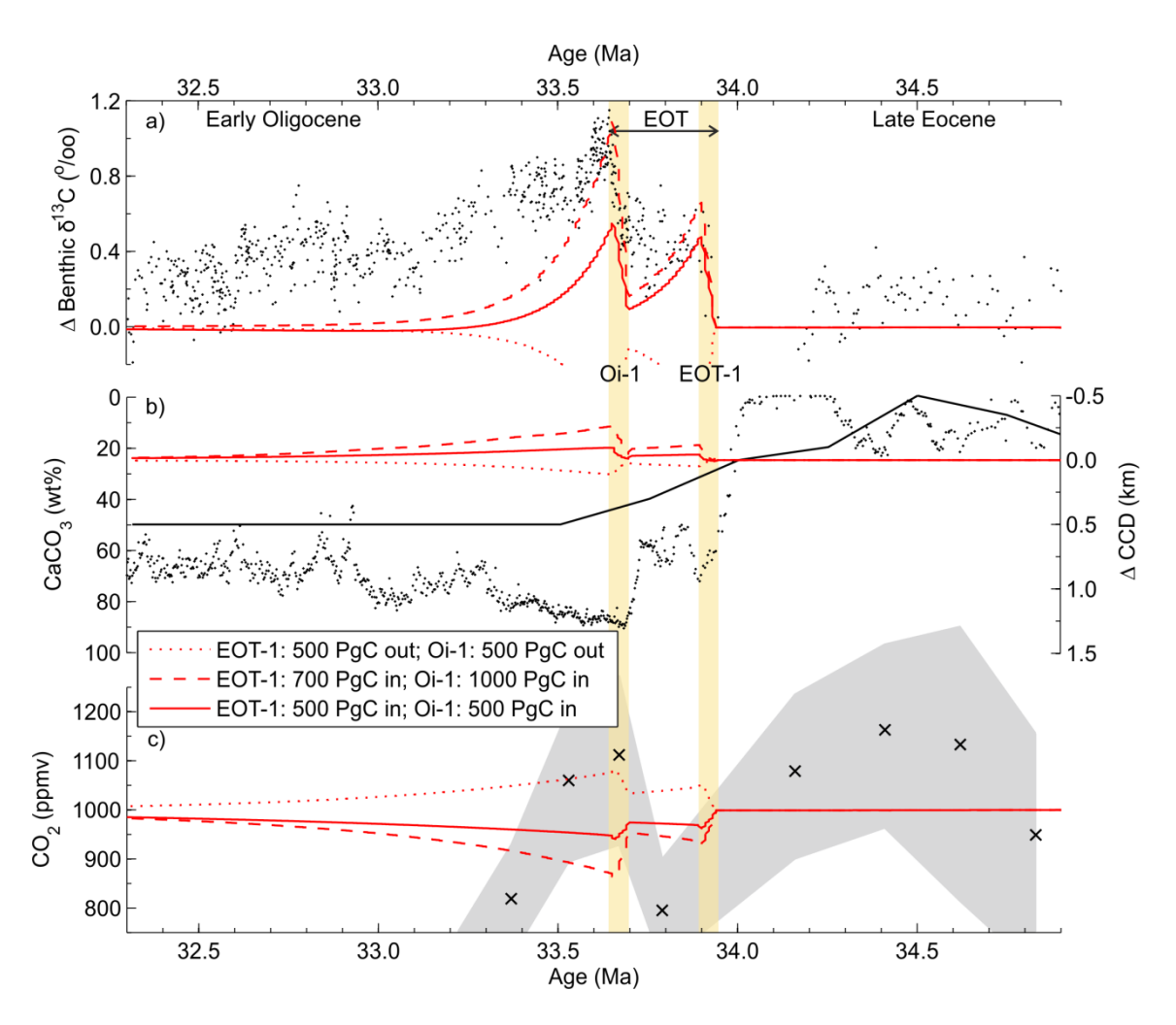


Figure 3-4: Simulation results for the carbon capacitor exchange (CCE) scenario. a) Benthic δ¹³C, b) global CCD, and c) atmospheric CO₂ outputs compared against EOT palaeorecords (see caption of Figure 3-2 for details) [Coxall et al., 2005; Pearson et al., 2009; Coxall and Wilson, 2011; Pälike et al., 2012; Westerhold et al., 2014]. The simulation scenarios are a net contraction (out) of 500 Pg C during both EOT-1 and Oi-1 (dotted red line), net expansions (in) of 700 Pg C at EOT-1 and 1000 Pg C at Oi-1 (dashed red line), and net expansions of 500 Pg C during both EOT-1 and Oi-1 (solid red line). The EOT-1 and Oi-1 cooling and glaciation steps within the EOT are highlighted by the yellow bars.

Antarctic highlands, while Northern Hemisphere PFSC subsequently grew during EOT-1 and Oi-1. Capacitor exchange leading to a match with δ^{13} C data has a relatively minor impact on the CCD and $_{atm}$ CO₂ (with the former shoaling by ~100 m and the latter decreasing by ~50 ppm by the end of Oi-1) due to the relatively small proportion of exogenic carbon needed to simulate the carbon isotope perturbation (which is more modest than that hypothesised for the Palaeocene-Eocene Thermal Maximum [*Zachos et al.*, 2008; *Zeebe at al.* 2009]).

3.4.1.4 Export and Burial Ratio changes (EBR)

Figure 3-5 illustrates the results of either decreasing the rain ratio (i.e. reducing $CaCO_3$ export) or increasing the proportion of $C_{\rm org}$ preserved in ocean sediment in order to increase $C_{\rm org}$ burial. We find that a permanent 25 %

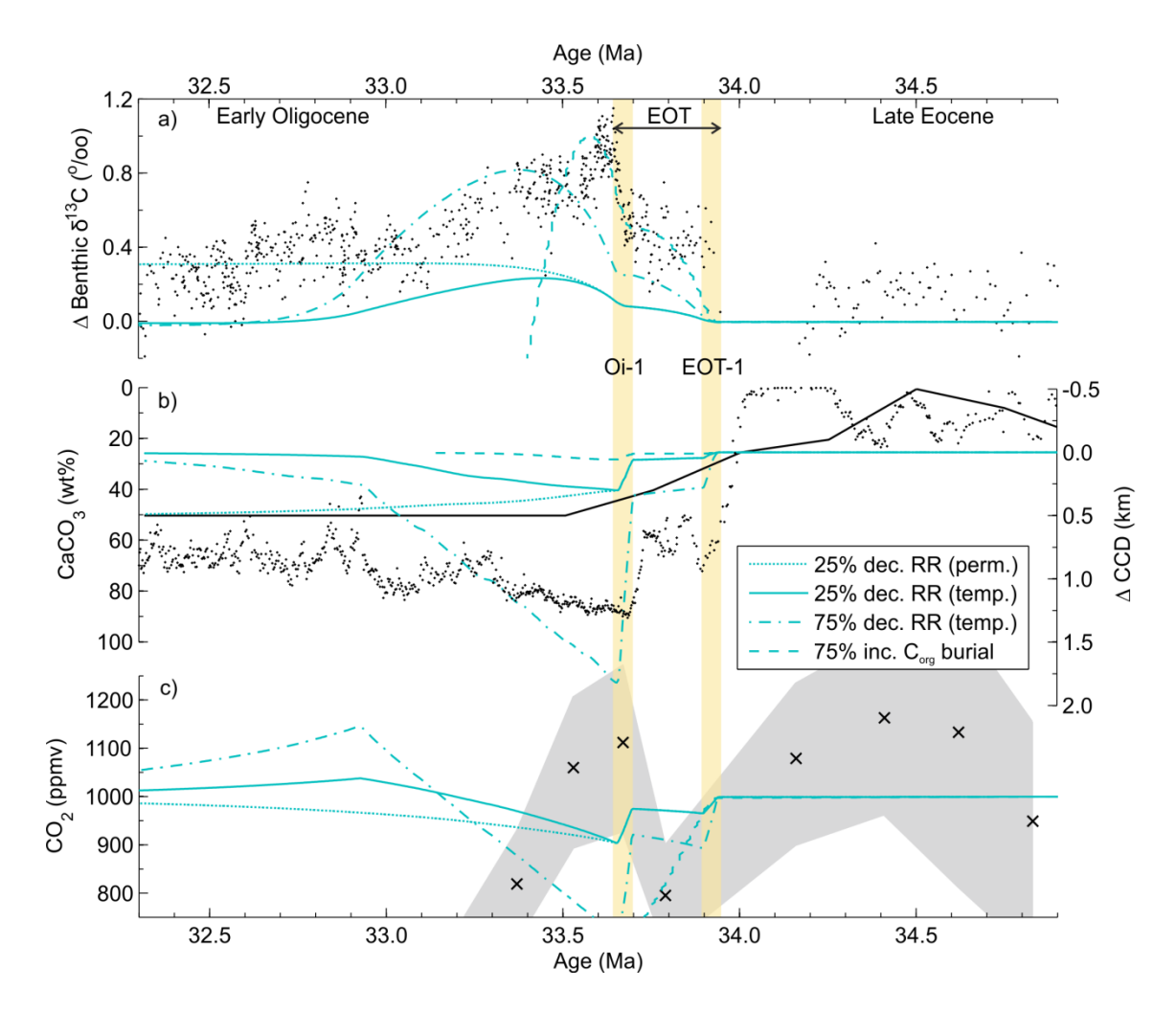


Figure 3-5: Simulation results for the decreased CaCO₃ export or increased C_{org} burial (EBR) scenario. a) Benthic δ¹³C, b) global CCD, and c) atmospheric CO₂ outputs compared against EOT palaeorecords (see caption of Figure 3-2 for details) [Coxall et al., 2005; Pearson et al., 2009; Coxall and Wilson, 2011; Pälike et al., 2012; Westerhold et al., 2014]. The simulation scenarios are a permanent two-step 25 % decrease in rain ratio (RR) (dotted cyan line), a temporary two-step 25 % decrease in rain ratio (solid cyan line), a temporary two-step 75 % decrease in rain ratio (dot-dashed cyan line), and a permanent two-step 75 % increase in C_{org} burial in sediment (dashed cyan line). The EOT-1 and Oi-1 cooling and glaciation steps within the EOT are highlighted by the yellow bars.

decrease in rain ratio results in a permanent 500 m deepening of the CCD and a permanent ~ 0.3 % increase in benthic δ^{13} C (contrasting with the temporary δ^{13} C excursion of the palaeorecord) along with $_{\rm atm}$ CO₂ temporarily falling by ~ 100 ppm. A temporary benthic δ^{13} C excursion can be achieved with a temporary rain ratio decrease, but this instead fails to produce a permanently deepened CCD. To achieve a ~ 0.7 % increase in benthic δ^{13} C the rain ratio must significantly decrease by ~ 75 %, which also results in a > 1.5 km temporary deepening of the CCD and a temporary ~ 300 ppm drop in atmospheric CO₂. This result shows that a positive benthic δ^{13} C excursion can only be achieved through a substantial decrease in the rain ratio, which conflicts with palaeorecords suggesting a stable or even an increasing rain ratio across the EOT [*Griffith et al.*, 2010]. In the second experiment we increase the

proportion of $C_{\rm org}$ buried in sediments up to 75 % in order to replicate the >0.7 % benthic $\delta^{13}C$ excursion, but this in turn results in a significant decrease in both DIC and alkalinity concentration, as total carbon output exceeds input, and the complete consumption of $_{\rm atm}CO_2$ by ~33.1 Ma. Benthic $\delta^{13}C$ increases initially as a result of ^{12}C removal via increased $C_{\rm org}$ burial but is followed by a large negative excursion as a result of the effect of intense ocean de-acidification on $\delta^{13}C$ fractionation. The CCD experiences a negligible but temporary deepening due to increasing $[CO_3^{2-}]$ (due to DIC drawdown induced de-acidification) initially outpacing decreasing $[Ca^{2+}]$ and $K_{\rm sp}$ to temporarily increase deep-water saturation state, but this is followed by a more significant disruption to the ocean carbonate system as DIC drawdown progresses.

3.4.1.5 Increased Silicate Weatherability and Calcium flux to the ocean (SWC)

Figure 3-6 illustrates the results of increasing silicate weatherability or directly adding Ca²⁺ to the ocean across the EOT. In the first of these experiments we simulate increased silicate weatherability, leading to a transient increase in global silicate weathering rates across the EOT, in order to both draw down atmCO2 and increase the input of Ca2+ and alkalinity to the ocean to deepen the CCD. However, in our simulations the decrease in atmCO₂ is sufficient to suppress as a consequence the global silicate weathering rate (effectively compensating for elevated Antarctic weatherability by reducing silicate weathering elsewhere). This also reduces the global carbonate weathering rate too as a result of the climate-weathering feedback, which in turn results in a net decrease in alkalinity input and therefore a CCD shoaling instead of deepening. Increasing carbonate weatherability by the same proportion as the increase in silicate weatherability fails to compensate for the impact of lowered atmCO2 and results in similar excursions. Removing the climate-weathering feedback by preventing the decline in global weathering rates in response to declining atmCO₂ instead results in a temporary CCD deepening (see Supporting Figure 3-8). As a result it is clear that, in keeping with the results of Merico et al. [2008], any additional input of Ca²⁺ and alkalinity to the ocean attributable to an increase in silicate weatherability is strongly counteracted by the climate-weathering negative feedback.

In a further experiment we isolate the impact of increasing [Ca²⁺] by adding Ca²⁺ to the ocean without increasing either silicate or carbonate weathering. We find that in order to initially deepen the CCD by \sim 1000 m [Ca²⁺] must increase substantially from \sim 20 to \sim 170 mol m⁻³ (a value at odds with reconstructions of past [Ca²⁺]), which requires Ca²⁺ input to temporarily increase to 25 % above the

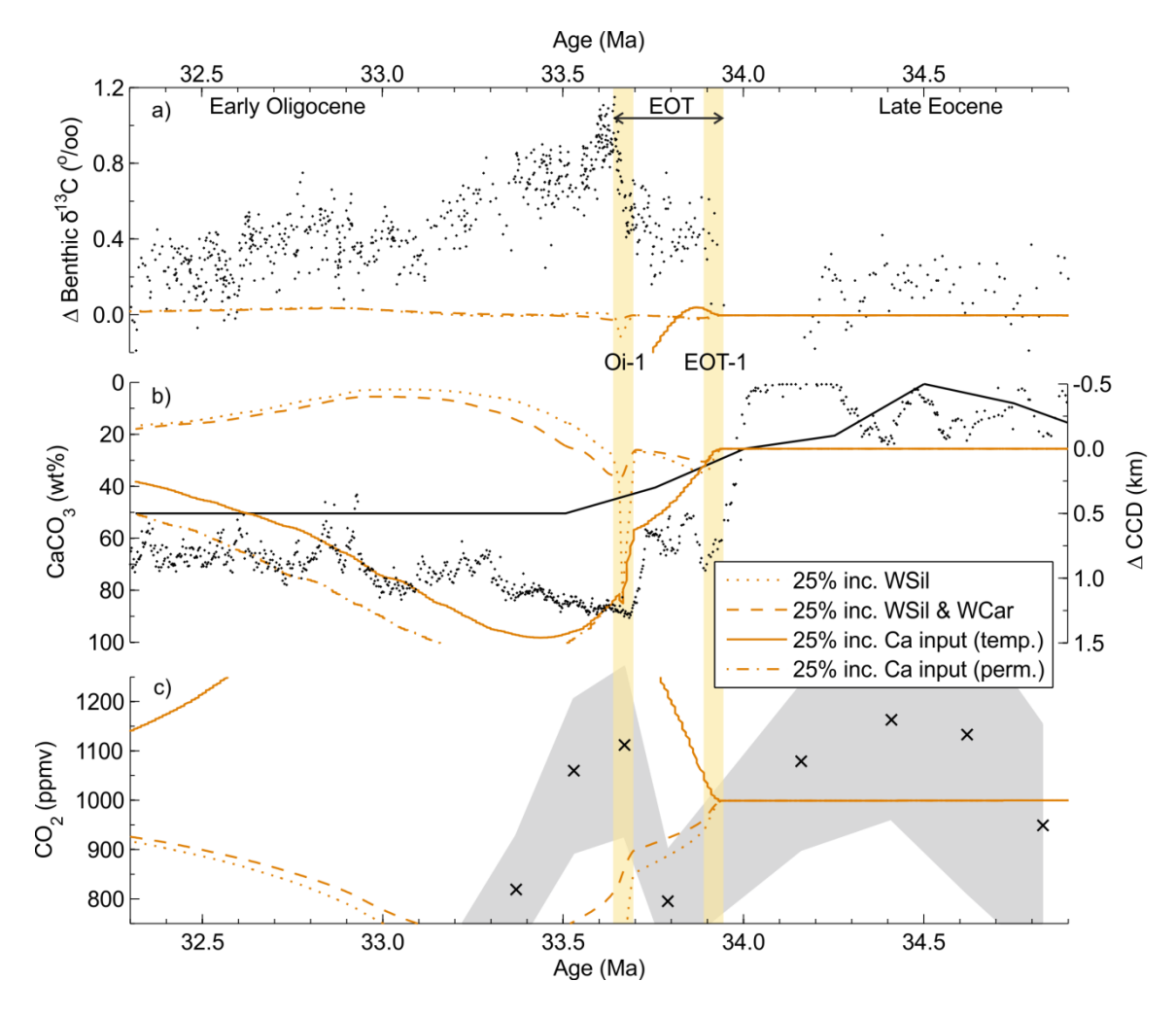


Figure 3-6: Simulation results for the silicate weathering and calcium (SWC) scenario. a) Benthic δ^{13} C, b) global CCD, and c) atmospheric CO₂ outputs compared against EOT palaeorecords (see caption of Figure 3-2 for details) [Coxall et al., 2005; Pearson et al., 2009; Coxall and Wilson, 2011; Pälike et al., 2012; Westerhold et al., 2014]. The simulation scenarios are a permanent two-step 25 % increase in calcium input (Ca input) (dot-dashed orange line), a temporary two-step 25 % increase in calcium input (solid orange line), a temporary two-step 25 % increase in silicate weathering rates (WSil) (dotted orange line), and a temporary two-step 25 % increase in both silicate and carbonate weathering rates (WCar) (dashed orange line). The EOT-1 and Oi-1 cooling and glaciation steps within the EOT are highlighted by the yellow bars.

baseline input to the ocean. However, the CCD deepening is only temporary and does not match the CCD palaeorecord beyond the initial over-deepening. This scenario also results in a ~ 4.0 % decrease in benthic $\delta^{13}C$ and a > 700 ppm increase in $_{\rm atm}CO_2$, signals that are untenable in light of the palaeorecord. Applying a permanent increase in Ca^{2+} input to the ocean also fails to result in a permanent CCD deepening and results in even more unrealistic changes in ocean $[Ca^{2+}]$, benthic $\delta^{13}C$, and $_{\rm atm}CO_2$. The extreme benthic $\delta^{13}C$ and $_{\rm atm}CO_2$ excursions are driven by a complex set of feedbacks on the initial Ca^{2+} addition (see Section 3.7.2 and Supporting Figure 3-9 for systems diagram and explanation of these feedbacks).

3.4.1.6 Combined scenarios

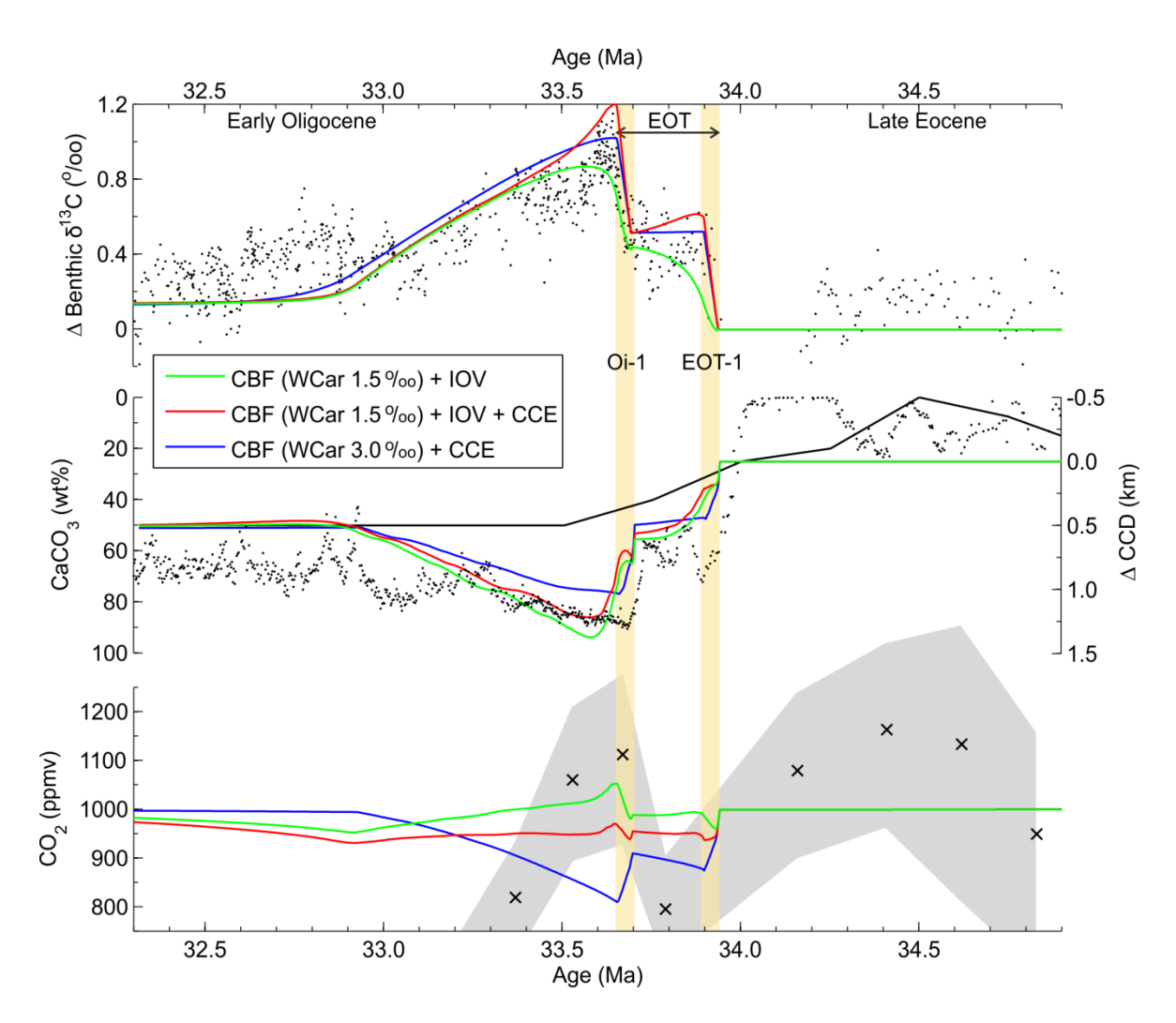


Figure 3-7: Simulation results of a) benthic δ^{13} C, b) global CCD, and c) atmospheric CO₂ for different combinations of the best-fit scenarios shown in the previous figures (CBF (WCar 1.5 ‰) + IOV, green; CBF (WCar 1.5 ‰) + IOV + CCE, red; CBF (WCar 3.0 ‰) + CCE, blue) compared against EOT palaeorecords (see caption of Figure 3-2 for details) [Coxall et al., 2005; Pearson et al., 2009; Coxall and Wilson, 2011; Pälike et al., 2012; Westerhold et al., 2014]. The EOT-1 and Oi-1 cooling and glaciation steps within the EOT are highlighted by the yellow bars.

In Figure 3-7 we plot the results of combining the scenarios we judge to best fit the palaeorecords within reasonable parameter changes. The combined CBF-IOV experiment (80% reduction in shelf carbonate burial, temporary 100% stepped increase in carbonate weathering, shelf carbonate δ^{13} C of 1.5 %, temporary 150 % stepped increase in ocean mixing rates) results in both a permanent ~500 m deepening of the CCD (with an initial over-deepening of ~1000 m) and a temporary ~0.6 % benthic δ^{13} C excursion featuring two steps, as seen in the palaeorecords. Adding CCE (500 Pg C drawdown during both EOT-1 and Oi-1) to this experiment accentuates the two steps in the benthic δ^{13} C excursion (making them more rapid) and briefly increases the benthic δ^{13} C excursion to ~1.0 % during Oi-1, fitting the

maximum shift observed in the benthic $\delta^{13}C$ palaeorecord. This experiment also produces a small ~50 ppm decline in $_{\rm atm}CO_2$ after EOT-1. Alternatively, by increasing shelf carbonate ^{13}C enrichment to 3.0 ‰ we are able to match both the benthic $\delta^{13}C$ and CCD palaeorecords using a combination of CBF and CCE without also including IOV. This is the only experiment of these combination runs that results in a major (~190 ppm) and permanent decline in $_{\rm atm}CO_2$.

3.4.2 Implications

3.4.2.1 Multiple drivers lead to best model-data fit

We find that no one hypothesis can completely achieve our two simple simulation targets (a permanent, 500 m CCD deepening with an initial overdeepening of <1200 m and a temporary > +0.7 % benthic δ^{13} C excursion with rapid 40 ky steps at EOT-1 and Oi-1). Of our experimental scenarios, only a permanent 80 % reduction in shallow ocean carbonate burial (Figure 3-2) or a permanent 25 % decrease in rain ratio (Figure 3-4) matches the CCD target. On the other hand, only a 150 to 300 % increase in ocean mixing rates (Figure 3-3), a 300 % increase in the weathering of shelf carbonates with a δ¹³C of 1.5 ‰ (Figure 3-2), a 100 % increase in the weathering of shelf carbonates with a δ^{13} C of 3.0 % (Figure 3-2), or a temporary 75 % decrease in rain ratio (Figure 3-4) matches the magnitude, but not quite the rapidity, of the benthic δ^{13} C target. Carbon capacitor expansion of ~1000 Pg C (Figure 3-4) yields the rapidity of the 40 ky steps but not the overall duration and magnitude of the benthic δ^{13} C excursion. Because a decrease in the rain ratio cannot achieve both simulation targets simultaneously and Ca²⁺ isotope evidence suggests that the rain ratio is more likely to have increased rather than decreased across the EOT [Griffith et al., 2010, we conclude that changes in the rain ratio did not play a major role in driving the EOT carbon cycle perturbation. It is highly implausible that a significant increase in silicate weathering or ocean [Ca²⁺] drove the perturbation because of the extreme mismatches between simulation results and the palaeorecords as well as the infeasible scale and rate of the changes required (several-fold changes within a few 100ky when the residence time is ~1 My) (Figure 3-6). A 300 % increase in carbonate weathering over-deepens the CCD by far more than observed in the palaeorecords, indicating that only a more modest increase in carbonate weathering can be accommodated [Rea and Lyle, 2005; Pälike et al., 2012]. The limited data available on shelf carbonate δ^{13} C indicates Eocene-Oligocene values of around 1.5 to 2.5 ‰ compared with benthic values of ~0.5 ‰, but modern shelf carbonates on the Great

Bahama Bank are enriched by ~4.8 % relative to pelagic carbonate [Zachos et al., 2001b; Swart and Eberli, 2005; Swart, 2008; Swart et al., 2009; Oehlert et al., 2012]. The paucity of data on Eocene shelf carbonate δ^{13} C makes it difficult to assess the degree to which the CBF scenario can explain the entire benthic δ^{13} C excursion. We therefore define two possible end-member scenarios that can achieve both of our simulation targets. End member scenario-1 describes a situation in which shelf carbonate δ^{13} C is relatively enriched (~3.0 %) meaning that a simple combination of only carbonate burial fractionation (CBF; Figure 3-2) and carbon capacitor expansion (CCE; Figure 3-4) is sufficient to match the palaeoclimate record. End member scenario-2 describes a situation in which shelf carbonate δ^{13} C is less enriched (~1.5 %) and a combination of carbonate burial fractionation (CBF; Figure 3-2), increased ocean ventilation (IOV; Figure 3-3), and carbon capacitor expansion (CCE; Figure 3-4) is required. New datasets of δ^{13} C in shelf carbonates of Palaeogene age provide a way to test the validity of these two end members and the quite different predictions that they make for change in $\frac{1}{4}$ and $\frac{1}{4}$ are constant of $\frac{1}{4}$.

3.4.2.2 Organic carbon sequestration

Sequestering carbon from the atmosphere box into $C_{\rm org}$ reservoirs during EOT-1 and Oi-1 helps to create rapid steps in the benthic $\delta^{13}{\rm C}$ excursion in our best-fit simulation (Figure 3-7). No other scenario tested was able to reproduce the rapidity of these steps. Our results therefore suggest that isotopically light carbon might have been rapidly sequestered from the ocean-atmosphere system to carbon capacitors during the EOT. One mechanism to explain such large-scale sequestration over such a short timescale is through expansion of the permafrost and global peatlands inventory in the Northern Hemisphere in response to EOT cooling [Klinger et al., 1996; Tarnocai et al., 2009; DeConto et al., 2012]. Up to ~1700 Pg C is thought to have existed in Antarctic permafrost in the Eocene [DeConto et al., 2012]. The absence of an overall negative $\delta^{13}{\rm C}$ excursion during the EOT implies that this Antarctic PFSC was either sequestered below advancing ice sheets, rapidly re-deposited offshore, or partially eroded prior to the EOT in keeping with some evidence [Coxall and Wilson, 2011] for a precursor negative $\delta^{13}{\rm C}$ excursion just prior to EOT-1.

3.4.2.3 Atmospheric CO₂ and glaciation feedbacks

End member scenario-2, involving lower shelf carbonate $\delta^{13}C$ enrichment (Figure 3-7), results in only small changes in $_{atm}CO_2$ across the EOT. This finding is important because, if shelf carbonate enrichment was low, it suggests against the

operation of a strong positive feedback via the carbon cycle on EOT glaciation. Maintenance of high baseline atmCO₂ levels across the EOT may help to explain the ice sheet volatility implied by high amplitude variability in the early Oligocene benthic oxygen isotope record [Coxall et al., 2005]. However, these findings conflict with a boron isotope-based proxy atmCO2 reconstruction which suggests that atmCO2 initially decreased by ~200 ppm across EOT-1 before rapidly increasing by 300-400 ppm during Oi-1, with levels remaining high for ~200 ky before falling below pre-EOT levels around 33.4 Ma [Pearson et al., 2009]. Having simulated changes in many of the major biogeochemical parameters hypothesised to have been affected during the EOT, we find that the pattern of atmCO2 changes shown in the boron palaeorecord are challenging to explain alongside the benthic δ^{13} C and CCD palaeorecords. One possible explanation for this finding is that some regional process not accounted for in our model, for example sea-ice expansion in the Southern Ocean in response to the development of a large East Antarctic Ice Sheet [DeConto et al., 2007; Goldner et al., 2014], plays an important role in determining the evolution of CO₂ across the EOT. Even so, a ~200 ky-long atmCO₂ peak after Oi-1 would be challenging to maintain through ocean processes given an ocean mixing timescale of ~1 ky. Another atmCO2 reconstruction based on alkenones instead suggests that atmCO₂ fell by ~200 ppm across the EOT and is interpreted to indicate a major increase in silicate weathering across the EOT [Pagani et al., 2011]. We find, however, that a major increase in silicate weathering is incompatible with the sign of the CCD response and the amplitude of the carbon isotope excursion (see Section 3.4.1.1). Alternatively, and in contrast to end member scenario-2, end member scenario-1 results in a major (~190 ppm) and permanent decrease in atmCO₂ (Figure 3-7). This is in line with the alkenone atmCO₂ reconstruction and would also result in a positive feedback on glaciation in the early Oligocene. This exercise underscores the need for new multi-proxy highresolution reconstructions of atmCO2 across the EOT.

3.4.2.4 Why was the EOT a unique event?

The carbon cycle perturbation at the EOT is a unique event in Cenozoic palaeorecords. No other event involves a permanent shift in ocean carbonate burial of a similar magnitude. However, the mechanisms proposed to explain the EOT carbon cycle perturbation are likely to have been at work throughout much of the Cenozoic. Some palaeorecords suggest there were many rapid changes in sea level across the Cenozoic that did not result in a major shift in the locus of ocean carbonate burial [Miller et al., 2009]. In comparison to the variability demonstrated during the Eocene,

the CCD remains relatively stable in the equatorial Pacific after the EOT despite fluctuations in Oligocene ice sheets and temperatures [Palike et al., 2006; Pälike et al., 2012]. CCD stability was only interrupted in the mid-Miocene by the shoaling and subsequent re-deepening of the CCD potentially associated with the deglaciation and reglaciation bracketing the Miocene Climatic Optimum [Lyle, 2003; Chapter 2 – Armstrong McKay et al., 2014]. This implies that post-EOT fluctuations in sea level and climate mostly failed to restore Eocene levels of shelf carbonate burial, suggesting that a threshold in the ocean carbonate system was crossed at the EOT beyond which a substantial fraction of carbonate burial permanently shifted to ocean basin settings. We conclude that the sensitivity of the ocean carbonate system to a shift from high to low shallow water carbonate burial rates was most likely enhanced during the Late Eocene by: 1) the relative abundance of carbonate platforms in shallow tropical epicontinental seas in the Eocene within 50-75 m of sea level [Opdyke and Wilkinson, 1988], and 2) the position of the CCD during the late Eocene poised some way above the abyssal plain (where the greatest surface area is available for carbonate burial and where the CCD is therefore less sensitive) [Pälike et al., 2012]. Future research is needed to quantify the sensitivity of the CCD to sea level and climate change during the Cenozoic (see Chapter 4 of this thesis).

3.5 Conclusions

We revisit the EOT carbon cycle perturbation modelling of *Merico et al.* [2008] in light of subsequent critiques and our new hypotheses. We use the same biogeochemical box model developed by *Merico et al.* [2008] with some additions in order to further investigate the hypothesised drivers of the perturbation. We find that, in keeping with *Merico et al.* [2008], a shift in carbonate burial from shallow to deep-water settings is the most likely process for permanently deepening the CCD. On the other hand, in contrast to *Merico et al.* [2008] we conclude that the form of the overall EOT benthic δ^{13} C excursion can only have been brought about by a shelf-to-basin carbonate shift if contemporaneous shelf carbonates were substantially enriched in 13 C (with a δ^{13} C of ~ 3.0 %). If this was not the case then a contribution from increased ocean ventilation is also required. Substantial increases in silicate weathering, direct addition of Ca^{2+} to the ocean, decreasing the $CaCO_3$: C_{org} rain ratio, and increasing C_{org} burial all fail to reproduce the observations and are therefore unlikely to have played a major role at the EOT. We find that the rapidity of the two steps in the benthic δ^{13} C palaeorecord could be attributed to the net sequestration of

~1000 Pg of organic carbon during the EOT through processes such as permafrost and peatland expansion. Antarctic permafrost soil carbon must have either been sequestered by advancing ice sheets or was eroded and oxidised prior to the EOT. We struggle to simulate the excursions in the boron isotope-based EOT _{atm}CO₂ reconstruction [*Pearson et al.*, 2009]. In our model runs that fit existing data sets most closely, atmospheric CO₂ either remains relatively stable or shows a major decrease across the EOT, a result that better matches the alkenone-based EOT _{atm}CO₂ reconstruction [*Pagani et al.*, 2011].

3.6 Acknowledgements

This work was supported by a Natural Environment Research Council (NERC) studentship to D.I.A.M. (grant number: NE/J500112/1). We thank Agostino Merico for sharing the model developed in *Merico et al.* [2008]. The palaeorecords used in this study can be found at the following locations: benthic isotopes and CaCO3 wt% from ODP site 1218 are available from Helen Coxall (helen.coxall@geo.su.se), the CCD in the equatorial Pacific is available from www.nature.com/nature/journal/v488/n7413/extref/nature11360-s1.pdf, and the boron isotope-based atmospheric CO2 reconstruction is available from http://doi.pangaea.de/10.1594/PANGAEA.815855. This work is dependent upon the many palaeorecords produced by the (Integrated) Ocean Drilling (Discovery) Program which is sponsored by the US National Science Foundation and participating countries (UK through a NERC Research Program) under management of Joint Oceanographic Institutions, Inc.

3.7 Supporting Information

3.7.1 The SWC scenario and the climate-weathering feedback

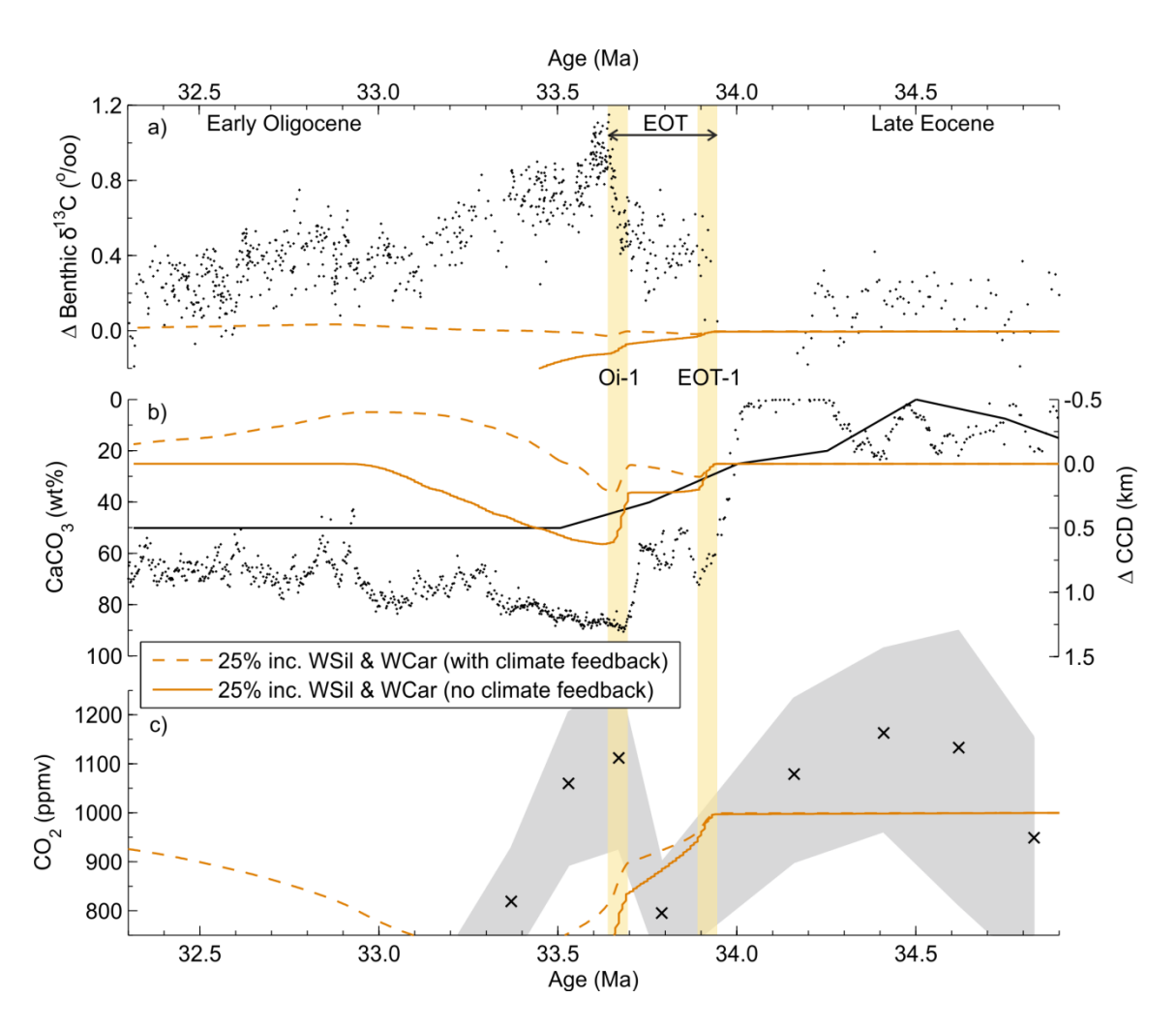


Figure 3-8: Sensitivity test results for the silicate weathering and calcium (SWC) scenario. a) Benthic δ^{13} C, b) global CCD, and c) atmospheric CO₂ outputs compared against EOT palaeorecords (see caption of Figure 3-2 for details) [Coxall et al., 2005; Pearson et al., 2009; Coxall and Wilson, 2011; Pälike et al., 2012; Westerhold et al., 2014]. The simulation scenarios are a temporary two-step 25 % increase in silicate and carbonate weathering rates both with the climate-weathering feedback (dashed orange line) and without the climate-weathering feedback (solid orange line). This comparison illustrates the impact of the climate-weathering feedback on the deepening of the CCD across the EOT. The EOT-1 and Oi-1 cooling and glaciation steps within the EOT are highlighted by the yellow bars.

3.7.2 Extra calcium input feedbacks

Extra Ca systems diagram

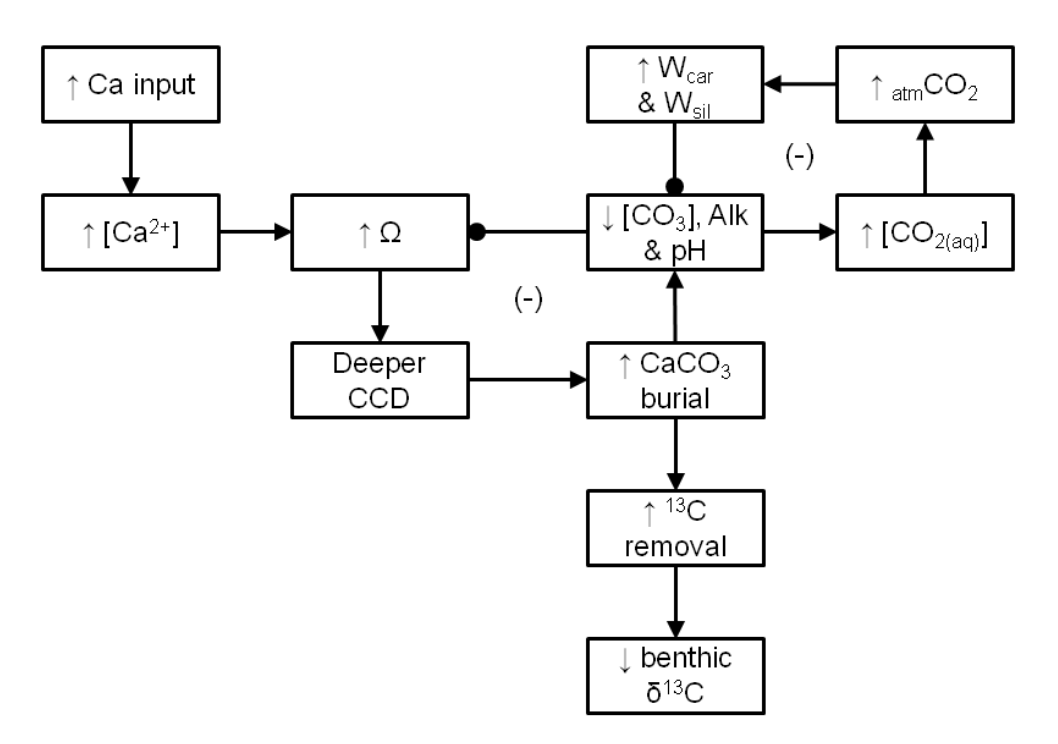


Figure 3-9: Systems diagram illustrating the feedbacks associated with increasing calcium input to the ocean in the SWC scenario. Arrows indicate positive impact, circles indicate negative impact, and (-) indicates a negative feedback loop. See Text S1 for further explanation.

As illustrated in Figure 3-9, increasing $[Ca^{2+}]$ results in increasing ocean Ω , the CCD deepening and therefore an increase in ocean $CaCO_3$ burial. This increase in $CaCO_3$ burial increases alkalinity removal from the ocean and also results in a reduction in $[CO_3^{2-}]$ and pH. Because increasing $[Ca^{2+}]$ enhances $CaCO_3$ burial it produces a strong negative feedback on increasing ocean Ω . However, this negative feedback is overwhelmed by the continuing massive input of Ca^{2+} which continues to drive up ocean Ω , allowing the CCD to carry on deepening despite the opposing feedback. The antagonistic feedback is the reason why $[Ca^{2+}]$ must increase so dramatically in order to achieve just a ~1000 m CCD deepening. The decrease in $[CO_3^{2-}]$ and pH also pushes the ocean carbonate system to higher $[CO_{2(aq)}]$, which in turn results in increased outgassing of CO_2 to the atmosphere. This leads to an increase in carbonate weathering via the climate-weathering feedback and therefore also acts to buffer against the reduction in $[CO_3^{2-}]$ and alkalinity. The substantial increase in $CaCO_3$ burial relative to C_{org} burial reduces the $\delta^{13}C$ of seawater DIC and

hence benthic foraminifera shells as the buried $CaCO_3$ has a $\delta^{13}C$ value of ~ 0.28 % and therefore preferentially removes ^{13}C from the ocean.

3.7.3 Model parameters

Table 3-1: MTW08 biogeochemical parameters (where different from *Merico et al.* [2008]).

Parameter	Description	Units	MTW08 value
[Ca] _{ini} ^a	Calcium ion concentration (initial)	mmol m ⁻³	20000
[Mg] ^a	Magnesium ion concentration (constant)	mmol m ⁻³	30000

^a based on *Tyrrell and Zeebe* [2004]

Table 3-2: Isotopic parameters and initial values for MTW08 used in this study.

Parameter	Description	MTW08 initial value (%)	
$\delta^{13}C_{\text{surf}}$	Surface ocean box (initial state)	0.86	
$\delta^{13}C_{\text{mid}}$	Middle ocean box (initial state)	-0.49	
$\delta^{13}C_{\text{deep}}$	Deep ocean box (initial state)	-1.50	
$\delta^{13}C_{\text{atm}}$	Atmosphere (initial state)	-8.15	
$\delta^{13}C_{\text{riv}}$	Regular carbonate deposits (riverine input)	0.28	
$\delta^{13}C_{\text{phy}}$	Phytoplankton fractionation	-24.0	
$\delta^{13}C_{\text{vol}}$	Volcanic carbon	-4.00	
$\delta^{13}C_{\text{ker}}$	Kerogenic carbon	-20.0	
$\delta^{13}C_{\text{car}}$	Shelf carbonate deposits	1.5 to 3.0	
$\delta^{13}C_{cap}$	'Carbon capacitor' e.g. permafrost, peat	-23.0	

Chapter 4:

Declining sensitivity of the carbonate compensation depth to sea level during the Cenozoic

In this chapter the shelf-basin carbonate burial fractionation hypothesis is investigated in order to quantify the relationship between shelf carbonate burial extent, the carbonate compensation depth, and changing sea-level during the Cenozoic. This chapter forms the basis of a manuscript in preparation for publication with the following authors: Armstrong McKay, D. I., Tyrrell, T., and Wilson, P. A.

4.1 Abstract

Over the course of the Cenozoic the global carbonate compensation depth (CCD), the depth in the ocean below which carbonate deposited on the seafloor is not preserved, has shifted from a relatively shallow average position (~3000 to 3500 m) in the Palaeocene to a relatively deep position (~4600 m) today. Various hypotheses have been proposed to explain this shift, including increased input of weathering products to the ocean, decreased bottom-water corrosivity, and the decline of shelf carbonates shifting carbonate burial to the deep ocean (known as 'carbonate burial fractionation'). Here we build on earlier attempts to quantify the impacts of carbonate burial fractionation on the CCD by analysing global hypsometric and carbonate burial data and determining the relationship between sea level, shelf carbonate burial extent, and the CCD. We show that if carbonate burial rates remain constant across the Cenozoic then carbonate burial fractionation can explain 550 to 800 m out of the long-term ~1600 m CCD deepening in the equatorial Pacific, ~430 m of which occurring across the Eocene-Oligocene Transition (EOT) ~34 million years ago. This finding indicates that other processes dominated CCD change before and after the EOT. We find that the sensitivity of the CCD to sea level change was at its greatest prior to the EOT and declined subsequently due to the loss of extensive carbonate platforms at the end of the Eocene and the intersection of the CCD with large tracts of the abyssal plain.

4.2 Background

4.2.1 Evolution of the Cenozoic carbonate system

The configuration of the Earth's carbon cycle has significantly changed during the course of the Cenozoic era (the last 66 My). One of the biggest changes has occurred in the ocean carbonate system, with a significant increase in ocean basin carbonate accumulation instigating the depth in the ocean below which carbonate is no longer preserved in seafloor sediment, known as the carbonate compensation depth (CCD), to deepen from about ~3000 m in the early Eocene to ~4600 m today in the equatorial Pacific (Figure 4-1) [van Andel, 1975; Hay, 1985; Opdyke and Wilkinson, 1988; Lyle, 2003; Pälike et al., 2012]. Much of this CCD deepening occurred during the Eocene-Oligocene Transition (EOT) ~34 million years ago (Ma), during which the CCD permanently deepened by at least 500 m in conjunction with a ~1 \% benthic δ^{13} C excursion [Coxall et al., 2005; Coxall and Wilson, 2011]. Biogeochemical modelling suggests that the EOT carbon cycle perturbation was mostly driven by carbonate burial shifting from shelf settings to the ocean basins because of glacioeustatic sea level fall, coupled with the weathering of freshly exposed ¹³C-rich shelf carbonates and potentially a degree of increased ocean ventilation and permafrost expansion [Chapter 3 – Armstrong McKay et al., in revision; Merico et al., 2008].

Significant questions remain though as to why the CCD change at the EOT was so unique, and whether carbonate burial shifted enough to drive the observed CCD deepening. The CCD also deepened over the course of the Eocene when the cryosphere is likely to have had a negligible global impact, implying that other factors drove a significant proportion of the long-term CCD deepening. The burial of carbonate in ocean sediments represents one of the largest reservoirs of carbon in the geological carbon cycle and therefore acts as a long-term sink for carbon [Walker et al., 1981; Kump et al., 1999, 2000]. The increase in ocean basin carbonate accumulation occurred in parallel to the Earth shifting from a high-CO₂ (>500 ppm) to a low-CO₂ (<500 ppm) atmosphere, leading to the suggestion that some of this decline in atmospheric CO₂ (atmCO₂) may be due to increased carbon sequestration in deep ocean sediment [Hay, 1985; Beerling and Royer, 2011]. As a result, establishing the drivers of the long-term CCD deepening and the impact this had on the magnitude of ocean carbonate accumulation is therefore crucial in understanding the evolution of the carbon cycle, and therefore climate change, during the Cenozoic.

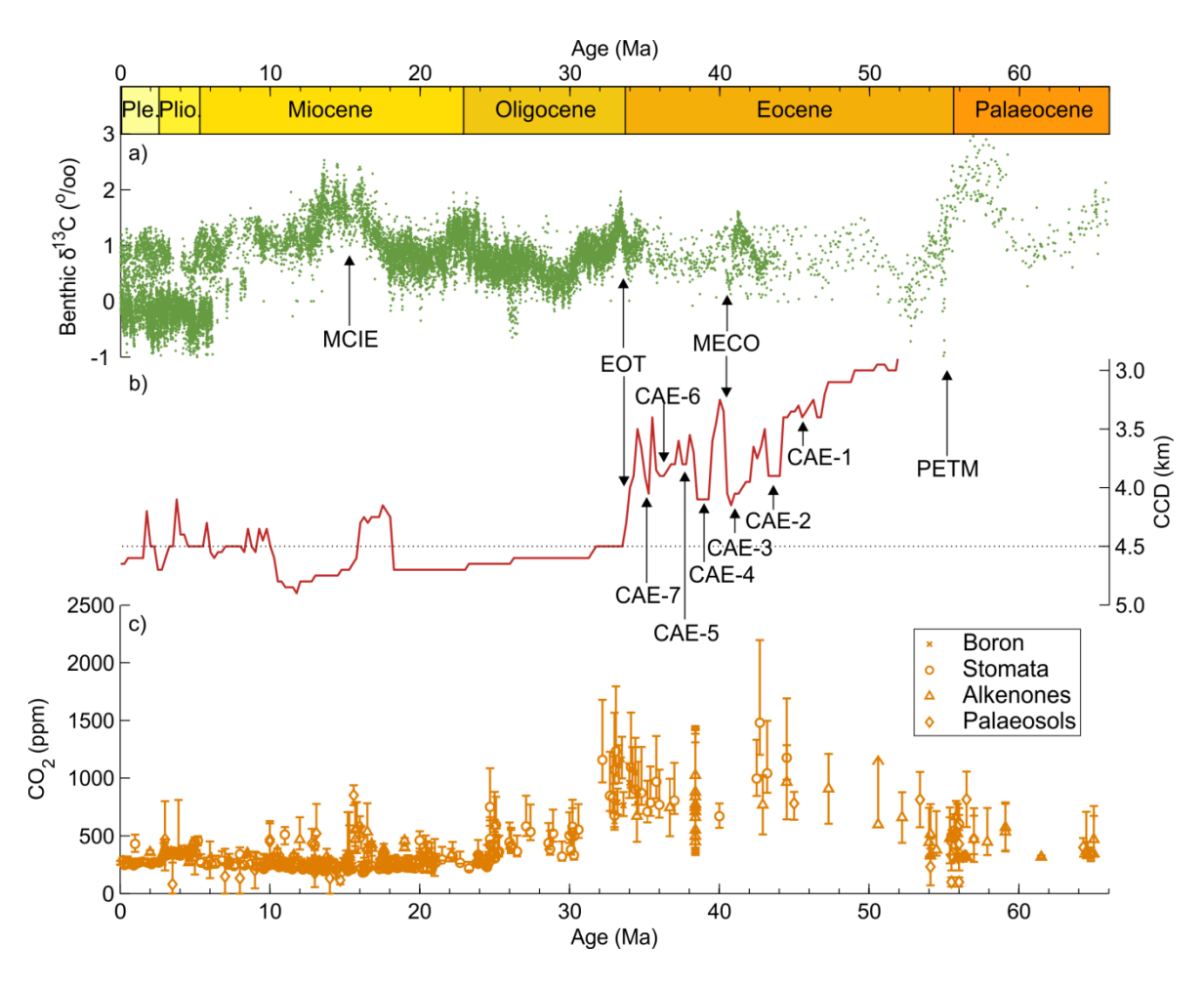


Figure 4-1: Cenozoic palaeorecords of: a) the global benthic δ^{13} C compilation, b) carbonate compensation depth (CCD) reconstructed in the equatorial Pacific, and c) atmospheric CO₂ reconstructions [Zachos et al., 2001b, 2008; Beerling and Royer, 2011; Pälike et al., 2012]. The black dotted line in panel b illustrates the depth (~4.5 km) at which the most abundant section of the seafloor begins and where the CCD is therefore most buffered against change.

4.2.2 Potential drivers of Cenozoic CCD change

4.2.2.1 Weathering and the CCD

One potential driver of the long-term deepening of the CCD during the Cenozoic is the increase in terrestrial weathering during the last 66 My, as suggested by the history of the secular change in the strontium, osmium, and lithium isotope composition of seawater [Palmer and Elderfield, 1985; Peucker-Ehrenbrink et al., 1995; Peucker-Ehrenbrink and Ravizza, 2000; Misra and Froelich, 2012]. Gradually increasing terrestrial weathering would result in increased delivery of alkalinity and Ca²⁺ to the ocean, which should in turn increase the carbonate saturation state of the ocean and thus deepen the CCD until river inputs and burial outputs are once more in balance [Walker et al., 1981; Rea and Lyle, 2005; Sluijs et al., 2013]. This mechanism has been invoked as a potential driver of the EOT CCD deepening as well as providing a positive feedback on glaciation through the drawdown of atmCO₂ [Kump and Arthur,

1997; Rea and Lyle, 2005; Zachos and Kump, 2005; Griffith et al., 2011; Scher et al., 2011; Basak and Martin, 2013].

In contrast, various reconstructions of Cenozoic weathering rates do not reflect the gradually increasing weathering rates implied by the strontium, osmium, and lithium isotope curves. While strontium and carbon mass balance calculations have suggested gradually increasing weathering rates during the Cenozoic [e.g. Raymo et al., 1988; Raymo and Ruddiman, 1992; Raymo, 1994], recent calculations also including osmium instead suggest that silicate weathering rates declined during most of the Cenozoic while carbonate and organic carbon weathering rates increased only in the last 20 My [Li et al., 2009]. Sediment accumulation and erosion rates imply relatively constant Cenozoic weathering rates overall once corrected for observational bias [Willenbring and von Blanckenburg, 2010]. Modelling of the impact of continental drift and weathering of different lithologies suggests weathering intensity has been relatively similar to modern during most of the Cenozoic [Lefebvre et al., 2013]. The lack of significant shifts in calcium isotope data during the Cenozoic also argues against any rapid change in weathering rates [De La Rocha, 2000; Griffith et al., 2011], while the episode of Himalayan uplift that potentially drove major weathering increases during the Miocene does not coincide with any long-term CCD deepening [Raymo et al., 1988; Raymo and Ruddiman, 1992; Raymo, 1994; Goddéris and François, 1996. Recent Earth system modelling has also questioned the hypothesised tight coupling between increased weathering and CCD deepening, with an increase in carbonate preservation above a relatively stable CCD modelled despite increasing weathering rates during the late Palaeocene [Greene et al., in review].

4.2.2.2 Ocean mixing, productivity and the CCD

It has also been suggested that the EOT CCD deepening was primarily driven by increased ocean ventilation as a result of either the opening of ocean gateways, a strengthening meridional temperature gradient due to global cooling, or the effects of ice sheet growth on polar deep-water formation [Kennett, 1977; Miller et al., 2009; Ladant et al., 2014a; Sijp et al., 2014]. An increase in ocean mixing rates reduces deep water acidity (at least initially), and so might be expected to enhance CaCO₃ preservation and thus deepen the CCD. The development of the intense upwelling zone in the Southern Ocean could have also shifted the balance of productivity from calcifying to silicifying phytoplankton, which would reduce CaCO₃ export and should therefore reduce CaCO₃ burial, increase the carbonate saturation state of the ocean (Ω), and deepen the CCD [Zachos et al., 1996; Salamy and Zachos, 1999; Coxall et al.,

2005; Zachos and Kump, 2005; Scher and Martin, 2006; Berger, 2007; Scher et al., 2011]. Ocean cooling is also predicted to lead to increased C_{org} preservation and burial [Zachos et al., 1996; Olivarez Lyle and Lyle, 2006; John et al., 2014], which in turn would reduce deep ocean Dissolved Inorganic Carbon (DIC) concentration relative to alkalinity and therefore lead to de-acidification and increased Ω in deep-water. However, biogeochemical modelling of increased ocean mixing rates and changing export and burial ratios has shown that these mechanisms are either only capable of driving temporary deepenings during times of glacial intensification or also result in major changes in benthic $\delta^{13}C$ in contrast to the palaeorecord [Chapter 3-Armstrong McKay et al., in revision; Merico et al., 2008].

4.2.2.3 Carbonate shelves and the CCD

During the last ~140 My the extent of shelf carbonate burial has declined relative to burial in deep ocean basins [Hay, 1985; Parrish, 1985; Hay et al., 1988; Opdyke and Wilkinson, 1988; Boss and Wilkinson, 1991; Nakamori, 2001]. This shelfbasin fractionation is hypothesised to be primarily the result of falling sea level as ice sheets grew in volume and mid ocean ridge volumes declined with decreased spreading rates [Berger and Winterer, 1975; Sclater et al., 1979; Kump and Arthur, 1997]. As a result of the reduction in shelf carbonate burial it is posited that the CCD deepened in order to increase pelagic CaCO3 burial so as to restore balance between alkalinity inputs and outputs. Biogeochemical modelling of this hypothesis found it to be sufficient to drive the EOT CCD deepening and at least part of the benthic δ^{13} C excursion [Chapter 3 – Armstrong McKay et al., in revision; Merico et al., 2008], while the inverse of this scenario (increased shelf carbonate burial driving a CCD shoaling) has been proposed as a major driver of the Middle Eocene Climatic Optimum (MECO) carbon cycle perturbation [Sluijs et al., 2013]. However, in order to deepen the CCD permanently by ~500 m at the EOT it is necessary to reduce permanently shelf carbonate burial by ~80 %, which raises the question of why other episodes of sea level fall of similar magnitude in the Eocene or sea level rises during the Oligocene did not also permanently affect shelf carbonate burial [Lyle et al., 2008; Miller et al., 2009]. Given the relative stability of the CCD in the equatorial Pacific during the Oligocene (Figure 4-1) it is necessary to explain why the CCD was apparently sensitive to sea level change across the EOT but not subsequently. The lack of significant ice sheets prior to the EOT also suggests that CCD fluctuations prior to the EOT are unlikely to be primarily driven by this mechanism [Edgar et al., 2007].

4.2.3 Study aims

The impact of changing shelf carbonate burial on the CCD has previously been explored by simply scaling decreased shelf carbonate burial coverage to increased basin carbonate extent and estimating the CCD deepening this requires [Berger and Winterer, 1975; Sclater et al., 1979; Kump and Arthur, 1997]. However, since then better estimates of changing carbonate burial rates and extent [Parrish, 1985; Opdyke and Wilkinson, 1988], more reliable sea level reconstructions [Müller et al., 2008; de Boer et al., 2010], higher-resolution global hypsometric data [Amante and Eakins, 2009; Eakins and Sharman, 2012], and a higher-resolution CCD palaeorecord from the equatorial Pacific [Pälike et al., 2012] have become available, and we can therefore perform a more rigorous and detailed analysis of the impact of changing shelf carbonate burial on the CCD. In this study we aim to provide a more accurate and quantitative understanding of the carbonate burial shelf-basin fractionation hypothesis by estimating the impact of the decline of shelf carbonate burial on the carbonate compensation depth using the available data on oceanic carbonate burial rates, global hypsometry, and carbonate burial extent. The resulting understanding sheds new light on the extent to which this hypothesis can be implicated in the evolution of the Cenozoic ocean carbonate system and what other mechanisms might be required.

4.3 Methodology

4.3.1 Carbonate burial rates and extent

The burial of carbonate on ocean shelves limits the deposition of carbonate in ocean basins by reducing the carbonate saturation state of the ocean and thus causing the CCD to shoal. In order to quantify this relationship we compare carbonate burial rates for both ocean shelves and basins and estimate the increase in basin carbonate burial necessary to compensate for a loss of shelf carbonate burial. Around 0.25 Pg of CaCO₃ is buried in shelf settings per year today and probably during the Oligocene as well, whereas the Eocene burial rate is thought to have been much higher (1.25 to 1.5 Pg CaCO₃ y⁻¹) [*Opdyke and Wilkinson*, 1988]. If correct, this represents a 1.0 to 1.25 Pg CaCO₃ y⁻¹ reduction in shelf carbonate burial between the Eocene and Oligocene, which, assuming a constant total ocean carbonate burial rate, implies that basin carbonate burial rates must have commensurately increased. Ocean basin carbonate

burial occurs over a much wider area than on ocean shelves, with a basin carbonate burial flux (i.e. burial rate per unit area) of ~2.8*10⁷ g CaCO₃ km⁻² y⁻¹ compared to ~9.0*10⁷ g CaCO₃ km⁻² y⁻¹ on shelves. Assuming that the shelf and basin carbonate burial fluxes have remained constant over time, all of the lost shelf carbonate burial is transferred to basins, and that sediment processes such as respiration-driven dissolution and sedimentation rates do not change sufficiently to decouple carbonate burial and the CCD, any transfer of carbonate burial from shelf to basin would therefore require an approximately three-fold larger increase in basin carbonate burial area than the area of shelf carbonate burial lost (Figure 4-2).

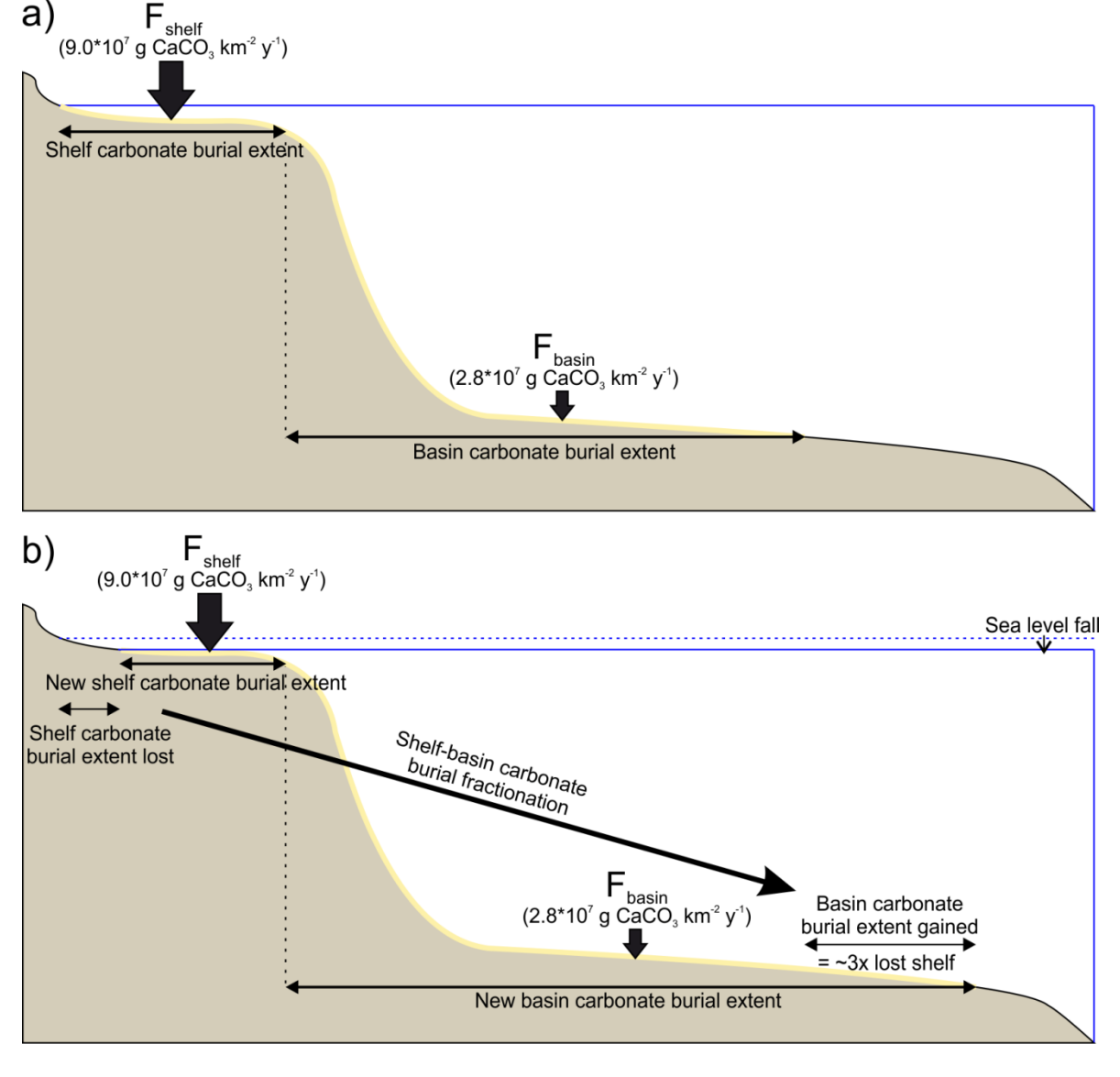


Figure 4-2: Schematic illustrating shelf-basin carbonate burial fractionation due to eustatic sea level fall. Panel a) shows the relative extent of shelf and basin carbonate burial, with the former occupying a smaller area but with a roughly threefold higher carbonate burial flux than the latter, prior to the fall in sea level shown in panel b), where, assuming constant carbonate burial fluxes, the reduction in shelf carbonate burial extent due to the falling sea level results in an increase in basin carbonate burial extent roughly threefold the area of lost shelf carbonate burial.

4.3.2 Linking hypsometry and carbonate burial

In order to transform the required increase in basin carbonate burial area into the CCD deepening that would bring it about, it is necessary to calculate the relationship between depth and ocean-floor area from global hypsographic curves. We assume that modern global hypsometry is approximately equal to global hypsometry in the Eocene as tectonic spreading rates were similar to today [Müller et al., 2008]. Prior to the Eocene, elevated seafloor spreading rates would have increased the height of mid-ocean ridges and thus significantly altered the hypsographic curve [Berger and Winterer, 1975. We use the 'NOAA Hypsographic Curve of Earth's Surface' from ETOPO1, which is based on a 1 arc-minute representation of Earth's solid surface integrating both terrestrial topography and ocean bathymetry from multiple datasets including SRTM30, GEBCO, IBCAO and regional bathymetric data [Amante and Eakins, 2009; Eakins and Sharman, 2012]. As can be seen in Figure 4-3, this dataset records the global area of each 1 m elevation of the Earth's solid surface, and, as a result, can be used to estimate how much extra seafloor area corresponds to each 1 m deepening of the CCD. Figure 4-4 illustrates the hypsometry curve between 3000 and 5500 m below modern sea level (mbmsl), showing how the area of the ocean floor at a given depth increases from $\sim 50000 \text{ km}^2 \text{ m}^{-1}$ at 3000 mbmsl to $\sim 120000 \text{ km}^2 \text{ m}^{-1}$ at

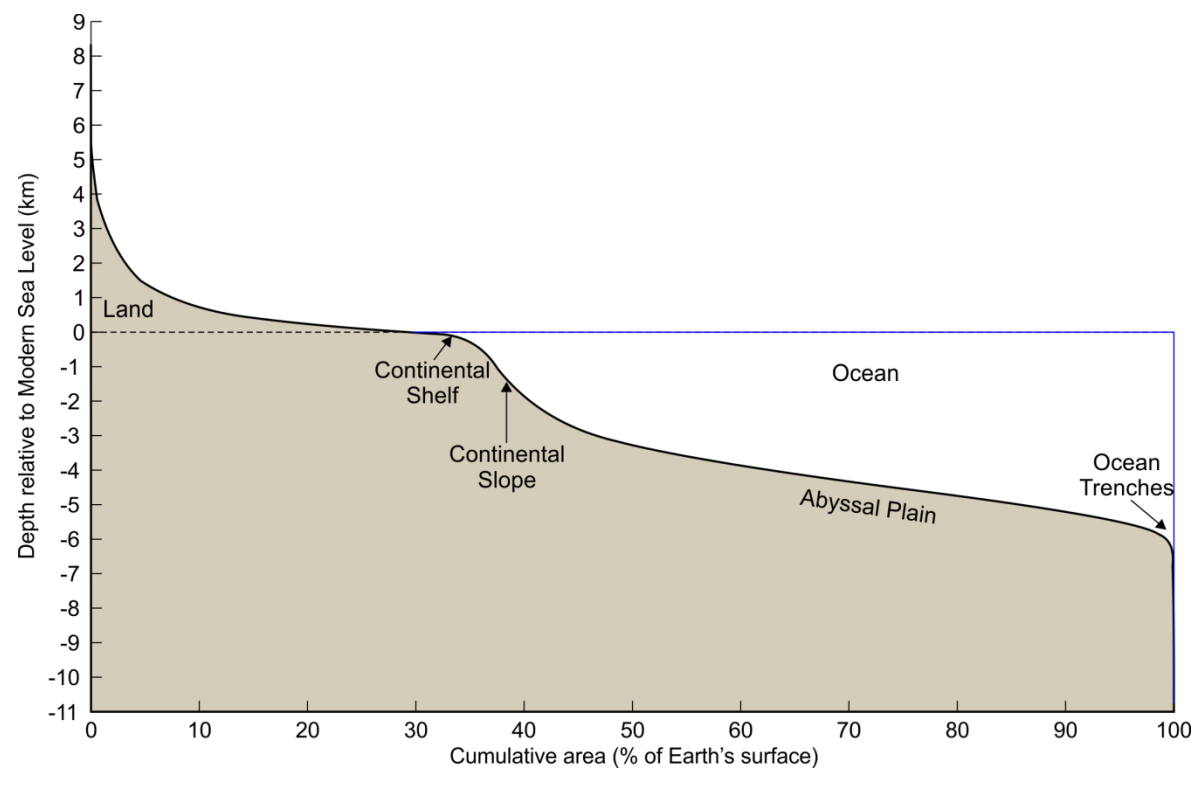
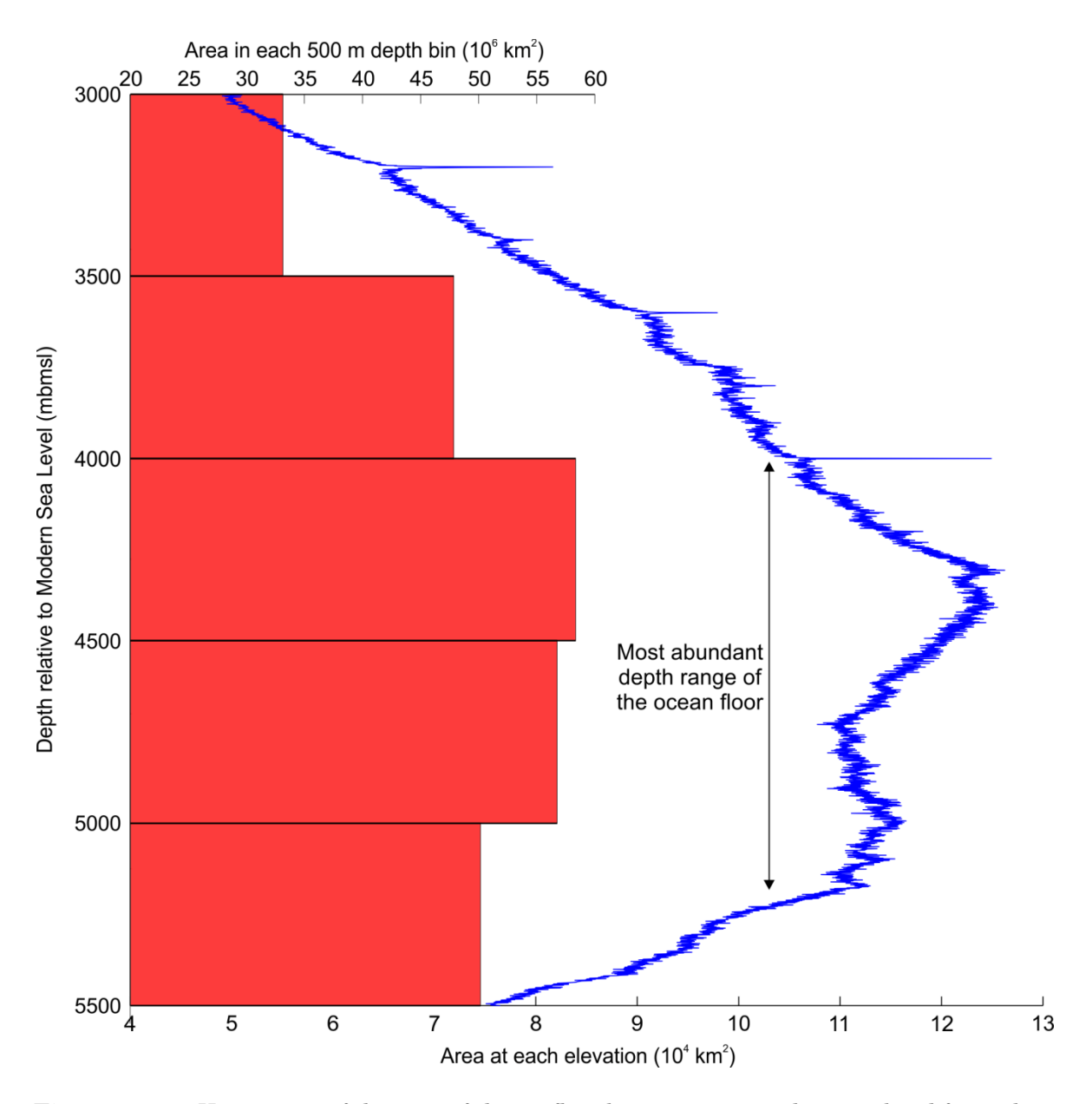


Figure 4-3: Global hypsographic curve of the Earth's surface. Plotted from the 'NOAA Hypsographic Curve of Earth's Surface' based on ETOPO1, a 1 arc-minute representation of Earth's solid surface integrating both terrestrial topography and ocean bathymetry from multiple different datasets [Amante and Eakins, 2009; Eakins and Sharman, 2012].



Histograms of the area of the seafloor between 3000 and 5500 mbmsl for each 1 m depth interval (bottom x-axis, blue line) and in 500 m depth bins (top x-axis, red bars). Plotted from the 'NOAA Hypsographic Curve of Earth's Surface' based on ETOPO1, a 1 arcminute representation of Earth's solid surface integrating both terrestrial topography and ocean bathymetry from multiple different datasets [Amante and Eakins, 2009; Eakins and Sharman, 2012].

~4500 mbmsl, before declining slightly to ~110'000 km² m⁻¹ at 5200 mbmsl and then declining even more rapidly below that. As a result of this pattern there is not a simple relationship between increasing depth and ocean floor area.

Between 3000 and 4500 mbmsl the seafloor increase per 1 m depth increment can be approximated by the following equation:

$$A_{inc} = 51.5D - 100278$$
 [3000 < $D \le 4500$]

Equation 4-1

where A_{inc} is the area of seafloor at each depth increment (km²) and D is the ocean depth (mbmsl). To calculate the cumulative area covered across a depth range, this equation becomes:

$$A_{basin} = \int_{D_{btm}}^{D_{top}} 51.5D - 100278 \text{ dD} = [25.75D^2 + 100278D]_{D_{btm}}^{D_{top}} \quad [3000 < D \le 4500]$$
 Equation 4-2

where A_{basin} is the cumulative area of seafloor (km²) over the depth range between D_{top} and D_{btm} (mbmsl). For the 4500< $D \le 5200$ depth range, in which the seafloor area per depth increment is relatively constant heaving reached an inflection point between 4300 and 4500 m, the cumulative area is instead given by:

$$A_{basin} = [113436D]_{D_{btm}}^{D_{top}}$$
 [4500 < D \le 5200] Equation 4-3

where A_{basin} is the cumulative area of seafloor (km²) over the depth range between D_{top} and D_{btm} (mbmsl). Equations 4-2 and 4-3 predict an ocean floor area of 33.7*10⁶ km² between 3000 and 3500 mbmsl, 46.4*10⁶ km² between 3500 and 4000 mbmsl, 59.5*10⁶ km² between 4000 and 4500 mbmsl, and 56.7*10⁶ km² between 4500 and 5000 mbmsl, all of which closely match the values given by the hypsometric curve for these depth ranges of 33.1*10⁶ km², 47.8*10⁶ km², 58.3*10⁶ km², and 56.7*10⁶ km² respectively (Figure 4-4). Based on Equations 4-2 and 4-3 we can construct the following equation relating the decline in shelf carbonate burial extent to the increase in basin carbonate burial extent:

$$A_{shelf} = \begin{cases} \left[25.75D^2 + 100278D\right]_{D_{btm}}^{D_{top}} * (F_{basin}/F_{shelf}) \ \left[3000 < D \le 4500\right] \\ \left[113436D\right]_{D_{btm}}^{D_{top}} * (F_{basin}/F_{shelf}) \ \left[4500 < D \le 5200\right] \end{cases}$$
 Equation 4-4

where A_{shelf} is the area of shelf carbonate burial lost (km²) and D is the depth in the range between D_{top} and D_{btm} (mbmsl), F_{shelf} is the shelf carbonate burial flux (9.0*10⁷ g CaCO₃ km⁻² y⁻¹), and F_{basin} is the basin carbonate burial flux (2.8*10⁷ g CaCO₃ km⁻² y⁻¹). The areas are converted into carbonate burial rates (R_{shelf} or R_{basin} ; in g CaCO₃ y⁻¹) by multiplying the carbonate burial extent by the carbonate burial flux for shelf and basin respectively.

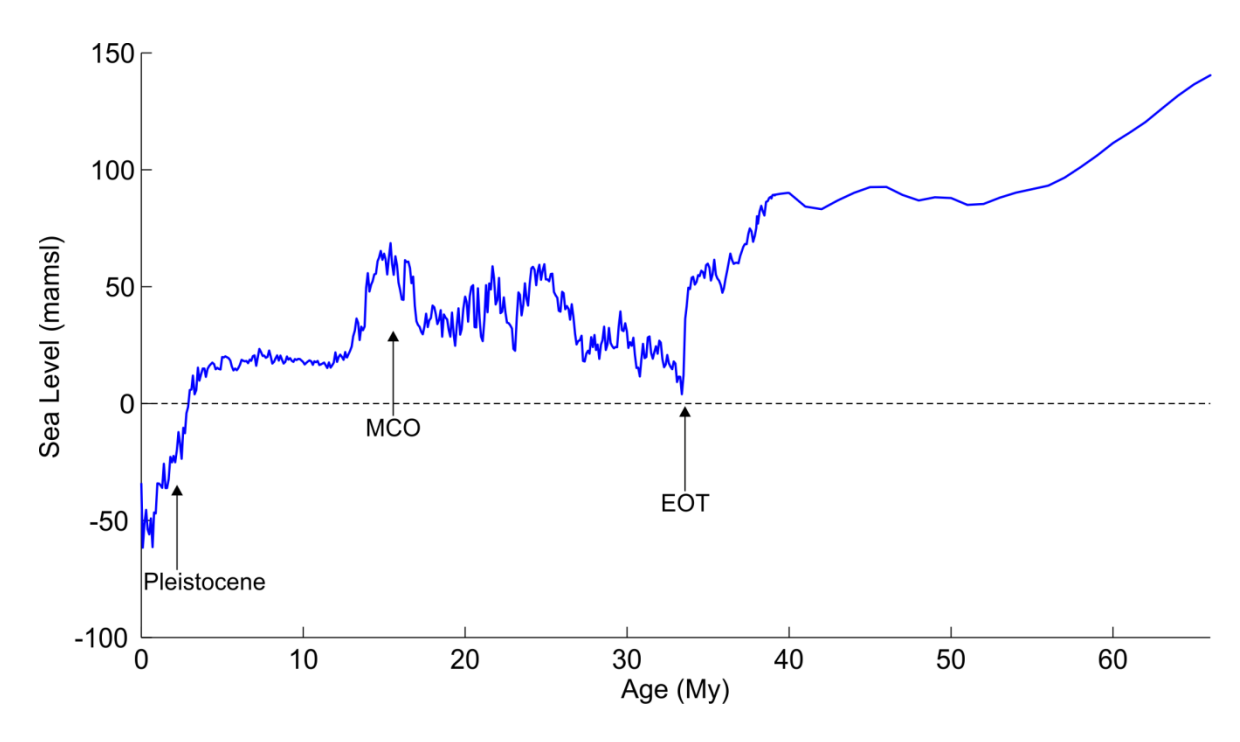


Figure 4-5: Reconstruction of Cenozoic sea level relative to modern sea level. Data compiled from inverse modelling of benthic δ^{18} O (interpolated and smoothed from original dataset at lower resolution) and the sea level impact of changing ocean ridge volume [*Müller et al.*, 2008; *de Boer et al.*, 2010]. Since ~55 Ma changing ocean ridge volume had a relatively minor impact on the sea level curve, with most variation coming from the modelled glacioeustatic changes. The occurrence of the Eocene-Oligocene Transition (EOT), Miocene Climatic Optimum (MCO), and the Pleistocene are labelled. During the Pleistocene smoothing results in the sea level curve dropping below modern sea level (black dashed line) as a result of glacial/interglacial cycling.

4.3.3 Shelf carbonate burial extent, sea level, and the CCD

One of the primary hypothesised drivers of shelf carbonate burial area loss is sea level fall as polar ice sheets grew (Figure 4-5). Figure 4-6 illustrates the relative abundance of the Earth's terrain between 150 m above modern sea level (mamsl) and 50 mbmsl, indicating that relatively small changes in sea level within this range can greatly alter the extent of shelf environments. Some 35.7*10⁶ km² (~7.1 %) of the Earth's surface lies between 100 mamsl and 50 mbmsl, the hypsometric range within which sea level has mostly fluctuated during the Cenozoic, yielding an average shelf area loss of ~2.4*10⁵ km² per 1 m of sea level fall. This does not include the impact of isostatic rebound which would tend to increase the exposure of land with sea level fall and thus increase the area of shelf lost with sea level fall [Berger and Winterer, 1975].

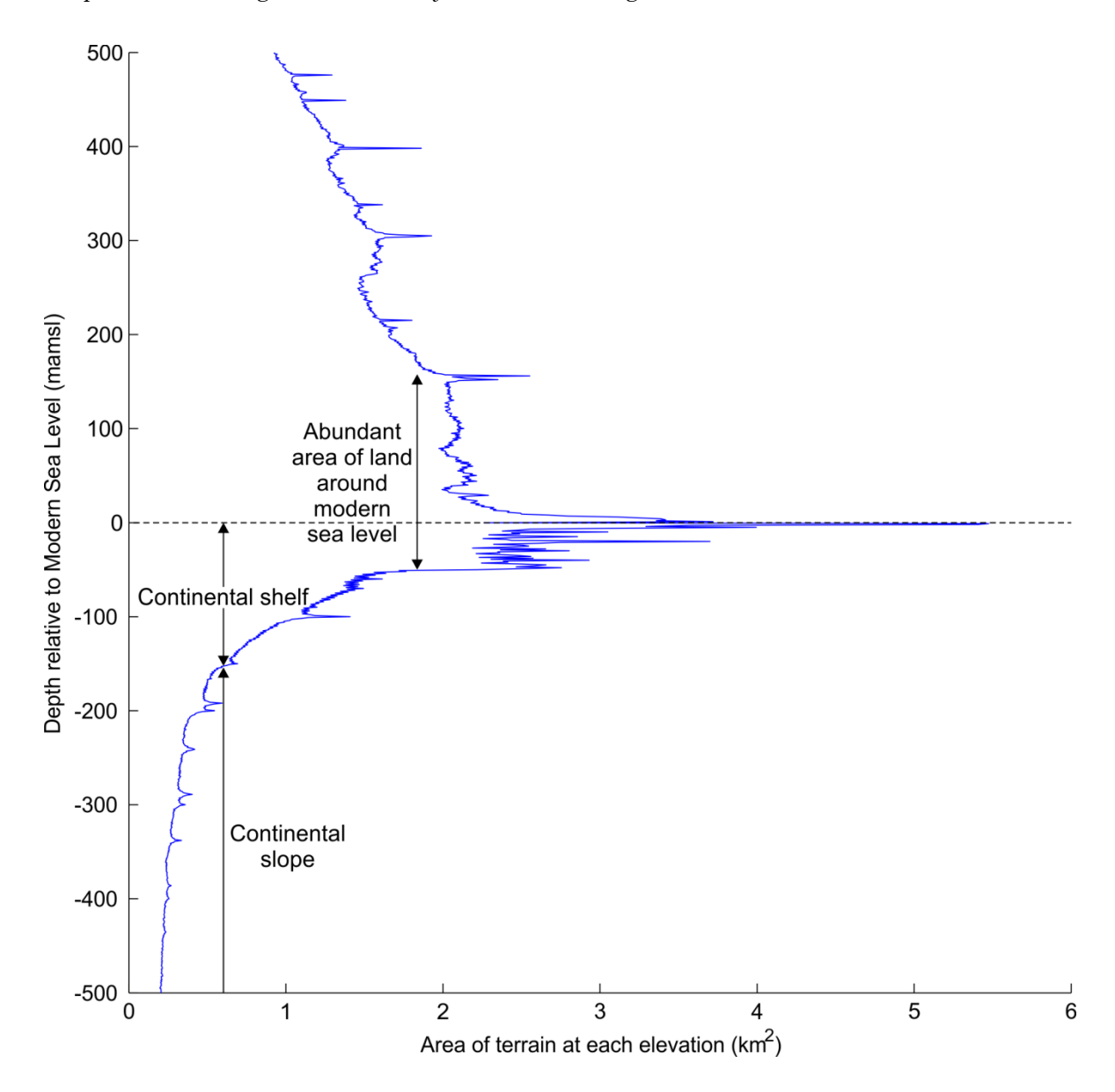


Figure 4-6: The hypsometry of the Earth's surface within 500 m of modern sea level. Plotted from the 'NOAA Hypsographic Curve of Earth's Surface' based on ETOPO1, a 1 arcminute representation of Earth's solid surface integrating both terrestrial topography and ocean bathymetry from multiple different datasets [Amante and Eakins, 2009; Eakins and Sharman, 2012].

Combined with an estimate of the global proportion of shelf settings in which carbonate burial occurs and the shelf carbonate burial flux F_{shelf} , it is possible to estimate the change in global shelf carbonate burial rate due to changing sea level:

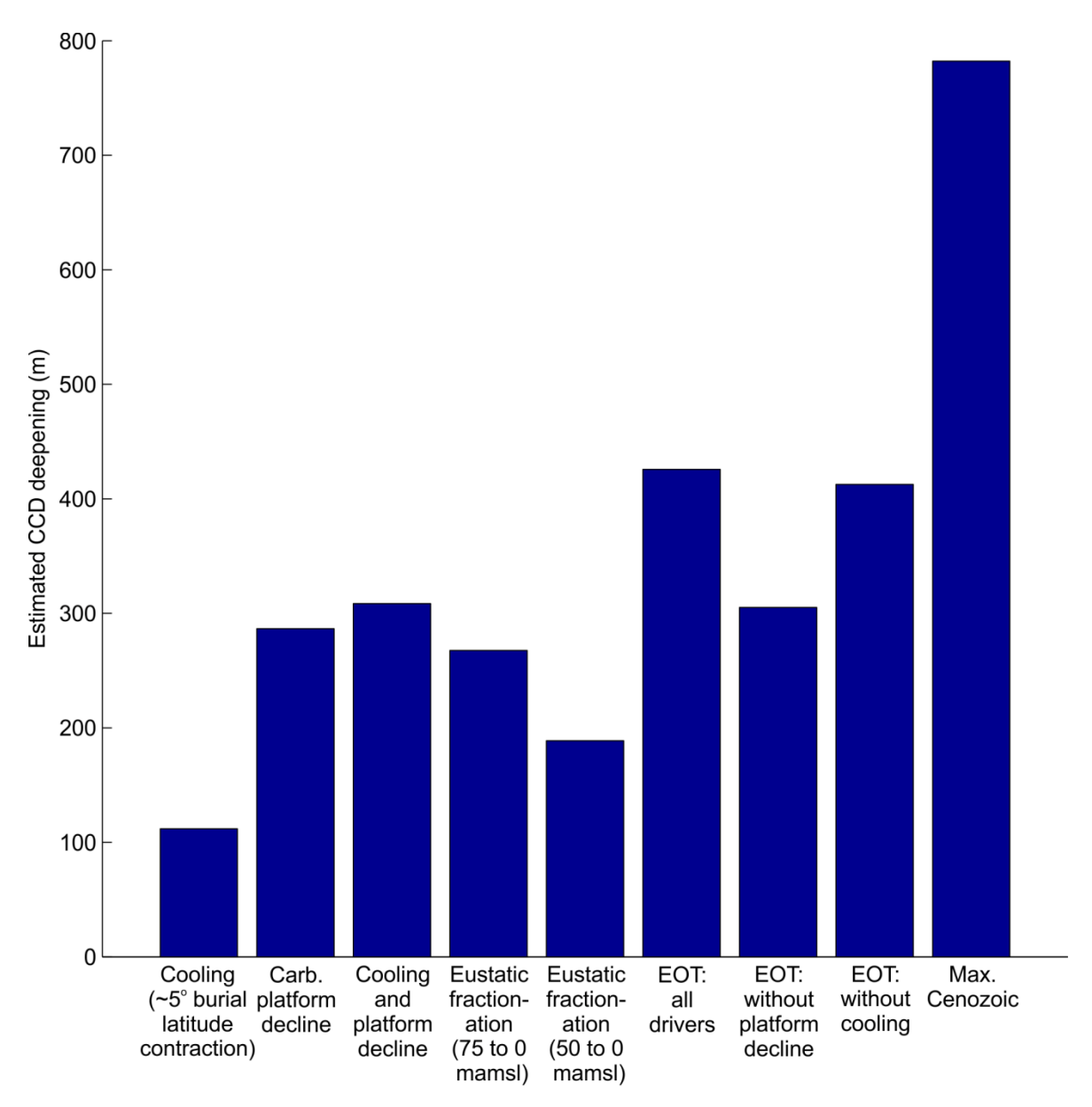
$$R_{shelf} = S * L * C * F_{shelf}$$
 [-150 < D < 50] Equation 4-5

where R_{shelf} is the change in global shelf carbonate burial rate (g CaCO₃ y⁻¹), S is the change in sea level (m), L is the average area of shelf lost per metre of sea level fall (~2.4*10⁵ km² m⁻¹ between 100 mamsl and 50 mbmsl; more than estimated in *Berger and Winterer* [1975]), C is the global proportion of shelf environments occupied by carbonate burial (~0.32 in the Eocene, ~0.06 today [Opdyke and Wilkinson, 1988]),

and F_{shelf} is the shelf carbonate burial flux (9.0*10⁷ g CaCO₃ km⁻² y⁻¹). Since R = A * F, we can then use Equations 4-4 and 4-5 to formulate a relationship between sea level change and carbonate burial shelf-basin fractionation:

$$S*L*C = \begin{cases} \left[25.75D^2 + 100278D\right]_{D_{btm}}^{D_{top}} * (F_{basin}/F_{shelf}) + S & \left[3000 < D \le 4500\right] \\ \left[113436D\right]_{D_{btm}}^{D_{top}} * (F_{basin}/F_{shelf}) + S & \left[4500 < D \le 5200\right] \end{cases}$$
 Equation 4-6

As a result it is possible to calculate the CCD deepening caused by the loss of shelf carbonate burial extent due to a given drop in sea level by solving the equations above for *D*. On top of this, as the CCD is relative to sea level the direct impact of falling sea level on the CCD is included in Equation 4-6 by adding S to the calculated deepening. For example, a drop in sea level from 75 to 0 mamsl, the estimated maximum glacioeustatic sea level fall across the EOT, would expose nearly half $(\sim 17*10^6 \text{ km}^2 \text{ of } 41*10^6 \text{ km}^2)$ of the continental shelf, which in turn results in a ~ 0.51 Pg y⁻¹ decrease in shelf carbonate burial and therefore deepens the CCD by ~270 m (~195 m from shifting carbonate burial, 75 m from falling sea level baseline) (Figure 4-7). A more modest sea level fall from 50 to 0 mamsl exposes $\sim 12*10^6$ km² out of 33.0*106 km² of continental shelf and would deepen the CCD by ~190 m (~140 m from shifting carbonate burial, 50 m from falling sea level baseline). The difference between the Cenozoic sea level extremes of up to ~100 mamsl in the Palaeocene-Eocene, providing a maximum shelf carbonate burial extent of ~15.0*106 km² [Opdyke and Wilkinson, 1988], to ~120 mbmsl in the Last Glacial Maximum, which effectively eliminates all shelf carbonate burial as the vast majority of continental shelves would be exposed, yields a maximum CCD variation of ~800 m (~560 m from shifting carbonate burial, ~220 m from falling sea level baseline) (Figure 4-7).



Processes driving shelf carbonate extent decline

Figure 4-7: Bar chart illustrating the estimated deepening of the CCD in response to different processes driving shelf carbonate extent decline during the Cenozoic and the Eocene-Oligocene Transition (EOT) in particular. The $\sim 5^{\circ}$ burial latitude contraction represents a reduction in potential carbonate burial extent from 56 to 46 % of global shelf area, carbonate (Carb.) platform decline represents a decline in actual carbonate burial extent within the potential carbonate burial extent from 43 to 14 % [*Opdyke and Wilkinson*, 1988], and eustatic fractionation represents the loss of global shelf area due to sea level fall combined with the shift in sea level baseline.

Based on the above calculations, we can estimate both the CCD deepening caused by declining shelf carbonate burial and the changing sensitivity of the CCD to sea level change during the Cenozoic. The sensitivity of the CCD is estimated by calculating the CCD deepening achieved per metre of sea level fall based on estimated changes in carbonate burial extent during the Cenozoic (Figure 4-8b) [Parrish, 1985; Opdyke and Wilkinson, 1988]. We estimate that declining shelf carbonate burial extent drove ~550 m of CCD deepening during the Cenozoic (Figure 4-8c), while the

sensitivity of the CCD to sea level change roughly halves from ~3.1 m per metre of sea level change in the early Cenozoic to ~1.6 m per metre of sea level change after the EOT (Figure 4-8d and Figure 4-9) (in contrast to the estimate of *Berger and Winterer* [1975] and *Sclater et al.* [1979] of 3 to 4 m per metre of sea level change in the present).

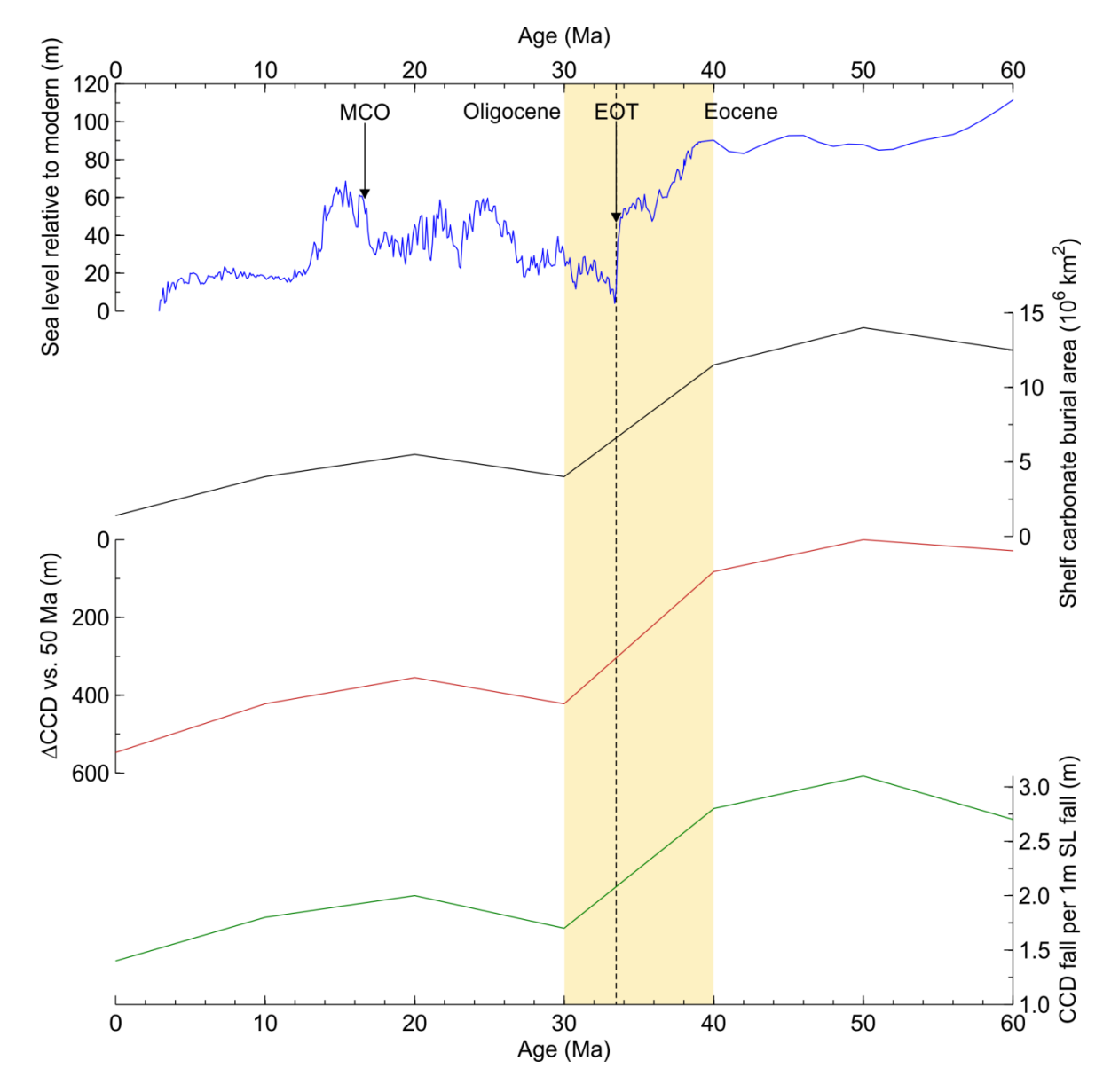


Figure 4-8: Cenozoic plots of: a) reconstructed sea level relative to modern (0 mamsl), b) estimated shelf carbonate burial extent [*Parrish*, 1985; *Opdyke and Wilkinson*, 1988], c) CCD deepening relative to 50 Ma (estimated using Equation 4-6 and shelf carbonate burial extent), and d) the sensitivity of the CCD to falling sea level illustrated by the estimated CCD deepening per 1 m of sea level fall. The Eocene-Oligocene Transition (EOT) and Miocene Climatic Optimum (MCO) are labelled (and the EOT marked by the vertical black dashed line) and the yellow bar between 40 and 30 Ma marks the period during which we conclude that the ocean carbonate system shifted state.

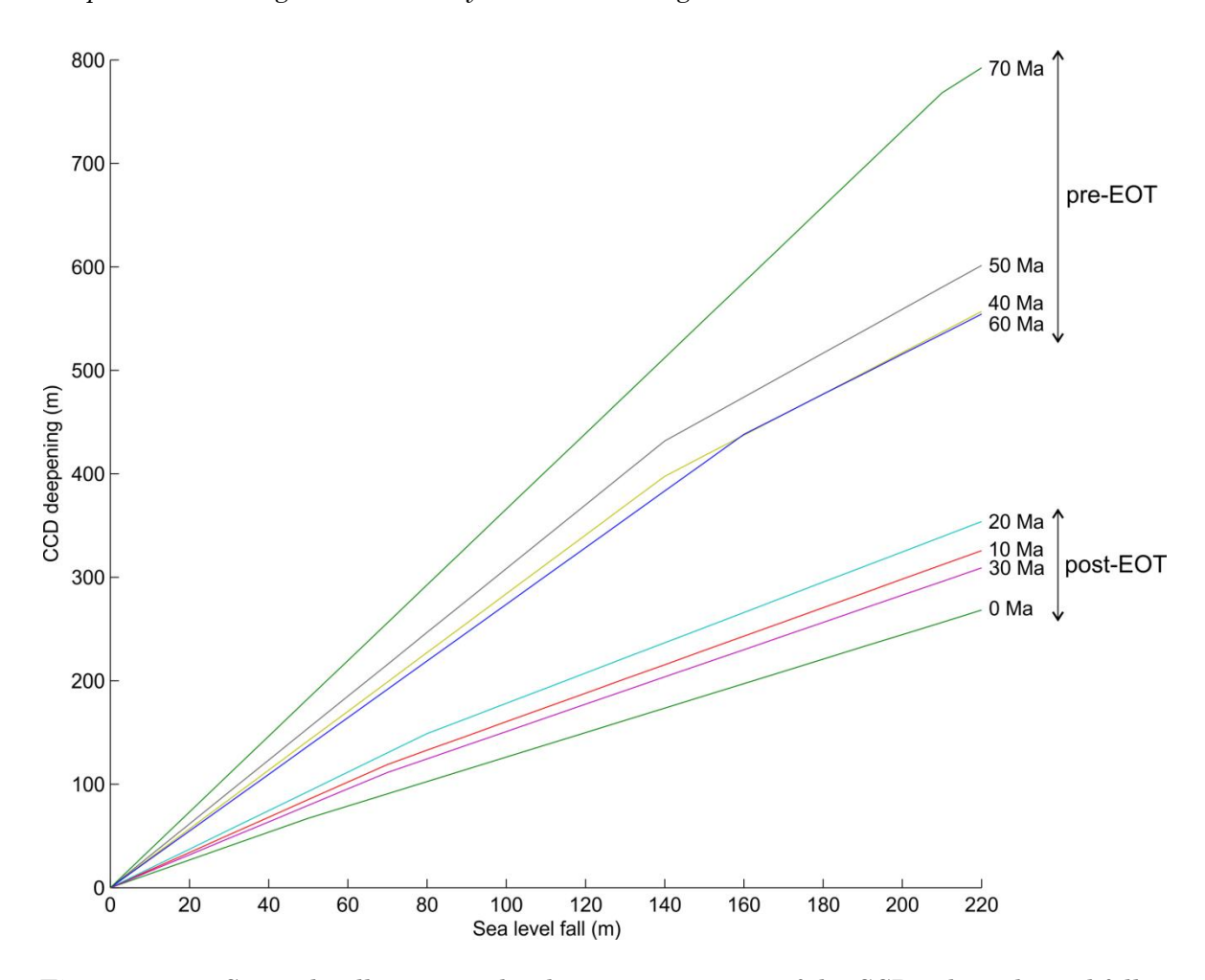


Figure 4-9: Cross-plot illustrating the changing sensitivity of the CCD to hypothetical falls in sea level during the last 70 My. The estimated relationship of CCD deepening to sea level fall in four time-slices prior to the EOT form a cluster of lines with gradients roughly double those of the time-slices after the EOT. The gradient inflection in each line represents the drop in sensitivity once sea level drops below 50 mbmsl (based on the height of average sea level around each time-slice in Figure 4-5 relative to 50 mbmsl).

4.3.4 Climate change, tectonics, and the CCD

Although sea level has been commonly invoked as the driver of shelf carbonate burial decline, Cenozoic cooling could have also affected shelf carbonate burial patterns in other ways. Palaeorecords indicate global cooling, the intensification of the global meridional gradient, and the latitudinal contraction of tropical and sub-tropical biomes across the EOT [Prothero, 1994; Lear et al., 2008; Liu et al., 2009; Coxall and Wilson, 2011; Wade et al., 2011; Bohaty et al., 2012; Houben et al., 2012]. Although not climate-driven, the shrinkage of the Tethys Ocean and epicontinental seas in sub-tropical regions between the Eocene and Miocene would have combined with global cooling to further reduce the warm shelf area suitable for carbonate burial [Higgins and Schrag, 2006; Allen and Armstrong, 2008; Okay et al., 2010; Bosboom et al., 2011]. Reconstructions of carbonate burial extent also indicate that the proportion of tropical shelf area in which carbonate platforms formed also declined from ~43 to ~14

% between the late Eocene and the early Oligocene [Opdyke and Wilkinson, 1988]. As most carbonate production occurs in warm waters and is concentrated in carbonate platform areas, all of these trends would have reduced the extent of shelf carbonate burial during the Cenozoic.

During the late Eocene (~40 Ma) there was ~41.0*106 km² of continental shelf, of which ~23.0*106 km² is estimated to have been within the latitudinal limits of carbonate deposition and ~11.5*106 km² estimated to be the site of carbonate accumulation [Parrish, 1985; Opdyke and Wilkinson, 1988; Eakins and Sharman, 2012]. Reducing the proportion of the potential regions of carbonate deposition within continental shelves from 56 % to 46 %, the estimated decrease into the early Oligocene, reduces the extent of potential regions of carbonate deposition to $\sim 18.9 \times 10^6$ km² and actual carbonate platform extent (assuming a constant ratio of carbonate platform extent to potential carbonate deposition area) to ~8.1*106 km², which in turn we estimate, based on calculating the reduction in shelf carbonate burial rate, would result in a ~110 m CCD deepening (Figure 4-7). Reducing the proportion of the extent of carbonate platforms within the potential regions of carbonate deposition from 43 % to 14 % reduces carbonate burial extent to ~3.2*106 km², which we estimate would result in a ~290 m CCD deepening. Combining the reductions in both potential carbonate deposition area and the proportion of carbonate platform extent within that area results in an estimated CCD deepening of ~310 m. This deepening is less than the summation of these drivers when considered separately because the decline in potential carbonate burial extent consequently limits the absolute impact of the declining proportion of carbonate platform extent.

4.4 Results and Discussion

4.4.1 Cenozoic case studies

In this section we explain how our new data analyses shed new light on known periods of major CCD change during the Cenozoic.

4.4.1.1 The Eocene-Oligocene Transition

A combination of glacioeustatic sea level fall and global cooling across the EOT would have driven the CCD-deepening processes of carbonate burial fractionation and carbonate platform decline simultaneously. Based on the calculations in the sections above, we estimate that combining (1) a fall in sea level from 75 to 0 mamsl, (2) a

decrease in potential carbonate burial extent from 56 % to 46 % of global shelf area, and (3) a decline in carbonate burial extent within the potential carbonate burial area from 43 % to 14% results in ~10.0*106 km² of shelf carbonate burial area being lost across the EOT, a four-fold reduction in carbonate burial extent compared to the Eocene. This would in turn require basin carbonate burial area to increase by ~31.9*106 km² through a ~430 m deepening of the CCD (Figure 4-7). Assuming no change in the proportion of potential carbonate burial extent reduces the CCD deepening to ~410 m, while assuming instead no change in the proportion of carbonate platform extent reduces the CCD deepening to ~310 m. These calculations compare favourably with the modelling of Chapter 3 [Armstrong McKay et al., in revision], in which a long-term CCD deepening of ~500 m at the EOT is achieved by an 80 % reduction in shelf carbonate burial compared to our estimate in this work of an ~87 % reduction in shelf carbonate burial resulting in a ~430 m deepening.

4.4.1.2 Miocene Climatic Optimum

In the mid-Miocene the CCD shoaled by ~450 m in the equatorial Pacific at ~18.0 Ma before re-deepening to its early Miocene depth after 16.0 Ma, after which it did not shoal substantially again in the rest of the Cenozoic [Pälike et al., 2012]. It has previously been suggested that this shoaling was due to a "carbonate famine" in which carbonate production significantly declined in the equatorial surface waters [Lyle, 2003; Pälike et al., 2012]. In contrast, biogeochemical modelling suggests that, assuming this is a global CCD change, the re-deepening of the CCD after 16.0 Ma could be driven by a combination of carbonate burial fractionation and weathering pulses of newly exposed carbonate shelves, implying in turn that the shoaling at ~18.0 Ma might instead represent a partial recovery in shelf carbonate burial compared to the Eocene [Chapter 2 – Armstrong McKay et al., 2014]. This shelf recovery could be linked with the global warming and Antarctic ice sheet retreat that took place during the Miocene Climatic Optimum and the subsequent return to icehouse conditions during the mid-Miocene Climate Transition [Zachos et al., 2001b; Billups and Schrag, 2003; Holbourn et al., 2007; Passchier et al., 2011]. However, our calculations suggest that the mid-Miocene CCD shoaling would require ~1.5 Pg of CaCO₃ burial to be shifted from deep to shelf settings, which, even if potential carbonate burial area was restored to late Eocene levels, would require an unrealistic ~420 m of sea level rise if the shoaling was entirely driven by sea level change. Even restoring shelf area and the extent of potential carbonate deposition regions and carbonate platforms from estimated to Eccene values, that is to say a complete reversal from icehouse to

greenhouse conditions, results in only ~320 m of CCD shoaling. This indicates that carbonate burial fractionation can explain some of the mid-Miocene CCD shoaling but another process is also required in order to drive at least another 130 m of CCD shoaling (assuming that the equatorial Pacific CCD record represents the global CCD change).

4.4.1.3 Mid-Eocene Climatic Optimum and the late Eocene

The temporary ~800 m global shoaling of the CCD associated with the Middle-Eocene Climatic Optimum (MECO) event at ~40 Ma has previously been partially attributed to a rise in sea level driving increased shelf carbonate burial [Bohaty et al., 2009; Spofforth et al., 2010; Sluijs et al., 2013]. We estimate that this process would call for a ~2.3 Pg y⁻¹ increase in the shelf carbonate burial rate during MECO, which would require at least a ~340 m increase in sea level. This is around three times larger than the sea level change seen during the Last Glacial Maximum, and as any ice sheets prior to the EOT are likely to have been relatively limited an increase in sea level of this magnitude is clearly impossible [Lear et al., 2004; Edgar et al., 2007; Eldrett et al., 2007; de Boer et al., 2010]. Increasing carbonate burial extent to cover all of the global shelf area instead could drive up to ~800 m of CCD shoaling in the Eocene, which would in turn reduce the sea level change required to a more reasonable ~50 m. However, rapidly increasing carbonate burial area to its maximum possible global extent is not supported by the geological record, and as a result we conclude it is unlikely that carbonate burial fractionation played a major role in the MECO CCD perturbation. Because the Eocene Carbonate Accumulation Events (CAEs) are of a similar magnitude to MECO and occurred within a similar context they are also unlikely to be related to carbonate burial fractionation, and whether the CAEs represent global or just a regional equatorial Pacific phenomenon is debated [Lyle et al., 2005, 2008, 2010; Pälike et al., 2012].

4.4.1.4 Early Eocene Climatic Optimum

During the Early Eocene Climatic Optimum (EECO) around 50 Ma global temperatures reached their highest point of the Cenozoic [*Zachos et al.*, 2001b, 2008] and the CCD was as shallow as ~3000 mbmsl in the equatorial Pacific [*Pälike et al.*, 2012]. Based on estimated areas of total global shelf, potential carbonate deposition, and carbonate platforms for 50 Ma, our calculations suggest a CCD only ~360 m shallower than just prior to the EOT (i.e. a CCD of 3600 to 3700 mbmsl), and the

calculations in the previous sections indicate that even if carbonate burial covered the total global shelf area the CCD would only reach ~3200 mbmsl.

4.4.1.5 Pleistocene glacial/interglacial cycle

During the Pleistocene sea level varied by up to ~145 m in step with the glacial/interglacial cycle. However, much of this sea level range was below 50 mbmsl, where the area of shelf exposed per 1 m of sea level fall is far less than it is between 150 mamsl and 50 mbmsl, and thus sea level fall had a far smaller impact on shelf carbonate burial (Figure 4-9). The CCD was also already below ~4500 mbmsl by the late Pliocene and so the CCD was already situated in the abundant abyssal plain where even a small deepening can cover a large area. This reduced CCD sensitivity to sea level (decreasing to ~1.3 m of CCD deepening per 1 m sea level fall by 0 Ma) may explain why the global CCD does not deepen significantly with the intensification of Northern Hemisphere glaciation and does not vary by more than 100 to 200 m during the subsequent glacial/interglacial cycles [Farrell and Prell, 1989; Lee et al., 2000; Lyle, 2003; Lyle et al., 2008; Pälike et al., 2012].

4.4.2 Cenozoic implications

From our calculations in Section 4.4.1.1 it is clear that up to ~430 m of the ~500 m long-term CCD deepening observed at the EOT can be achieved through a decline in shelf carbonate burial driven by a combination of glacioeustatic sea level fall and the decline of carbonate platforms. However, in Section 4.3.3 we estimate that the maximum possible CCD deepening achievable during the Cenozoic is ~800 m, based on ~220 m of sea level fall between the early Cenozoic and the Last Glacial Maximum and the complete loss of a maximum Cenozoic carbonate burial area extent of ~15.0*106 km². Estimates of the actual decline in shelf carbonate burial extent during the Cenozoic indicate a more modest ~550 m of CCD deepening since the Eocene (Figure 4-8). Shelf-basin carbonate burial fractionation can therefore only explain 120 to 370 m of the ~1100 m equatorial Pacific CCD deepening that did not take place during the EOT. The significant variability of the CCD prior to the EOT is probably mostly driven by processes other than carbonate burial fractionation as the majority of the potential carbonate burial fractionation-induced CCD deepening occurred during the EOT. After the EOT the sensitivity of the CCD to sea level change declined and CCD variability declined, but ice sheet retreat and global warming during the Miocene Climatic Optimum may have allowed a temporary and partial

recovery in shelf carbonate burial in the mid-Miocene. This suggests that shelf-basin carbonate burial fractionation can partially explain how the mid-Miocene CCD shoaling interrupted an otherwise stable CCD during the Oligocene and Miocene.

4.4.3 Why is the EOT unique?

Palaeorecords of sea level and benthic $\delta^{18}O$ suggest that ice sheet volume and sea level varied considerably during the Oligocene and Miocene [Wade and Pälike, 2004; Palike et al., 2006; Liebrand et al., 2011], but despite these fluctuations the CCD appears to have remained relatively stable. This observation implies that carbonate burial fractionation was not a significant driver of CCD change in these times despite being implicated in the EOT and mid-Miocene CCD perturbations. Our results indicate that this is because the sensitivity of the CCD to sea level change decreased from ~3.1 to ~1.6 m per 1 m of sea level fall before and after the EOT, indicating that sea level fluctuations after the EOT would have had much less impact (around half as much) on the CCD as beforehand. This drop in CCD sensitivity arises from a combination of factors. Firstly, shelf carbonate burial extent sharply declined across the EOT from an average of ~12.7*106 km² beforehand to ~3.7*106 km² since the EOT (Figure 4-8). This rapid decline was driven by the large area of terrain within ~75 mamsl that was lost as a carbonate deposition setting (Figure 4-6), the preponderance of shelf environments in sub-tropical latitudes such as the Tethys Ocean and epicontinental seas, and the decline in carbonate platform extent within potential carbonate deposition regions [Berger and Winterer, 1975; Opdyke and Wilkinson, 1988; Kump and Arthur, 1997; Higgins and Schrag, 2006; Allen and Armstrong, 2008; Amante and Eakins, 2009; Okay et al., 2010; Bosboom et al., 2011; Eakins and Sharman, 2012]. Secondly, after the EOT the CCD intersects the abyssal plain (between 4500 and 5200 mbmsl), which is the depth range of the ocean with the largest seafloor area (Figure 4-5). The CCD does not need to deepen significantly in this depth range to add a large area of new seafloor for CaCO3 accumulation (Figure 4-10). This therefore reduces the CCD deepening necessary to compensate for reductions in shelf carbonate burial. Conversely, when the CCD is above 4000 mbmsl the CCD has to deepen significantly more in order to cover the same sea floor area, and so the CCD is more sensitive to changes in shelf carbonate burial above this depth. As a result of these two factors there appears to be a significant threshold within the ocean carbonate system between two states: (1) extensive carbonate

platforms and a shallow, sensitive CCD, and (2) small carbonate platforms and a deeper, better buffered CCD. We conclude that this threshold was crossed at the EOT.

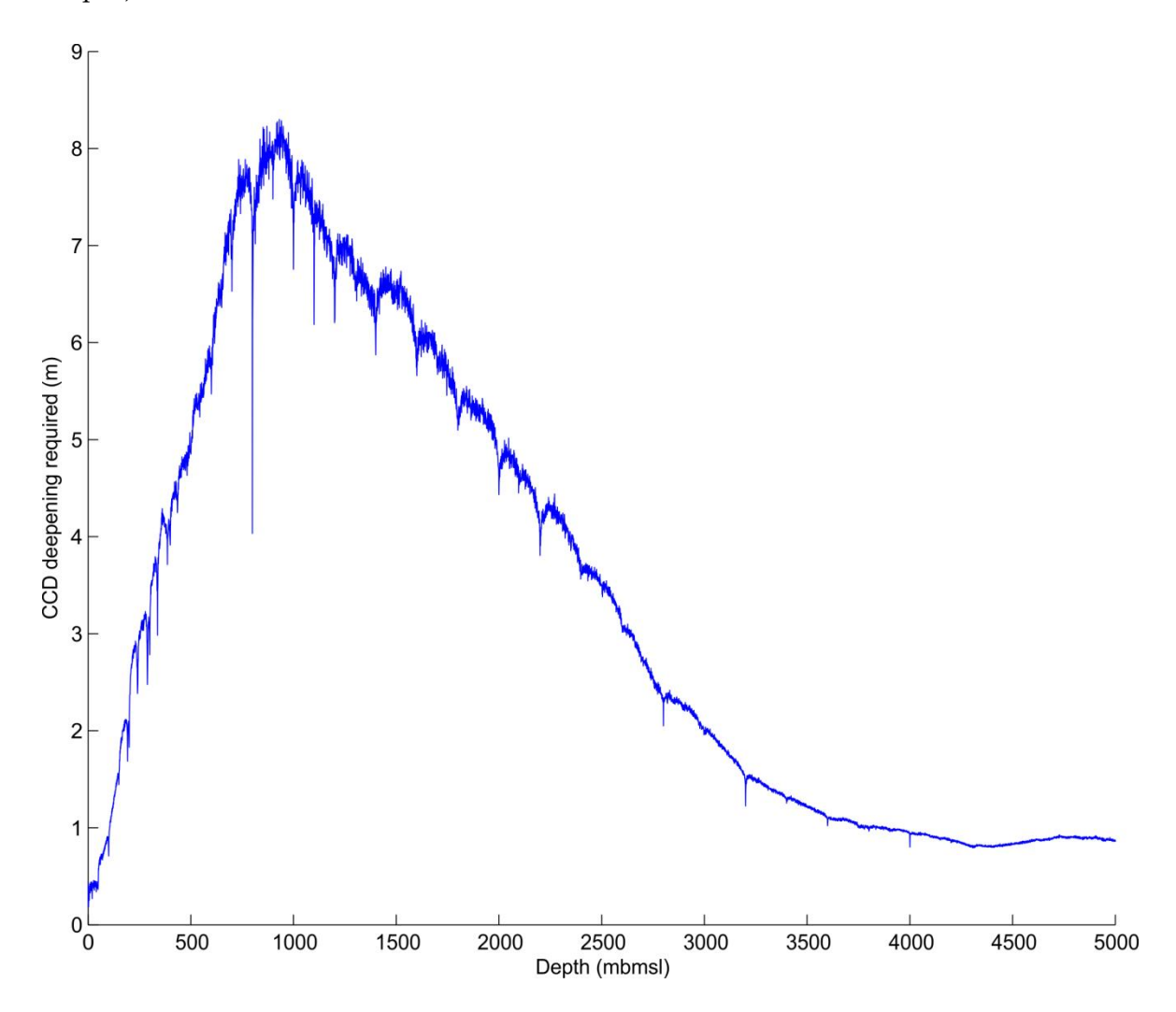


Figure 4-10: CCD deepening required to extend basin carbonate burial extent by 100000 km^2 . Whereas at ~1000 mbmsl the CCD would have to deepen by ~8 m to cover 100000 km^2 , at ~4500 mbmsl the CCD would only have to deepen by ~1 m to cover the same area.

4.4.4 Other potential drivers of Cenozoic CCD change

CCD variability and long-term deepening prior to the EOT cannot easily be explained by shelf-basin carbonate burial fractionation. In our calculations we assume that ocean carbonate production and burial fluxes in both shelf and basin settings remain constant throughout the Cenozoic. Alternatively, if carbonate production increased and the basin carbonate burial rate and/or flux increased during the Cenozoic the CCD could have deepened without the aid of carbonate burial fractionation. We calculate that the ~900 m of equatorial Pacific CCD deepening during the Cenozoic that cannot be explained by carbonate burial fractionation would require, assuming this correctly represents the global CCD change, an additional ~2.57 Pg of CaCO₃ burial in the deep ocean (beyond the maximum of ~1.35 Pg CaCO₃

available to be shifted from shelves). This would require the global basin carbonate burial rate to increase by an additional ~170 % above the Eocene estimate used in this study, not including the estimated increase in basin carbonate burial due to shelfbasin fractionation. This increase would have to be the result of an increase in carbonate export coupled to increased ocean alkalinity input, as a burial increase driven by increased carbonate productivity or preservation within sediment without additional alkalinity input would result in the CCD shoaling in order to balance the increase in burial. Modelling indicating more vigorous ocean mixing increasing surface nutrient supply and palaeorecords of increasing pelagic vertical sedimentation rates support increasing carbonate productivity over the course of the Cenozoic, while reconstructions of elevated carbonate weathering rates also support an increasing input of weathering products to the ocean [Opdyke and Wilkinson, 1988; Zachos and Kump, 2005; Scher and Martin, 2006; Dunkley Jones et al., 2008; Li et al., 2009; Goldner et al., 2014]. However, a post-EOT basin carbonate burial rate increase to nearly three times the Eocene rate (~3.6 times if the maximum shelf-basin fractionation-driven burial rate increase is also included) is not supported by current estimates. The basin carbonate burial rate is estimated to have increased by a maximum of ~1.9 Pg CaCO³ y⁻¹ between the Eocene and today (based on pelagic carbonate accumulation rates increasing from as little as ~0.05*106 km³ y-1 at 50 Ma up to $\sim 0.8*10^6$ km³ y¹ today [Opdyke and Wilkinson, 1988]), of which up to ~ 1.35 Pg CaCO3 y-1 is likely to have been the result of shelf-basin fractionation. This leaves a shortfall in the deep carbonate burial rate of ~2 Pg CaCO³ y⁻¹ between what is required to drive all of the observed CCD deepening and what is actually observed in the carbonate burial palaeorecord.

Pälike et al. [2012] propose that the Carbonate Accumulation Events of the late Eocene [Lyle et al., 2005, 2008] could be driven by a reduction in the proportion of labile to refractory Corg and thus a decrease in organic matter available in seafloor sediment for respiration by microbes that drive carbonate dissolution as a side-effect. If global Corg burial rates decreased during the Cenozoic [e.g. Li et al., 2009] this could in turn result in greater carbonate preservation and therefore a greater ocean carbonate burial flux (i.e. burial per unit area). However, as described in the previous paragraph an increase in basin carbonate burial without an increase in alkalinity input and carbonate production as well would result in the CCD shoaling to the compensate for increased alkalinity removal. As a result, a decrease in global Corg burial rates and a deepening CCD implies an increase in both global carbonate production and terrestrial carbonate weathering. As the CCD palaeorecord is biased

to the equatorial Pacific it is also possible that both the CAEs and the mechanism proposed by *Pälike et al.* [2012] to explain them occurred regionally rather than globally, and that a fully global CCD reconstruction would feature less CCD change to explain than the equatorial Pacific reconstruction.

Alternatively, if the shelf carbonate burial flux was substantially higher during the early Cenozoic then this would have amplified the efficacy of shelf-basin carbonate burial fractionation. In order to amplify carbonate burial fractionation sufficiently to explain all of the CCD deepening observed during the Cenozoic the shelf carbonate burial flux would have to be around threefold larger (from ~9*10⁷ g km⁻² y⁻¹ to ~2.6*10⁸ g km⁻² y⁻¹) in the early Cenozoic than the present flux, resulting in an equivalent increase in the shallow carbonate burial rate. As with the scenarios described above though this would also necessitate a higher alkalinity input and carbonate production in order to prevent a compensatory CCD shoaling, and also requires significantly higher shelf carbonate burial rates in the Eocene (and similarly higher basin carbonate burial rates since the EOT after this excessive carbonate burial is shifted from shelf to basin settings) than currently estimated [*Opdyke and Wilkinson*, 1988].

We conclude that a combination of limited shelf-basin carbonate burial fractionation and modest increases in both shelf and basin carbonate burial rates driven by a long-term increase in carbonate weathering and carbonate production is potentially capable of explaining some but not all of the behaviour of the CCD palaeorecord before and after the EOT. This would also imply an increase in ocean sediment carbon sequestration over this time. Alternatively, it is possible that the Eocene CCD fluctuations and trend seen in the equatorial Pacific focused CCD palaeorecord may be at least partially the result of regional processes and events [Pälike et al., 2012], which a better constrained, global CCD palaeorecord would help confirm. Another difficult to constrain factor that could have also played a role in Cenozoic CCD dynamics is whether sediment processes such as respiration-driven dissolution significantly changed during this time, as this could weaken the coupling between carbonate weathering, carbonate burial fluxes and the CCD [Greene et al., in review].

4.5 Conclusions

We revisit the shelf-basin carbonate burial fractionation hypothesis and quantify the relationship between falling sea level, loss of shelf carbonate burial area and deepening of the CCD. We find that carbonate burial fractionation could have driven the majority (~430 m) of the long-term CCD deepening at the Eocene-Oligocene Transition and may have also played a role during the mid-Miocene CCD shoaling, but that it is unlikely to have been a major driver of the CCD fluctuations and longterm CCD deepening during the Eocene. Analysis of the sensitivity of the CCD to changes in sea level demonstrates that this sensitivity declined across the EOT as a result of the rapid decline in carbonate platforms, extra-tropical shelf area available for carbonate accumulation, and the intersection of the deepening CCD with the abundant abyssal plain. This decline in sensitivity suggests that a threshold in the ocean carbonate system was crossed at the EOT which subsequently limited the impact of post-EOT sea level variability on the CCD and thus contributed to the stability of the CCD since the EOT (with the potential exception of the mid-Miocene shoaling). A further ~900 m of CCD deepening across the Cenozoic is unlikely to have been primarily driven by carbonate burial fractionation. This additional deepening may be the result of either an increase in carbonate weathering and export during the Cenozoic, elevated shelf carbonate burial fluxes amplifying shelf-basin fractionation in the Eocene, or a regional artefact of the equatorial Pacific-based CCD reconstruction.

4.6 Acknowledgements

This work was supported by a Natural Environment Research Council studentship to D.I.A.M (NERC grant number: NE/J500112/1).

Chapter 5:

Can early warning signals be reliably detected in the Cenozoic palaeoclimate record?

In this chapter palaeorecords of a number of perturbations to the carbon-climate system during the Cenozoic are analysed in search for 'early warning signals' indicative of systemic instability and impending critical transitions, and the reliability of this method when applied to palaeorecords critically explored. This chapter forms the basis of a manuscript in preparation for publication with the following authors: Armstrong McKay, D. I., Tyrrell, T., and Wilson, P. A. Supporting online-only information is included at the end of this chapter (Section 5.8).

5.1 Abstract

Several episodes of rapid climate change and perturbations to the carbon cycle in Earth's history are hypothesised to be the result of the Earth system reaching a tipping point beyond which an abrupt transition to a new state occurs. These critical transitions are common in other complex dynamical systems and are often preceded in datasets by indicators known as 'early warning signals' (EWS), such as critical slowing down and increasing variability, which suggest a tipping point may be about to be reached. Dakos et al. [2008] and subsequent studies analysed palaeorecords from across several past climate shifts and found that EWS can be detected prior to many of these events, suggesting that EWS can successfully be detected in the palaeoclimate record and that these events are examples of critical transitions in the Earth system. However, doubts have been raised about the reliability of EWS analysis on the palaeoclimate record, the degree to which parameter selection can affect the results, and the risk of committing the 'prosecutor's fallacy' when analysing suspected critical transitions. Here we analyse the highest-resolution palaeorecords currently available across a number of perturbations to the carbon-climate system in the Cenozoic, including the Eocene-Oligocene Transition, mid-Miocene Climate Transition, and the Palaeocene-Eocene Thermal Maximum. We find that some but not all of the EWS indicators can be detected in the run-up to these events, but that some

of the results are highly dependent on the parameter selection. Despite these problems our results appear to be relatively robust in most cases, and they reveal useful information about the behaviour of the Earth system prior to Cenozoic carbon-climate system perturbations. As a result, this study illustrates how EWS analysis can be a useful tool in palaeoclimatology when used with sufficient caution.

5.2 Introduction

Many complex systems have been found to include critical thresholds, widely known as tipping points, beyond which they undergo a regime shift by rapidly transitioning into a new equilibrium state [Scheffer et al., 2009, 2012; Lenton, 2013; Dakos et al., 2014]. It has been proposed that, prior to reaching these tipping points, the behaviour of these systems begins to change subtly in a way that can be detected using time-series analysis. These 'early warning signals' (EWS) could therefore indicate the approach of a critical transition in a system such as the modern Earth's climate. If this is so then EWS should also be detectable prior to previous climate transitions in the palaeorecord [Dakos et al., 2008; Lenton, 2011]. However, palaeorecords suffer from greater dating uncertainties and a less frequent and/or consistent sampling rate than is possible with modern climate data, making robust time-series analysis more challenging. Concerns have also been raised over the likelihood of producing either 'false alarms' (where EWS appear to indicate an impending transition which never occurs) or 'missed alarms' (when no EWS occur prior to a transition), the extent to which these methods are dependent on subjective parameter choices, and the risk of confirmation bias when seeking EWS in lower quality environmental data prior to hypothesised climate transitions [Lenton, 2011; Boettiger and Hastings, 2012; Boettiger et al., 2013].

In this study we follow published methodologies for finding EWS indicators [e.g. *Dakos*, 2008; *Dakos et al.*, 2012; *Lenton et al.*, 2012a, 2012b] and apply them to the highest-resolution palaeorecords currently available for key Cenozoic carbon-climate system shifts hypothesised to involve tipping points. These include the strongly suspected cases of the Eocene-Oligocene Transition and the Palaeocene-Eocene Thermal Maximum, as well as the possible cases of the mid-Miocene Climate Transition and the Oligocene-Miocene Transition. We also analyse episodes which are not hypothesised to involve tipping points, including the K/Pg boundary and the early Miocene. By doing so, we critically assess the use of this methodology in the context of the limitations of the palaeoclimate record and attempt to increase our understanding

both about the nature of the events in question and whether the EWS approach is a useful and valid technique in palaeoclimate research.

5.3 Background

5.3.1 Critical transitions and early warning signals

One of the most important changes theorised to affect dynamical systems prior to a critical transition is the process known as 'critical slowing down' (CSD). As a critical transition (whether catastrophic, for example featuring a fold bifurcation in phase space, or non-catastrophic) approaches, the recovery rate of the system in response to small exogenic or noise-driven perturbations decreases and the system's short-term 'memory' increases [Dakos et al., 2008; Scheffer et al., 2009; Lenton, 2011; Kéfi et al., 2013]. This generally results in an increase in autocorrelation at lag 1 (i.e. in the short-term) in the time-series of a representative system parameter, as datapoints increasingly correlate with recently preceding values as the rate of change of the system slows. Increasing autocorrelation has been observed in palaeoclimate data prior to several hypothesised climate tipping point transgressions, including the Eocene-Oligocene Transition and during several Pleistocene climate shifts [Dakos et al., 2008; Lenton, 2011; Lenton et al., 2012a, 2012b].

The approach of a tipping point can also result in increasing variability in the system in question, as the slower system feedback response to perturbations allows more extreme values to become more common as the system moves further away from the mean state, which is observed in datasets as an increase in standard deviation and/or the coefficient of variation [Carpenter and Brock, 2006; Scheffer et al., 2009; Lenton, 2011; Dakos et al., 2012; Lenton et al., 2012a]. The skewness of the data may also increase (either positively or negatively depending on the direction of the new attractor state), as the extreme of one side of the normal distribution in the dataset is drawn asymmetrically towards the new attractor state. The presence of more extreme values in the dataset than normal can result in the dataset's kurtosis increasing as the data distribution becomes 'fatter' than expected at the extreme ends of its tails. Alternatively, instead of exhibiting CSD a system may 'flicker', a behaviour in which the system sporadically jumps to a new attractor state and back without experiencing CSD beforehand [Scheffer et al., 2009; Dakos et al., 2012, 2013; Wang et al., 2012; Carstensen et al., 2013]. Flickering also tends to result in increasing variance, kurtosis, skewness, and/or bimodality and so can potentially be difficult to distinguish from CSD, but these indices often peak prior to the critical transition itself and occur over a longer time-period.

One limitation with searching for EWS indicators in palaeoclimate data, however, is that none of the indicators reveal much information about the nature of the transition itself, with increasing CSD and variability detected prior to both catastrophic and non-catastrophic transitions featuring a bifurcation in phase space and even before non-catastrophic transitions without a bifurcation [Kéfi et al., 2013]. It has also been argued that CSD heralding the approach of a bifurcation in a dynamical system can only be reliably detected if both increasing autocorrelation and variance are seen prior to the transition rather than one of these indicators alone [Ditlevsen and Johnsen, 2010]. There is also a risk that seeking EWS indicators in the palaeoclimate record is subject to the 'prosecutor's fallacy', as the case studies chosen could potentially be 'false positives' representing transitions that occurred purely by chance rather than due to systemic instability [Lenton, 2011; Boettiger and Hastings, 2012; Boettiger et al., 2013]. Conversely, EWS may be entirely absent prior to some known critical transitions and would therefore constitute 'missed alarms'. However, detecting multiple, consistent, and robust EWS indicators in a palaeorecord can still be indicative of decreasing system stability, resilience, and the approach towards a transition even if a catastrophic transition is not actually reached.

5.3.2 Potential tipping points in the palaeoclimate record

Several Cenozoic climate shifts and carbon cycle perturbations are hypothesised to have occurred when tipping points were reached as the Earth system gradually shifted from a high-CO₂, Greenhouse climate state to a low-CO₂, Icehouse climate state (Figure 5-1).

5.3.2.1 Eocene-Oligocene Transition

Arguably the most significant climate shift during the Cenozoic was the Eocene-Oligocene Transition (EOT) ~34 million years ago, during which major ice sheets developed on Antarctica, global temperatures fell significantly, and the carbonate compensation depth (CCD) permanently deepened by ~500 m [Coxall et al., 2005; Lear et al., 2008; Miller et al., 2008; Liu et al., 2009; Coxall and Wilson, 2011; Scher et al., 2011; Tigchelaar et al., 2011; Wade et al., 2011; Bohaty et al., 2012]. The EOT has been hypothesised to result from slowly declining atmospheric CO₂ (atmCO₂) during

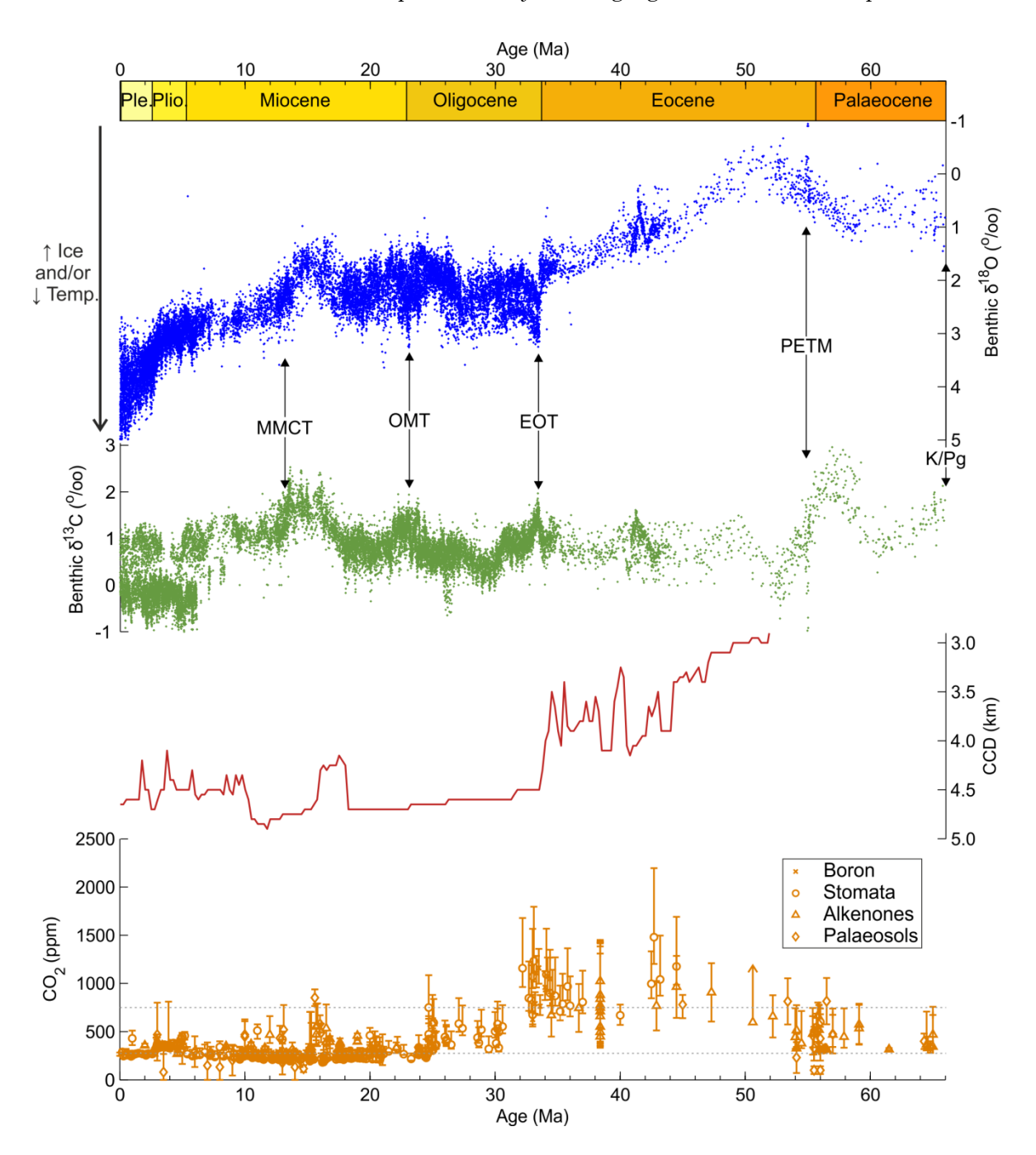


Figure 5-1: Cenozoic palaeorecords of: a) benthic δ^{18} O, b) benthic δ^{13} C, c) carbonate compensation depth (CCD) reconstructed in the equatorial Pacific, and d) atmospheric CO₂ reconstructions from different proxies [*Zachos et al.*, 2001b, 2008; *Beerling and Royer*, 2011; *Pälike et al.*, 2012]. Events analysed in this paper are labelled and include the mid-Miocene Climate Transition (MMCT), Oligocene-Miocene Transition (OMT), Eocene-Oligocene Transition (EOT), Palaeocene-Eocene Thermal Maximum (PETM), and the K/Pg boundary. The grey dotted lines in the bottom panel mark the hypothesised ~750 ppm and ~280 ppm Antarctic and Greenland glaciation thresholds respectively, and Epochs are labelled on the top axis (Ple. is the Pleistocene, Plio. is the Pliocene).

the middle to late Eocene triggering rapid Antarctic glaciation once a critical threshold in $_{atm}CO_2$ was crossed (between ~750 and ~950 ppm) [DeConto and Pollard, 2003; DeConto et al., 2008; Pearson et al., 2009; Pagani et al., 2011; Ladant et al., 2014b]. In this interpretation the EOT is an excellent example of a critical transition in the carbon-climate system, and therefore may have been preceded by EWS

indicators. In support of this hypothesis, *Dakos et al.* [2008] discovered a clear increase in autocorrelation in CaCO₃ wt% data in the run-up to EOT. However, CaCO₃ wt% is not an ideal proxy to use for investigating this tipping point as it primarily reflects the state of the CCD and the ocean carbonate system, which is not necessarily coupled with the carbon-climate tipping point in question (with the CCD likely to be responding to the consequences rather than the trigger of the EOT climate change [Chapter 3 – *Armstrong McKay et al.*, in revision; *Coxall et al.*, 2005; *Merico et al.*, 2008]).

5.3.2.2 Palaeocene-Eocene Thermal Maximum

The Palaeocene-Eocene Thermal Maximum (PETM) is another potential example of a tipping point in the carbon-climate system being transgressed. During the PETM there was an abrupt release of isotopically-light carbon (between 2000 and 13000 Pg C, best estimate ~3000 Pg C) into the ocean and atmosphere system in under 10 ky, accompanied by global warming of ~5 °C, a 2.5 to 3.0 % benthic δ¹³C excursion, and a significant shoaling of the CCD [Zachos et al., 2005, 2008; Zeebe et al., 2009; Dickens, 2011; Foster et al., 2013; Kirtland Turner et al., 2014; Littler et al., 2014]. It is hypothesised that a more gradual precursor warming eventually (after exceeding an Earth system tipping point) triggered the extensive dissociation of a carbon cycle 'capacitor', such as methane hydrates in ocean sediments [Dickens, 2011], permafrost soil carbon [DeConto et al., 2012], or organic carbon from a source such as peat [Cui et al., 2011]. This carbon release led to a rapid increase in atmCO₂ and the subsequent amplification of the carbon cycle perturbation and global warming in a positive feedback loop. In this case the tipping point in the carbon-climate system is the threshold beyond which carbon was abruptly released from a carbon capacitor, which resulted in the Earth system shifting to a warmer state for ~100 ky.

5.3.2.3 Mid-Miocene Climate Transition

Another significant shift in the carbon-climate system occurred during the mid-Miocene Climate Transition (MMCT) at ~13.9 Ma. Following the global warmth and glacial minimum of the Miocene Climate Optimum (MCO, ~17 to 15 Ma), gradual global cooling and ice sheet recovery began after ~15 Ma [Billups and Schrag, 2003; Holbourn et al., 2007, 2013; Shevenell et al., 2008; Passchier et al., 2011; Feakins et al., 2012; Foster et al., 2012; Chapter 2 – Armstrong McKay et al., 2014]. At ~13.9 Ma both oxygen and carbon benthic isotopes abruptly shift to more positive and negative values respectively and the Antarctic ice sheet became fully re-established. The

rapidity of this shift and the gradual trends beforehand suggest that the MMCT could also be a potential example of a carbon-climate system tipping point.

5.3.2.4 Oligocene-Miocene Transition

The Oligocene-Miocene Transition (OMT) at ~23 Ma also marks a significant but temporary glacial expansion following a gradual decline in Antarctic glacial extent in the late Oligocene [Miller et al., 1991; de Boer et al., 2010; Liebrand et al., 2011; Mawbey and Lear, 2013]. During this glaciation Antarctic ice sheets reached near-modern extent for <400 ky, and is marked by an abrupt but temporary ~1 ‰ increase in the benthic δ^{18} O palaeorecord and a ~50 m fall in sea level. Benthic δ^{13} C also experienced a perturbation across the OMT, which, along with evidence of a carbon release event during the deglacial phase, indicates that the carbon cycle was also perturbed during the OMT. Together these features suggest that the OMT might have occurred after a threshold in the carbon-climate system was exceeded, although the evidence for this event is weaker than for the events described earlier.

5.3.2.5 'Null' cases

In contrast to the previous examples, some other major climate events in the Cenozoic should not be preceded by EWS, and their presence would raise doubts about the utility of EWS in detecting critical transitions in the palaeorecord. For example, one would not expect any consistent increase in EWS indicators during relatively 'quiet' periods of the Cenozoic, such as during the mid-Oligocene, early Miocene, or much of the Palaeocene [Zachos et al., 2001b; 2008]. Finding EWS indicators in one of these periods would weaken the case for the robustness of EWS as a reliable record of critical transitions in the palaeorecord, and therefore by analysing some of these 'null cases' we can assess whether this is the case.

5.3.2.6 K/Pg boundary and the Deccan Traps

Similar to above 'null' cases, we should also not expect EWS prior to the K/Pg asteroid impact, because this was a sudden and completely exogenic perturbation to the carbon-climate system that triggered a spontaneous regime shift [Hsu and McKenzie, 1985]. However, the carbon-climate system was already being somewhat perturbed by Deccan Traps volcanism prior to the impact [Westerhold et al., 2011; Schoene et al., 2015], and so instability may be detectable prior to the K/Pg boundary even if that instability did not directly cause the subsequent transition.

5.4 Methodology

5.4.1 Early warning signal analysis

In order to find EWS indicators in the palaeorecord we follow the methodology first outlined by Dakos et al. [2008] and subsequently used by other studies [Dakos et al., 2012; Lenton et al., 2012a, 2012b] and the 'Early Warning Signals Toolbox' developed based on this work (documented at www.early-warning-signals.org and available as 'earlywarnings' in R). After selecting the dataset on which to perform EWS analysis (see Section 5.4.2 for details) and terminating the dataset just prior to the hypothesised transition to avoid biasing the analysis, the data are first interpolated (using linear interpolation by default with the interp1 function in Matlab) to provide the equidistant data-points required for rigorous statistical analysis. However, interpolation itself can introduce statistical artefacts into the analysis as, by definition, the addition of interpolated data-points increases selfsimilarity and thus autocorrelation in the dataset. In palaeorecords this tends to result in an artificial increase in autocorrelation in parts of the dataset with either sparser data-points or complete gaps in the data. As a result we also repeat EWS analysis on non-interpolated data in order to assess the sensitivity of our results to interpolation. Following interpolation, the data are then detrended by subtracting the smoothed dataset, estimated with a Gaussian kernel smoothing function (using the ksmooth function in R), in order to remove any long-term trends because these are not the focus of the analysis. This makes the dataset stationary. Bandwidth is an important consideration in this process and is adjusted heuristically for each dataset in order to best remove long-term trends while leaving the short-term fluctuations.

In order to calculate the autocorrelation (at lag 1) of the dataset, an autoregressive model of order 1 (AR1) is fitted to the data within a rolling window (using the generic_ews function of the earlywarnings toolbox in R). The AR1 model is of the form: $x_{t+1} = \alpha_1 x_t + \varepsilon_t$, fitted by an ordinary least-squares method and with a Gaussian random error. Following previous studies the default window size is set at half the length of the dataset, but as part of our sensitivity testing we also repeat our analyses for window sizes of 25 % and 75 %. The choice of window length is a trade-off between dataset resolution and the reliability of the estimate of the EWS indicator, with a short window allowing shorter-term changes in indicators to be tracked at the cost of lower estimate reliability (and vice versa). On the same rolling window the skewness, kurtosis, and standard deviation of the dataset are also calculated (using

the generic_ews function of the earlywarnings toolbox in R). Finally, the likelihood of there being a real trend in the results is calculated by estimating the nonparametric Kendall rank-correlation statistic (τ), which measures the strength of an indicator's tendency to increase ($\tau >>0$) or decrease ($\tau <<0$) against the null hypothesis of randomness ($\tau =\sim 0$) (using the generic_ews function of the earlywarnings toolbox in R). It is worth noting though that this statistic is most robust when the trend is consistent over a long period, while increasing but oscillating trends or trends only at the very end of the record can produce weak or even negative values despite a clearly visible trend [Dakos et al., 2012].

5.4.2 Palaeorecords

In order to achieve reliable EWS analysis results the datasets in question should ideally be as high-resolution as possible in order to capture the dynamics of that system. However, palaeorecords are notoriously low-resolution in many cases and so special care must be taken to use appropriate datasets. In this study we use recently generated, moderate to high-resolution benthic oxygen and carbon isotope datasets that cover the EOT [Coxall and Wilson, 2011], PETM [Littler et al., 2014], MCO/MMCT [Holbourn et al., 2007], and the OMT [Liebrand et al., 2011]. These isotope records track the global state of high latitude climate and the carbon cycle respectively and are therefore an appropriate choice of dataset for an analysis of global carbon-climate shifts. In most cases these datasets are also of a sufficiently high-resolution to capture the main details of each event and also represent the records by which these events are currently typically defined. However, the records prior to the EOT and the OMT are relatively short in duration and are therefore likely to produce less robust results, while the EOT record also features a small core gap just prior to the event itself which has to be excluded to prevent interpolation artefacts. The EOT record is still sufficient to record EWS if the processes driving the hypothesised critical transition occur over the length of the record available. We also analyse benthic oxygen and carbon isotope datasets prior to the K/Pg boundary [Hull et al., in prep.] and during the 'quiet' early Miocene past the OMT [Liebrand et al., 2011], in order to analyse periods which in theory should not feature consistent EWS indicators and therefore act as 'null cases'. A major limitation of the palaeorecords available is that their resolution is of the order of 1 ky to ~10 ky, which allows only EWS generated by processes that take substantially longer than this to be detected. In practice this means that only EWS generated by the slower parts of the climate

system and carbon cycle (such as geological carbon cycle-driven atmCO₂ change, long-term ice sheet dynamics, and the longer orbital forcing frequencies such as eccentricity) will be detectable in this study, and that any EWS driven by short-term drivers of instability and critical transitions will be missed and thus constitute 'missed alarms'.

5.5 Results and Discussion

The results of the EWS analysis on the palaeorecords presented in Section 5.4.2 are presented in Figures 5-2 to 5-13 (with additional sensitivity tests presented in Supporting Figures 5-14 to 5-25), and our interpretation of these results summarised in Table 5-1 and discussed in the sections below. Overall we find that EWS indicators can be detected in the run-up to some, but not all, of the hypothesised carbon-climate system tipping points in the Cenozoic, and that our results are moderately sensitive to interpolation and sliding window length but in most cases remain relatively reliable.

Table 5-1: Table summarising the results of conducting early warning signal analysis on the palaeorecords in the run-up to a number of Cenozoic carbon-climate perturbations. The EWS indices tested for include autocorrelation, standard deviation, skewness, and kurtosis, and the palaeorecords tested include benthic $\delta^{18}O$ and $\delta^{13}C$ datasets (representing the climate system and carbon cycle respectively) for the Eocene-Oligocene Transition (EOT), Palaeocene-Eocene Thermal Maximum (PETM), mid-Miocene Climate Transition (MMCT), and the Oligocene-Miocene Transition (OMT), plus the 'null cases' of the early Miocene and the K/Pg boundary. \checkmark indicates evidence is detected of either an impending critical transition, increasing instability, or a disruption to that system; (\checkmark) indicates possible evidence of a critical transition or a system disruption; and \ast indicates either no consistent EWS, a decline in the index, or a severe mismatch with sensitivity tests [each with further notes in brackets].

Event	Palaeo- record	Autocorrelation	Standard Deviation	Skewness	Kurtosis
EOT	δ ¹⁸ O (climate)	✓ [↑ <34.3 Ma]	✓ [↑ <34.3 Ma]	✓ [↑ <34.3 Ma]	✓ [↑ <34.3 Ma]
	δ ¹³ C (carbon)	(√) [disruption ~34.2 Ma, ↑ in no-interp]	(√) [disruption ~34.2 Ma]	(√) [disruption ~34.2 Ma]	(√) [disruption ~34.2 Ma]
PETM	δ ¹⁸ Ο (climate)	✓ [↑ <57.7 Ma]	(√) [peak ~56.5 Ma then ↓]	(√) [↑ <57.7 Ma, later in no-interp]	x [↓ <57.5 Ma, ↑ in no-interp]
	δ ¹³ C (carbon)	✓ [↑]	✓ [↑]	✓ [↑]	x [↓ <57.5 Ma]
MMCT	δ ¹⁸ Ο (climate)	(√) [peak >14.4 Ma, then ↓]	(√) [peak >14.4 Ma, then ↓]	(√) [peak >14.0 Ma, then ↓]	(√) [peak >14.0 Ma, then ↓]
	δ ¹³ C (carbon)	(√) [peak >14.4 Ma then ↓]	(√) [peak >14.4 Ma then ↓]	x [↓ in default, ↑ in no-interp]	x [↓ in default, ↑ in no-interp]
OMT	δ ¹⁸ O (climate)	* [↓]	x [\doldar	√ [↑]	√ [↑]
	δ ¹³ C (carbon)	✓ [↑ ~23.5 Ma]	* [↓]	✓ [↑ <23.5 Ma]	✓ [↑ <23.5 Ma]
Early Miocene 'null' case	δ ¹⁸ O (climate)	x [↓]	*	√ [↑]	√ [↑, weak]
	δ ¹³ C (carbon)	x [weak ↑ at end, x in no-interp]	x [weak peak ~19.6 Ma]	(√) [↑, weak]	(√) [↑, weak]
K/Pg and Deccan Traps	δ ¹⁸ O (climate)	✓ [↑ <66.5 Ma, ↑ <66.2 Ma in no-interp]	(√) [disruption ~66.3 Ma, ↑ <66.2 Ma]	(√) [disruption ~66.3 Ma, ↑ <66.2 Ma]	(√) [disruption ~66.3 Ma, ↑ <66.2 Ma]
	δ ¹³ C (carbon)	✓ [↑ <66.3 Ma, ↑ <66.2 Ma in no-interp]	(√) [disruption ~66.3 Ma, ↑ <66.2 Ma]	(√) [disruption ~66.3 Ma, ↑ in no-interp]	(✓) [disruption ~66.3 Ma, ↑ in no-interp]

5.5.1 Eocene-Oligocene Transition

Prior to the EOT, increases in autocorrelation, standard deviation, skewness, and kurtosis are detected in all of the different analyses of benthic $\delta^{18}O$ after ~34.3 Ma (Figure 5-2 and Supporting Figure 5-14), suggesting that the long-term climate system was both slowing down and becoming more variable in the run up to the EOT. This supports the hypothesis that the EOT may represent a critical transition of the Earth's climate system driven by long-term atm CO₂ decline. In contrast, the benthic δ^{13} C data records a rapid drop at ~34.2 Ma followed by a recovery in all of the EWS indices in the default and non-interpolated analyses (with permanent decreases in skewness and kurtosis in the 75 % sliding window analysis) (Figure 5-3 and Supporting Figure 5-15). This indicates that, assuming that the indices are indeed capturing all EWS and that the missing short-term processes did not drive any EWS, the geological carbon cycle may have been disrupted ~200 ky before the EOT (~100 ky after the slowing down of the climate system) but was not close to a critical threshold itself. The drop at ~34.2 Ma is preceded by increases in skewness and kurtosis in the default and non-interpolated analyses and in autocorrelation in just the noninterpolated analysis, suggesting that there may have been some increase in geological carbon cycle instability prior to this disruption. Datasets of higher resolution and including the last ~50 ky before the start of the EOT are required in order to build a stronger case for a critical transition in the Earth's climate at the EOT and to resolve the state of the carbon cycle. Nevertheless, the EOT analysis presented here marks a step forward from the EOT analysis presented in Dakos et al. [2008], as we use palaeorecords that are more directly representative of the climate system and carbon cycle and analyse multiple EWS indices beyond just autocorrelation.

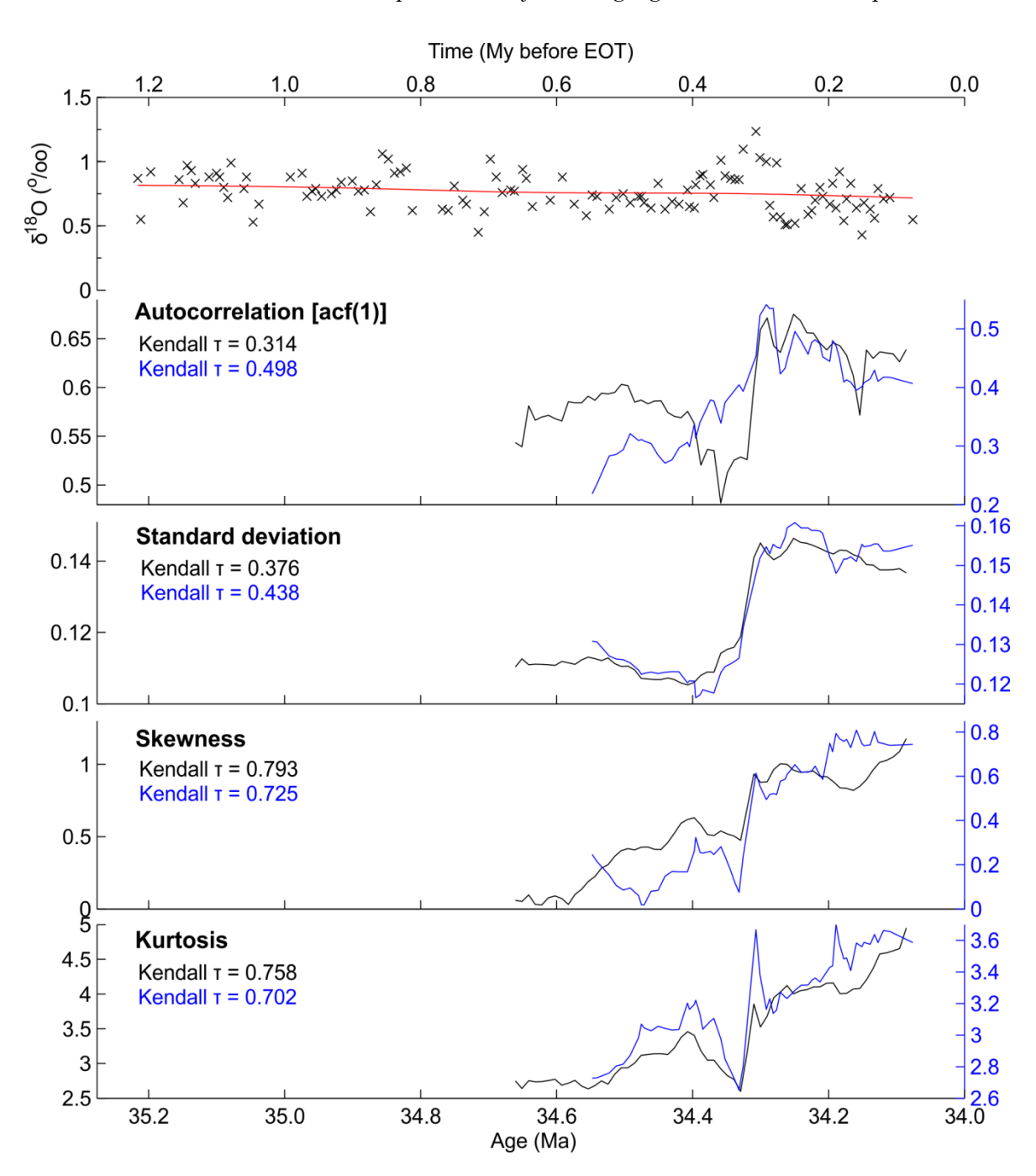


Figure 5-2: EWS analyses of benthic $\delta^{18}O$ in the run-up to the Eocene-Oligocene Transition (EOT). The top panel illustrates the benthic $\delta^{18}O$ palaeorecord (black crosses) and the detrending applied to the data (red line), with the panels below illustrating the results of the analyses for autocorrelation, standard deviation, skewness, and kurtosis calculated across the time-series. Black lines represent the default analysis (linear interpolation, Gaussian detrending with filtering bandwidth 0.5, sliding window 50 %), while the blue lines represent the non-interpolated analysis. The Kendall τ rank-correlation value is given for both analyses in their respective colour.

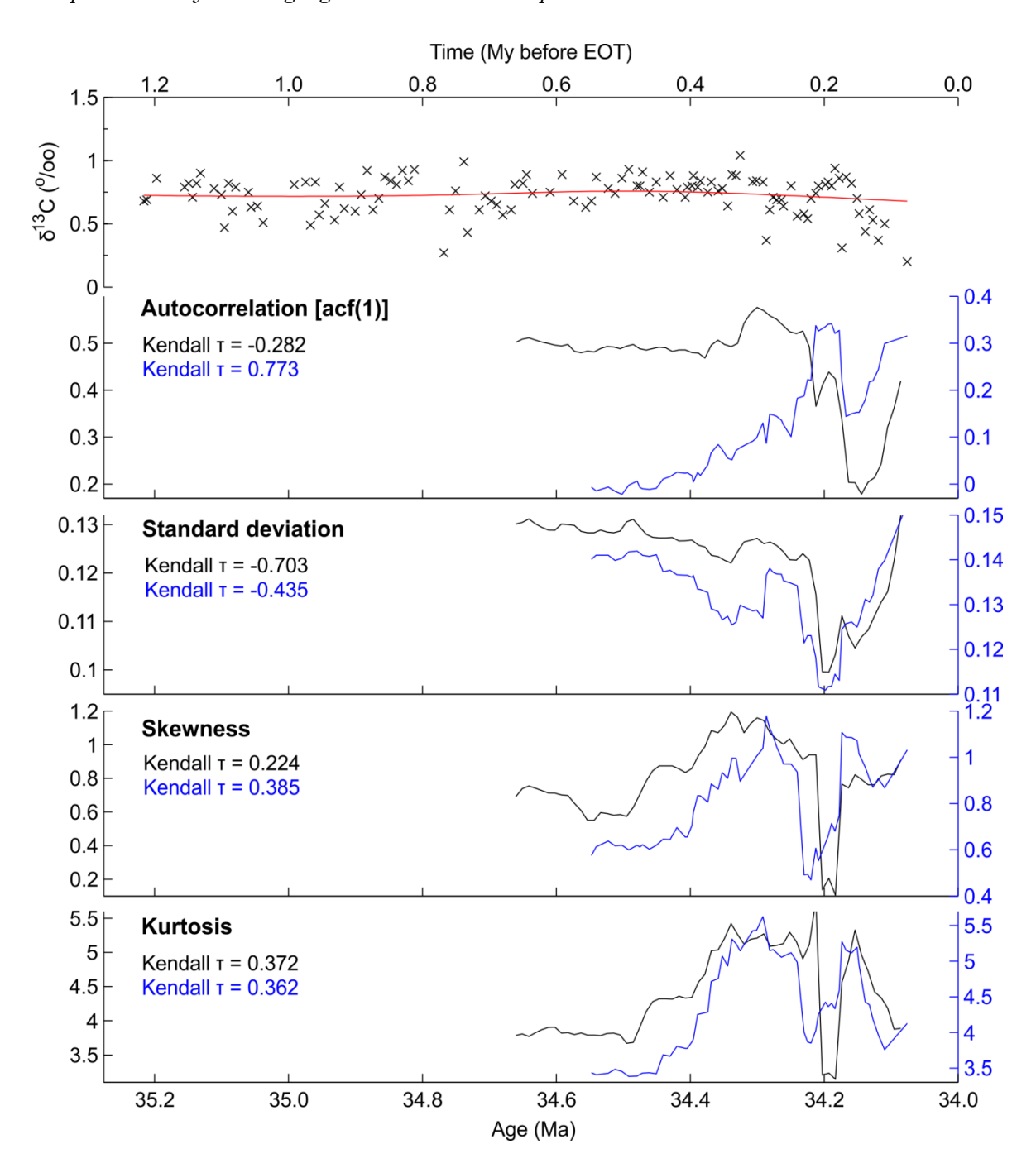


Figure 5-3: EWS analyses of benthic $\delta^{13}C$ in the run-up to the Eocene-Oligocene Transition (EOT). The top panel illustrates the benthic $\delta^{13}C$ palaeorecord (black crosses) and the detrending applied to the data (red line), with the panels below illustrating the results of the analyses for autocorrelation, standard deviation, skewness, and kurtosis calculated across the time-series. Black lines represent the default analysis (linear interpolation, Gaussian detrending with filtering bandwidth 0.5, sliding window 50 %), while the blue lines represent the non-interpolated analysis. The Kendall τ rank-correlation value is given for both analyses in their respective colour.

5.5.2 Palaeocene-Eocene Thermal Maximum

A sudden increase in the EWS indices after ~ 57.7 Ma in the benthic $\delta^{18}O$ record suggests some degree of increasing instability in the long-term climate system prior to the PETM (Figure 5-4 and Supporting Figure 5-16). However, the subsequent decline of both standard deviation and kurtosis (and in skewness in the variable sliding window sensitivity analyses) suggests either that the PETM may not represent a critical threshold in the climate system or that this represents a 'missed alarm' due to short-term process-driven EWS not being sufficiently resolved by the available data. Evidence of EWS is clearer in the benthic δ^{13} C record, where increases in autocorrelation, standard deviation, and skewness with sudden step increases at ~57.7 Ma and ~56.8 Ma are observed in the run-up to the PETM (kurtosis, in contrast, rapidly increases at ~57.7 Ma but then declines up to the PETM) (Figure 5-5 and Supporting Figure 5-17), suggesting both slowing down and increasing variability in the geological carbon cycle. Together these results suggest that the slow part of the climate system became increasingly unstable between ~57.7 Ma and ~56.5 Ma, but that the geological carbon cycle carried on being destabilised after ~56.5 Ma until the PETM itself and so may have been approaching a critical transition. These results may reflect a gradual atmCO₂-forced global warming prior to the PETM that eventually triggered the abrupt release of carbon from a carbon capacitor such as methane hydrates.

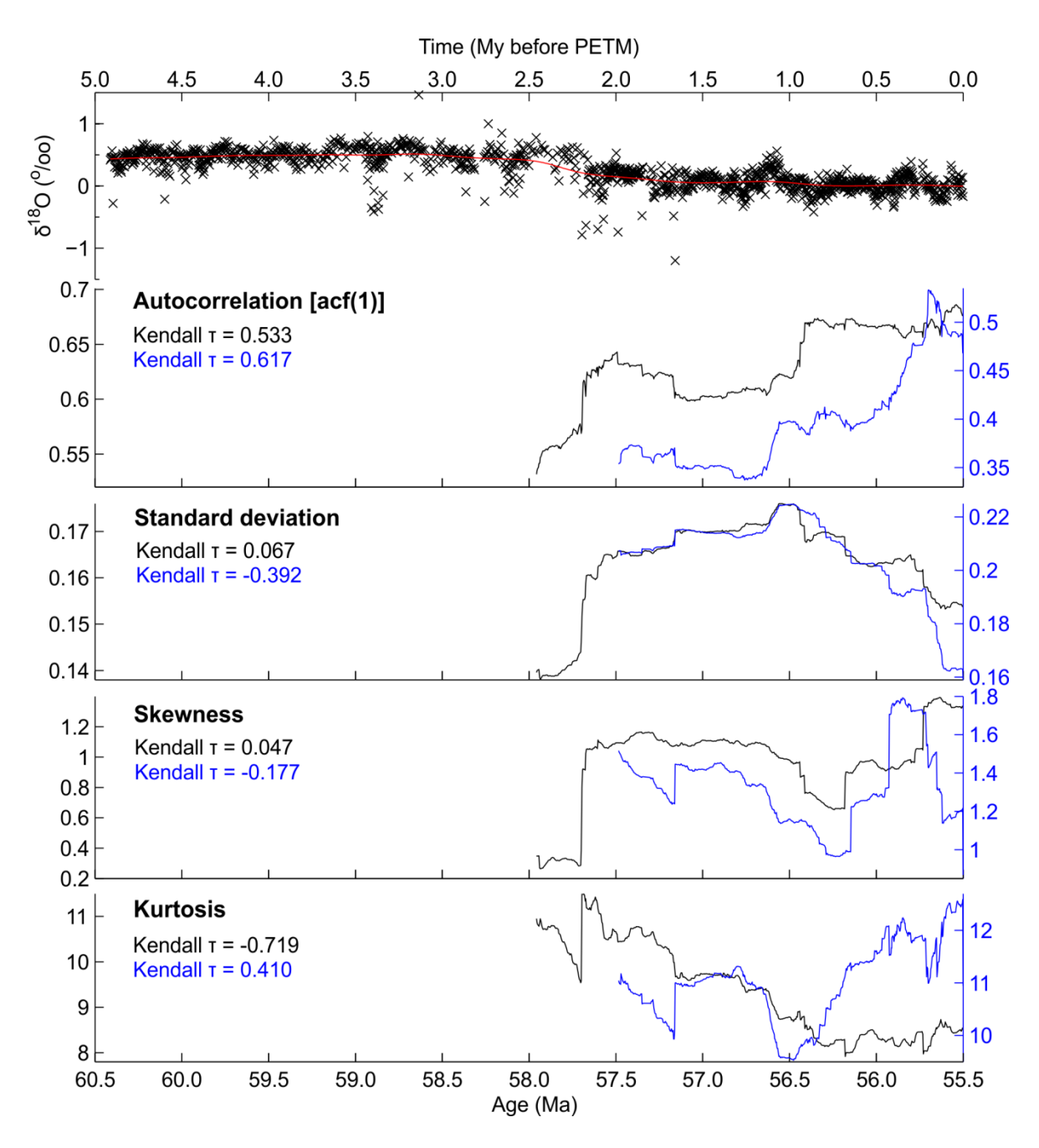


Figure 5-4: EWS analyses of benthic $\delta^{18}O$ in the run-up to the Palaeocene-Eocene Thermal Maximum (PETM). The top panel illustrates the benthic $\delta^{18}O$ palaeorecord (black crosses) and the detrending applied to the data (red line), with the panels below illustrating the results of the analyses for autocorrelation, standard deviation, skewness, and kurtosis calculated across the time-series. Black lines represent the default analysis (linear interpolation, Gaussian detrending with filtering bandwidth 0.5, sliding window 50 %), while the blue lines represent the non-interpolated analysis. The Kendall τ rank-correlation value is given for both analyses in their respective colour.

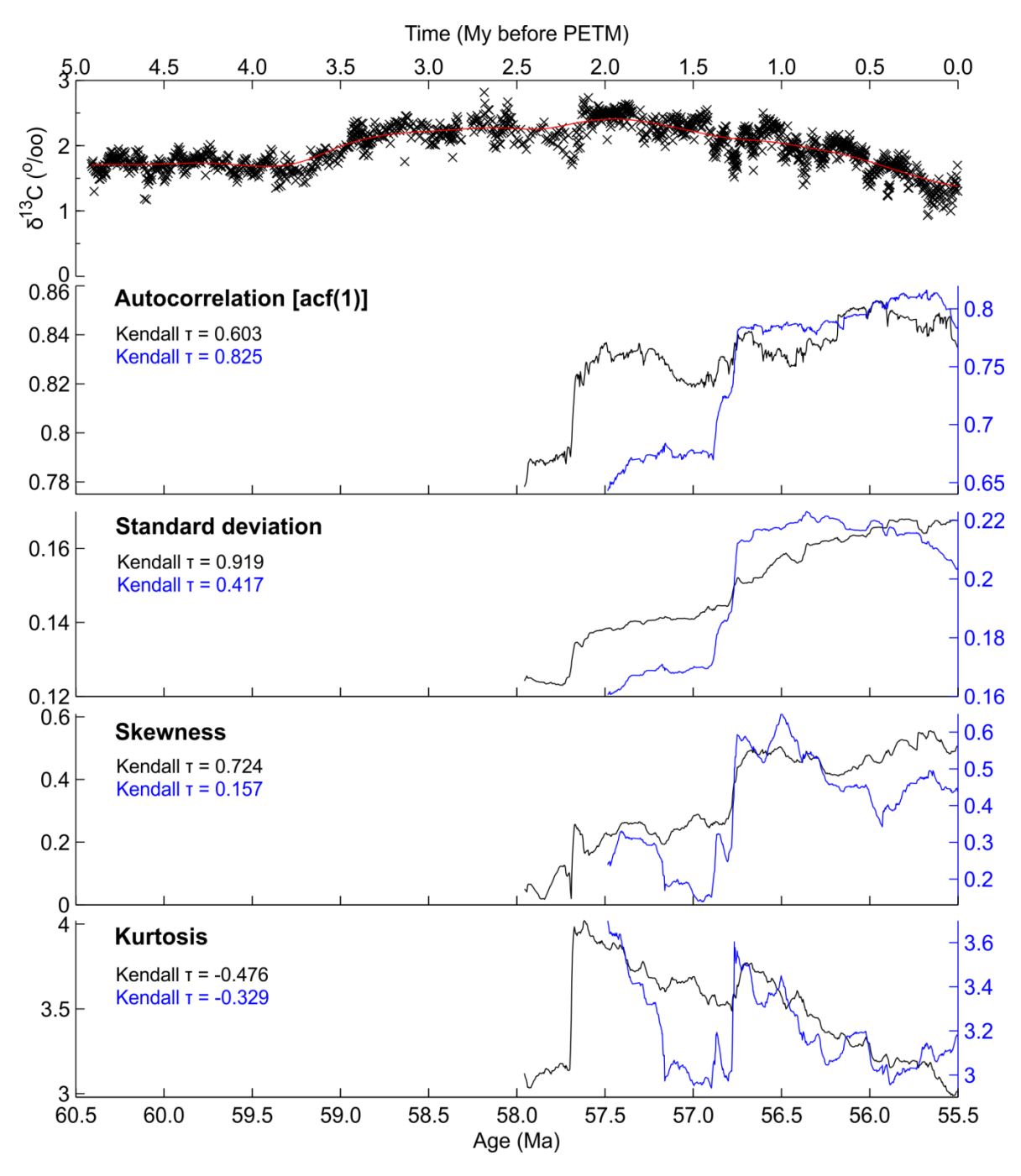


Figure 5-5: EWS analyses of benthic $\delta^{13}C$ in the run-up to the Palaeocene-Eocene Thermal Maximum (PETM). The top panel illustrates the benthic $\delta^{13}C$ palaeorecord (black crosses) and the detrending applied to the data (red line), with the panels below illustrating the results of the analyses for autocorrelation, standard deviation, skewness, and kurtosis calculated across the time-series. Black lines represent the default analysis (linear interpolation, Gaussian detrending with filtering bandwidth 0.5, sliding window 50 %), while the blue lines represent the non-interpolated analysis. The Kendall τ rank-correlation value is given for both analyses in their respective colour.

5.5.3 Mid-Miocene Climate Transition

In contrast to the EOT and the PETM, the EWS indices tend to peak early and then decrease prior to the MMCT. Both autocorrelation and standard deviation decline in the benthic δ^{18} O record after peaking or plateauing prior to ~14.4 Ma, while skewness and kurtosis values rapidly drop at ~14.0 Ma after peaking just beforehand (Figure 5-6 and Supporting Figure 5-18). A similar picture emerges from the benthic δ^{13} C record, with both autocorrelation and standard deviation peaking and then declining after ~14.4 Ma (although skewness and kurtosis increase in the noninterpolated analyses, and skewness and standard deviation increase in the 75 % sliding window analysis) (Figure 5-7 and Supporting Figure 5-19). Together these results suggest that long-term climate system and geological carbon cycle instability peaked ~500 ky earlier (at around 14.4 Ma) than the main isotope shift at ~13.9 Ma (ignoring any missed EWS driven by unresolved short-term processes), which reflects geological data suggesting that global cooling and ice growth had begun after ~14.7 Ma rather than in a sudden onset at ~13.9 Ma [Passchier et al., 2011]. This suggests that the MMCT was not the result of a catastrophic transition but instead might represent an example of a non-catastrophic threshold being crossed in the run-up to ~14.4 Ma in both the slow parts of the climate system and carbon cycle, with the ~13.9 Ma isotope shift representing the final culmination of longer, more gradual changes in the long-term carbon-climate system.

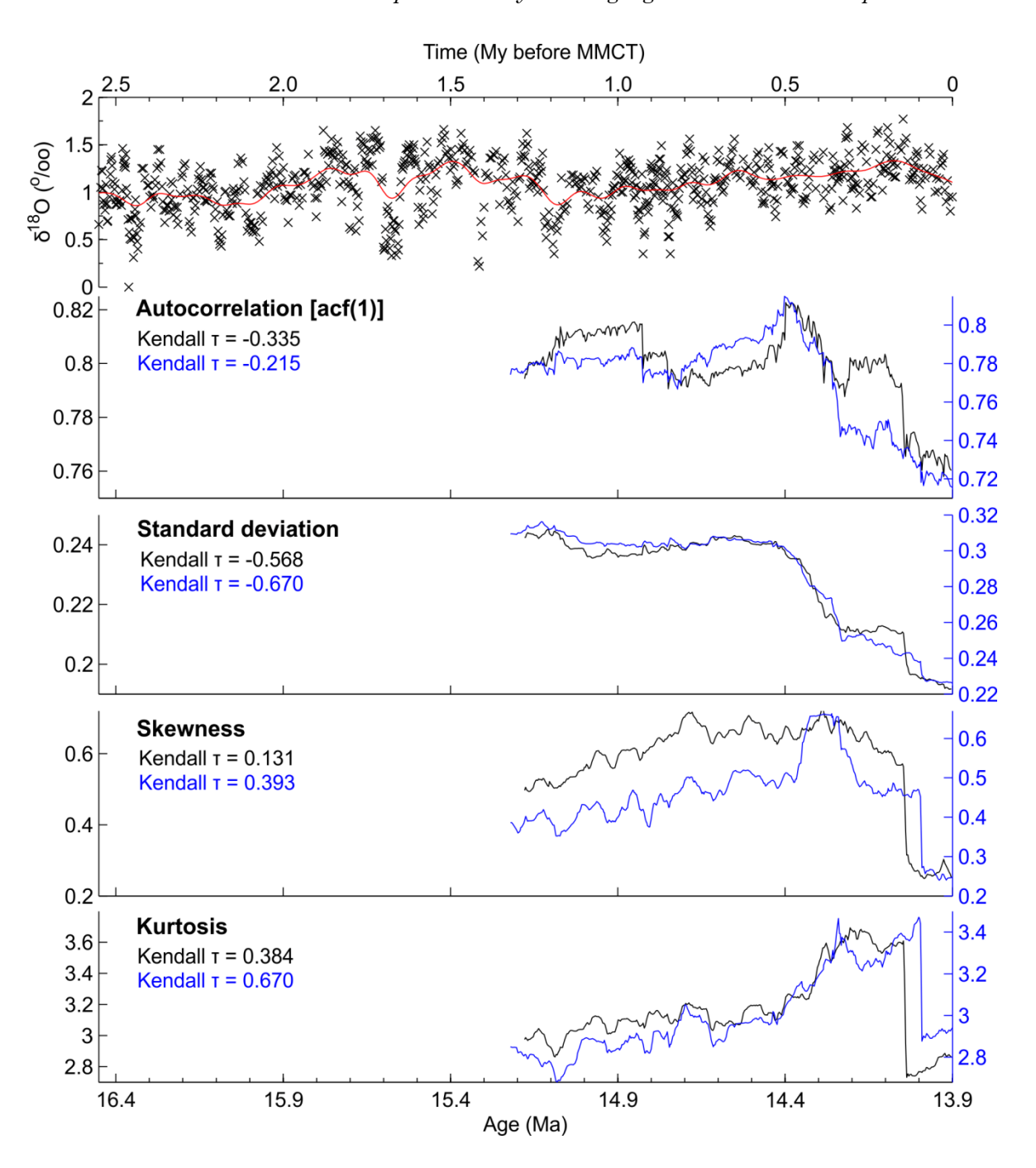


Figure 5-6: EWS analyses of benthic $\delta^{18}O$ in the run-up to the mid-Miocene Climate Transition (MMCT). The top panel illustrates the benthic $\delta^{18}O$ palaeorecord (black crosses) and the detrending applied to the data (red line), with the panels below illustrating the results of the analyses for autocorrelation, standard deviation, skewness, and kurtosis calculated across the time-series. Black lines represent the default analysis (linear interpolation, Gaussian detrending with filtering bandwidth 0.1, sliding window 50 %), while the blue lines represent the non-interpolated analysis. The Kendall τ rank-correlation value is given for both analyses in their respective colour.

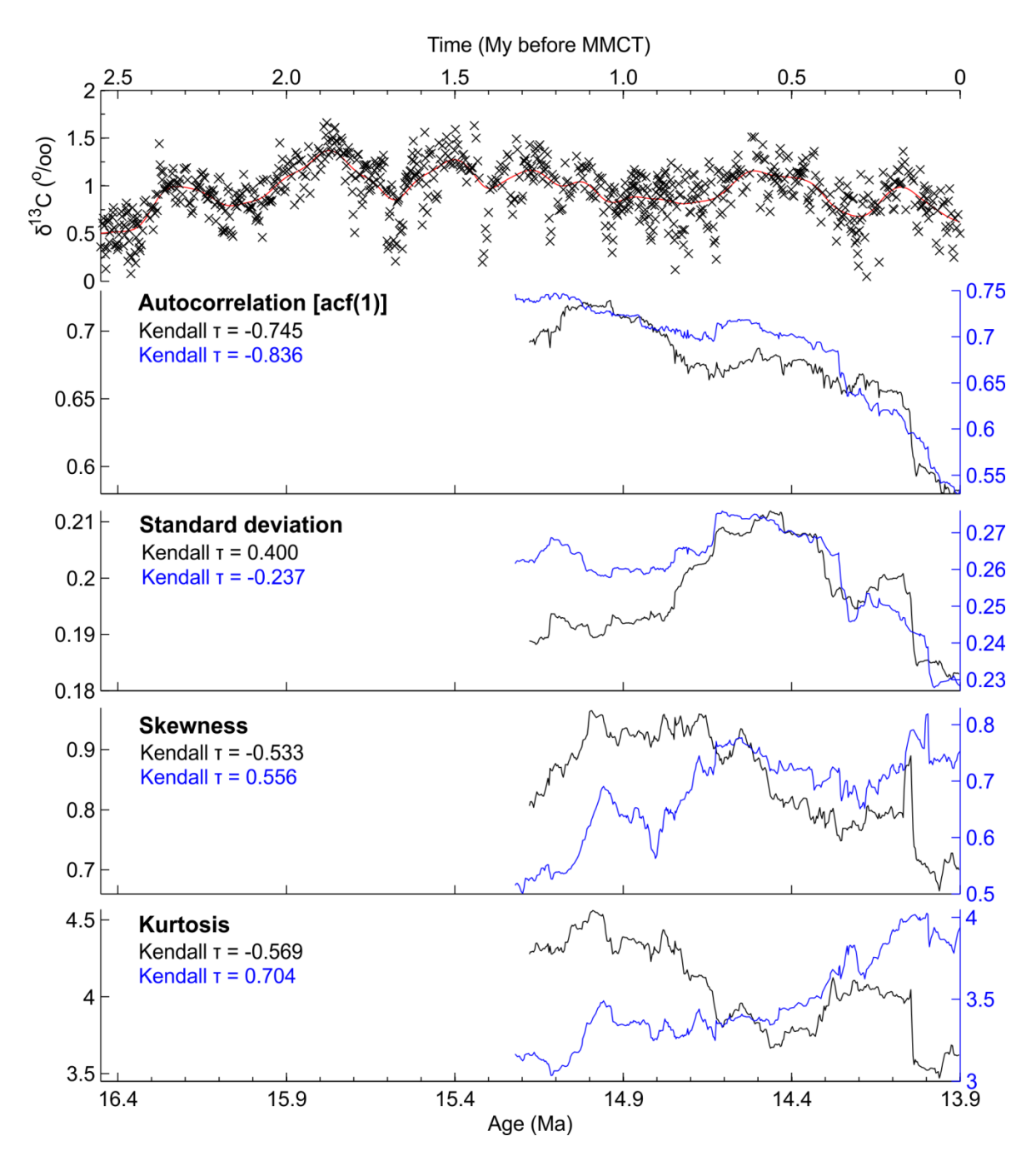


Figure 5-7: EWS analyses of benthic $\delta^{13}C$ in the run-up to the mid-Miocene Climate Transition (MMCT). The top panel illustrates the benthic $\delta^{13}C$ palaeorecord (black crosses) and the detrending applied to the data (red line), with the panels below illustrating the results of the analyses for autocorrelation, standard deviation, skewness, and kurtosis calculated across the time-series. Black lines represent the default analysis (linear interpolation, Gaussian detrending with filtering bandwidth 0.1, sliding window 50 %), while the blue lines represent the non-interpolated analysis. The Kendall τ rank-correlation value is given for both analyses in their respective colour.

5.5.4 Oligocene-Miocene Transition

Palaeorecords prior to the OMT also demonstrate mixed EWS indicator responses. The benthic δ¹8O record in the latest Oligocene features declines in autocorrelation and standard deviation in contrast to increases in skewness and kurtosis in the default, non-interpolated, and 75 % sliding window analyses (Figure 5-8 and Supporting Figure 5-20). The benthic δ¹³C record features increasing autocorrelation, skewness, and kurtosis after ~23.5 Ma, but in contrast to benthic δ¹³O there is also a decline in standard deviation (Figure 5-9 and Supporting Figure 5-21). As a result, no consistent evidence of CSD can be observed in the long-term climate system in the late Oligocene, but there is some evidence of increasing instability in the geological carbon cycle prior to the OMT. However, it is debatable whether this evidence is sufficient for this to be considered a critical transition in the geological carbon cycle. Datasets with greater resolution and length in the late Oligocene would help to further clarify the nature of this event.

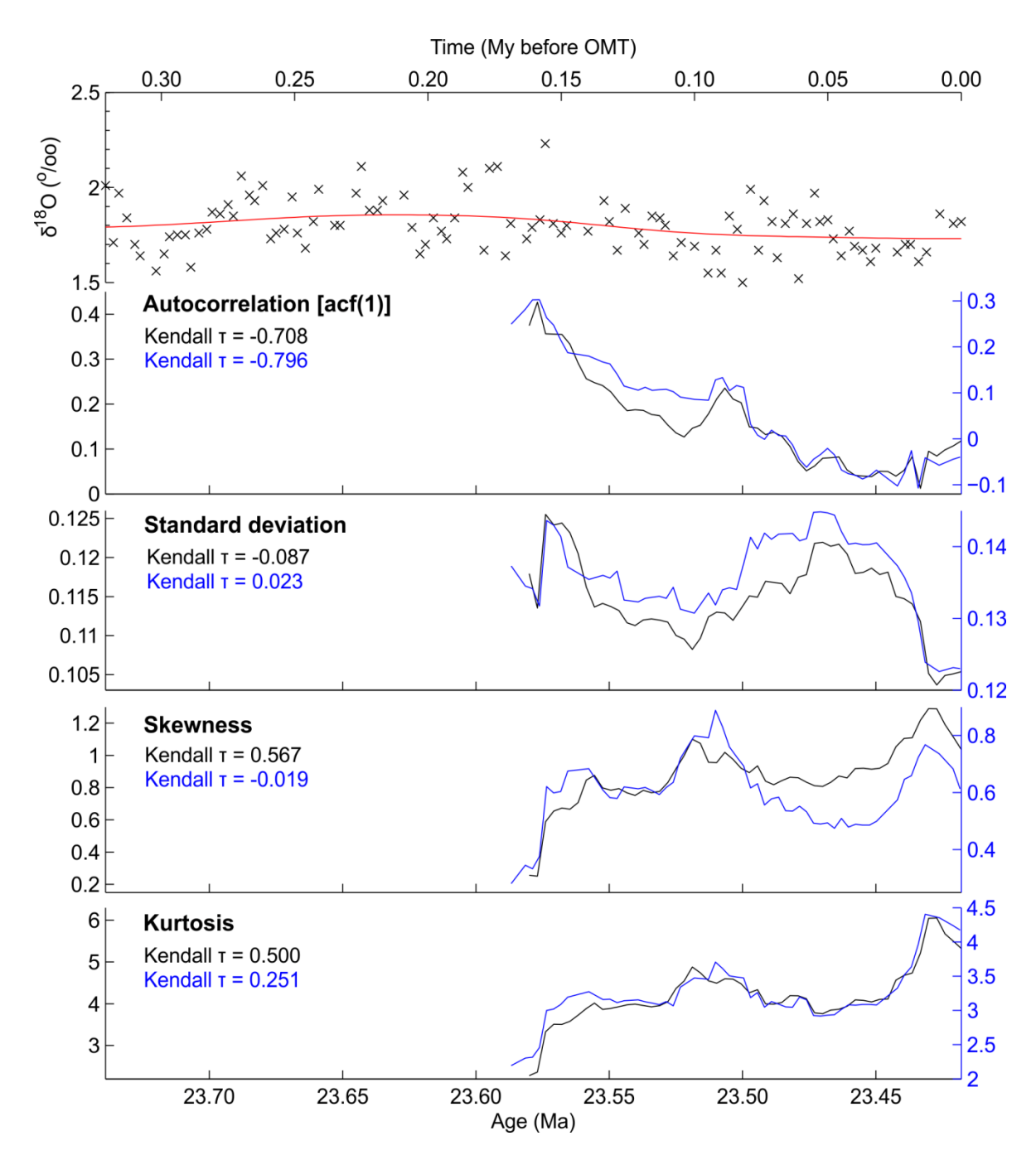


Figure 5-8: EWS analyses of benthic $\delta^{18}O$ in the run-up to the Oligocene-Miocene Transition (OMT). The top panel illustrates the benthic $\delta^{18}O$ palaeorecord (black crosses) and the detrending applied to the data (red line), with the panels below illustrating the results of the analyses for autocorrelation, standard deviation, skewness, and kurtosis calculated across the time-series. Black lines represent the default analysis (linear interpolation, Gaussian detrending with filtering bandwidth 0.1, sliding window 50 %), while the blue lines represent the non-interpolated analysis. The Kendall τ rank-correlation value is given for both analyses in their respective colour.

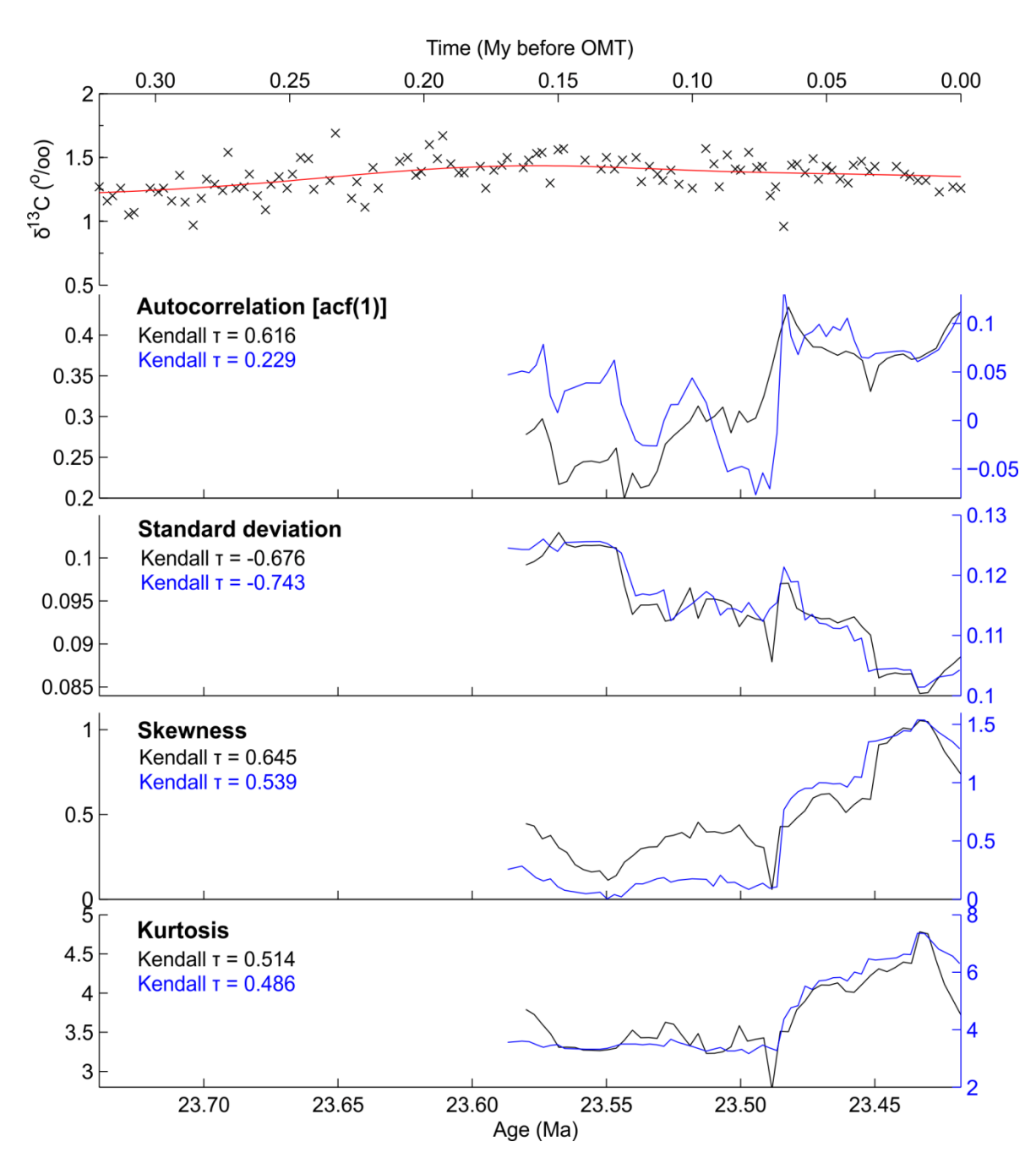


Figure 5-9: EWS analyses of benthic $\delta^{13}C$ in the run-up to the Oligocene-Miocene Transition (OMT). The top panel illustrates the benthic $\delta^{13}C$ palaeorecord (black crosses) and the detrending applied to the data (red line), with the panels below illustrating the results of the analyses for autocorrelation, standard deviation, skewness, and kurtosis calculated across the time-series. Black lines represent the default analysis (linear interpolation, Gaussian detrending with filtering bandwidth 0.1, sliding window 50 %), while the blue lines represent the non-interpolated analysis. The Kendall τ rank-correlation value is given for both analyses in their respective colour.

5.5.5 Early Miocene 'null' case

Extending the analysis on the previous dataset past the OMT and into the early Miocene provides an opportunity to investigate a 'null case' where no strong or consistent pattern should be seen in the EWS indices. In both the benthic δ^{18} O and δ^{13} C records there are considerable mismatches between the results of the different analyses, illustrating the lack of consistent trends in the data. In the benthic δ^{18} O record decreases in autocorrelation and standard deviation around 20.0 Ma contrast with the increase in skewness and the weak increase in kurtosis (although these increases are not reflected by the variable sliding window analyses) (Figure 5-10 and Supporting Figure 5-22). In the benthic δ^{13} C record most of the indices contain relatively weak trends, except for a peak in standard deviation at ~19.6 Ma and a small increase in autocorrelation at the end of the record in the default and variable sliding window analyses (Figure 5-11 and Supporting Figure 5-23). These results demonstrate that there are indeed no clear long-term trends in the EWS indices during the early Miocene, as would be expected in a time period with no suspected critical transitions or instability.

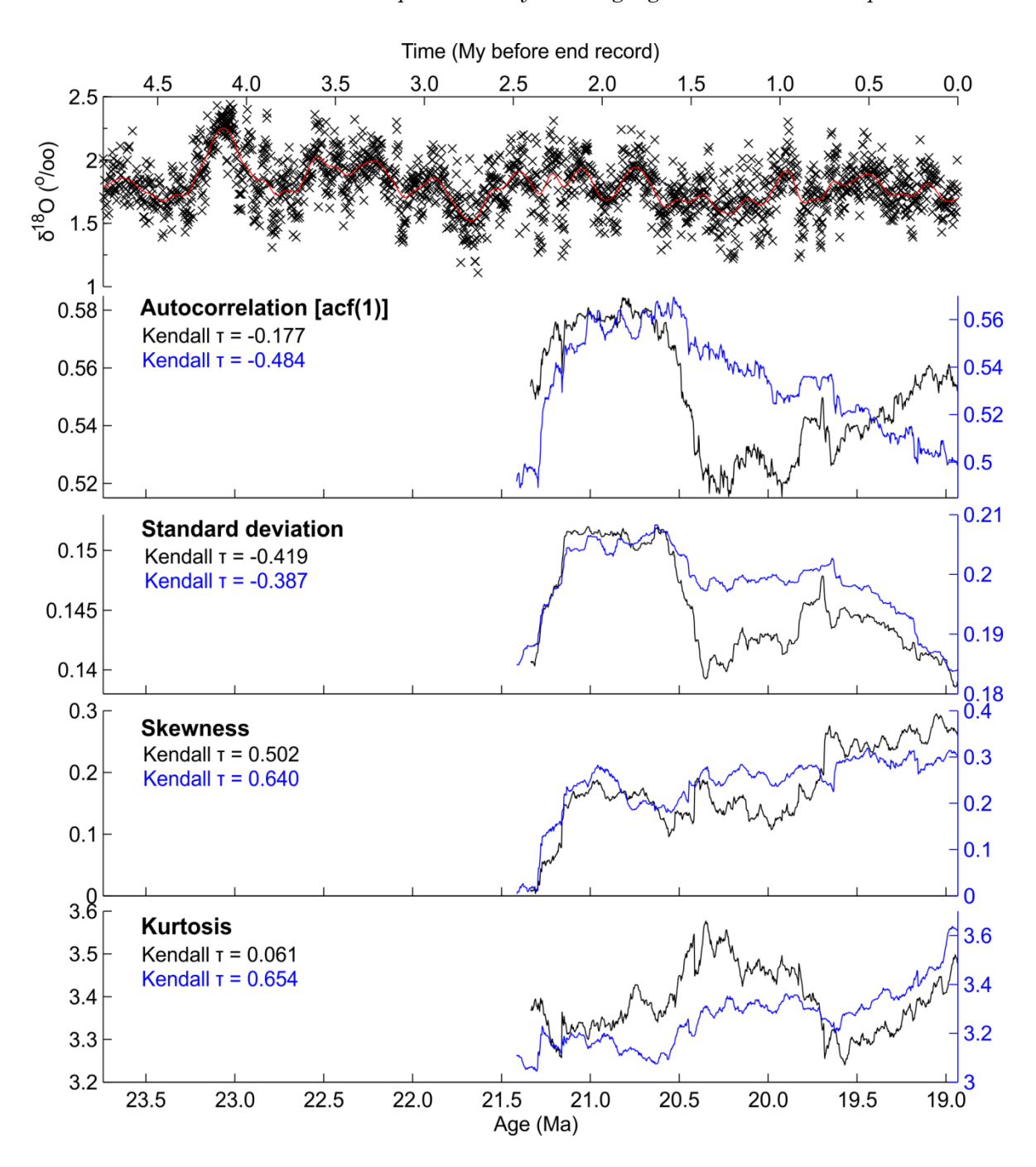


Figure 5-10: EWS analyses of benthic $\delta^{18}O$ from the late Oligocene to the early Miocene. The top panel illustrates the benthic $\delta^{18}O$ palaeorecord (black crosses) and the detrending applied to the data (red line), with the panels below illustrating the results of the analyses for autocorrelation, standard deviation, skewness, and kurtosis calculated across the time-series. Black lines represent the default analysis (linear interpolation, Gaussian detrending with filtering bandwidth 0.1, sliding window 50 %), while the blue lines represent the non-interpolated analysis. The Kendall τ rank-correlation value is given for both analyses in their respective colour.

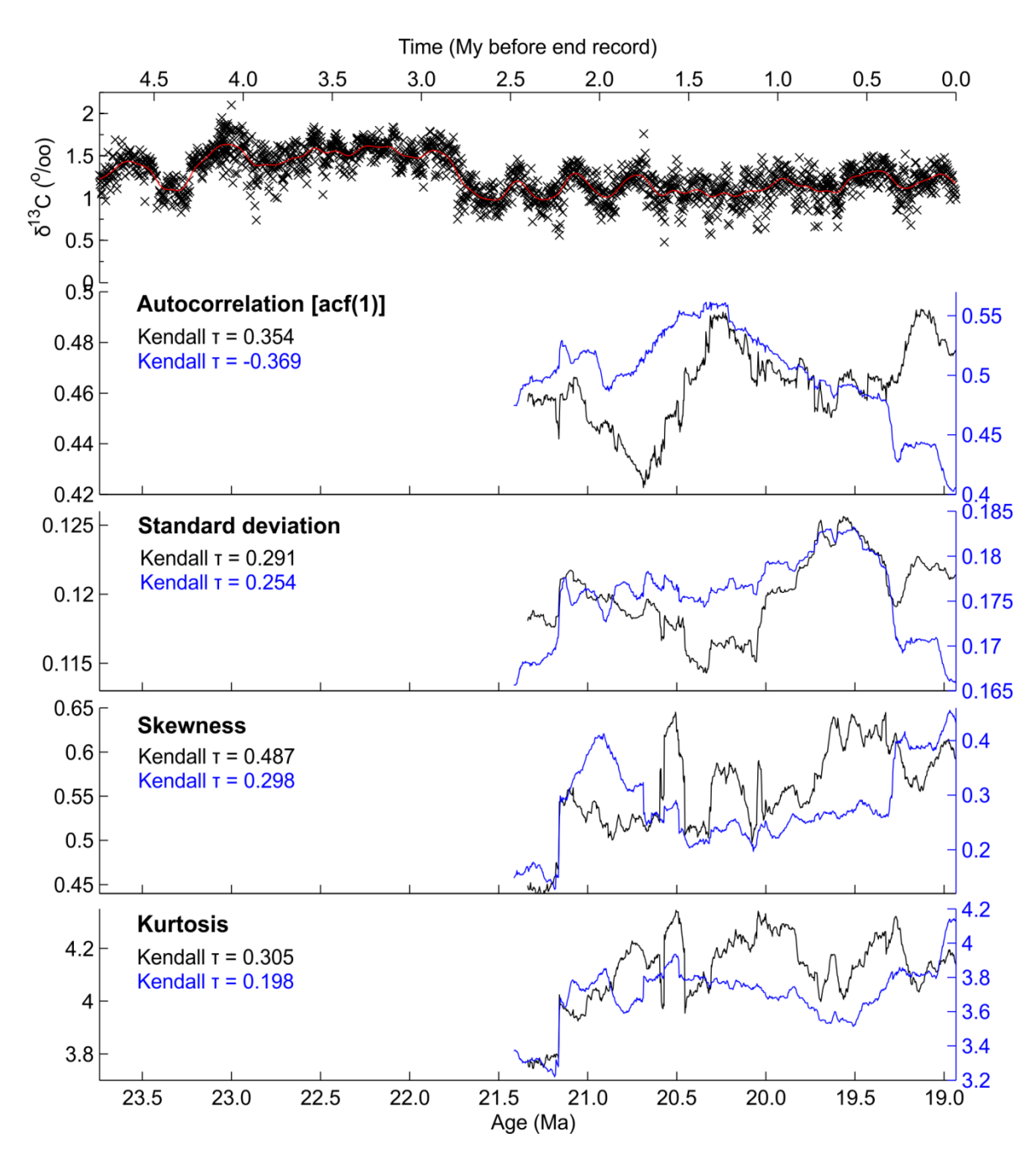


Figure 5-11: EWS analyses of benthic $\delta^{13}C$ from the late Oligocene to the early Miocene. The top panel illustrates the benthic $\delta^{13}C$ palaeorecord (black crosses) and the detrending applied to the data (red line), with the panels below illustrating the results of the analyses for autocorrelation, standard deviation, skewness, and kurtosis calculated across the time-series. Black lines represent the default analysis (linear interpolation, Gaussian detrending with filtering bandwidth 0.1, sliding window 50 %), while the blue lines represent the non-interpolated analysis. The Kendall τ rank-correlation value is given for both analyses in their respective colour.

5.5.6 K/Pg boundary and the Deccan Traps

In the run-up to the K/Pg boundary, which, as with the early Miocene, should in theory not be an example of a critical transition, some interesting trends are nonetheless evident. Although there are some discrepancies before ~66.2 Ma between the different analyses of the benthic $\delta^{18}O$ data, the results consistently suggest a rapid slowing down and increase in variability in the long-term climate system in the last ~200 ky before the K/Pg boundary (Figure 5-12 and Supporting Figure 5-24). This is also partially the case in the benthic δ^{13} C record, excepting rapid drops in skewness and kurtosis in the default and 75 % sliding window analyses which we interpret as potential evidence of geological carbon cycle disruption (Figure 5-13 and Supporting Figure 5-25). Although this would at first appear to suggest that the indices have produced a misleading 'false alarm', the apparent EWS occur rapidly after the commencement of the eruption of the Deccan Traps [Westerhold et al., 2011; Schoene et al., 2015]. As a result, as was postulated in Section 5.3.2.6, we hypothesise that the EWS indices are recording the increasing instability of the slow parts of the climate system and the carbon cycle in response to the Deccan Traps regardless of the impending asteroid impact. If these EWS are confirmed this would in turn be further evidence of the K/Pg impact occurring during a time of an already destabilised Earth system.

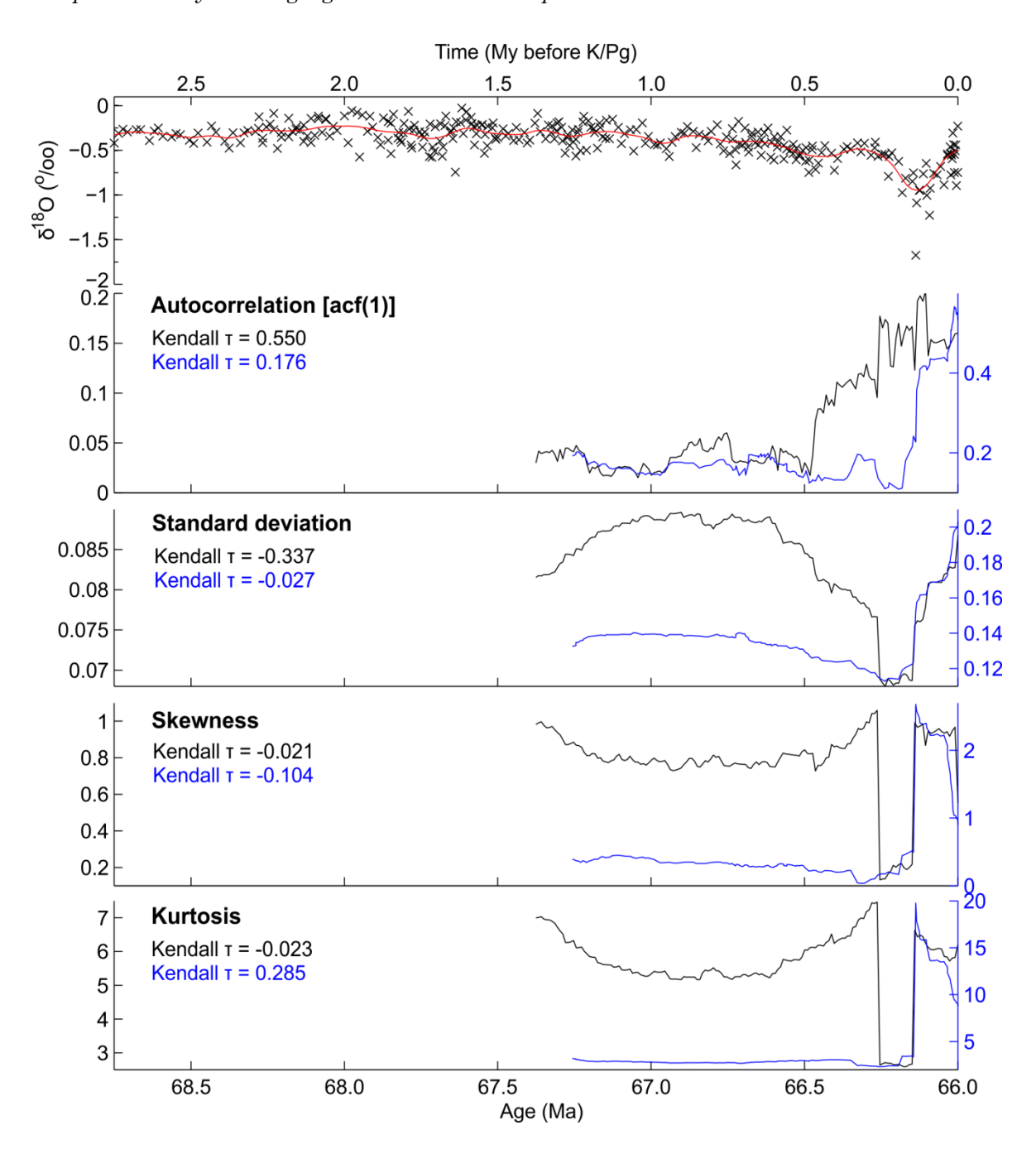


Figure 5-12: EWS analyses of benthic $\delta^{18}O$ in the run-up to the K/Pg boundary. The top panel illustrates the benthic $\delta^{18}O$ palaeorecord (black crosses) and the detrending applied to the data (red line), with the panels below illustrating the results of the analyses for autocorrelation, standard deviation, skewness, and kurtosis calculated across the time-series. Black lines represent the default analysis (linear interpolation, Gaussian detrending with filtering bandwidth 0.1, sliding window 50 %), while the blue lines represent the non-interpolated analysis. The Kendall τ rank-correlation value is given for both analyses in their respective colour.

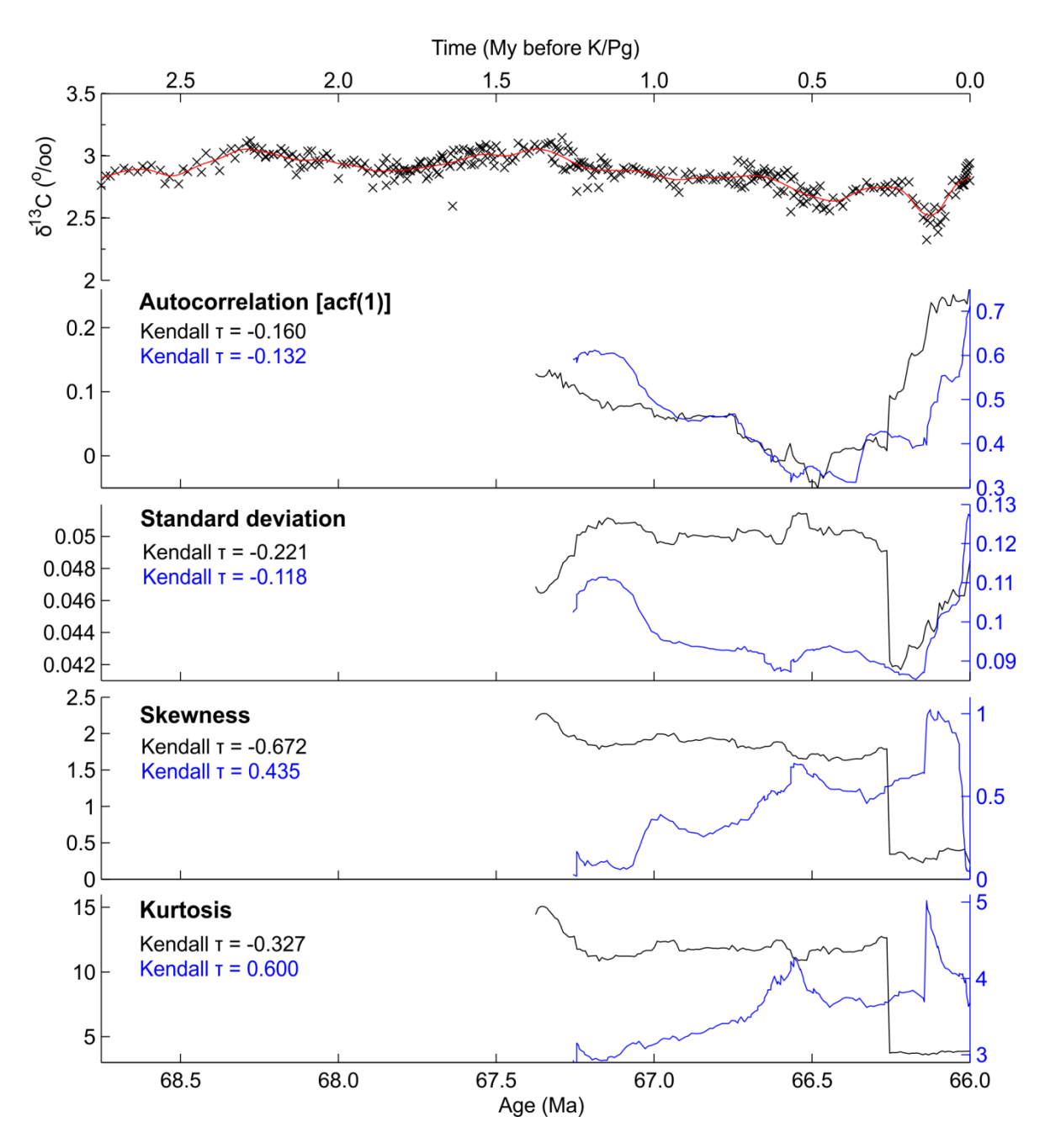


Figure 5-13: EWS analyses of benthic $\delta^{13}C$ in the run-up to the K/Pg boundary. The top panel illustrates the benthic $\delta^{13}C$ palaeorecord (black crosses) and the detrending applied to the data (red line), with the panels below illustrating the results of the analyses for autocorrelation, standard deviation, skewness, and kurtosis calculated across the time-series. Black lines represent the default analysis (linear interpolation, Gaussian detrending with filtering bandwidth 0.1, sliding window 50 %), while the blue lines represent the non-interpolated analysis. The Kendall τ rank-correlation value is given for both analyses in their respective colour.

5.5.7 Sensitivity to parameter selection

By varying the sliding window length and removing interpolation we can investigate the impact of these parameter choices on our results. Although in many cases both the interpolated and non-interpolated analyses give broadly similar results (e.g. EOT δ^{18} O, PETM δ^{13} C, MCT δ^{18} O, OMT), in other cases moderately to very different results arise (e.g. EOT δ^{13} C, PETM δ^{18} O, MCT δ^{13} C, K/Pg, early Miocene) when interpolation is removed from the pre-processing procedure. Although all of the original datasets have non-equidistant data (as is inevitable for palaeorecords), none of the datasets have a distribution of data-point time intervals consistently biased to increase or decrease significantly in the latter part of the record (Supporting Figures 5-26 to 5-31). Several of the datasets produce similar outputs for both interpolated and non-interpolated analyses on one variable (e.g. EOT δ^{18} O), but at the same time produce very different results with and without interpolation for the other variable (e.g. EOT δ^{13} C). This difference cannot be due to a change in data-point spacing, as we would expect similar artefacts to appear in both $\delta^{18}O$ and $\delta^{13}C$ analyses with both datasets sharing the same time-points, indicating that some other feature in the data must cause these artefacts. The sometimes considerable differences caused by interpolation in our results supports the methodology of repeating EWS analysis both with and without interpolation in order to allow consistent features in the results to be identified and focused on.

As expected, varying the sliding window length of the analysis also makes a large difference to the results, with larger sliding windows emphasising smaller changes in the indices over a longer period and shorter sliding windows emphasising stronger trends close to the end of the record. For shorter records a larger window size is more reliable as more data-points are captured in the analysis, while longer records allow a shorter window to be used without losing as much reliability. This would suggest that for the shorter palaeorecords used in this study (i.e. the EOT and OMT) the 75 % sliding window analysis is the more reliable sensitivity test for comparison to the default analysis, while the 25 % sliding window can provide relatively reliable insights for the longer palaeorecords (i.e. the PETM, MMCT, early Miocene, and K/Pg). In many cases the general trends in the 25 % and 75 % sliding window analyses correlate with trends observed in the default 50 % sliding window analysis (e.g. EOT, K/Pg), but sometimes changing the sliding window length can produce trends very different to that observed in the default analysis (e.g. PETM δ^{18} O, early Miocene). This illustrates the sensitivity of EWS analysis to subjective parameter choices such as sliding window size, and although in many cases the default 50 %

sliding window appears to be a relatively robust choice, in other cases it is difficult to be as confident in the results. This finding strongly supports the approach of varying sliding window size when conducting EWS analysis on palaeorecords.

5.5.8 Is early warning signal analysis reliable for the palaeorecord?

Environmental records based on geological data are of significantly lower quality than those based on present-day instrumental data, and as such present a greater challenge for EWS analysis. The inconsistent data-point spacing and core gaps endemic to palaeorecords are problematic when using statistical techniques that assume equidistant data-points, but, as described in Section 5.4.1, interpolating the data to account for this problem may result in statistical artefacts being introduced to the results. As described in Section 5.5.7, our results are also somewhat sensitive to the choice of sliding window length in the analysis. Age model uncertainty and sedimentary diagenesis also limits the extent to which we can trust the reliability of the palaeorecords themselves and thus the results of EWS analyses performed on them. In the absence of robust and extensively tried-and-tested procedures, the risk of committing the 'prosecutor's fallacy' [Boettiger and Hastings, 2012] remains high when analysing palaeorecords.

Despite these problems, analysing palaeorecords for EWS still has merits. Although an increase in just one EWS index is not a sufficient or reliable indicator of increasing instability or an impending critical transition in the palaeorecord, finding indicators in multiple different indices helps to ensure our conclusions are more robust. Many of our analyses detected consistent increases in multiple EWS indices prior to a climate shift, while our analysis of the 'quiet' early Miocene, where no critical transition is known, showed no consistent pattern in the EWS indicators. Although EWS were unexpectedly detected prior to the K/Pg boundary, the implied increase in instability occurs simultaneously with the commencement of the Deccan Traps eruptions and as a result has a viable explanation. Repeating our analyses without interpolation and with different sliding window lengths also helped to reveal the extent to which the observed trends are sensitive to parameter and methodology choices, and makes it clear that for some events there are consistent EWS indicators across all of the different analyses. However, to further increase confidence in these conclusions, more advanced EWS analysis techniques would be required in order to rule out the possibility of 'false positives' and to differentiate between increasing instability with and without a subsequent critical transition. Higher resolution

palaeorecords would also enable EWS generated by faster processes within the carbon-climate system, which are currently 'missed alarms', to be detected.

5.6 Conclusions

In this study we analyse Cenozoic palaeorecords prior to several perturbations to the carbon-climate system in order to search for evidence of pre-critical transition early warning signals, and find that indications of growing instability in the longterm carbon-climate system can be detected prior to some but not all of these events. Our analyses suggest increasing long-term climate instability and a disruption to the geological carbon cycle in the run-up to the Eocene-Oligocene Transition, and signs of instability in both the slow parts of the climate system and the carbon cycle prior to the Palaeocene-Eocene Thermal Maximum. However, instability appears to peak at least ~500 ky before the ~13.9 Ma shift of the mid-Miocene Climate Transition, and there is limited evidence of instability prior to the Oligocene-Miocene Transition. No consistent evidence of early warning signals are found during the 'null' case of the early Miocene, but increasing instability is detected prior to the exogenic K/Pg event, a discrepancy we ascribe to the preceding eruption of the Deccan Traps. However, some results are more sensitive to analysis choices such as interpolation and sliding window length than others, and the technique used remains susceptible to false positives. Analysis of the EOT and OMT is also limited by short palaeorecords, while the resolution of the palaeorecords currently available for all of the events prevents early warning signals driven by shorter-term processes from being detected. As a result, further analysis using more advanced techniques and improved datasets as they become available is required in order to confirm these results.

5.7 Acknowledgements

This work was supported by a Natural Environment Research Council studentship to D.I.A.M. (NERC grant number: NE/J500112/1). We thank James Dyke and Tim Lenton for constructive discussions on the study methodology.

5.8 Supporting Information

5.8.1 Sliding window sensitivity analyses

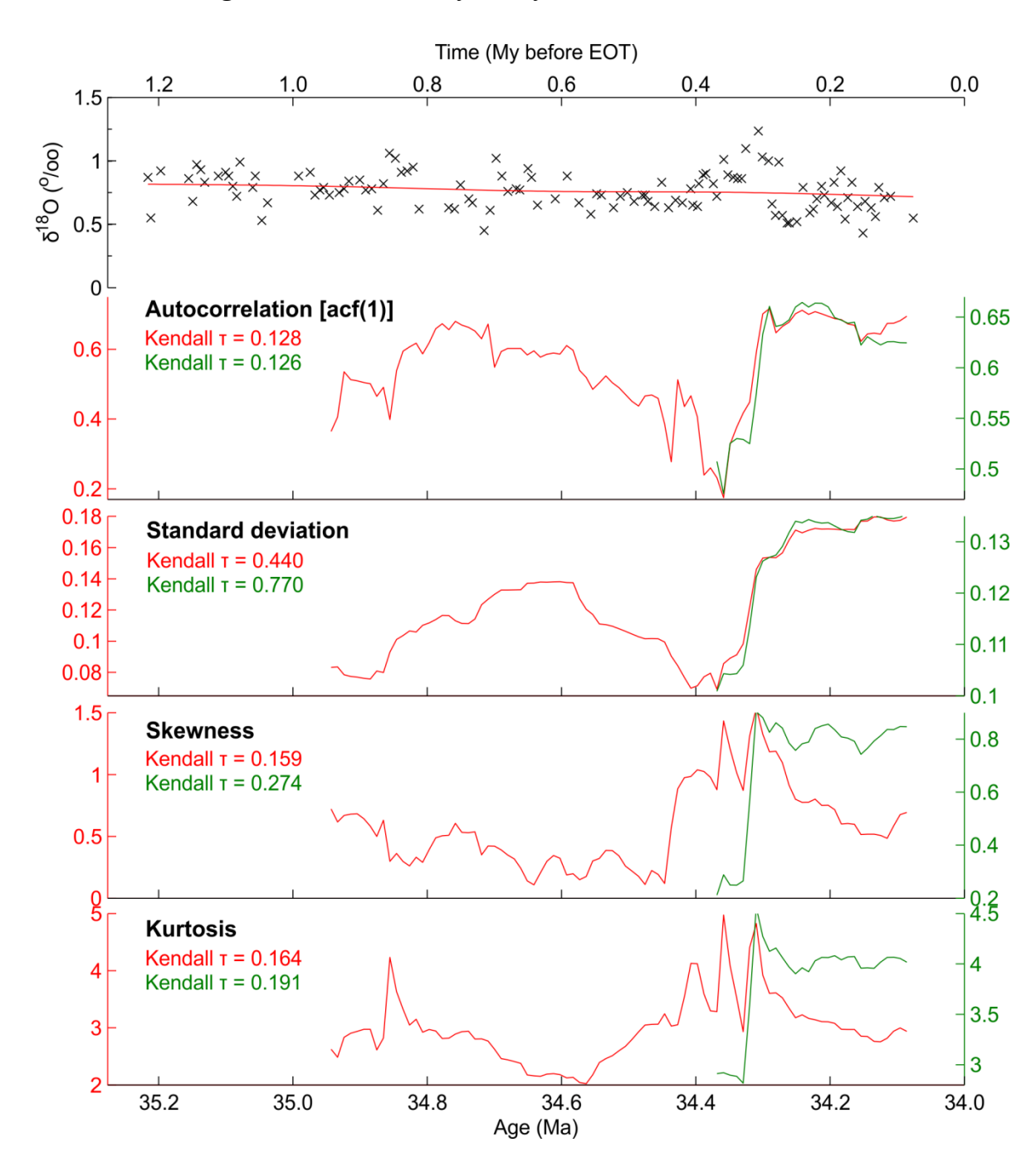


Figure 5-14: EWS analyses of benthic $\delta^{18}O$ in the run-up to the Eocene-Oligocene Transition (EOT). The top panel illustrates the benthic $\delta^{18}O$ palaeorecord (black crosses) and the detrending applied to the data (red line), with the panels below illustrating the results of the analyses for autocorrelation, standard deviation, skewness, and kurtosis calculated across the time-series. Red lines represent the analysis with a sliding window of 25 %, while the green lines represent the analysis with a sliding window of 75 %. The Kendall τ rank-correlation value is given for both analyses in their respective colour.

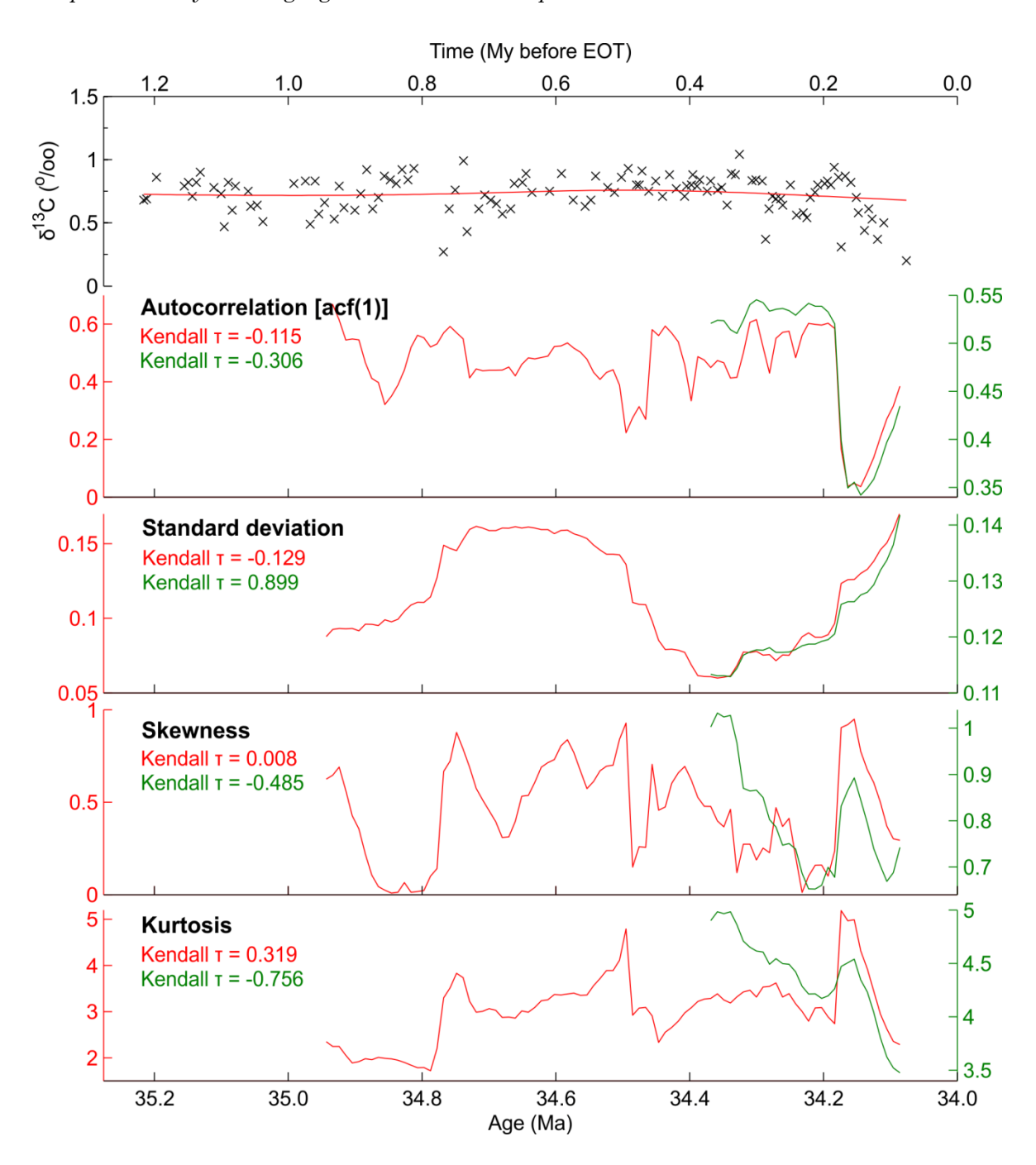


Figure 5-15: EWS analyses of benthic $\delta^{13}C$ in the run-up to the Eocene-Oligocene Transition (EOT). The top panel illustrates the benthic $\delta^{13}C$ palaeorecord (black crosses) and the detrending applied to the data (red line), with the panels below illustrating the results of the analyses for autocorrelation, standard deviation, skewness, and kurtosis calculated across the time-series. Red lines represent the analysis with a sliding window of 25 %, while the green lines represent the analysis with a sliding window of 75 %. The Kendall τ rank-correlation value is given for both analyses in their respective colour.

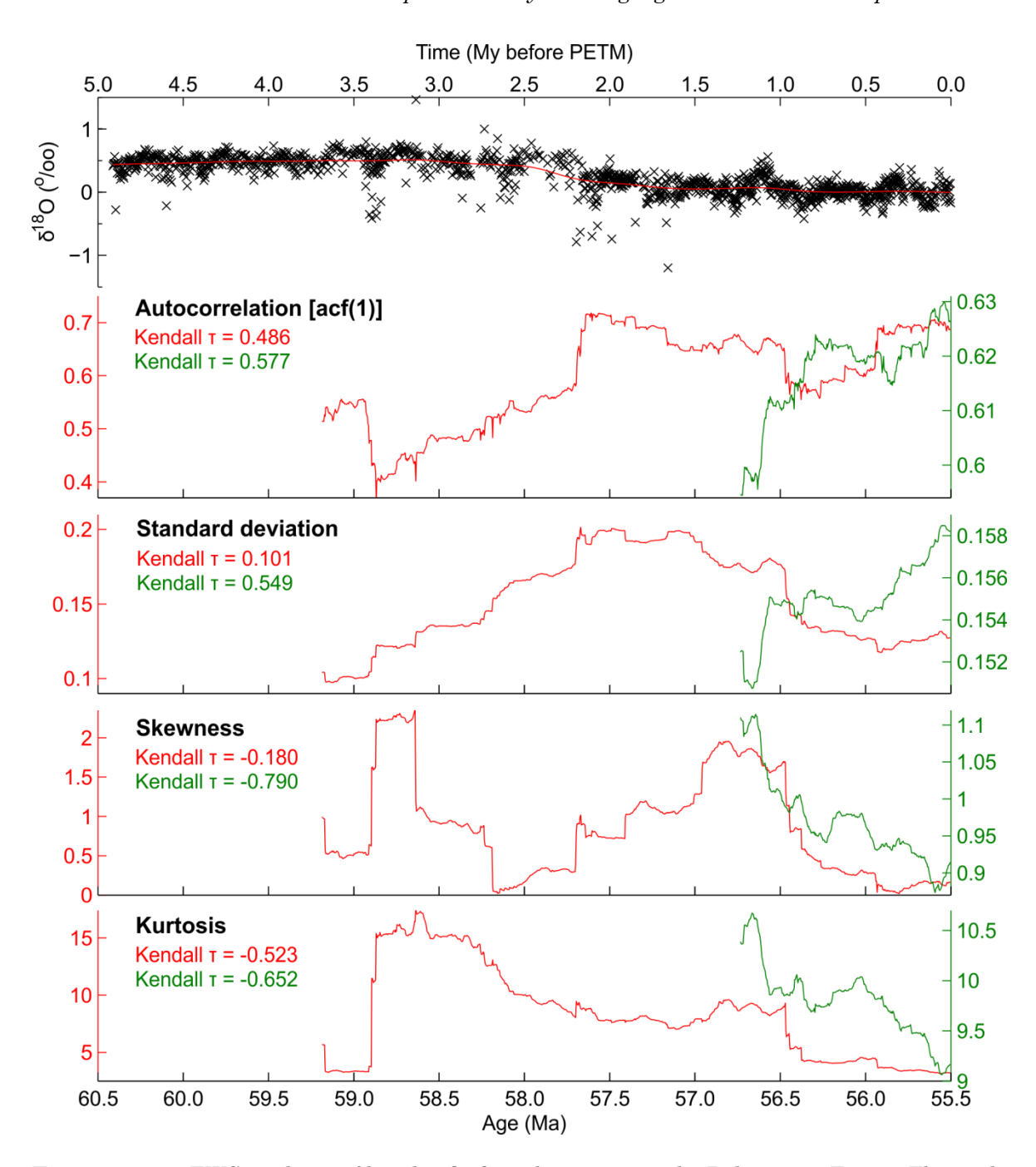


Figure 5-16: EWS analyses of benthic $\delta^{18}O$ in the run-up to the Palaeocene-Eocene Thermal Maximum (PETM). The top panel illustrates the benthic $\delta^{18}O$ palaeorecord (black crosses) and the detrending applied to the data (red line), with the panels below illustrating the results of the analyses for autocorrelation, standard deviation, skewness, and kurtosis calculated across the time-series. Red lines represent the analysis with a sliding window of 25 %, while the green lines represent the analysis with a sliding window of 75 %. The Kendall τ rank-correlation value is given for both analyses in their respective colour.

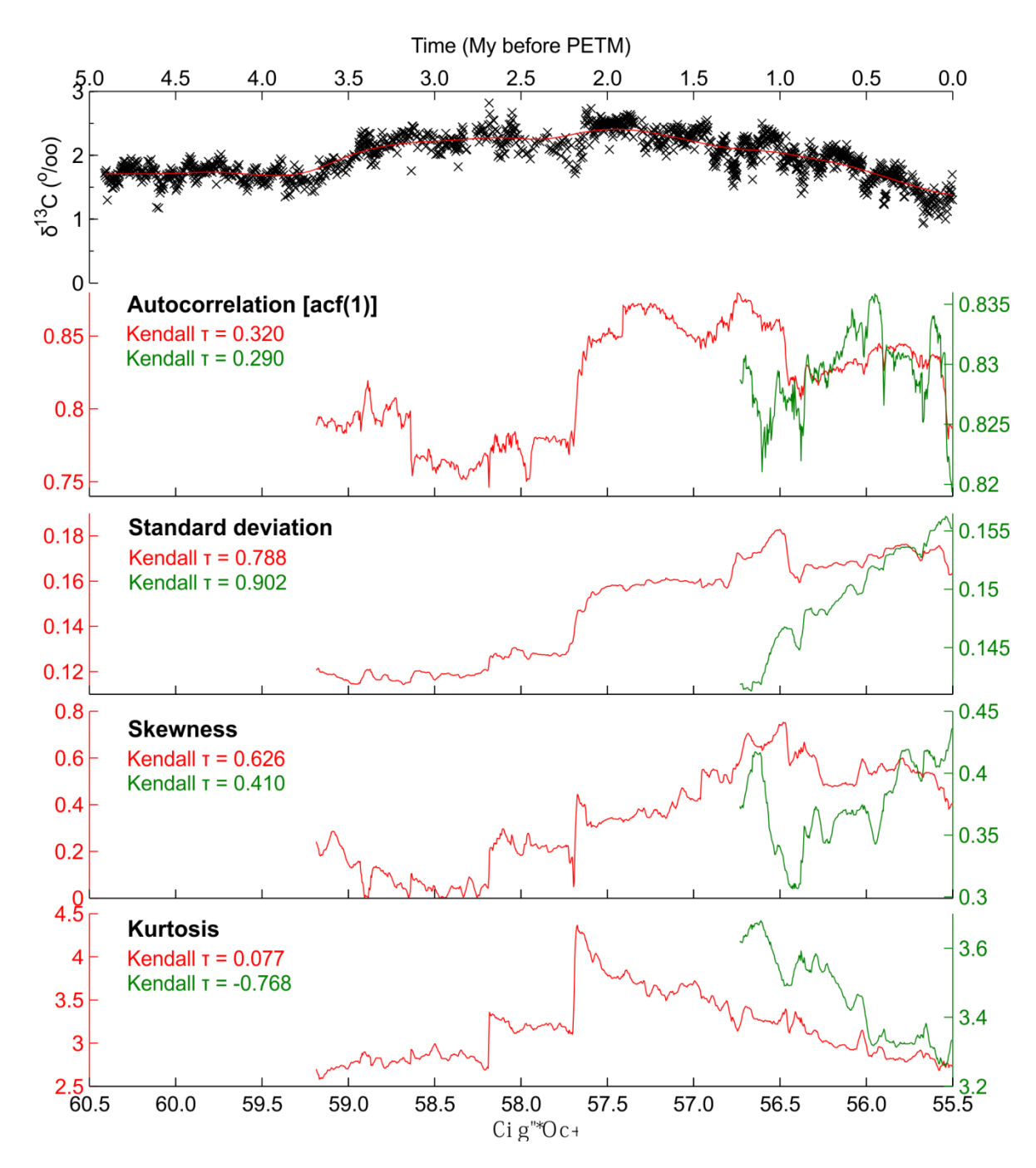


Figure 5-17: EWS analyses of benthic $\delta^{13}C$ in the run-up to the Palaeocene-Eocene Thermal Maximum (PETM). The top panel illustrates the benthic $\delta^{13}C$ palaeorecord (black crosses) and the detrending applied to the data (red line), with the panels below illustrating the results of the analyses for autocorrelation, standard deviation, skewness, and kurtosis calculated across the time-series. Red lines represent the analysis with a sliding window of 25 %, while the green lines represent the analysis with a sliding window of 75 %. The Kendall τ rank-correlation value is given for both analyses in their respective colour.

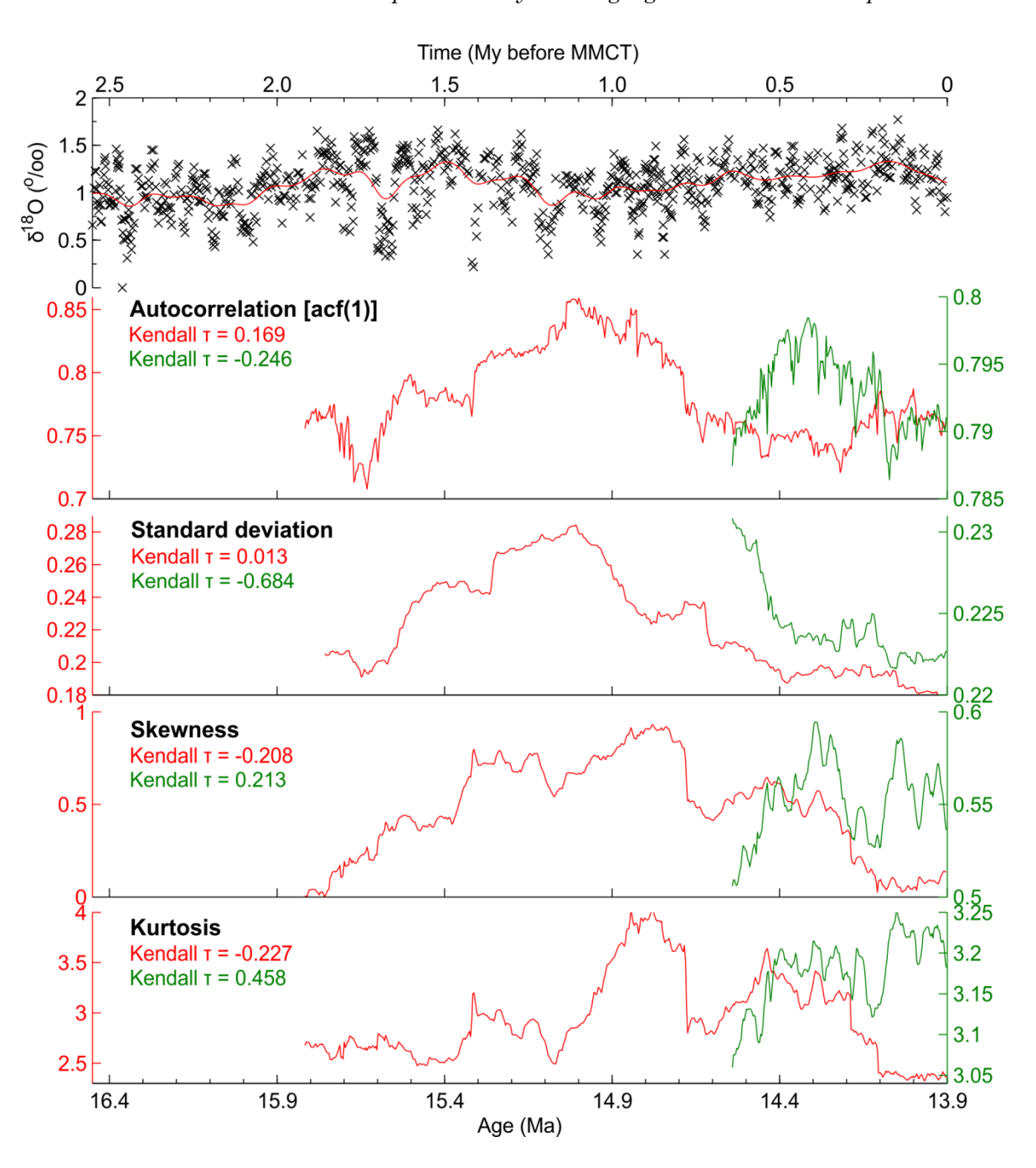


Figure 5-18: EWS analyses of benthic $\delta^{18}O$ in the run-up to the mid-Miocene Climate Transition (MMCT). The top panel illustrates the benthic $\delta^{18}O$ palaeorecord (black crosses) and the detrending applied to the data (red line), with the panels below illustrating the results of the analyses for autocorrelation, standard deviation, skewness, and kurtosis calculated across the time-series. Red lines represent the analysis with a sliding window of 25 %, while the green lines represent the analysis with a sliding window of 75 %. The Kendall τ rank-correlation value is given for both analyses in their respective colour.

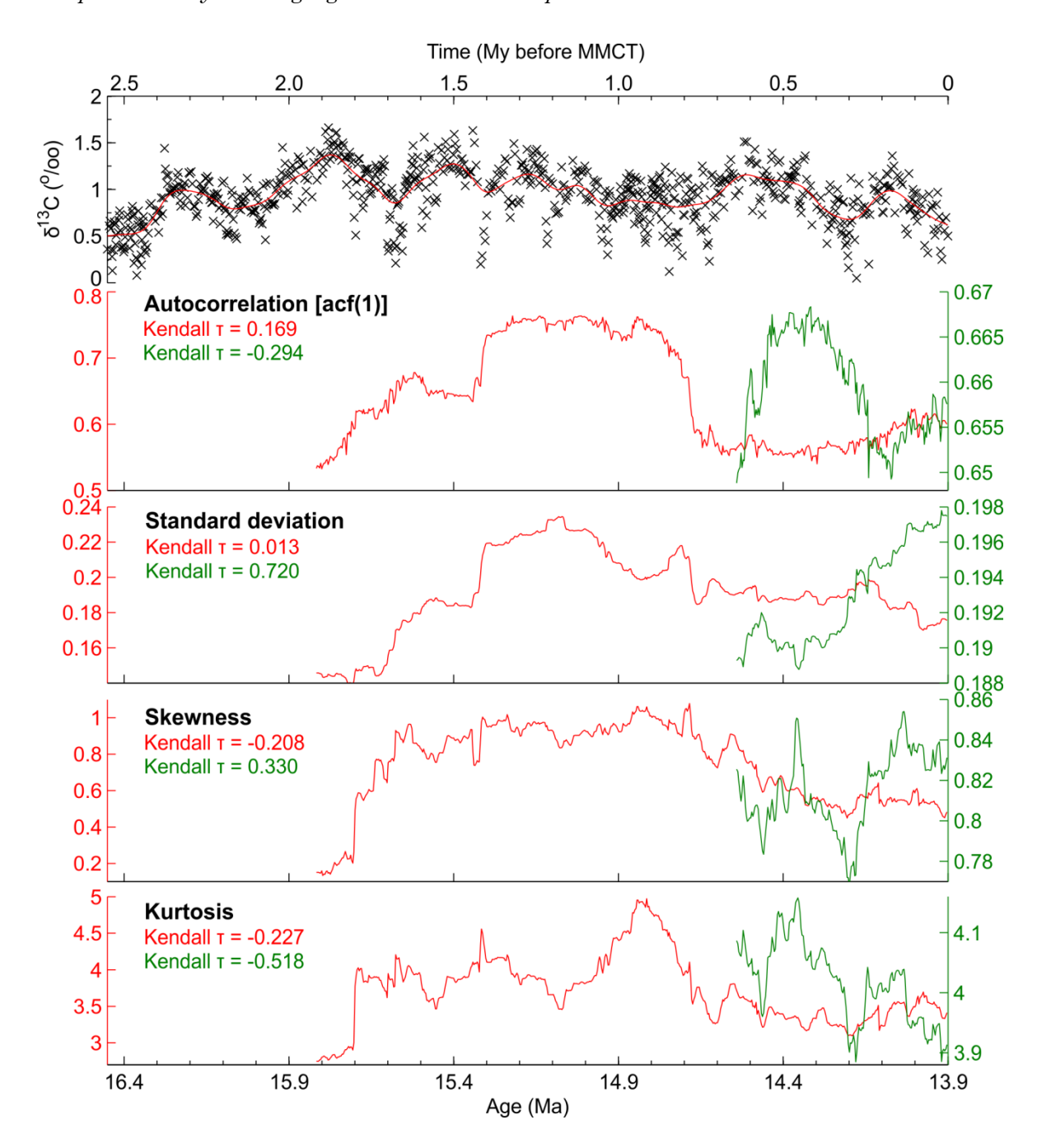


Figure 5-19: EWS analyses of benthic $\delta^{13}C$ in the run-up to the mid-Miocene Climate Transition (MMCT). The top panel illustrates the benthic $\delta^{13}C$ palaeorecord (black crosses) and the detrending applied to the data (red line), with the panels below illustrating the results of the analyses for autocorrelation, standard deviation, skewness, and kurtosis calculated across the time-series. Red lines represent the analysis with a sliding window of 25 %, while the green lines represent the analysis with a sliding window of 75 %. The Kendall τ rank-correlation value is given for both analyses in their respective colour.

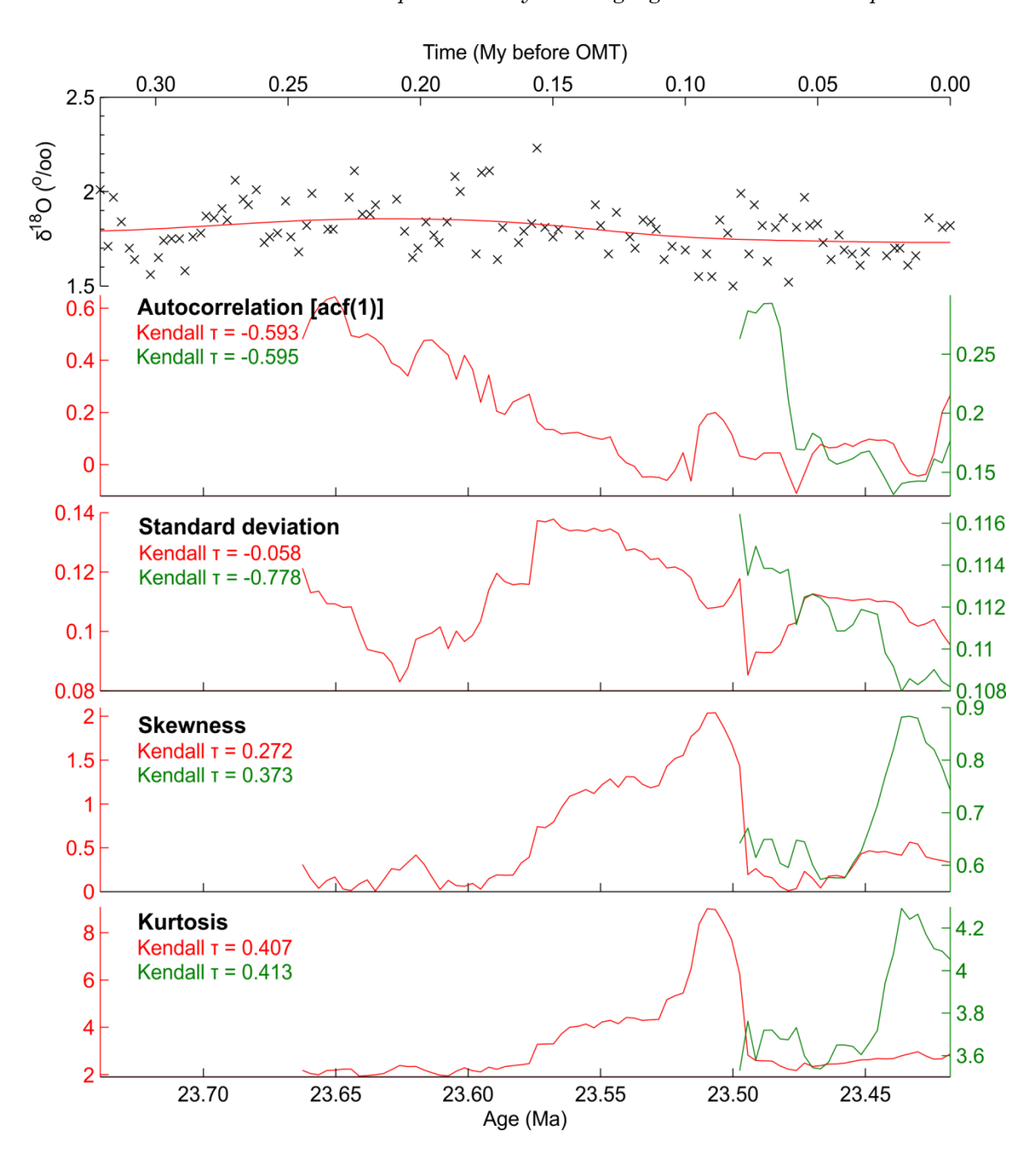


Figure 5-20: EWS analyses of benthic $\delta^{18}O$ in the run-up to the Oligocene-Miocene Transition (OMT). The top panel illustrates the benthic $\delta^{18}O$ palaeorecord (black crosses) and the detrending applied to the data (red line), with the panels below illustrating the results of the analyses for autocorrelation, standard deviation, skewness, and kurtosis calculated across the time-series. Red lines represent the analysis with a sliding window of 25 %, while the green lines represent the analysis with a sliding window of 75 %. The Kendall τ rank-correlation value is given for both analyses in their respective colour.

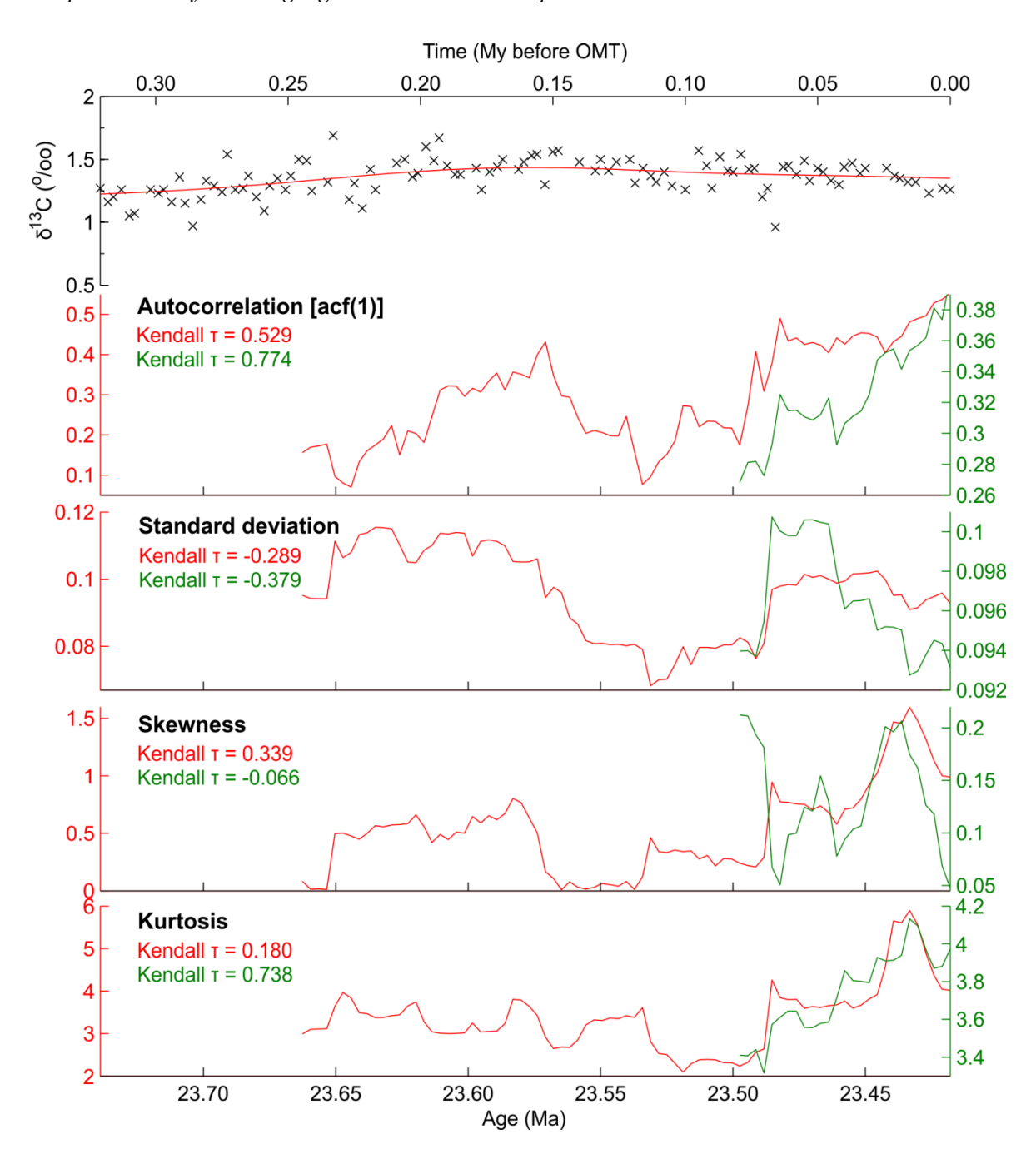


Figure 5-21: EWS analyses of benthic $\delta^{13}C$ in the run-up to the Oligocene-Miocene Transition (OMT). The top panel illustrates the benthic $\delta^{13}C$ palaeorecord (black crosses) and the detrending applied to the data (red line), with the panels below illustrating the results of the analyses for autocorrelation, standard deviation, skewness, and kurtosis calculated across the time-series. Red lines represent the analysis with a sliding window of 25 %, while the green lines represent the analysis with a sliding window of 75 %. The Kendall τ rank-correlation value is given for both analyses in their respective colour.

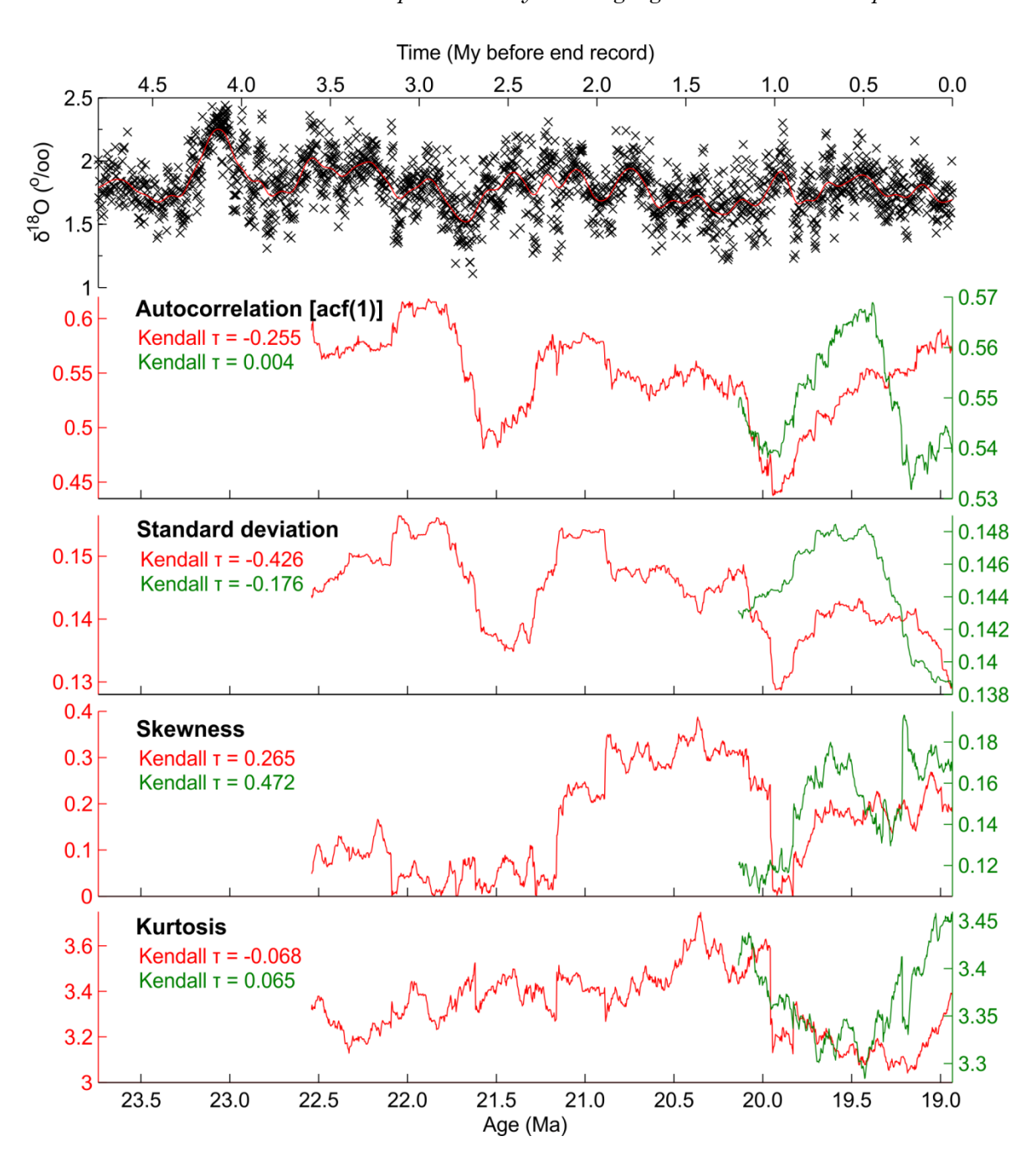


Figure 5-22: EWS analyses of benthic $\delta^{18}O$ from the late Oligocene to the early Miocene. The top panel illustrates the benthic $\delta^{18}O$ palaeorecord (black crosses) and the detrending applied to the data (red line), with the panels below illustrating the results of the analyses for autocorrelation, standard deviation, skewness, and kurtosis calculated across the time-series. Red lines represent the analysis with a sliding window of 25 %, while the green lines represent the analysis with a sliding window of 75 %. The Kendall τ rank-correlation value is given for both analyses in their respective colour.

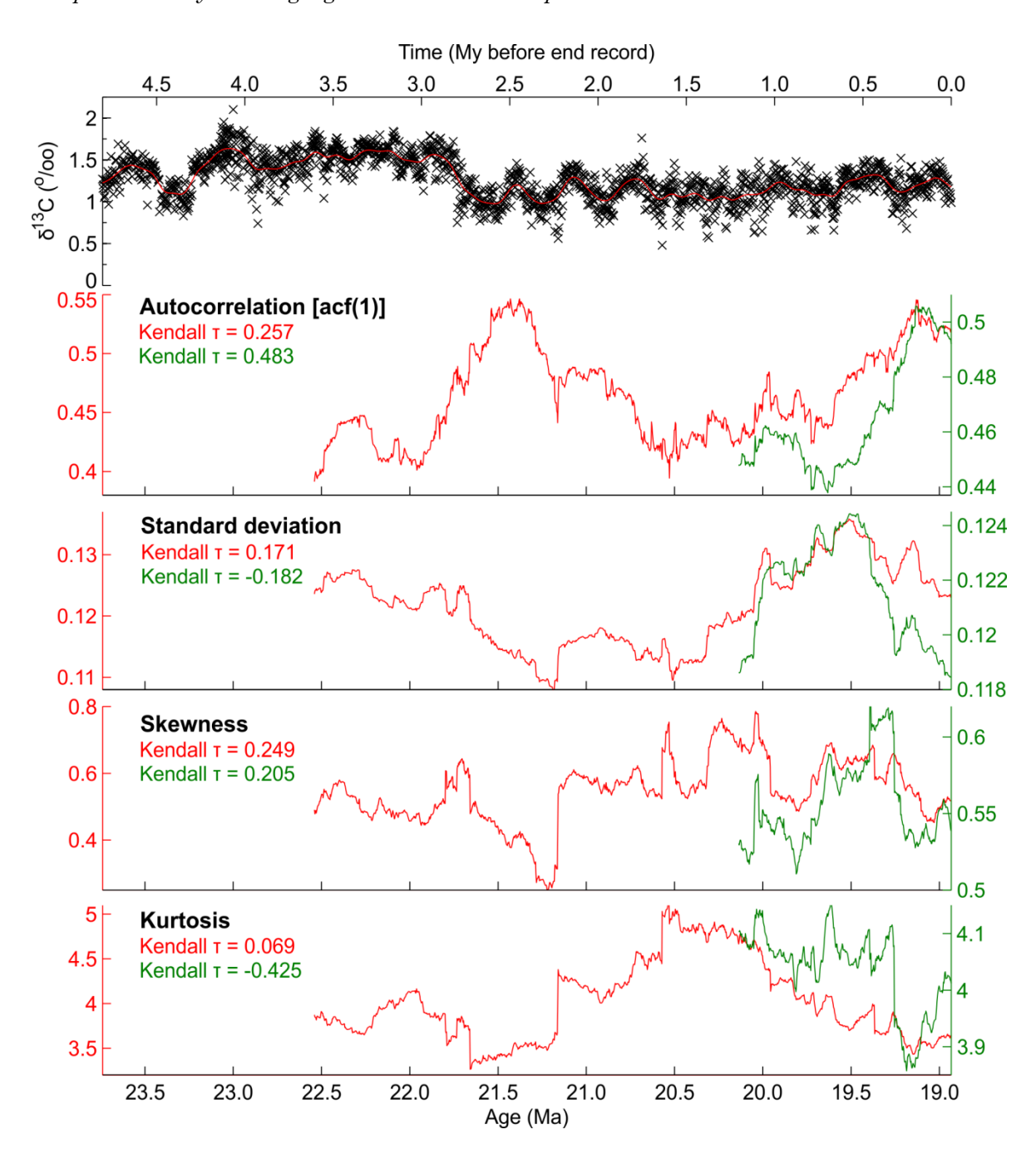


Figure 5-23: EWS analyses of benthic $\delta^{13}C$ from the late Oligocene to the early Miocene. The top panel illustrates the benthic $\delta^{13}C$ palaeorecord (black crosses) and the detrending applied to the data (red line), with the panels below illustrating the results of the analyses for autocorrelation, standard deviation, skewness, and kurtosis calculated across the time-series. Red lines represent the analysis with a sliding window of 25 %, while the green lines represent the analysis with a sliding window of 75 %. The Kendall τ rank-correlation value is given for both analyses in their respective colour.

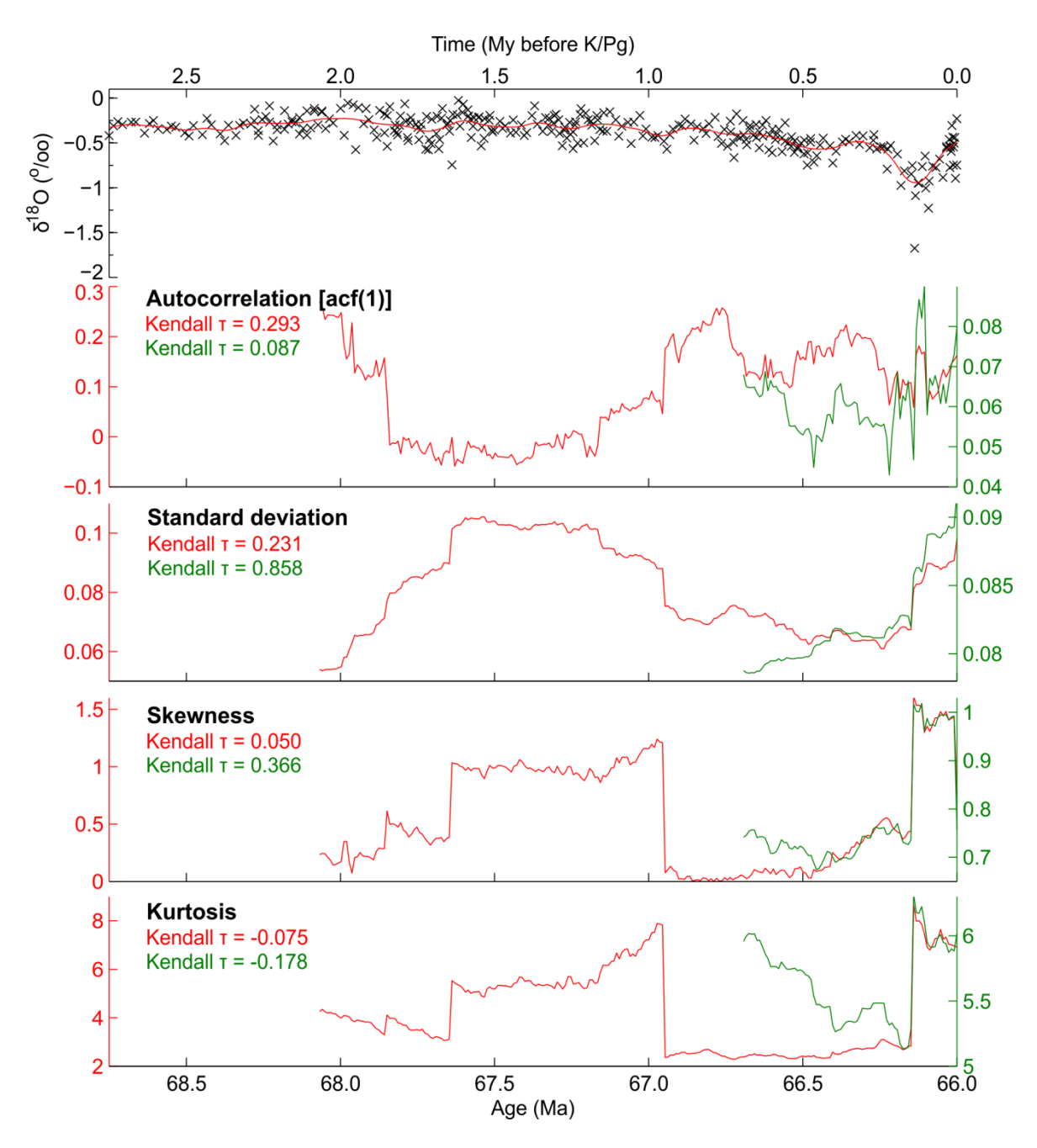


Figure 5-24: EWS analyses of benthic $\delta^{18}O$ in the run-up to the K/Pg boundary. The top panel illustrates the benthic $\delta^{18}O$ palaeorecord (black crosses) and the detrending applied to the data (red line), with the panels below illustrating the results of the analyses for autocorrelation, standard deviation, skewness, and kurtosis calculated across the time-series. Red lines represent the analysis with a sliding window of 25 %, while the green lines represent the analysis with a sliding window of 75 %. The Kendall τ rank-correlation value is given for both analyses in their respective colour.

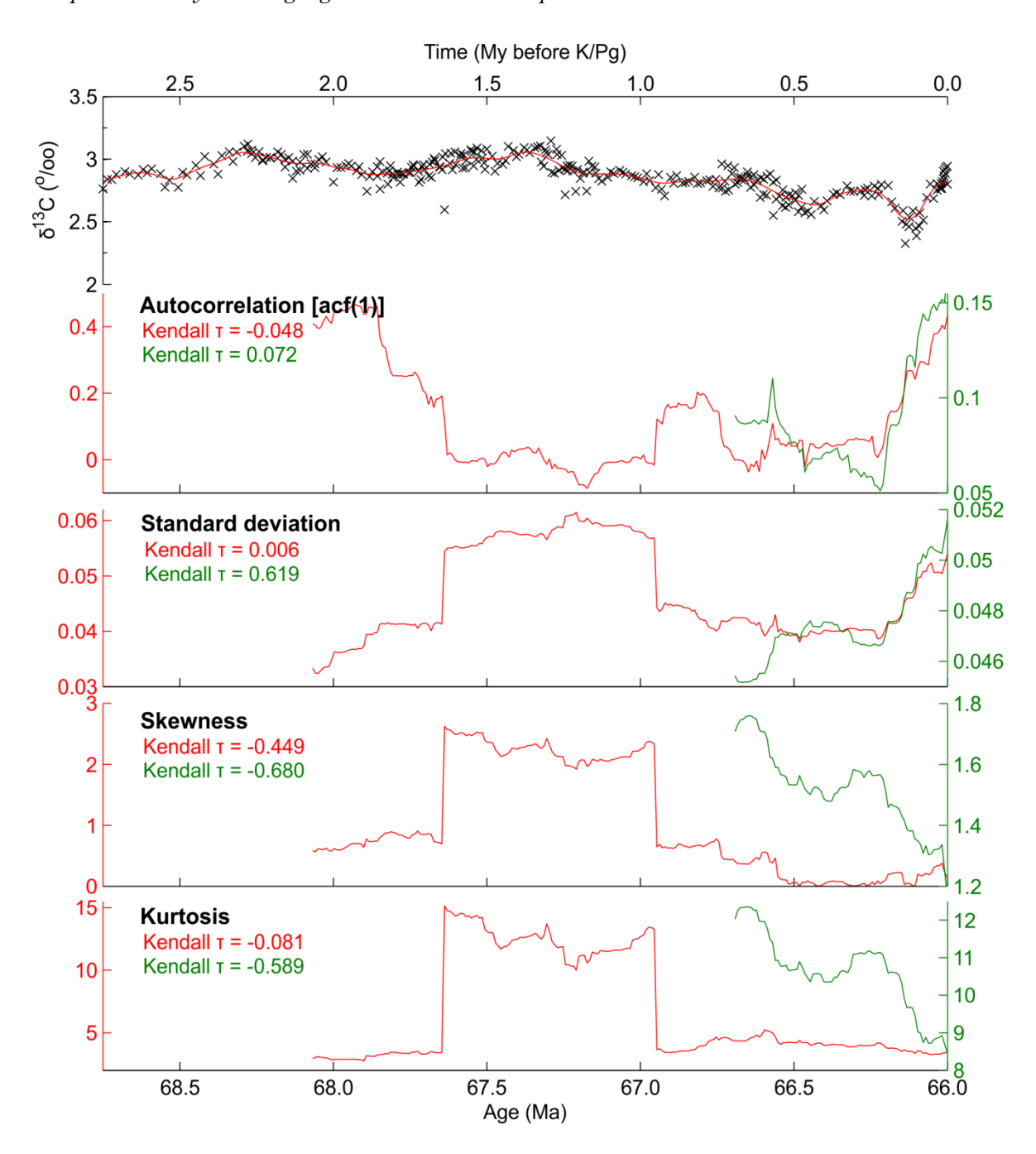


Figure 5-25: EWS analyses of benthic $\delta^{13}C$ in the run-up to the K/Pg boundary. The top panel illustrates the benthic $\delta^{13}C$ palaeorecord (black crosses) and the detrending applied to the data (red line), with the panels below illustrating the results of the analyses for autocorrelation, standard deviation, skewness, and kurtosis calculated across the time-series. Red lines represent the analysis with a sliding window of 25 %, while the green lines represent the analysis with a sliding window of 75 %. The Kendall τ rank-correlation value is given for both analyses in their respective colour.

5.8.2 Data-point spacing

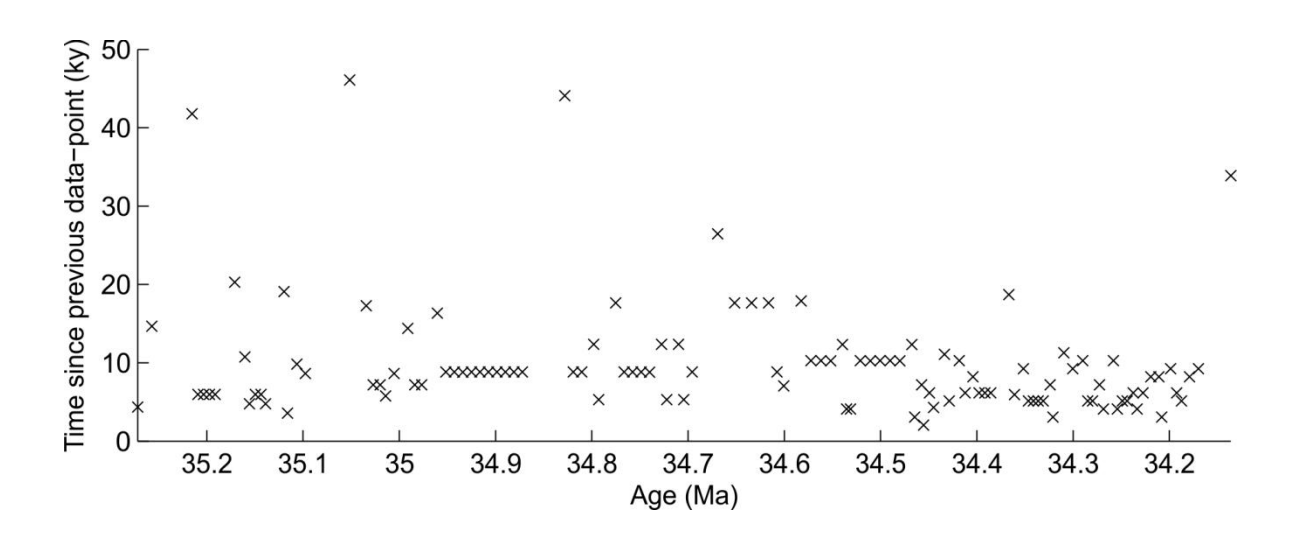


Figure 5-26: Time since the previous data-point plotted for each data-point, illustrating the variable spacing of the data-points for the isotope records prior to the Eocene-Oligocene Transition (EOT).

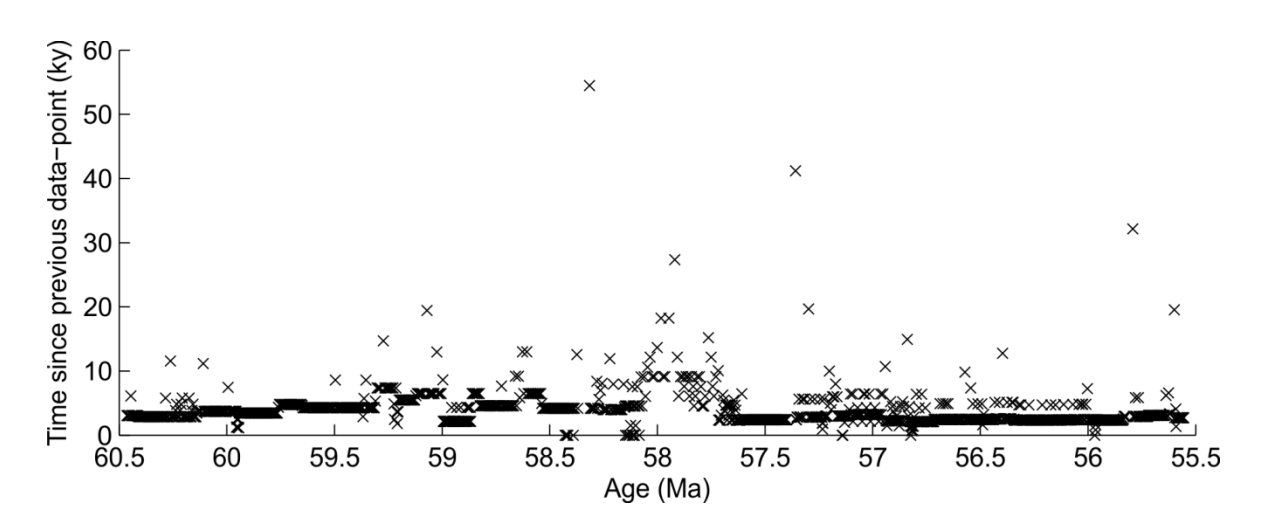


Figure 5-27: Time since the previous data-point plotted for each data-point, illustrating the variable spacing of the data-points for the isotope records prior to the Palaeocene-Eocene Thermal Maximum (PETM).

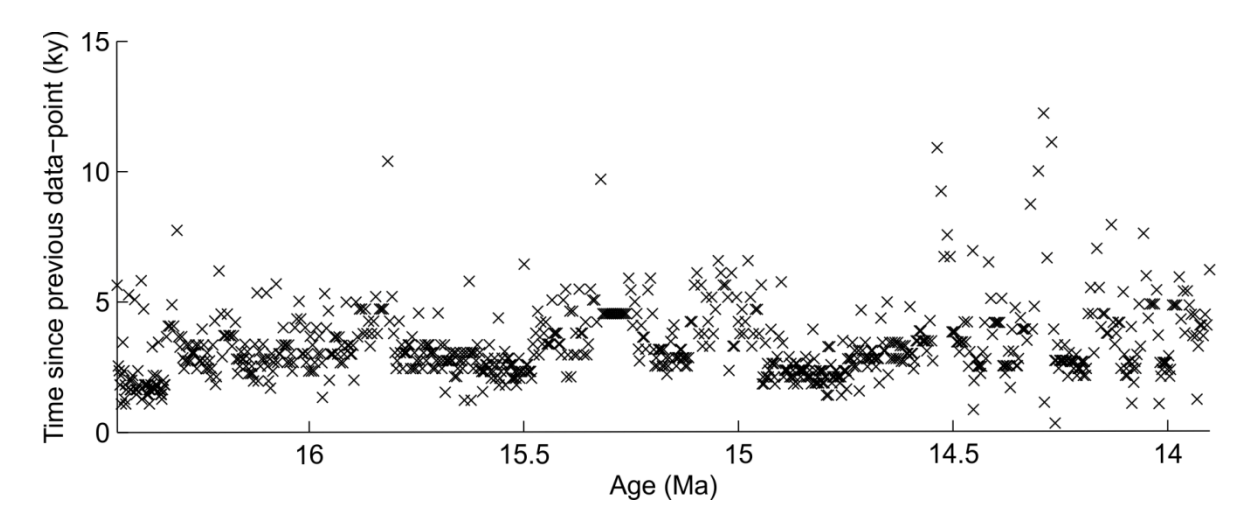


Figure 5-28: Time since the previous data-point plotted for each data-point, illustrating the variable spacing of the data-points for the isotope records prior to the mid-Miocene Climate Transition (MMCT).

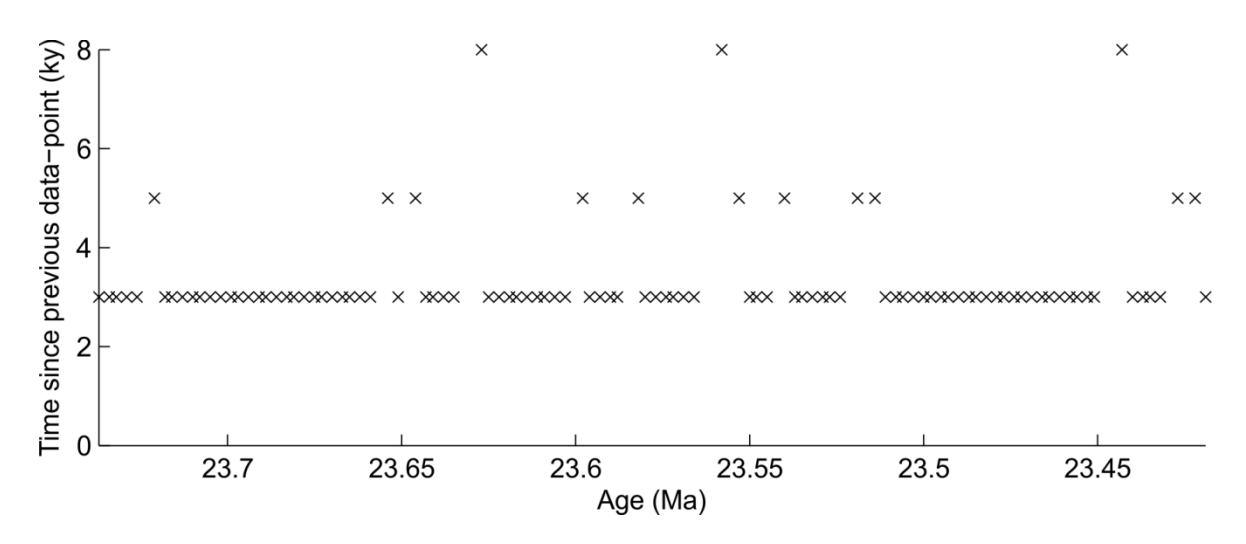


Figure 5-29: Time since the previous data-point plotted for each data-point, illustrating the variable spacing of the data-points for the isotope records prior to the Oligocene-Miocene Transition (OMT)

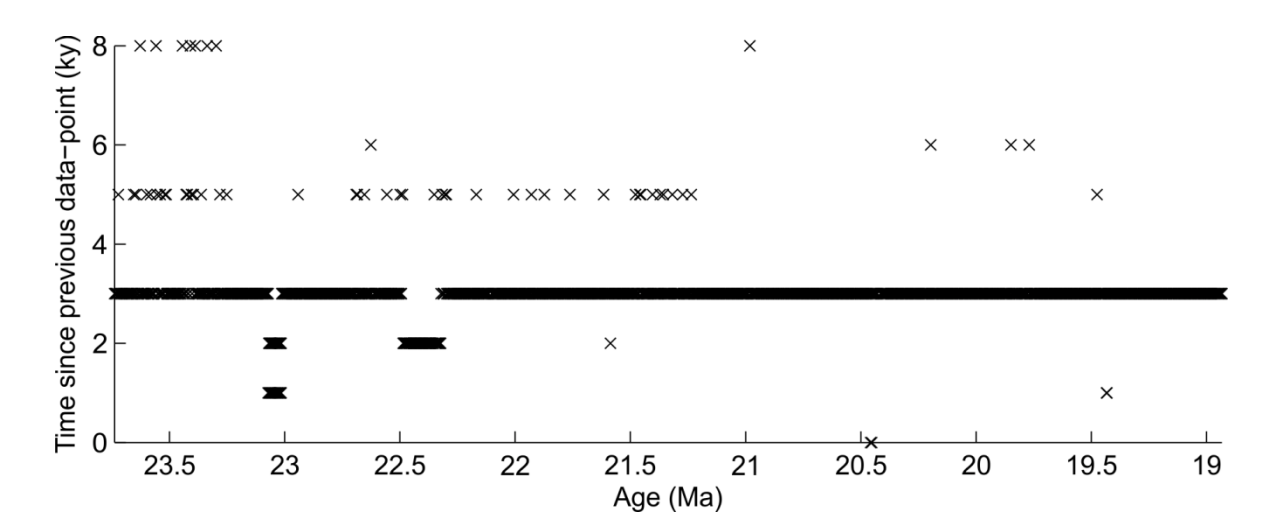


Figure 5-30: Time since the previous data-point plotted for each data-point, illustrating the variable spacing of the data-points for the isotope records during the late Oligocene and early Miocene.

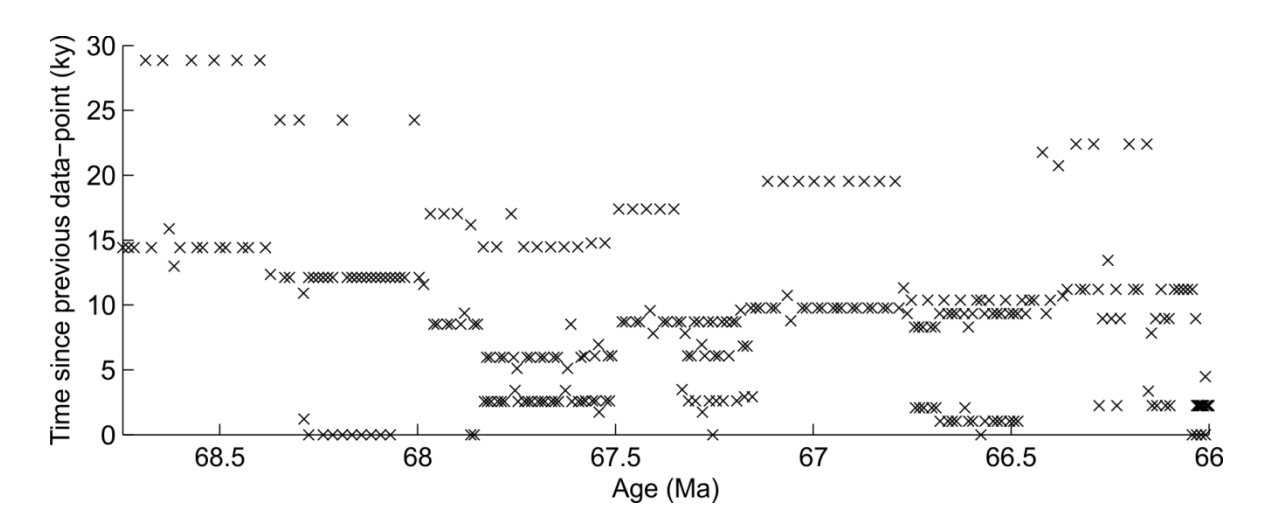


Figure 5-31: Time since the previous data-point plotted for each data-point, illustrating the variable spacing of the data-points for the isotope records prior to the K/Pg boundary.

Chapter 6:

Summary and Further Work

In this chapter the main findings of this thesis are summarised, their implications with regards to the key research question of the thesis discussed, and recommendations made for further work on the basis of the limitations of this research.

6.1 Summary of findings

In Section 1.4.1 the following key research question motivating this thesis was identified as:

What were the drivers of carbon-climate system perturbations during the Cenozoic? which was further subdivided into the following pending research questions to be addressed in this thesis:

- 1. Were Large Igneous Provinces capable of significantly impacting the carbonclimate system during the Cenozoic?
- 2. Was the Miocene Climatic Optimum driven by emissions from the Columbia River Basalt large igneous province eruptions?
- 3. To what extent did shelf-basin carbonate burial fractionation drive the deepening of the carbonate compensation depth at the Eocene-Oligocene Transition and during the rest of the Cenozoic?
- 4. Did processes other than carbonate burial fractionation contribute to the Eocene-Oligocene Transition carbon cycle perturbation?
- 5. Why has the carbonate compensation depth remained relatively deep and stable since the Eocene Oligocene Transition?
- 6. Were the main Cenozoic carbon-climate perturbations the result of tipping points being reached in the carbon-climate system, and are they preceded by 'early warning signals' in the palaeorecord?
- 7. How reliable is early warning signal analysis when used on palaeorecords?

This thesis has addressed these questions through the work presented in Chapters 2 to 5 as summarised below.

In Chapter 2 the potential impact of the cryptic degassing of the Columbia River Basalt (CRB) Large Igneous Province (LIP) during the Miocene Climate Optimum (MCO) is investigated using two biogeochemical models of the carbon cycle. While emissions from sub-aerial basalts are found to have a minimal global impact on the Earth system, emissions of a greater but still physically possible magnitude from 'cryptic degassing' (intrusive degassing, magmatic contamination by mafic crust, and country rock metamorphism) can recreate the palaeorecord perturbations around 16.0 Ma (Question 2). This illustrates the potential importance of occasional pulses of volcanism in the evolution of the Cenozoic carbon-climate system (Question 1), with other, larger LIPs that erupted during the Palaeocene, Eocene, and Oligocene being worthy of further study to ascertain the potential magnitude and impact of their cryptic degassing. This study also indicates that the mid-Miocene carbonate compensation depth (CCD) deepening may have been driven by shelf-basin carbonate burial fractionation from ~15.4 Ma; that the warmth of the MCO prior to ~16.3 Ma is unlikely to have been caused by the CRB; and that the brief glacial maxima at ~16.2 Ma might have been linked to SO₂ emissions during the start of the cryptic degassing. This study underlines the importance of considering the whole LIP when investigating its impact on the Earth system, and of using models capable of capturing complex feedbacks such as the CCD deepening in response to slow volcanic emissions and a positive δ^{13} C perturbation in response to the emission of a large magnitude of light carbon.

In Chapter 3 the drivers of the carbon cycle perturbation during the Eocene-Oligocene Transition (EOT) glaciation event are investigated by extending and improving upon the work of *Merico et al.* [2008]. The original hypothesis – that the fall in sea level during the EOT drove the CCD deepening by reducing the area of shallow sea available for carbonate burial relative to the deep sea, coupled with the weathering of newly exposed carbonate rocks from shelves – was modified to account for subsequent critiques. This work demonstrates that although carbonate burial fractionation can drive the majority of the CCD deepening at the EOT, either isotopically heavier shelf carbonates or a simultaneous increase in ocean mixing rates are required for the whole perturbation to be explained (Question 3). This study also introduces the possibility of carbon cycle capacitors playing a significant role during the EOT, with the expansion of the permafrost soil carbon reservoir in the Northern

Hemisphere during the EOT-1 and Oi-1 cooling steps modelled as being capable of driving the rapid step increases in the positive benthic δ^{13} C excursion (Question 4).

In Chapter 4 the role of shelf-basin carbonate burial fractionation in the evolution of the ocean carbonate system during the Cenozoic is further examined. By analysing high-resolution hypsometric data and estimates of changing shelf carbonate burial extent this study presents a formula linking changes in the sea level to changes in the CCD. This reveals that most (~430 m) of the CCD deepening at the EOT can indeed be ascribed to carbonate burial fractionation (Question 3), but that other processes are also required to explain the behaviour of the CCD during the rest of the Cenozoic. This study also demonstrates that the sensitivity of the CCD to sea level change halved between the Eocene and Oligocene, which could help to explain the relative stability of the CCD since the EOT (Question 5). The mid-Miocene CCD shoaling is hypothesised to potentially represent a temporary and partial reversal of the shelf-basin carbonate burial fractionation achieved at the EOT, but further data on Miocene shelf carbonate burial extent and rate is required to test this hypothesis.

In Chapter 5 palaeorecords across multiple carbon-climate system perturbations are analysed to search for 'early warning signals' (EWS) indicative of impending critical transitions and system instability. Despite the potential pitfalls of this approach, evidence of increasing instability in the carbon-climate system is detected prior to the Eocene-Oligocene Transition, the Palaeocene-Eocene Thermal Maximum, and ~500 ky before the Miocene Climate Transition (Question 6). EWS indicators are also unexpectedly detected within the ~200 ky prior to the K/Pg boundary despite this being an exogenic event, a disparity that we ascribe to the Deccan Trap eruptions starting at this time. This study illustrates that, although the results are sensitive to parameter selection and the 'prosecutor's fallacy', using multiple EWS indices and sensitivity analyses can allow relatively robust conclusions to be drawn when conducting EWS analysis on the palaeoclimate record (Question 7).

6.2 Recommendations for further work

There are several possible follow-ups to the work conducted in Chapter 2 that would help to understand further the impact of LIPs during the Cenozoic. Better estimates of the total volume of the CRB's intrusive component and its likely degassing rate would help to constrain further the cryptic degassing estimates presented in this thesis, as would more data on the likely scale and impact of mafic crust contamination of the CRB's magma and the type and extent of country rock that

underwent metamorphosis around the CRB's intrusions. A similar methodology to that presented in Chapter 2 could also be applied to other LIPs during the Cenozoic in order to investigate why, for example, the Ethiopian-Yemen Flood Basalts appear to have had a minimal impact on the palaeorecords whereas the Deccan Traps had a more significant impact, and whether the North Atlantic Volcanic Province eruptions played any role in early Eocene warming. Employing a wider set of carbon isotope datasets (e.g. from different terrestrial and marine settings) would also provide additional carbon cycle variables with which to compare the model against. Lastly, incorporating the sulphur cycle into the simple carbon-silica-phosphorus biogeochemical model used in this thesis would potentially help to constrain better the total environmental impact of LIP eruptions and allow an additional set of data to constrain the biogeochemical modelling.

Differentiating between the two scenarios proposed in Chapter 3 to explain the EOT carbon cycle perturbation would require better constraints on the global average value of shelf carbonate δ^{13} C in the late Eocene, so new data on this would help to identify which of our hypothesised end member scenarios is most likely. Further data on the likely extent of permafrost soil carbon before, during and after the glaciation of Antarctica is necessary to provide constraints for the permafrost expansion hypothesis proposed in this thesis. This could potentially be achieved through high-resolution modelling of the interaction between the growing ice sheets, regional climate change in both the Northern and Southern Hemispheres, and the likely biomes into which the ice sheets expanded. Geochemical proxies that could detect the erosion of Antarctic permafrost in circum-Antarctic sediment would also help to constrain whether permafrost was eroded by the expanding ice sheet, and if so when.

To improve the relationship established in Chapter 4 and the results generated using this analysis it would be necessary to have a record of shelf carbonate extent with a better temporal resolution than every ~10 My, with additional resolution around the EOT being especially valuable in order to constrain the rapidity and magnitude of the reduction in shelf burial extent. Additionally, more estimates of how carbonate burial fluxes and global rates may have changed during the Cenozoic would help to quantify better the contribution that this may have had to deepening the CCD during the Cenozoic. A CCD reconstruction based on a global dataset rather than data just from the equatorial Pacific would also help to clarify which CCD changes are global rather than regional phenomena, and therefore constrain the magnitudes of the total global Cenozoic CCD deepening and the drivers needed to explain it. To extend the analysis further back in time (limited within the of the last ~200 My due to

seafloor subduction destroying older carbonate records) it would be necessary to incorporate the impact of higher mid-ocean ridge spreading rates on global hypsometry prior to $\sim \! 50$ Ma by enabling the hypsometric curve to change over time during the analysis, which would also moderately improve the estimates of hypsometry since $\sim \! 50$ Ma and further improve the relationship presented.

In order to increase the robustness of the results of Chapter 5 it would be valuable to repeat the analyses with longer and higher-resolution palaeorecords as they become available. Longer records without any core gaps prior to the EOT and the OMT would be especially useful in order to improve upon the short records used in this thesis. Other palaeorecords representing different aspects of the climate and carbon cycle would also help to confirm that any EWS indicators detected are common to multiple variables of the same system and can be found in multiple independent records. Re-analysing the same events with other and more advanced EWS analysis techniques, such as detrended fingerprint analysis and model-based approaches, would also help to increase confidence in the conclusions we draw and help minimise the likelihood that our results are 'false positives'. It would also be worthwhile extending the same methodology to the initiation of Northern Hemisphere Glaciation in the late Pliocene, as this represents another example of a hypothesised tipping point-driven shift in the Cenozoic carbon-climate system.

This thesis has shed new light on several of the perturbations to the carbonclimate system during the Cenozoic, but the potential drivers of the long-term decline in atmospheric CO₂ (atmCO₂) and global temperatures have not been directly investigated. The main carbon cycle model used in this thesis (MTW08 [Merico et al., 2008) is well-suited to simulating large perturbations to a carbon cycle assumed to be in equilibrium, which made it suitable for the various perturbations investigated in this thesis. However, it does not allow parameters such as weathering rates, volcanic emission rate, and the concentrations of key ions like magnesium to freely vary with time and therefore it is not well-suited to studying the long-term drift of the carbon cycle's equilibrium through the Cenozoic. In order to investigate the longer-term processes affecting the evolution of the Cenozoic carbon-climate system it would be valuable to develop and use a geological carbon cycle model that allows the carbon cycle to evolve freely in response to different forcings, rather than being forced to follow a prescribed Cenozoic trend. This would allow the extent to which the observed long-term Cenozoic trend was inevitable or down to chance to be investigated and assessed.

6.3 What were the drivers of carbon-climate system perturbations during the Cenozoic?

Returning to the key research question posed in Sections 1.4.1 and 6.1, this thesis has added to our understanding of several key processes that perturbed and shaped the evolution of the carbon-climate system during the Cenozoic.

The episodic eruption of Large Igneous Provinces such as the Columbia River Basalt (Chapter 2) and the Deccan Traps (Chapter 5) significantly destabilised the carbon-climate system several times in the Cenozoic, triggering large carbon cycle perturbations and global warming for up to ~1 My. The Palaeocene-Eocene Thermal Maximum (PETM) is also likely to have been the result of background warming destabilising the carbon-climate system and pushing it towards a carbon cycle tipping point (Chapter 5). These excursions to higher atmCO₂ and global warmth were only temporary interruptions though to the longer-term decline in atmCO₂ and global temperatures, which in itself may have been the result of the long-term decline in volcanism rates during the Palaeogene and high terrestrial weathering driven by LIP weathering in tropical latitudes [Lefebvre et al., 2013].

Once atm CO₂ declined below a critical threshold (between ~750 and ~950 ppm; [DeConto and Pollard, 2003; DeConto et al., 2008; Ladant et al., 2014b]) a tipping point in the climate system (Chapter 5) triggered the rapid continental-scale glaciation of Antarctica at the Eocene-Oligocene Transition. This in turn drove a perturbation to the carbon cycle via some combination of shelf-basin carbonate burial fractionation, shelf carbonate weathering, increased ocean ventilation, and potentially the net expansion of the global permafrost soil carbon reservoir (Chapter 3). Shelf-basin carbonate burial fractionation is likely to have been the most important driver of the CCD deepening during the EOT (Chapters 3 and 4), but during the rest of the Cenozoic shelf-basin fractionation probably played a more minor role in driving changes in the CCD. Increased carbonate weathering and oceanic carbonate burial rates may have driven some but not all of the rest of the long-term CCD deepening instead, and thus may have also led to a gradual increase in the sequestration of carbon into the sedimentary carbonate reservoir during the Cenozoic (Chapter 4).

The declining sensitivity of the CCD to sea level fluctuations after the EOT as a result of the collapse in shelf carbonate extent probably led to the relative stability of the CCD during most of the later Cenozoic (Chapter 4). However, it is possible that the CCD state shift at the EOT was partially and temporarily reversed during the MCO, until a combination of the CRB eruptions and glacial re-expansion during the

mid-Miocene Climate Transition (MMCT) re-deepened the CCD (Chapters 2 and 4). Despite the main isotopic excursion of the MMCT occurring at ~13.9 Ma, carbonate burial fractionation and peak instability in the carbon-climate system appear to have occurred earlier between 15.4 and 14.4 Ma (Chapters 2 and 5). This suggests that the isotopic shift at ~13.9 Ma marks the culmination rather than the start of the MMCT.

In conclusion, this thesis finds that Large Igneous Province emissions and shelf carbonate burial decline (driven by glacioeustatic sea level fall and global cooling) are likely to have played significant roles in driving the observed instability and perturbations in the Cenozoic carbon-climate system; while permafrost expansion and increases in ocean ventilation, carbonate weathering, and possibly ocean carbonate burial may have also been important processes during some of the perturbations. This thesis also finds some evidence of early warning signals – which are indicative of increasing systemic instability and/or impending critical transitions – occurring prior to several Cenozoic carbon-climate system perturbations.

List of References

- Aarnes, I., H. Svensen, S. Polteau, and S. Planke (2011a), Contact metamorphic devolatilization of shales in the Karoo Basin, South Africa, and the effects of multiple sill intrusions, *Chem. Geol.*, 281(3-4), 181–194, doi:10.1016/j.chemgeo.2010.12.007.
- Aarnes, I., K. Fristad, S. Planke, and H. Svensen (2011b), The impact of host-rock composition on devolatilization of sedimentary rocks during contact metamorphism around mafic sheet intrusions, *Geochemistry, Geophys. Geosystems*, 12(10), doi:10.1029/2011GC003636.
- Aarnes, I., Y. Podladchikov, and H. Svensen (2012), Devolatilization-induced pressure build-up: Implications for reaction front movement and breccia pipe formation, *Geofluids*, 12(4), 265–279, doi:10.1111/j.1468-8123.2012.00368.x.
- Allen, M. B., and H. A. Armstrong (2008), Arabia-Eurasia collision and the forcing of mid-Cenozoic global cooling, *Palaeogeogr. Palaeoclimatol. Palaeoecol.*, 265(1-2), 52–58, doi:10.1016/j.palaeo.2008.04.021.
- Amante, C., and B. W. Eakins (2009), ETOPO1 1 Arc-Minute Global Relief Model: Procedures, Data Sources and Analysis, *NOAA Tech. Memo. NESDIS NGDC-24*, 19pp, doi:10.7289/V5C8276M.
- Armstrong McKay, D. I., T. Tyrrell, P. A. Wilson, and G. L. Foster (2014), Estimating the impact of the cryptic degassing of Large Igneous Provinces: A mid-Miocene case-study, *Earth Planet. Sci. Lett.*, 403, 254–262, doi:10.1016/j.epsl.2014.06.040.
- Armstrong McKay, D. I., T. Tyrrell, and P. A. Wilson (in revision), Global carbon cycle perturbation across the Eocene-Oligocene climate transition, *Paleoceanography*.
- Arrhenius, S. (1897), On the Influence of Carbonic Acid in the Air upon the Temperature of the Earth, *Publ. Astron. Soc. Pacific*, 9(54), 14–24, doi:10.1086/121158.
- Bailey, I., G. M. Hole, G. L. Foster, P. A. Wilson, C. D. Storey, C. N. Trueman, and M. E. Raymo (2013), An alternative suggestion for the Pliocene onset of major northern hemisphere glaciation based on the geochemical provenance of North Atlantic Ocean ice-rafted debris, *Quat. Sci. Rev.*, 75, 181–194, doi:10.1016/j.quascirev.2013.06.004.
- Baksi, A. K. (2013), Timing and duration of volcanism in the Columbia River Basalt Group: A review of existing radiometric data and new constraints on the age of the Steens through Wanapum Basalt extrusion, *Geol. Soc. Am. Spec. Pap.*, 497, 67–85, doi:10.1130/2013.2497(03).
- Barron, E. J. (1981), Paleogeography as a climatic forcing factor, *Geol. Rundschau*, 70(2), 737–747, doi:10.1007/BF01822147.
- Barron, E. J. (1985), Explanations of the tertiary global cooling trend, *Palaeogeogr. Palaeoclimatol. Palaeoecol.*, 50(1), 45–61, doi:10.1016/S0031-0182(85)80005-5.

- Barron, E. J., and W. M. Washington (1984), The role of geographic variables in explaining paleoclimates: Results from Cretaceous climate model sensitivity studies, *J. Geophys. Res.*, 89(D1), 1267, doi:10.1029/JD089iD01p01267.
- Barron, E. J., J. L. Sloan, and C. G. A. Harrison (1980), Potential significance of land—sea distribution and surface albedo variations as a climatic forcing factor; 180 m.y. to the present, *Palaeogeogr. Palaeoclimatol. Palaeoecol.*, 30, 17–40, doi:10.1016/0031-0182(80)90047-4.
- Barron, E. J., S. L. Thompson, and W. W. Hay (1984), Continental distribution as a forcing factor for global-scale temperature, *Nature*, 310(5978), 574–575, doi:10.1038/310574a0.
- Barry, T. L., S. Self, S. P. Kelley, S. P. Reidel, P. R. Hooper, and M. Widdowson (2010), New ⁴⁰Ar/³⁹Ar dating of the Grande Ronde lavas, Columbia River Basalts, USA: Implications for duration of flood basalt eruption episodes, *Lithos*, 118(3-4), 213–222, doi:10.1016/j.lithos.2010.03.014.
- Barry, T. L., S. P. Kelley, V. E. Camp, S. Self, N. A. Jarboe, and R. Duncan (2013), Eruption chronology of the Columbia River Basalt Group, in *The Columbia River Flood Basalt Province: Geological Society of America Special Paper 497*, vol. 2497, edited by S. P. Reidel, V. E. Camp, M. E. Ross, J. A. Wolff, B. S. Martin, T. L. Tolan, and R. . Wells, pp. 45–66.
- Basak, C., and E. E. Martin (2013), Antarctic weathering and carbonate compensation at the Eocene–Oligocene transition, *Nat. Geosci.*, *6*(2), 121–124, doi:10.1038/ngeo1707.
- Batjes, N. H. (1996), Total carbon and nitrogen in the soils of the world, *Eur. J. Soil Sci.*, 47(2), 151–163, doi:10.1111/j.1365-2389.1996.tb01386.x.
- Beerling, D. J., and D. L. Royer (2011), Convergent Cenozoic CO₂ history, *Nat. Geosci.*, 4(7), 418–420, doi:10.1038/ngeo1186.
- Ben-Yaakov, S., and M. B. Goldhaber (1973), The influence of seawater composition on the apparent constants of the carbonate system, *Deep. Res.*, 20, 87–99.
- Berger, W. H. (2007), Cenozoic cooling, Antarctic nutrient pump, and the evolution of whales, *Deep Sea Res. Part II Top. Stud. Oceanogr.*, 54(21-22), 2399–2421, doi:10.1016/j.dsr2.2007.07.024.
- Berger, W. H., and E. L. Winterer (1975), Plate Stratigraphy and the Fluctuating Carbonate Line, in *Pelagic Sediments On Land and under the Sea*, edited by K. J. Hsü and H. C. Jenkyns, pp. 11–48, Blackwell Publishers Ltd., Oxford, UK.
- Berner, R. A. (1991), A model for atmospheric CO₂ over Phanerozoic time, *Am. J. Sci.*, 291(4), 339–376, doi:10.2475/ajs.291.4.339.
- Berner, R. A. (1992), Weathering, plants, and the long-term carbon cycle, *Geochim. Cosmochim. Acta*, *56*(8), 3225–3231, doi:10.1016/0016-7037(92)90300-8.
- Berner, R. A. (1994), Geocarb II: A Revised Model of Atmospheric CO₂ Over Phanerozoic Time, Am. J. Sci., 294(1), 56–91, doi:10.2475/ajs.294.1.56.

- Berner, R. A. (2006), GEOCARBSULF: A combined model for Phanerozoic atmospheric O₂ and CO₂, *Geochim. Cosmochim. Acta*, 70, 5653–5664, doi:10.1016/j.gca.2005.11.032.
- Berner, R. A., and Z. Kothavala (2001), GEOCARB III; a revised model of atmospheric CO₂ over Phanerozoic time, *Am. J. Sci.*, 301(1), 182–204, doi:10.2475/ajs.294.1.56.
- Berner, R. A., A. C. Lasaga, and R. M. Garrels (1983), The carbonate-silicate geochemical cycle and its effect on atmospheric carbon dioxide over the past 100 million years, *Am. J. Sci.*, 283, 641–683.
- Bernie, D., J. Lowe, T. Tyrrell, and O. Legge (2010), Influence of mitigation policy on ocean acidification, *Geophys. Res. Lett.*, *37*(15), 1–5, doi:10.1029/2010GL043181.
- Bice, K. L., C. R. Scotese, D. Seidov, and E. J. Barron (2000), Quantifying the role of geographic change in Cenozoic ocean heat transport using uncoupled atmosphere and ocean models, *Palaeogeogr. Palaeoclimatol. Palaeoecol.*, 161(3-4), 295–310, doi:10.1016/S0031-0182(00)00072-9.
- Bierman, P. R., L. B. Corbett, J. A. Graly, T. A. Neumann, A. Lini, B. T. Crosby, and D. H. Rood (2014), Preservation of a preglacial landscape under the center of the Greenland Ice Sheet., *Science*, 344(6182), 402–5, doi:10.1126/science.1249047.
- Bijl, P. K., S. Schouten, A. Sluijs, G.-J. Reichart, J. C. Zachos, and H. Brinkhuis (2009), Early Palaeogene temperature evolution of the southwest Pacific Ocean., *Nature*, 461(7265), 776–779, doi:10.1038/nature08399.
- Bijl, P. K., A. J. P. Houben, S. Schouten, S. M. Bohaty, A. Sluijs, G.-J. Reichart, J. S. Sinninghe Damsté, and H. Brinkhuis (2010), Transient Middle Eocene atmospheric CO₂ and temperature variations., *Science*, 330(6005), 819–21, doi:10.1126/science.1193654.
- Billups, K., and D. P. Schrag (2003), Application of benthic foraminiferal Mg/Ca ratios to questions of Cenozoic climate change, *Earth Planet. Sci. Lett.*, 209(1-2), 181–195, doi:10.1016/S0012-821X(03)00067-0.
- Bjöorkström, A. (1979), A Model of CO₂ Interaction between Atmosphere, Oceans, and Land Biota, in *SCOPE 13 The Global Carbon Cycle*, pp. 403–457, John Wiley & Sons, Chichester.
- Boettiger, C., and A. Hastings (2012), Early warning signals and the prosecutor's fallacy., *Proc. Biol. Sci.*, 279(1748), 4734–9, doi:10.1098/rspb.2012.2085.
- Boettiger, C., N. Ross, and A. Hastings (2013), Early warning signals: The charted and uncharted territories, *Theor. Ecol.*, *6*(3), 255–264, doi:10.1007/s12080-013-0192-6.
- Bohaty, S. M., J. C. Zachos, F. Florindo, and M. L. Delaney (2009), Coupled greenhouse warming and deep-sea acidification in the middle Eccene, *Paleoceanography*, 24(PA2207), 1–16, doi:10.1029/2008PA001676.

- Bohaty, S. M., J. C. Zachos, and M. L. Delaney (2012), Foraminiferal Mg/Ca evidence for Southern Ocean cooling across the Eocene–Oligocene transition, *Earth Planet. Sci. Lett.*, 317-318, 251–261, doi:10.1016/j.epsl.2011.11.037.
- Bolin, B., and E. Eriksson (1959), Changes in the Carbon Dioxide Content of the Atmosphere and Sea due to Fossil Fuel Combustion, in *The Atmosphere and The Sea in Motion*, edited by B. Bolin, pp. 130–142, The Rockefeller Institute Press.
- Bolin, B., A. Bjorkstrom, C. D. Keeling, R. Bacastow, and U. Siegenthaler (1981), Carbon Cycle Modelling, in *SCOPE 16: Carbon Cycle Modelling*, edited by B. Bolin, pp. 1–28, John Wiley & Sons, Chichester, New York, Brisbane, Toronto,.
- Bosboom, R. E., G. Dupont-Nivet, A. J. P. Houben, H. Brinkhuis, G. Villa, O. Mandic, M. Stoica, W. J. Zachariasse, Z. Guo, and C. Li (2011), Late Eccene sea retreat from the Tarim Basin (west China) and concomitant Asian paleoenvironmental change, *Palaeogeogr. Palaeoclimatol. Palaeoecol.*, 299(3-4), 385–398, doi:10.1016/j.palaeo.2010.11.019.
- Boss, S. K., and B. H. Wilkinson (1991), Planktogenic/Eustatic Control on Cratonic/Oceanic Carbonate Accumulation, *J. Geol.*, 99(4), 497–513.
- Bryan, S. E., and R. E. Ernst (2008), Revised definition of Large Igneous Provinces (LIPs), *Earth-Science Rev.*, 86(1-4), 175–202, doi:10.1016/j.earscirev.2007.08.008.
- Buffett, B., and D. Archer (2004a), Global inventory of methane clathrate: sensitivity to changes in the deep ocean, *Earth Planet. Sci. Lett.*, 227(3-4), 185–199, doi:10.1016/j.epsl.2004.09.005.
- Buffett, B., and D. Archer (2004b), Global inventory of methane clathrate: sensitivity to changes in the deep ocean, *Earth Planet. Sci. Lett.*, 227(3-4), 185–199, doi:10.1016/j.epsl.2004.09.005.
- Caldeira, K., and M. R. Rampino (1990), Carbon dioxide emissions from Deccan Volcanism and a K/T boundary greenhouse effect, *Geophys. Res. Lett.*, 17(9), 1299–1302.
- Came, R. E., J. M. Eiler, J. Veizer, K. Azmy, U. Brand, and C. R. Weidman (2007), Coupling of surface temperatures and atmospheric CO₂ concentrations during the Palaeozoic era., *Nature*, 449(7159), 198–201, doi:10.1038/nature06085.
- Camp, V. E., and B. B. Hanan (2008), A plume-triggered delamination origin for the Columbia River Basalt Group, *Geosphere*, 4(3), 480, doi:10.1130/GES00175.1.
- Carpenter, S. R., and W. A. Brock (2006), Rising variance: a leading indicator of ecological transition., *Ecol. Lett.*, *9*(3), 311–318, doi:10.1111/j.1461-0248.2005.00877.x.
- Carstensen, J., R. J. Telford, and H. J. B. Birks (2013), Diatom flickering prior to regime shift., *Nature*, 498(7455), E11–2, doi:10.1038/nature12272.
- Chamberlin, T. C. (1898), The Influence of Great Epochs of Limestone Formation upon the Constitution of the Atmosphere, *J. Geol.*, *6*(6), 609–621.

- Chuck, A., T. Tyrrell, I. J. Totterdell, and P. M. Holligan (2005), The oceanic response to carbon emissions over the next century: investigation using three ocean carbon cycle models, *Tellus B*, *57*(1), 70–86, doi:10.1111/j.1600-0889.2005.00127.x.
- Coffin, M. F., and O. Eldholm (1994), Large Igneous Provinces: crustal structure, dimensions, and external consequences, *Rev. Geophys.*, 32(1), 1–36.
- Courtillot, V. E., and P. R. Renne (2003), On the ages of flood basalt events, *Comptes Rendus Geosci.*, 335(1), 113–140.
- Coxall, H. K., and P. A. Wilson (2011), Early Oligocene glaciation and productivity in the eastern equatorial Pacific: Insights into global carbon cycling, *Paleoceanography*, 26(PA2221), 1–18, doi:10.1029/2010PA002021.
- Coxall, H. K., P. A. Wilson, H. Pälike, C. H. Lear, and J. Backman (2005), Rapid stepwise onset of Antarctic glaciation and deeper calcite compensation in the Pacific Ocean., *Nature*, 433(7021), 53–57, doi:10.1038/nature03135.
- Craig, H. (1957), The Natural Distribution of Radiocarbon and the Exchange Time of Carbon Dioxide Between Atmosphere and Sea, *Tellus*, *9*(I).
- Crowell, J. C., and L. A. Frakes (1970), Phanerozoic glaciation and the causes of ice ages, *Am. J. Sci.*, 268(3), 193–224, doi:10.2475/ajs.268.3.193.
- Cui, Y., L. R. Kump, A. J. Ridgwell, A. J. Charles, C. K. Junium, A. F. Diefendorf, K. H. Freeman, N. M. Urban, and I. C. Harding (2011), Slow release of fossil carbon during the Palaeocene–Eocene Thermal Maximum, *Nat. Geosci.*, 4(7), 481–485, doi:10.1038/ngeo1179.
- Dakos, V. (2008), Slowing down as an early warning signal for abrupt climate change: Supporting Information, *Proc. Natl. Acad. Sci. U. S. A.*, 105(38).
- Dakos, V., M. Scheffer, E. H. van Nes, V. Brovkin, V. Petoukhov, and H. Held (2008), Slowing down as an early warning signal for abrupt climate change., *Proc. Natl. Acad. Sci. U. S. A.*, 105(38), 14308–12, doi:10.1073/pnas.0802430105.
- Dakos, V. et al. (2012), Methods for detecting early warnings of critical transitions in time series illustrated using simulated ecological data, *PLoS One*, 7(7), doi:10.1371/journal.pone.0041010.
- Dakos, V., E. H. Nes, and M. Scheffer (2013), Flickering as an early warning signal, *Theor. Ecol.*, 6(3), 309–317, doi:10.1007/s12080-013-0186-4.
- Dakos, V., S. R. Carpenter, E. H. van Nes, and M. Scheffer (2014), Resilience indicators: prospects and limitations for early warnings of regime shifts, *Philos. Trans. R. Soc. B Biol. Sci.*, 370(1659), 20130263–20130263, doi:10.1098/rstb.2013.0263.
- De Boer, B., R. S. W. Van de Wal, R. Bintanja, L. J. Lourens, and E. Tuenter (2010), Cenozoic global ice-volume and temperature simulations with 1-D ice-sheet models forced by benthic δ¹⁸O records, *Ann. Glaciol.*, *51*(55), 23–33, doi:10.3189/172756410791392736.

- De La Rocha, C. L. (2000), Isotopic Evidence for Variations in the Marine Calcium Cycle Over the Cenozoic, *Science*, 289(5482), 1176–1178, doi:10.1126/science.289.5482.1176.
- DeConto, R. M., and D. Pollard (2003), Rapid Cenozoic glaciation of Antarctica induced by declining atmospheric CO₂., *Nature*, 421(6920), 245–9, doi:10.1038/nature01290.
- DeConto, R. M., D. Pollard, and D. M. Harwood (2007), Sea ice feedback and Cenozoic evolution of Antarctic climate and ice sheets, *Paleoceanography*, 22(PA3214), 1–18, doi:10.1029/2006PA001350.
- DeConto, R. M., D. Pollard, P. A. Wilson, H. Pälike, C. H. Lear, and M. Pagani (2008), Thresholds for Cenozoic bipolar glaciation, *Nature*, 455(7213), 652–6, doi:10.1038/nature07337.
- DeConto, R. M., S. Galeotti, M. Pagani, D. Tracy, K. Schaefer, T. Zhang, D. Pollard, and D. J. Beerling (2012), Past extreme warming events linked to massive carbon release from thawing permafrost., *Nature*, 484(7392), 87–91, doi:10.1038/nature10929.
- Derry, L. A., and C. France-Lanord (1996), Neogene growth of the sedimentary organic carbon reservoir, *Paleoceanography*, 11(3), 267, doi:10.1029/95PA03839.
- Dessert, C., B. Dupré, J. Gaillardet, L. M. François, and C. J. Allègre (2003), Basalt weathering laws and the impact of basalt weathering on the global carbon cycle, *Chem. Geol.*, 202(3-4), 257–273, doi:10.1016/j.chemgeo.2002.10.001.
- Dickens, G. R. (2011), Down the Rabbit Hole: toward appropriate discussion of methane release from gas hydrate systems during the Paleocene-Eocene thermal maximum and other past hyperthermal events, *Clim. Past*, 7(3), 831–846, doi:10.5194/cp-7-831-2011.
- Diester-Haass, L., K. Billups, D. R. Gröcke, L. M. François, V. Lefebvre, and K. C. Emeis (2009), Mid-Miocene paleoproductivity in the Atlantic Ocean and implications for the global carbon cycle, *Paleoceanography*, 24(PA1209), 1–19, doi:10.1029/2008PA001605.
- Ditlevsen, P. D., and S. J. Johnsen (2010), Tipping points: Early warning and wishful thinking, *Geophys. Res. Lett.*, 37(L19703), 1–4, doi:10.1029/2010GL044486.
- Donnadieu, Y., Y. Goddéris, G. Ramstein, A. Nédélec, and J. Meert (2004a), A "snowball Earth" climate triggered by continental break-up through changes in runoff., *Nature*, 428(6980), 303–306, doi:10.1038/nature02408.
- Donnadieu, Y., G. Ramstein, Y. Goddéris, and F. Fluteau (2004b), Global Tectonic Setting and Climate of the Late Neoproterozoic: A Climate-Geochemical Coupled Study, in *The Extreme Proterozoic: Geology, Geochemistry, and Climate*, edited by G. S. Jenkins, M. A. S. McMenamin, C. P. McKay, and L. Sohl, pp. 79–89.
- Donnadieu, Y., Y. Goddéris, R. Pierrehumbert, G. Dromart, R. Jacob, and F. Fluteau (2006), A GEOCLIM simulation of climatic and biogeochemical consequences of Pangea breakup, *Geochemistry, Geophys. Geosystems*, 7(11), doi:10.1029/2006GC001278.

- Dunkley Jones, T., P. R. Bown, P. N. Pearson, B. S. Wade, H. K. Coxall, and C. H. Lear (2008a), Major shifts in calcareous phytoplankton assemblages through the Eocene-Oligocene transition of Tanzania and their implications for low-latitude primary production, *Paleoceanography*, 23(PA4204), 1–14, doi:10.1029/2008PA001640.
- Dyke, J. G., and I. S. Weaver (2013), The Emergence of Environmental Homeostasis in Complex Ecosystems, edited by S. A. Levin, *PLoS Comput. Biol.*, *9*(5), e1003050, doi:10.1371/journal.pcbi.1003050.
- Eakins, B. W., and G. F. Sharman (2012), Hypsographic Curve of Earth's Surface from ETOPO1, NOAA Natl. Geophys. Data Center, Boulder, CO.
- Edgar, K. M., P. A. Wilson, P. F. Sexton, and Y. Suganuma (2007), No extreme bipolar glaciation during the main Eocene calcite compensation shift., *Nature*, 448(7156), 908–11, doi:10.1038/nature06053.
- Edgar, K. M., P. A. Wilson, P. F. Sexton, S. J. Gibbs, A. P. Roberts, and R. D. Norris (2010), New biostratigraphic, magnetostratigraphic and isotopic insights into the Middle Eocene Climatic Optimum in low latitudes, *Palaeogeogr. Palaeoclimatol. Palaeoecol.*, 297(3-4), 670–682, doi:10.1016/j.palaeo.2010.09.016.
- Eldrett, J. S., I. C. Harding, P. A. Wilson, E. Butler, and A. P. Roberts (2007), Continental ice in Greenland during the Eocene and Oligocene., *Nature*, 446(7132), 176–179, doi:10.1038/nature05591.
- Ernst, R. E., K. L. Buchan, and I. H. Campbell (2005), Frontiers in large igneous province research, *Lithos*, 79(3-4), 271–297.
- Erwin, D. H. (2006), Extinction: how life on Earth nearly ended 250 million years ago, Princeton University Press, Princeton.
- Exon, N. et al. (2000), The opening of the tasmanian gateway drove global cenozoic paleoclimatic and paleoceanographic changes: Results of leg 189, JOIDES J., 26(2), 11-17.
- Fantle, M. S. (2010), Evaluating the Ca isotope proxy, *Am. J. Sci.*, 310(3), 194–230, doi:10.2475/03.2010.03.
- Farkaš, J., F. Böhm, K. Wallmann, J. Blenkinsop, A. Eisenhauer, R. van Geldern, A. Munnecke, S. Voigt, and J. Veizer (2007a), Calcium isotope record of Phanerozoic oceans: Implications for chemical evolution of seawater and its causative mechanisms, *Geochim. Cosmochim. Acta*, 71(21), 5117–5134, doi:10.1016/j.gca.2007.09.004.
- Farkaš, J., D. Buhl, J. Blenkinsop, and J. Veizer (2007b), Evolution of the oceanic calcium cycle during the late Mesozoic: Evidence from δ⁴⁴/⁴⁰Ca of marine skeletal carbonates, *Earth Planet. Sci. Lett.*, 253(1-2), 96–111, doi:10.1016/j.epsl.2006.10.015.
- Farrell, J. W., and W. L. Prell (1989), Climatic change and CaCO₃ preservation: An 800,000 year bathymetric reconstruction from the central equatorial Pacific Ocean, *Paleoceanography*, 4(4), 447, doi:10.1029/PA004i004p00447.

- Feakins, S. J., S. Warny, and J.-E. Lee (2012), Hydrologic cycling over Antarctica during the middle Miocene warming, *Nat. Geosci.*, 5(8), 557–560, doi:10.1038/ngeo1498.
- Fischer, A. G. (1982), Long-term climatic oscillations recorded in stratigraphy, in *Climate in Earth history*, edited by W. H. Berger, pp. 97–104, National Research Council, Studies in Geophysics, National Academy Press, Washington DC.
- Flower, B. P. (1999), Cenozoic Deep-Sea Temperatures and Polar Glaciation: the Oxygen Isotope Record, *Terra Antart. Reports*, *3*, 27–42.
- Flower, B. P., and J. P. Kennett (1993), Middle Miocene Transition: Ocean-Climate high-resolution oxygen and carbon isotopic records from Deep Sea Drilling Project Site 588A, southwest Pacific, *Paleoceanography*, 8(6), 811–843.
- Flower, B. P., and J. P. Kennett (1994), The middle Miocene climatic transition: East Antarctic ice sheet development, deep ocean circulation and global carbon cycling, *Palaeogeogr. Palaeoclimatol. Palaeoecol.*, 108, 537–555.
- Foster, G. L., and E. J. Rohling (2013), Relationship between sea level and climate forcing by CO₂ on geological timescales., *Proc. Natl. Acad. Sci. U. S. A.*, 110(4), 1209–14, doi:10.1073/pnas.1216073110.
- Foster, G. L., C. H. Lear, and J. W. B. Rae (2012), The evolution of pCO₂, ice volume and climate during the middle Miocene, *Earth Planet. Sci. Lett.*, 341-344, 243–254, doi:10.1016/j.epsl.2012.06.007.
- Foster, L. C., D. N. Schmidt, E. Thomas, S. Arndt, and A. J. Ridgwell (2013), Surviving rapid climate change in the deep sea during the Paleogene hyperthermals., *Proc. Natl. Acad. Sci. U. S. A.*, 110(23), 9273–6, doi:10.1073/pnas.1300579110.
- Frakes, L. A., and E. M. Kemp (1972), Influence of Continental Positions on Early Tertiary Climates, *Nature*, 240(5376), 97–100, doi:10.1038/240097a0.
- France-Lanord, C., and L. A. Derry (1997), Organic carbon burial forcing of the carbon cycle from Himalayan erosion, *Nature*, *390*(November), 65–67.
- Ganino, C., and N. T. Arndt (2009), Climate changes caused by degassing of sediments during the emplacement of large igneous provinces, *Geology*, 37(4), 323–326, doi:10.1130/G25325A.1.
- Ganino, C., and N. T. Arndt (2010), Climate changes caused by degassing of sediments during the emplacement of large igneous provinces: REPLY, *Geology*, 38(6), e211, doi:10.1130/G31071Y.1.
- Gibbs, M. T., and L. R. Kump (1994), Global chemical erosion during the last glacial maximum and the present: Sensitivity to changes in lithology and hydrology, *Paleoceanography*, 9(4), 529–543.
- Goddéris, Y., and L. M. François (1996), Balancing the Cenozoic carbon and alkalinity cycles: Constraints from isotopic records, *Geophys. Res. Lett.*, 23(25), 3743–3746.

- Goddéris, Y., Y. Donnadieu, C. Dessert, B. Dupré, F. Fluteau, L. M. François, J. Meert, A. Nédélec, and G. Ramstein (2007), Coupled modeling of global carbon cycle and climate in the Neoproterozoic: links between Rodinia breakup and major glaciations, *Comptes Rendus Geosci.*, 339(3-4), 212–222, doi:10.1016/j.crte.2005.12.002.
- Goldblatt, C., T. D. Robinson, K. J. Zahnle, and D. Crisp (2013), Low simulated radiation limit for runaway greenhouse climates, *Nat. Geosci.*, *6*(8), 661–667, doi:10.1038/ngeo1892.
- Goldner, A., N. Herold, and M. Huber (2014), Antarctic glaciation caused ocean circulation changes at the Eocene–Oligocene transition, *Nature*, *511*(7511), 574–577, doi:10.1038/nature13597.
- Greene, S. E., A. Ridgwell, D. N. Schmidt, S. Kirtland Turner, H. Pälike, E. Thomas, L. K. Greene, and B. Hoogakker (in revision), Early Cenozoic Decoupling of Carbonate Compensation Depth and Climate Trends, *Nature Geoscience*.
- Grard, A., L. Francois, C. Dessert, B. Dupré, and Y. Goddéris (2005), Basaltic volcanism and mass extinction at the Permo-Triassic boundary: Environmental impact and modeling of the global carbon cycle, *Earth Planet. Sci. Lett.*, 234, 207–221, doi:10.1016/j.epsl.2005.02.027.
- Griffith, E. M., M. Calhoun, E. Thomas, K. Averyt, T. J. Bralower, M. W. Lyle, A. Olivarez-lyle, and A. Paytan (2010), Export Productivity and Carbonate Accumulation in the Pacific Basin at the Transition from a Greenhouse to Icehouse Climate (Late Eccene to Early Oligocene), *Paleoceanography*, 25(PA3212).
- Griffith, E. M., A. Paytan, A. Eisenhauer, T. D. Bullen, and E. Thomas (2011), Seawater calcium isotope ratios across the Eocene-Oligocene transition, *Geology*, 39(7), 683–686, doi:10.1130/G31872.1.
- Haefner, J. W. (1996), *Modeling Biological Systems: Principles and Applications*, Chapman and Hull.
- Hain, M. P., D. M. Sigman, J. A. Higgins, and G. H. Haug (2015), The effects of secular calcium and magnesium concentration changes on the thermodynamics of seawater acid/base chemistry: Implications for Eocene and Cretaceous ocean carbon chemistry and buffering, *Global Biogeochem. Cycles*, *29*(5), 517–533, doi:10.1002/2014GB004986.
- Hansen, J., M. Sato, P. Kharecha, D. J. Beerling, R. A. Berner, V. Masson-delmotte, M. Pagani, M. Raymo, D. L. Royer, and J. C. Zachos (2008), Target Atmospheric CO₂: Where Should Humanity Aim?, *Open Atmos. Sci. J.*, 217–231.
- Hartmann, J., and N. Moosdorf (2011), Chemical weathering rates of silicate-dominated lithological classes and associated liberation rates of phosphorus on the Japanese Archipelago—Implications for global scale analysis, *Chem. Geol.*, 287(3-4), 125–157, doi:10.1016/j.chemgeo.2010.12.004.
- Hay, W. W. (1985), Potential Errors in Estimates of Carbonate Rock Accumulating Through Geologic Time, in *The Carbon Cycle and Atmospheric CO₂: Natural*

- Variations Archean to Present, vol. 32, edited by E. T. Sundquist and W. S. Broecker, pp. 573–583, American Geophysical Union, Washington, D. C.
- Hay, W. W., J. L. Sloan, and C. N. Wold (1988), Mass/age distribution and composition of sediments on the ocean floor and the global rate of sediment subduction, *J. Geophys. Res.*, 93(B12), 14933, doi:10.1029/JB093iB12p14933.
- Haywood, A. M., and P. J. Valdes (2004), Modelling Pliocene warmth: Contribution of atmosphere, oceans and cryosphere, *Earth Planet. Sci. Lett.*, 218(3-4), 363–377, doi:10.1016/S0012-821X(03)00685-X.
- Henrot, A.-J., L. M. François, E. Favre, M. Butzin, M. Ouberdous, and G. Munhoven (2010), Effects of CO₂, continental distribution, topography and vegetation changes on the climate at the Middle Miocene: a model study, *Clim. Past*, 6(5), 675–694, doi:10.5194/cp-6-675-2010.
- Herold, N., M. Huber, and R. D. Müller (2011), Modeling the Miocene Climatic Optimum. Part I: Land and Atmosphere*, *J. Clim.*, 24(24), 6353–6372, doi:10.1175/2011JCLI4035.1.
- Heuser, A., A. Eisenhauer, F. Böhm, K. Wallmann, N. Gussone, P. N. Pearson, T. F. Nägler, and W. C. Dullo (2005), Calcium isotope (δ⁴⁴/⁴⁰Ca) variations of Neogene planktonic foraminifera, *Paleoceanography*, 20(PA2013), 1–13, doi:10.1029/2004PA001048.
- Higgins, J. A., and D. P. Schrag (2006), Beyond methane: Towards a theory for the Paleocene–Eocene Thermal Maximum, *Earth Planet. Sci. Lett.*, 245(3-4), 523–537, doi:10.1016/j.epsl.2006.03.009.
- Hodell, D. A., and F. Woodruff (1994), Variations in the strontium isotopic ratio of seawater during the Miocene: Stratigraphic and geochemical implications, *Paleoceanography*, 9(3), 405–426.
- Hoffman, P. F. (1998), A Neoproterozoic Snowball Earth, *Science*, 281(5381), 1342–1346, doi:10.1126/science.281.5381.1342.
- Hofmann, M., and H. J. Schellnhuber (2010), Ocean acidification: a millennial challenge, *Energy Environ. Sci.*, *3*(12), 1883, doi:10.1039/c000820f.
- Hofmann, M., W. S. Broecker, and J. Lynch-Stieglitz (1999), Influence of a [CO_{2(aq)}] dependent biological C-isotope fractionation on glacial ¹³C/¹²C ratios in the ocean, *Global Biogeochem. Cycles*, 13(4), 873–883, doi:10.1029/1999GB900063.
- Holbourn, A., W. Kuhnt, M. Schulz, and H. Erlenkeuser (2005), Impacts of orbital forcing and atmospheric carbon dioxide on Miocene ice-sheet expansion., *Nature*, 438(7067), 483–7, doi:10.1038/nature04123.
- Holbourn, A., W. Kuhnt, M. Schulz, J.-A. Flores, and N. Andersen (2007), Orbitally-paced climate evolution during the middle Miocene "Monterey" carbon-isotope excursion, *Earth Planet. Sci. Lett.*, 261(3-4), 534–550, doi:10.1016/j.epsl.2007.07.026.

- Holbourn, A., W. Kuhnt, M. W. Lyle, L. J. Schneider, O. Romero, and N. Andersen (2013), Middle Miocene climate cooling linked to intensification of eastern equatorial Pacific upwelling, *Geology*, 42(1), 19–22, doi:10.1130/G34890.1.
- Hoogakker, B., E. J. Rohling, M. Palmer, T. Tyrrell, and R. Rothwell (2006),
 Underlying causes for long-term global ocean δ¹³C fluctuations over the last 1.20
 Myr, Earth Planet. Sci. Lett., 248(1-2), 1–15, doi:10.1016/j.epsl.2006.05.007.
- Hooper, P. R. (1988), The Columbia River Basalt, in *Continental flood basalts*, edited by J. D. Macdougall, pp. 1–33, Kluwer Academic Publishers, Dordrecht, The Netherlands.
- Hooper, P. R. (1997), The Columbia River Flood Basalt: Current Status, in *Large igneous provinces: continental, oceanic, and planetary flood volcanism*, edited by J. J. Mahoney and M. F. Coffin, pp. 1–27, American Geophysical Union, Washington DC.
- Houben, A. J. P., C. A. van Mourik, A. Montanari, R. Coccioni, and H. Brinkhuis (2012), The Eocene-Oligocene transition: Changes in sea level, temperature or both?, *Palaeogeogr. Palaeoclimatol. Palaeoecol.*, 335-336, 75–83, doi:10.1016/j.palaeo.2011.04.008.
- Hsu, K. J., and J. A. Mckenzie (1985), A "Strangelove" Ocean in the Earliest Tertiary, in *The Carbon Cycle and Atmospheric CO₂: Natural Variations Archean to Present*, vol. 32, edited by E. T. Sundquist and W. S. Broecker, pp. 487–492, American Geophysical Union, Washington, D. C.
- Hull, P. M., et al. (in prep.), Disentangling Impact and Volcanism in Marine Extinctions across the Cretaceous-Paleogene Boundary.
- Iacono-Marziano, G., V. Marecal, M. Pirre, F. Gaillard, J. Arteta, B. Scaillet, and N. T. Arndt (2012), Gas emissions due to magma-sediment interactions during flood magmatism at the Siberian Traps: Gas dispersion and environmental consequences, *Earth Planet. Sci. Lett.*, 357-358, 308-318, doi:10.1016/j.epsl.2012.09.051.
- Ingersoll, A. P. (1969), The Runaway Greenhouse: A History of Water on Venus, *J. Atmos. Sci.*, *26*(6), 1191–1198, doi:10.1175/1520-0469(1969)026<1191:TRGAHO>2.0.CO;2.
- IPCC (2001), Climate Change 2001: The Scientific Basis, edited by J. T. Houghton, Y. Ding, D. J. Griggs, M. Noguer, P. J. van der Linden, X. Dai, K. Maskell, and C. A. Johnson, Cambridge University Press, Cambridge, United Kingdom and New York, NY, USA.
- IPCC (2013), Climate Change 2013: The Physical Science Basis. Contribution of Working Group I to the Fifth Assessment Report of the Intergovernmental Panel on Climate Change, edited by T. F. Stocker, G. D. Qin, K. Plattner, M. Tignor, S. K. Allen, J. Boschung, A. Nauels, Y. Xia, V. Bex, and P. M. Midgley, Cambridge University Press, Cambridge, United Kingdom and New York, NY, USA.
- Jansen, H., R. E. Zeebe, and D. A. Wolf-Gladrow (2002), Modeling the dissolution of settling CaCO₃ in the ocean, *Global Biogeochem. Cycles*, *16*(2), doi:10.1029/2000GB001279.

- Jarboe, N. A., R. S. Coe, P. R. Renne, and J. M. G. Glen (2010), The age of the Steens reversal and the Columbia River Basalt Group, *Chem. Geol.*, 274(3-4), 158–168, doi:10.1016/j.chemgeo.2010.04.001.
- John, E. H., J. D. Wilson, P. N. Pearson, and A. Ridgwell (2014), Temperature-dependent remineralization and carbon cycling in the warm Eocene oceans, *Palaeogeogr. Palaeoclimatol. Palaeoecol.*, 413, 158–166, doi:10.1016/j.palaeo.2014.05.019.
- Karlstrom, L., and M. Richards (2011), On the evolution of large ultramafic magma chambers and timescales for flood basalt eruptions, *J. Geophys. Res.*, 116(B08216), 1–13, doi:10.1029/2010JB008159.
- Kasting, J. F. (1984), Comments on the BLAG model: the carbonate-silicate geochemical cycle and its effect on atmospheric carbon dioxide over the past 100 million years., *Am. J. Sci.*, 284(10), 1175–1182, doi:10.2475/ajs.284.10.1175.
- Keeling, C. D. (1973), The Carbon Dioxide Cycle: Reservoir Models to Depict the Exchange of Atmospheric Carbon Dioxide with the Oceans and Land Plants, *Chem. Low. Atmos.*, 251–329, doi:10.1007/978-1-4684-1986-3_6.
- Kéfi, S., V. Dakos, M. Scheffer, E. H. Van Nes, and M. Rietkerk (2013), Early warning signals also precede non-catastrophic transitions, *Oikos*, *122*(5), 641–648, doi:10.1111/j.1600-0706.2012.20838.x.
- Kender, S., V. L. Peck, R. W. Jones, and M. A. Kaminski (2009), Middle Miocene oxygen minimum zone expansion offshore West Africa: Evidence for global cooling precursor events, *Geology*, 37(8), 699–702, doi:10.1130/G30070A.1.
- Kender, S., J. Yu, and V. L. Peck (2014), Deep ocean carbonate ion increase during mid Miocene CO₂ decline, *Sci. Rep.*, 4(4187), 1–6, doi:10.1038/srep04187.
- Kennett, J., and N. Shackleton (1976), Oxygen isotopic evidence for the initiation of the psychrosphere 38 Myr ago, *Nature*, *260*, 513–515.
- Kennett, J. P. (1977), Cenozoic Evolution of Antarctic Glaciation, the Circum-Antarctic Ocean, and Their Impact on Global Paleoceanography, *J. Geophys. Res.*, 82(27), 3843–3860.
- Kennett, J. P., and B. P. Flower (1993), Relations between Monterey Formation deposition and middle Miocene global cooling: Naples Beach section, California, *Geology*, 21(10), 877–880.
- Kent, D. V, and G. Muttoni (2008), Equatorial convergence of India and early Cenozoic climate trends., *Proc. Natl. Acad. Sci. U. S. A.*, 105(42), 16065–16070, doi:10.1073/pnas.0805382105.
- Kent, D. V., and G. Muttoni (2013), Modulation of Late Cretaceous and Cenozoic climate by variable drawdown of atmospheric pCO₂ from weathering of basaltic provinces on continents drifting through the equatorial humid belt, *Clim. Past*, 9(2), 525–546, doi:10.5194/cp-9-525-2013.

- Kirschvink, J. L. (1992), Late Proterozoic low-latitude global glaciation: the snowball Earth, in *The Proterozoic Biosphere: A Multidisciplinary Study*, edited by J. W. Schopf and C. Klein, pp. 51–52, Cambridge University Press, Cambridge, UK; New York, USA; Melbourna, Australia.
- Kirtland Turner, S., P. F. Sexton, C. D. Charles, and R. D. Norris (2014), Persistence of carbon release events through the peak of early Eocene global warmth, *Nat. Geosci.*, 7(10), 748–751, doi:10.1038/ngeo2240.
- Klinger, L. F. (1991), Peatland formation and ice ages: A possible Gaian mechanism related to community succession, in *Scientists on Gaia*, edited by S. Schneider and P. Boston, pp. 247–255, MIT Press, Cambridge, MA (United States).
- Klinger, L. F., J. A. Taylor, and L. G. Franzen (1996), The Potential Role of Peatland Dynamics in Ice-Age Initiation, *Quat. Res.*, 45(1), 89–92, doi:10.1006/qres.1996.0008.
- Knorr, G., M. Butzin, A. Micheels, and G. Lohmann (2011), A warm Miocene climate at low atmospheric CO₂ levels, *Geophys. Res. Lett.*, 38(20), 1–5, doi:10.1029/2011GL048873.
- Komar, N., and R. E. Zeebe (2011), Oceanic calcium changes from enhanced weathering during the Paleocene-Eocene thermal maximum: No effect on calcium-based proxies, *Paleoceanography*, 26(PA3211), 1–13, doi:10.1029/2010PA001979.
- Koven, C. D., B. Ringeval, P. Friedlingstein, P. Ciais, P. Cadule, D. Khvorostyanov, G. Krinner, and C. Tarnocai (2011), Permafrost carbon-climate feedbacks accelerate global warming., *Proc. Natl. Acad. Sci. U. S. A.*, (15), doi:10.1073/pnas.1103910108.
- Kump, L. R., and M. A. Arthur (1997), Global Chemical Erosion during the Cenozoic: Weatherability Balances the Budgets, in *Tectonic uplift and climate change*, edited by W. F. Ruddiman, pp. 399–426, Springer US, Boston, MA.
- Kump, L. R., and M. A. Arthur (1999), Interpreting carbon-isotope excursions: carbonates and organic matter, *Chem. Geol.*, 161(1-3), 181–198, doi:10.1016/S0009-2541(99)00086-8.
- Kump, L. R., J. F. Kasting, and R. G. Crane (1999), *The Earth System*, 1st ed., Prentice Hall, New Jersey.
- Kump, L. R., S. L. Brantley, and M. A. Arthur (2000), Chemical Weathering, Atmospheric CO₂, and Climate, *Annu. Rev. Earth Planet. Sci.*, 28(1), 611–667, doi:10.1146/annurev.earth.28.1.611.
- Kürschner, W. M., Z. Kvacek, and D. L. Dilcher (2008), The impact of Miocene atmospheric carbon dioxide fluctuations on climate and the evolution of terrestrial ecosystems, *Proc. Natl. Acad. Sci. U. S. A.*, 105(2), 449–53, doi:10.1073/pnas.0708588105.
- Ladant, J.-B., Y. Donnadieu, and C. Dumas (2014a), Links between CO₂, glaciation and water flow: reconciling the Cenozoic history of the Antarctic Circumpolar Current, *Clim. Past*, 10(6), 1957–1966, doi:10.5194/cp-10-1957-2014.

- Ladant, J.-B., Y. Donnadieu, V. Lefebvre, and C. Dumas (2014b), The respective role of atmospheric carbon dioxide and orbital parameters on ice sheet evolution at the Eocene-Oligocene transition, *Paleoceanography*, 29(8), 810–823, doi:10.1002/2013PA002593.
- LaMaskin, T. A., J. D. Vervoort, R. J. Dorsey, and J. E. Wright (2011), Early Mesozoic paleogeography and tectonic evolution of the western United States: Insights from detrital zircon U-Pb geochronology, Blue Mountains Province, northeastern Oregon, *Geol. Soc. Am. Bull.*, 123(9-10), 1939–1965, doi:10.1130/B30260.1.
- Larson, R. L. (1991), Latest pulse of Earth: Evidence for a mid-Cretaceous superplume, *Geology*, 19, 547–550, doi:10.1130/0091-7613(1991)019<0547.
- Lasmanis, R. (1991), The geology of Washington, Rocks Miner., 66(4), 262–277.
- Lear, C. H. (2000), Cenozoic Deep-Sea Temperatures and Global Ice Volumes from Mg/Ca in Benthic Foraminiferal Calcite, *Science*, 287(5451), 269–272, doi:10.1126/science.287.5451.269.
- Lear, C. H., and Y. Rosenthal (2006), Benthic foraminiferal Li/Ca: Insights into Cenozoic seawater carbonate saturation state, *Geology*, 34(11), 985, doi:10.1130/G22792A.1.
- Lear, C. H., Y. Rosenthal, H. K. Coxall, and P. A. Wilson (2004), Late Eocene to early Miocene ice sheet dynamics and the global carbon cycle, *Paleoceanography*, 19(PA4015), 1–11, doi:10.1029/2004PA001039.
- Lear, C. H., T. R. Bailey, P. N. Pearson, H. K. Coxall, and Y. Rosenthal (2008), Cooling and ice growth across the Eocene-Oligocene transition, *Geology*, 36(3), 251, doi:10.1130/G24584A.1.
- Lee, G. H., S. C. Park, and D. C. Kim (2000), Fluctuations of the calcite compensation depth (CCD) in the East Sea (Sea of Japan), *Geo-Marine Lett.*, 20(1), 20–26, doi:10.1007/s003670000029.
- Lefebvre, V., Y. Donnadieu, Y. Goddéris, F. Fluteau, and L. Hubert-Théou (2013), Was the Antarctic glaciation delayed by a high degassing rate during the early Cenozoic?, *Earth Planet. Sci. Lett.*, 1–9, doi:10.1016/j.epsl.2013.03.049.
- Lenton, T. M. (2011), Early warning of climate tipping points, *Nat. Clim. Chang.*, 1(4), 201–209, doi:10.1038/nclimate1143.
- Lenton, T. M. (2013), Environmental Tipping Points, *Annu. Rev. Environ. Resour.*, 38(1), 1–29, doi:10.1146/annurev-environ-102511-084654.
- Lenton, T. M., V. N. Livina, V. Dakos, and M. Scheffer (2012a), Climate bifurcation during the last deglaciation?, *Clim. Past*, 8(4), 1127–1139, doi:10.5194/cp-8-1127-2012.
- Lenton, T. M., V. N. Livina, V. Dakos, E. H. van Nes, and M. Scheffer (2012b), Early warning of climate tipping points from critical slowing down: comparing methods to improve robustness., *Philos. Trans. A. Math. Phys. Eng. Sci.*, 370(1962), 1185–204, doi:10.1098/rsta.2011.0304.

- Li, G., J. Ji, J. Chen, and D. B. Kemp (2009), Evolution of the Cenozoic carbon cycle: The roles of tectonics and CO₂ fertilization, *Global Biogeochem. Cycles*, 23(1), 1–11, doi:10.1029/2008GB003220.
- Liebrand, D., L. J. Lourens, D. A. Hodell, B. De Boer, R. S. W. Van De Wal, and H. Pälike (2011), Antarctic ice sheet and oceanographic response to eccentricity forcing during the early Miocene, *Clim. Past*, 7(3), 869–880, doi:10.5194/cp-7-869-2011.
- Lisiecki, L. E., and M. E. Raymo (2005), A Pliocene-Pleistocene stack of 57 globally distributed benthic δ¹⁸O records, *Paleoceanography*, 20(PA1003), 1–17, doi:10.1029/2004PA001071.
- Littler, K., U. Röhl, T. Westerhold, and J. C. Zachos (2014), A high-resolution benthic stable-isotope record for the South Atlantic: Implications for orbital-scale changes in Late Paleocene–Early Eocene climate and carbon cycling, *Earth Planet. Sci. Lett.*, 401, 18–30, doi:10.1016/j.epsl.2014.05.054.
- Liu, L., and D. R. Stegman (2012), Origin of Columbia River flood basalt controlled by propagating rupture of the Farallon slab., *Nature*, 482(7385), 386–9, doi:10.1038/nature10749.
- Liu, Z., M. Pagani, D. Zinniker, R. M. DeConto, M. Huber, H. Brinkhuis, S. R. Shah, R. M. Leckie, and A. Pearson (2009), Global Cooling During the Eocene-Oligocene Climate Transition, *Science*, 323(5918), 1187–1190.
- Loptson, C. A., D. J. Lunt, and J. E. Francis (2014), Investigating vegetation—climate feedbacks during the early Eocene, *Clim. Past*, 10(2), 419–436, doi:10.5194/cp-10-419-2014.
- Lovelock, J. E. (1972), Gaia as seen through the atmosphere, *Atmos. Environ.*, *6*(8), 579–580, doi:10.1016/0004-6981(72)90076-5.
- Lovelock, J. E. (1979), Gaia: A new look at life on earth, Oxford University Press.
- Lovelock, J. E., and L. Margulis (1974), Atmospheric homeostasis by and for the biosphere: the gaia hypothesis, *Tellus A*, *26*(1-2), 1–2, doi:10.3402/tellusa.v26i1-2.9731.
- Lunt, D. J., A. M. Haywood, G. A. Schmidt, U. Salzmann, P. J. Valdes, and H. J. Dowsett (2010), Earth system sensitivity inferred from Pliocene modelling and data, *Nat. Geosci.*, 3(1), 60–64, doi:10.1038/ngeo706.
- Lyle, M., A. Olivarez Lyle, J. Backman, and A. Tripati (2005), Biogenic Sedimentation in the Eocene Equatorial Pacific-The Stuttering Greenhouse and Eocene Carbonate Compensation Depth, in *Proceedings of the Ocean Drilling Program*, 199 Scientific Results, vol. 199, Ocean Drilling Program.
- Lyle, M., J. Barron, T. J. Bralower, M. Huber, A. O. Lyle, A. C. Ravelo, D. K. Rea, and P. A. Wilson (2008), Pacific ocean and cenozoic evolution of climate, *Rev. Geophys.*, 46(2), 1–47, doi:10.1029/2005RG000190.

- Lyle, M. W. (2003), Neogene carbonate burial in the Pacific Ocean, *Paleoceanography*, 18(3), 1–19, doi:10.1029/2002PA000777.
- Lyle, M. W., H. Pälike, H. Nishi, I. Raffi, K. Gamage, and A. Klaus (2010), The Pacific Equatorial Age Transect, IODP Expeditions 320 and 321: Building a 50-Million-Year-Long Environmental Record of the Equatorial Pacific Ocean, *Sci. Drill.*, (9, April 2010), doi:10.2204/iodp.sd.9.01.2010.
- MacDonald, G. M., D. W. Beilman, K. V Kremenetski, Y. Sheng, L. C. Smith, and A. A. Velichko (2006), Rapid early development of circumarctic peatlands and atmospheric CH₄ and CO₂ variations., *Science*, 314(5797), 285–8, doi:10.1126/science.1131722.
- Martínez-Botí, M. A., G. L. Foster, T. B. Chalk, E. J. Rohling, P. F. Sexton, D. J. Lunt, R. D. Pancost, M. P. S. Badger, and D. N. Schmidt (2015), Plio-Pleistocene climate sensitivity evaluated using high-resolution CO₂ records, *Nature*, *518*, 49–54, doi:10.1038/nature14145.
- Maslin, M. A., X. S. Li, M. F. Loutre, and A. Berger (1998), The contribution of orbital forcing to the progressive intensification of Northern Hemisphere glaciation, *Quat. Sci. Rev.*, 17(4-5), 411–426, doi:10.1016/S0277-3791(97)00047-4.
- Mawbey, E. M., and C. H. Lear (2013), Carbon cycle feedbacks during the Oligocene-Miocene transient glaciation, *Geology*, 41(9), 963–966, doi:10.1130/G34422.1.
- McInerney, F. A., and S. L. Wing (2011), The Paleocene-Eocene Thermal Maximum: A Perturbation of Carbon Cycle, Climate, and Biosphere with Implications for the Future, *Annu. Rev. Earth Planet. Sci.*, 39(1), 489–516, doi:10.1146/annurevearth-040610-133431.
- McNeall, D., P. R. Halloran, P. Good, and R. A. Betts (2011), Analyzing abrupt and nonlinear climate changes and their impacts, *Wiley Interdiscip. Rev. Clim. Chang.*, 2(5), 663–686, doi:10.1002/wcc.130.
- Menand, T., and J. C. Phillips (2007), Gas segregation in dykes and sills, *J. Volcanol. Geotherm. Res.*, 159, 393–408, doi:10.1016/j.jvolgeores.2006.08.003.
- Merico, A., T. Tyrrell, and P. A. Wilson (2008), Eocene/Oligocene ocean deacidification linked to Antarctic glaciation by sea-level fall., *Nature*, *452*(7190), 979–82, doi:10.1038/nature06853.
- Miller, K. G., J. D. Wright, and G. Fairbanks (1991), Unlocking the Ice House: Oligocene-Miocene Oxygen Isotopes, Eustasy, and Margin Erosion, *J. Geophys. Res.*, 96(B4), 6829–6848.
- Miller, K. G., J. V. Browning, M.-P. Aubry, B. S. Wade, M. E. Katz, A. A. Kulpecz, and J. D. Wright (2008), Eocene-Oligocene global climate and sea-level changes: St. Stephens Quarry, Alabama, *Geol. Soc. Am. Bull.*, 120(1-2), 34–53, doi:10.1130/B26105.1.
- Miller, K. G., J. D. Wright, M. E. Katz, B. S. Wade, J. V. Browning, and B. S. Cramer (2009), Climate threshold at the Eocene-Oligocene transition: Antarctic ice sheet influence on ocean circulation, in *SPE452: The Late Eocene Earth—Hothouse*,

- Icehouse, and Impacts: Geological Society of America Special Paper 452, vol. 80301, The Geological Society of America, Boulder, CO.
- Miller, K. G., J. D. Wright, J. V. Browning, A. Kulpecz, M. Kominz, T. R. Naish, B. S. Cramer, Y. Rosenthal, W. R. Peltier, and S. Sosdian (2012), High tide of the warm pliocene: Implications of global sea level for Antarctic deglaciation, Geology, 40(5), 407–410, doi:10.1130/G32869.1.
- Misra, S., and P. N. Froelich (2012), Lithium Isotope History of Cenozoic Seawater: Changes in Silicate Weathering and Reverse Weathering., *Science*, 335, 818–823, doi:10.1126/science.1214697.
- Moore, T. C. J. (2013), Erosion and reworking of Pacific sediments near the Eocene-Oligocene boundary, *Paleoceanography*, 28(2), 263–273, doi:10.1002/palo.20027.
- Mucci, A., and J. W. Morse (1984), The solubility of calcite in seawater solutions of various magnesium concentration, It = 0.697 m at 25°C and one atmosphere total pressure, *Geochim. Cosmochim. Acta*, 48(1984), 815–822.
- Müller, R. D., M. Sdrolias, C. Gaina, and W. R. Roest (2008), Age, spreading rates, and spreading asymmetry of the world's ocean crust, *Geochemistry Geophys. Geosystems*, 9(4), 1–19, doi:10.1029/2007GC001743.
- Munhoven, G. (2002), Glacial interglacial changes of continental weathering: flux variations estimates of the related CO₂ and HCO₃ and their uncertainties, *Glob. Planet. Change*, 33, 155–176.
- Nakamori, T. (2001), Global carbonate accumulation rates from Cretaceous to Present and their implications for the carbon cycle model, *Isl. Arc*, 10, 1–8.
- Oehlert, A. M., K. A. Lamb-Wozniak, Q. B. Devlin, G. J. Mackenzie, J. J. G. Reijmer, and P. K. Swart (2012), The stable carbon isotopic composition of organic material in platform derived sediments: Implications for reconstructing the global carbon cycle, *Sedimentology*, 59(1), 319–335, doi:10.1111/j.1365-3091.2011.01273.x.
- Ogg, J. G., and A. G. Smith (2004), The geomagnetic polarity time scale, in *A Geologic Time Scale*, edited by F. M. Gradstein, J. G. Ogg, and A. G. Smith, pp. 63–86, Cambridge University Press.
- Ohtomo, Y., T. Kakegawa, A. Ishida, T. Nagase, and M. T. Rosing (2014), Evidence for biogenic graphite in early Archaean Isua metasedimentary rocks, *Nat. Geosci.*, 7(1), 25–28, doi:10.1038/ngeo2025.
- Okay, A. I., M. Zattin, and W. Cavazza (2010), Apatite fission-track data for the Miocene Arabia-Eurasia collision, *Geology*, 38(1), 35–38, doi:10.1130/G30234.1.
- Olivarez Lyle, A., and M. W. Lyle (2006), Missing organic carbon in Eocene marine sediments: Is metabolism the biological feedback that maintains end-member climates?, *Paleoceanography*, 21(PA2007), 1–13, doi:10.1029/2005PA001230.
- Opdyke, B. N., and B. H. Wilkinson (1988), Surface area control of shallow cratonic to deep marine carbonate accumulation, *Paleoceanography*, *3*(6), 685–703.

- Pagani, M., M. Huber, Z. Liu, S. M. Bohaty, J. Henderiks, W. Sijp, S. Krishnan, and R. M. DeConto (2011), The role of carbon dioxide during the onset of Antarctic glaciation., *Science*, 334(6060), 1261–4, doi:10.1126/science.1203909.
- Pälike, H., R. D. Norris, J. O. Herrle, P. A. Wilson, H. K. Coxall, C. H. Lear, N. J. Shackleton, A. K. Tripati, and B. S. Wade (2006), The Heartbeat of the Oligocene Climate System, *Science*, 314(5807), 1894–1898, doi:10.1126/science.1133822.
- Pälike, H. et al. (2012), A Cenozoic record of the equatorial Pacific carbonate compensation depth, *Nature*, 488(7413), 609–614, doi:10.1038/nature11360.
- Palmer, M. R., and H. Elderfield (1985), Sr isotope composition of sea water over the past 75 Myr, *Nature*, 314(6011), 526–528, doi:10.1038/314526a0.
- Panchuk, K., A. J. Ridgwell, and L. R. Kump (2008), Sedimentary response to Paleocene-Eocene Thermal Maximum carbon release: A model-data comparison, *Geology*, 36(4), 315, doi:10.1130/G24474A.1.
- Park, J., and D. L. Royer (2011), Geologic constraints on the glacial amplification of Phanerozoic climate sensitivity, *Am. J. Sci.*, *311*(1), 1–26, doi:10.2475/01.2011.01.
- Parrish, J. T. (1985), Latitudinal distribution of land and shelf and absorbed solar radiation during the Phanerozoic, *USGS Open-File Rep. 85-31*, 1–21.
- Passchier, S., G. Browne, B. Field, C. R. Fielding, L. A. Krissek, K. Panter, and S. F. Pekar (2011), Early and middle Miocene Antarctic glacial history from the sedimentary facies distribution in the AND-2A drill hole, Ross Sea, Antarctica, *Geol. Soc. Am. Bull.*, 123(11-12), 2352–2365, doi:10.1130/B30334.1.
- Pavlov, A. A., J. F. Kasting, L. L. Brown, K. A. Rages, and R. Freedman (2000), Greenhouse warming by CH₄ in the atmosphere of early Earth, *J. Geophys. Res.*, 105(E5), 11981, doi:10.1029/1999JE001134.
- Payne, J. L., and L. R. Kump (2007), Evidence for recurrent Early Triassic massive volcanism from quantitative interpretation of carbon isotope fluctuations, *Earth Planet. Sci. Lett.*, 256(1-2), 264–277, doi:10.1016/j.epsl.2007.01.034.
- Pearson, P. N., and M. R. Palmer (2000), Atmospheric carbon dioxide concentrations over the past 60 million years., *Nature*, 406(6797), 695–9, doi:10.1038/35021000.
- Pearson, P. N., G. L. Foster, and B. S. Wade (2009), Atmospheric carbon dioxide through the Eocene-Oligocene climate transition., *Nature*, 461(7267), 1110–3, doi:10.1038/nature08447.
- Pekar, S. F., N. Christie-Blick, M. A. Kominz, and K. G. Miller (2002), Calibration between eustatic estimates from backstripping and oxygen isotopic records for the Oligocene, *Geology*, 30(10), 903, doi:10.1130/0091-7613(2002)030<0903:CBEEFB>2.0.CO;2.
- Peucker-Ehrenbrink, B., and G. Ravizza (2000), The marine osmium isotope record, *Terra Nov.*, 12(5), 205–219, doi:10.1046/j.1365-3121.2000.00295.x.

- Peucker-Ehrenbrink, B., G. Ravizza, and A. W. Hofmann (1995), The marine ¹⁸⁷Os/¹⁸⁶Os record of the past 80 million years, *Earth Planet. Sci. Lett.*, 130(1-4), 155–167, doi:10.1016/0012-821X(95)00003-U.
- Prothero, D. R. (1994), The Late Eocene-Oligocene Extinctions, *Annu. Rev. Earth Planet. Sci.*, 22(1), 145–165, doi:10.1146/annurev.ea.22.050194.001045.
- Ramos, F. C., J. A. Wolff, W. Starkel, A. Eckberg, D. L. Tollstrup, and S. Scott (2013), The changing nature of sources associated with Columbia River fl ood basalts: Evidence from strontium isotope ratio variations in plagioclase phenocrysts, *Geol. Soc. Am. Spec. Pap.*, 497, 231–257, doi:10.1130/2013.2497(09).
- Rampino, M. R., and K. Caldeira (1994), The Goldilocks Problem: Climatic Evolution and Long-Term Habitability of Terrestrial Planets, *Annu. Rev. Astron. Astrophys.*, 32(1), 83–114, doi:10.1146/annurev.aa.32.090194.000503.
- Rasool, S. I., and C. De Bergh (1970), The runaway greenhouse and the accumulation of CO₂ in the Venus atmosphere., *Nature*, *226*(5250), 1037–1039, doi:10.1038/2261037a0.
- Raymo, M. E. (1994), The Himalayas, organic carbon burial, and climate in the Miocene, *Paleoceanography*, *9*(3), 399, doi:10.1029/94PA00289.
- Raymo, M. E., and W. F. Ruddiman (1992), Tectonic forcing of late Cenozoic climate, *Nature*, 359, 117–122.
- Raymo, M. E., W. F. Ruddiman, and P. N. Froelich (1988), Influence of late Cenozoic mountain building on ocean geochemical cycles, *Geology*, *16*(7), 649, doi:10.1130/0091-7613(1988)016<0649:IOLCMB>2.3.CO;2.
- Rea, D. K., and M. W. Lyle (2005), Paleogene calcite compensation depth in the eastern subtropical Pacific: Answers and questions, *Paleoceanography*, 20(PA1012), 1–9, doi:10.1029/2004PA001064.
- Reidel, S. P., and T. L. Tolan (2013), The Grande Ronde Basalt, Columbia River Basalt Group, *Geol. Soc. Am. Spec. Pap.*, 497, 117–153, doi:10.1130/2013.2497(05).For.
- Reidel, S. P., V. E. Camp, T. L. Tolan, J. D. Kauffman, and D. L. Garwood (2013a), Tectonic evolution of the Columbia River flood basalt province, *Geol. Soc. Am. Spec. Pap.*, 497, 293–324, doi:10.1130/2013.2497(12).
- Reidel, S. P., V. E. Camp, T. L. Tolan, and B. S. Martin (2013b), The Columbia River flood basalt province: Stratigraphy, areal extent, volume, and physical volcanology, *Geol. Soc. Am. Spec. Pap.*, 497, 1–43, doi:10.1130/2013.2497(01).
- Retallack, G. J., and A. H. Jahren (2008), Methane Release from Igneous Intrusion of Coal during Late Permian Extinction Events, *J. Geol.*, 116(1), 1–20, doi:10.1086/524120.
- Revelle, R., and W. Munk (1977), The carbon dioxide cycle and the biosphere, in *Energy and Climate: Studies in Geophysics*, pp. 140–158.

- Revelle, R., and H. E. Suess (1957), Carbon Dioxide Exchange Between Atmosphere and Ocean and the Question of an Increase of Atmospheric CO₂ during the Past Decades, *Tellus*, 9(1), 18–27.
- Ridgwell, A. J., and J. C. Hargreaves (2007), Regulation of atmospheric CO₂ by deepsea sediments in an Earth system model, *Global Biogeochem. Cycles*, 21(2), 1–14, doi:10.1029/2006GB002764.
- Ridgwell, A. J. (2005), A Mid Mesozoic Revolution in the regulation of ocean chemistry, *Mar. Geol.*, 217(3-4), 339–357, doi:10.1016/j.margeo.2004.10.036.
- Ridgwell, A. J., J. C. Hargreaves, N. R. Edwards, J. D. Annan, T. M. Lenton, R. Marsh, A. Yool, and A. Watson (2007), Marine geochemical data assimilation in an efficient Earth System Model of global biogeochemical cycling, *Biogeosciences*, 4(1), 87–104, doi:10.5194/bg-4-87-2007.
- Robin, G. de Q. (1988), The Antarctic ice sheet, its history and response to sea level and climatic changes over the past 100 million years, *Palaeogeogr. Palaeoclimatol. Palaeoecol.*, 67(1-2), 31–50, doi:10.1016/0031-0182(88)90121-6.
- Rodriguez, S., and G. Sen (2013), Eruption of the Grande Ronde Basalt lavas, Columbia River Basalt Group: Results of numerical modeling, *Geol. Soc. Am. Spec. Pap.*, 497, 259–272, doi:10.1130/2013.2497(10).
- Rohling, E. J. et al. (2012), Making sense of palaeoclimate sensitivity., *Nature*, 491(7426), 683–91, doi:10.1038/nature11574.
- Royer, D. L., S. L. Wing, D. J. Beerling, D. W. Jolley, P. L. Koch, L. J. Hickey, and R. A. Berner (2001), Paleobotanical evidence for near present-day levels of atmospheric CO₂ during part of the tertiary., *Science*, 292(5525), 2310–3, doi:10.1126/science.292.5525.2310.
- Royer, D. L., R. A. Berner, I. P. Montañez, N. J. Tabor, and D. J. Beerling (2004a), CO₂ as a primary driver of Phanerozoic climate, *GSA Today*, *14*(3), 4–10, doi:10.1130/1052-5173(2004)014<4.
- Royer, D. L., R. A. Berner, I. P. Montañez, N. J. Tabor, D. J. Beerling, N. Shaviv, and J. Veizer (2004b), Comment and Reply CO₂ as a primary driver of Phanerozoic climate, *GSA Today*, 14(3), 4–10.
- Sagan, C., and G. Mullen (1972), Earth and Mars: evolution of atmospheres and surface temperatures., *Science*, 177(4043), 52–56, doi:10.1126/science.177.4043.52.
- Salamy, K. A., and J. C. Zachos (1999), Latest Eocene–Early Oligocene climate change and Southern Ocean fertility: inferences from sediment accumulation and stable isotope data, *Palaeogeogr. Palaeoclimatol. Palaeoecol.*, 145(1-3), 61–77, doi:10.1016/S0031-0182(98)00093-5.
- Sandroni, S., and F. M. Talarico (2011), The record of Miocene climatic events in AND-2A drill core (Antarctica): Insights from provenance analyses of basement clasts, *Glob. Planet. Change*, 75(1-2), 31–46, doi:10.1016/j.gloplacha.2010.10.002.

- Schaller, M. F., J. D. Wright, D. V. Kent, and P. E. Olsen (2012), Rapid emplacement of the Central Atlantic Magmatic Province as a net sink for CO₂, *Earth Planet*. *Sci. Lett.*, 323-324, 27–39, doi:10.1016/j.epsl.2011.12.028.
- Schaller, M. F., J. D. Wright, and D. V. Kent (2014), A 30 Myr record of Late Triassic atmospheric pCO₂ variation reflects a fundamental control of the carbon cycle by changes in continental weathering, *Geol. Soc. Am. Bull.*, (X), 1–11, doi:10.1130/B31107.1.
- Scheffer, M., J. Bascompte, W. A. Brock, V. Brovkin, S. R. Carpenter, V. Dakos, H. Held, E. H. van Nes, M. Rietkerk, and G. Sugihara (2009), Early-warning signals for critical transitions., *Nature*, 461(7260), 53–9, doi:10.1038/nature08227.
- Scheffer, M. et al. (2012), Anticipating critical transitions., *Science*, 338(6105), 344–8, doi:10.1126/science.1225244.
- Scher, H. D., and E. E. Martin (2006), Timing and climatic consequences of the opening of Drake Passage., *Science*, 312(5772), 428–30, doi:10.1126/science.1120044.
- Scher, H. D., S. M. Bohaty, J. C. Zachos, and M. L. Delaney (2011), Two-stepping into the icehouse: East Antarctic weathering during progressive ice-sheet expansion at the Eocene-Oligocene transition, *Geology*, 39(4), 383–386, doi:10.1130/G31726.1.
- Schoene, B., K. M. Samperton, M. P. Eddy, G. Keller, T. Adatte, S. A. Bowring, S. F. R. Khadri, and B. Gertsch (2015), Earth history. U-Pb geochronology of the Deccan Traps and relation to the end-Cretaceous mass extinction., *Science*, 347(6218), 182–4, doi:10.1126/science.aaa0118.
- Sclater, J. G., E. Boyle, and J. M. Edmond (1979), A Quantitative Analysis of some factors affecting Carbonate Sedimentation in the Oceans, in *Deep Drilling Results in the Atlantic Ocean: Continental Margins and Paleoenvironment*, vol. 3, edited by M. Talwani, W. Hay, and W. B. F. Ryan, pp. 235–248, American Geophysical Union, Washington D.C.
- Self, S., M. Widdowson, T. Thordarson, and A. E. Jay (2006), Volatile fluxes during flood basalt eruptions and potential effects on the global environment: A Deccan perspective, *Earth Planet. Sci. Lett.*, 248(1-2), 518–532, doi:10.1016/j.epsl.2006.05.041.
- Shaviv, N. J., and J. Veizer (2003), Celestial driver of Phanerozoic climate?, *GSA Today*, 13(7), 4, doi:10.1130/1052-5173(2003)013<0004:CDOPC>2.0.CO;2.
- Shellito, C., L. C. Sloan, and M. Huber (2003), Climate model sensitivity to atmospheric CO₂ levels in the Early–Middle Paleogene, *Palaeogeogr. Palaeoclimatol. Palaeoecol.*, 193(1), 113–123, doi:10.1016/S0031-0182(02)00718-6.
- Shevenell, A. E., J. P. Kennett, and D. W. Lea (2008), Middle Miocene ice sheet dynamics, deep-sea temperatures, and carbon cycling: A Southern Ocean perspective, *Geochemistry Geophys. Geosystems*, 9(2), doi:10.1029/2007GC001736.
- Shinohara, H. (2008), Excess degassing from volcanoes and its role on eruptive and intrusive activity, *Rev. Geophys.*, 46(2007), 1–31, doi:10.1029/2007RG000244.

- Siegenthaler, U., and H. Oeschger (1978), Predicting Future Atmospheric Carbon Dioxide Levels, *Science*, 199(4327), 388–395.
- Sigman, D. M., D. C. McCorkle, and W. R. Martin (1998), The calcite lysocline as a constraint on glacial/interglacial low-latitude production changes, *Global Biogeochem. Cycles*, 12(3), 409, doi:10.1029/98GB01184.
- Sijp, W. P., M. H. England, and M. Huber (2011), Effect of the deepening of the Tasman Gateway on the global ocean, *Paleoceanography*, *26*(PA4207), 1–18, doi:10.1029/2011PA002143.
- Sijp, W. P., A. S. von der Heydt, H. A. Dijkstra, S. Flögel, P. M. J. Douglas, and P. K. Bijl (2014), The role of ocean gateways on cooling climate on long time scales, *Glob. Planet. Change*, 119, 1–22, doi:10.1016/j.gloplacha.2014.04.004.
- Sluijs, A., R. E. Zeebe, P. K. Bijl, and S. M. Bohaty (2013), A middle Eocene carbon cycle conundrum, *Nat. Geosci.*, *6*(6), 429–434, doi:10.1038/ngeo1807.
- Smith, A. G., and K. T. Pickering (2003), Oceanic gateways as a critical factor to initiate icehouse Earth, , 160, 337–340, doi:10.1144/0016-764902-115.
- Sobolev, S. V., A. V. Sobolev, D. V. Kuzmin, N. A. Krivolutskaya, A. G. Petrunin, N. T. Arndt, V. A. Radko, and Y. R. Vasiliev (2011), Linking mantle plumes, large igneous provinces and environmental catastrophes, *Nature*, 477(7364), 312–316, doi:10.1038/nature10385.
- Spero, H. J., J. Bijma, D. W. Lea, and B. E. Bemis (1997), Effect of seawater carbonate concentration on foraminiferal carbon and oxygen isotopes, *Nature*, 390(6659), 497–500, doi:10.1038/37333.
- Spofforth, D. J. A., C. Agnini, H. Pälike, D. Rio, E. Fornaciari, L. Giusberti, V. Luciani, L. Lanci, and G. Muttoni (2010), Organic carbon burial following the middle Eocene climatic optimum in the central western Tethys, *Paleoceanography*, 25(PA3210), 1–11, doi:10.1029/2009PA001738.
- Sundquist, E. T. (1986), Geologic analogs: Their value and limitations in carbon dioxide research, in *The Changing Carbon Cycle*, pp. 371–402, Springer, New York.
- Svensen, H., S. Planke, A. Malthe-Sørenssen, B. Jamtveit, R. Myklebust, T. Rasmussen Eidem, and S. S. Rey (2004), Release of methane from a volcanic basin as a mechanism for initial Eocene global warming, *Nature*, 429(6991), 542–545, doi:10.1038/nature02566.
- Svensen, H., S. Planke, A. G. Polozov, N. Schmidbauer, F. Corfu, Y. Y. Podladchikov, and B. Jamtveit (2009), Siberian gas venting and the end-Permian environmental crisis, *Earth Planet. Sci. Lett.*, 277(3-4), 490–500, doi:10.1016/j.epsl.2008.11.015.
- Swart, P. K. (2008), Global synchronous changes in the carbon isotopic composition of carbonate sediments unrelated to changes in the global carbon cycle., *Proc. Natl. Acad. Sci. U. S. A.*, 105(37), 13741–13745, doi:10.1073/pnas.0802841105.

- Swart, P. K., and G. Eberli (2005), The nature of the δ^{13} C of periplatform sediments: Implications for stratigraphy and the global carbon cycle, *Sediment. Geol.*, 175, 115–129, doi:10.1016/j.sedgeo.2004.12.029.
- Swart, P. K., J. J. G. Reijmer, and R. Otto (2009), A re-evaluation of facies on Great Bahama Bank II: variations in the δ¹³C, δ¹⁸O and mineralogy of surface sediments, *Int. Assoc. Sedimentol. Spec. Publ.*, 41, 47–59, doi:10.1002/9781444312065.ch4.
- Tarnocai, C., J. G. Canadell, E. A. G. Schuur, P. Kuhry, G. Mazhitova, and S. Zimov (2009), Soil organic carbon pools in the northern circumpolar permafrost region, *Global Biogeochem. Cycles*, 23(GB2023), 1–11, doi:10.1029/2008GB003327.
- Taylor, A. S., and A. C. Lasaga (1999), The role of basalt weathering in the Sr isotope budget of the oceans, *Chem. Geol.*, *161*(1-3), 199–214, doi:10.1016/S0009-2541(99)00087-X.
- Thordarson, T., and S. Self (1996), Sulfur, chlorine and fluorine degassing and atmospheric loading by the Roza eruption, Columbia River Basalt Group, Washington, USA, *J. Volcanol. Geotherm. Res.*, 74(1-2), 49–73, doi:10.1016/S0377-0273(96)00054-6.
- Tigchelaar, M., A. S. Von Der Heydt, and H. A. Dijkstra (2011), A new mechanism for the two-step δ¹⁸O signal at the Eocene-Oligocene boundary, *Clim. Past*, 7, 235– 247, doi:10.5194/cp-7-235-2011.
- Tyrrell, T. (1999), The relative influences of nitrogen and phosphorus on oceanic primary production, *Nature*, 400(6744), 525–531, doi:10.1038/22941.
- Tyrrell, T. (2013), On Gaia: a critical investigation of the relationship between life and earth, Princeton University Press, Princeton Meadows, USA.
- Tyrrell, T., and R. E. Zeebe (2004), History of carbonate ion concentration over the last 100 million years, *Geochim. Cosmochim. Acta*, 68(17), 3521–3530, doi:10.1016/j.gca.2004.02.018.
- Tyrrell, T., J. G. Shepherd, and S. Castle (2007), The long-term legacy of fossil fuels, *Tellus B*, *59*(4), 664–672, doi:10.1111/j.1600-0889.2007.00290.x.
- Tyrrell, T., A. Merico, and D. I. Armstrong McKay (2015), Severity of ocean acidification following the end-Cretaceous asteroid impact, *Proc. Natl. Acad. Sci.*, (5), 201418604, doi:10.1073/pnas.1418604112.
- Urey, H. C. (1952), The planets, their origin and development, *Mrs. Hepsa Ely Silliman Meml. Lect. Yale Univ.*
- Van Andel, T. H. (1975), Distribution of Calcareous Sediments, *Earth Planet. Sci. Lett.*, 26, 187–194.
- Van de Flierdt, T. (2011), Continental weathering through the onset of Antarctic glaciation, *Geology*, 39(4), 415–416, doi:10.1130/focus042011.1.

- Veizer, J. et al. (1999), ${}^{87}\mathrm{Sr}/{}^{86}\mathrm{Sr}$, $\delta^{13}\mathrm{C}$ and $\delta^{18}\mathrm{O}$ evolution of Phanerozoic seawater, *Chem. Geol.*, 161, 59–88.
- Veizer, J., Y. Goddéris, and L. M. François (2000), Evidence for decoupling of atmospheric CO₂ and global climate during the Phanerozoic eon., *Nature*, 408(6813), 698–701, doi:10.1038/35047044.
- Vincent, E., and W. H. Berger (1985), Carbon dioxide and polar cooling in the Miocene: The Monterey hypothesis, in *The Carbon Cycle and Atmospheric CO₂: Natural Variations Archean to Present, Geophys. Monogr. Ser., vol. 32*, vol. 32, edited by W. S. Broecker and E. T. Sundquist, pp. 455–468, AGU, Washington, D. C.
- Wade, B. S., and H. Pälike (2004), Oligocene climate dynamics, *Paleoceanography*, 19(PA4019), 1–16, doi:10.1029/2004PA001042.
- Wade, B. S., A. J. P. Houben, W. Quaijtaal, S. Schouten, Y. Rosenthal, K. G. Miller, M. E. Katz, J. D. Wright, and H. Brinkhuis (2011), Multiproxy record of abrupt sea-surface cooling across the Eocene-Oligocene transition in the Gulf of Mexico, Geology, 40(2), 159–162, doi:10.1130/G32577.1.
- Wadham, J. L. et al. (2012), Potential methane reservoirs beneath Antarctica., *Nature*, 488(7413), 633–7, doi:10.1038/nature11374.
- Walker, J. C. G. (1985), Carbon dioxide on the early Earth, *Orig. Life Evol. Biosph.*, 16, 117–127.
- Walker, J. C. G., and J. F. Kasting (1992), Effects of fuel and forest conservation on future levels of atmospheric carbon dioxide., *Palaeogeogr. Palaeoclimatol. Palaeoecol.*, 97(1902), 151–89.
- Walker, J. C. G., P. B. Hays, and J. F. Kasting (1981), A negative feedback mechanism for the long-term stabilization of Earth's surface temperature, *J. Geophys. Res.*, 86(C10), 9776–9782.
- Wallmann, K., E. Pinero, E. Burwicz, M. Haeckel, C. Hensen, A. Dale, and L. Ruepke (2012), The Global Inventory of Methane Hydrate in Marine Sediments: A Theoretical Approach, *Energies*, 5(12), 2449–2498, doi:10.3390/en5072449.
- Wang, R., J. A. Dearing, P. G. Langdon, E. Zhang, X. Yang, V. Dakos, and M. Scheffer (2012), Flickering gives early warning signals of a critical transition to a eutrophic lake state., *Nature*, 492(7429), 419–22, doi:10.1038/nature11655.
- Watson, A. J. (2004), Gaia and observer self-selection, in *Scientists Debate Gaia: The Next Century*, edited by S. H. Scheider, J. R. Miller, E. Crist, and P. J. Boston, pp. 201–208, MIT Press, Cambridge, MA (United States).
- Watson, A. J., and J. E. Lovelock (1983), Biological homeostasis of the global environment: the parable of Daisyworld, *Tellus B*, *35B*(4), 284–289, doi:10.1111/j.1600-0889.1983.tb00031.x.
- Westerhold, T., U. Röhl, B. Donner, H. K. McCarren, and J. C. Zachos (2011), A complete high-resolution Paleocene benthic stable isotope record for the central

- Pacific (ODP Site 1209), Global Biogeochem. Cycles, 25(2), 1–13, doi:10.1029/2011WR010620.
- Westerhold, T., U. Röhl, H. Pälike, R. Wilkens, P. A. Wilson, and G. Acton (2014), Orbitally tuned timescale and astronomical forcing in the middle Eocene to early Oligocene, *Clim. Past*, 10(3), 955–973, doi:10.5194/cp-10-955-2014.
- Wignall, P. (2001), Large igneous provinces and mass extinctions, *Earth-Science Rev.*, 53(1-2), 1–33.
- Wignall, P. (2005), The Link between Large Igneous Province Eruptions and Mass Extinctions, *Elements*, 1(5), 293–297.
- Willenbring, J. K., and F. von Blanckenburg (2010), Long-term stability of global erosion rates and weathering during late-Cenozoic cooling., *Nature*, *465*(7295), 211–4, doi:10.1038/nature09044.
- Wolff, J. A., and F. C. Ramos (2013), Source materials for the main phase of the Columbia River Basalt Group: Geochemical evidence and implications for magma storage and transport, *Geol. Soc. Am. Spec. Pap.*, 497, 273–291, doi:10.1130/2013.2497(11).
- Wolff, J. A., F. C. Ramos, G. L. Hart, J. D. Patterson, and A. D. Brandon (2008), Columbia River flood basalts from a centralized crustal magmatic system, *Nat. Geosci.*, 1(3), 177–180, doi:10.1038/ngeo124.
- Wright, D., G. Miller, and G. Fairbanks (1992), Early and Middle Miocene Stable isotopes: Implications for Deepwated Circulation and Climate, *Paleoceanography*, 7(3), 357–389.
- Yoshimura, S., and M. Nakamura (2012), Flux of volcanic CO₂ emission estimated from melt inclusions and fluid transport modelling, *Earth Planet. Sci. Lett.*, *361*, 497–503, doi:10.1016/j.epsl.2012.11.020.
- You, Y. (2010), Climate-model evaluation of the contribution of sea-surface temperature and carbon dioxide to the Middle Miocene Climate Optimum as a possible analogue of future climate change, *Aust. J. Earth Sci.*, *57*(2), 207–219, doi:10.1080/08120090903521671.
- You, Y., M. Huber, R. D. Müller, C. J. Poulsen, and J. Ribbe (2009), Simulation of the Middle Miocene Climate Optimum, *Geophys. Res. Lett.*, 36(4), 1–5, doi:10.1029/2008GL036571.
- Zachos, J. C., and L. R. Kump (2005), Carbon cycle feedbacks and the initiation of Antarctic glaciation in the earliest Oligocene, *Glob. Planet. Change*, 47(1), 51–66, doi:10.1016/j.gloplacha.2005.01.001.
- Zachos, J. C., T. M. Quinn, and K. A. Salamy (1996), High-resolution (10⁴ years) deep-sea foraminiferal stable isotope records of the Eocene-Oligocene climate transition, *Paleoceanography*, 11(3), 251–266.

- Zachos, J. C., B. N. Opdyke, T. M. Quinn, C. E. Jones, and A. N. Halliday (1999), Early cenozoic glaciation, antarctic weathering, and seawater: is there a link?, *Chem. Geol.*, 161(1-3), 165–180, doi:10.1016/S0009-2541(99)00085-6.
- Zachos, J. C., N. J. Shackleton, J. S. Revenaugh, H. Pälike, and B. P. Flower (2001a), Climate response to orbital forcing across the Oligocene-Miocene boundary., *Science*, 292(5515), 274–278, doi:10.1126/science.1058288.
- Zachos, J. C., M. Pagani, L. Sloan, E. Thomas, and K. Billups (2001b), Trends, rhythms, and aberrations in global climate 65 Ma to present., *Science*, *292*(5517), 686–93, doi:10.1126/science.1059412.
- Zachos, J. C. et al. (2005), Rapid acidification of the ocean during the Paleocene-Eocene thermal maximum., *Science*, 308(5728), 1611–5, doi:10.1126/science.1109004.
- Zachos, J. C., G. R. Dickens, and R. E. Zeebe (2008), An early Cenozoic perspective on greenhouse warming and carbon-cycle dynamics., *Nature*, *451*(7176), 279–83, doi:10.1038/nature06588.
- Zech, R., Y. Huang, M. Zech, R. Tarozo, and W. Zech (2011), High carbon sequestration in Siberian permafrost loess-paleosols during glacials, *Clim. Past*, 7(2), 501–509, doi:10.5194/cp-7-501-2011.
- Zeebe, R. E. (2012), LOSCAR: Long-term Ocean-atmosphere-Sediment CArbon cycle Reservoir Model v2.0.4, *Geosci. Model Dev.*, 5, 149–166, doi:10.5194/gmdd-4-1435-2011.
- Zeebe, R. E., and P. Westbroek (2003), A simple model for the CaCO₃ saturation state of the ocean: The "Strangelove," the "Neritan," and the "Cretan" Ocean, *Geochemistry Geophys. Geosystems*, 4(12), doi:10.1029/2003GC000538.
- Zeebe, R. E., and D. Wolf-Gladrow (2001), CO₂ in Seawater: Equilibrium, Kinetics, Isotopes, Elsevier Oceanography Series (65).
- Zeebe, R. E., and J. C. Zachos (2007), Reversed deep-sea carbonate ion basin gradient during Paleocene-Eocene thermal maximum, *Paleoceanography*, 22(PA3201), 1–17, doi:10.1029/2006PA001395.
- Zeebe, R. E., J. C. Zachos, K. Caldeira, and T. Tyrrell (2008), Carbon emissions and acidification., *Science*, 321(5885), 51–2, doi:10.1126/science.1159124.
- Zeebe, R. E., J. C. Zachos, and G. R. Dickens (2009), Carbon dioxide forcing alone insufficient to explain Palaeocene–Eocene Thermal Maximum warming, *Nat. Geosci.*, 2(8), 576–580, doi:10.1038/ngeo578.
- Zeng, N. (2003), Glacial-interglacial atmospheric CO₂ change —The glacial burial hypothesis, *Adv. Atmos. Sci.*, 20(5), 677–693, doi:10.1007/BF02915395.
- Zhang, Y. G., M. Pagani, Z. Liu, S. M. Bohaty, and R. M. DeConto (2013), A 40-million-year history of atmospheric CO₂, *Philos. Trans. R. Soc. London. Ser. A*, 371(20130096).

Zimov, N. S., S. A. Zimov, A. E. Zimova, G. M. Zimova, V. I. Chuprynin, and F. S. Chapin (2009), Carbon storage in permafrost and soils of the mammoth tundrasteppe biome: Role in the global carbon budget, *Geophys. Res. Lett.*, *36*(2), doi:10.1029/2008GL036332.